HAL open science

Li-rich Li3MO4 model compounds for deciphering capacity and voltage aspects in anionic redox materials

Quentin Jacquet

To cite this version:

Quentin Jacquet. Li-rich Li3MO4 model compounds for deciphering capacity and voltage aspects in anionic redox materials. Material chemistry. Sorbonne Université, 2018. English. NNT : 2018SORUS332 . tel-02796087v2

HAL Id: tel-02796087

https://theses.hal.science/tel-02796087v2

Submitted on 8 Jun 2020

HAL is a multi-disciplinary open access archive for the deposit and dissemination of scientific research documents, whether they are published or not. The documents may come from teaching and research institutions in France or abroad, or from public or private research centers.

L'archive ouverte pluridisciplinaire **HAL**, est destinée au dépôt et à la diffusion de documents scientifiques de niveau recherche, publiés ou non, émanant des établissements d'enseignement et de recherche français ou étrangers, des laboratoires publics ou privés.

Sorbonne Université

ED 397 – Physique et Chimie des Matériaux

Laboratoire de chimie du solide et énergie – Collège de France

Li-rich Li_3MO_4 model compounds for deciphering capacity and voltage aspects in anionic redox electrodes for Li-ion Batteries

By Quentin Jacquet

PhD thesis in Chemistry

Directed by Gwenaëlle Rousse and Jean-Marie Tarascon

Presented and defended in public on December 12th, 2018

In front of jury :

Dr. Jean-Pierre Pereira Ramos	Research Director, ICMPE, Thiais	Referee
Dr. Pierre Bordet	Research Director, Institut Néel, Grenoble	Referee
Prof. Teófilo Rojo	Professor, CIC Energigune, Miñano	Examiner
Dr. Antoine Maignan	Research Director, CRISMAT, Caen	Examiner
Dr. Olivier Mentré	Research Director, UCCS, Lille	Examiner
Prof. Xavier Carrier	Professor, Sorbonne Université, Paris	Examiner
Dr. Gwenaëlle Rousse	Associate Professor, Sorbonne Université, Paris	Director
Prof. Jean-Marie Tarascon	Professor, Collège de France, Paris	Director

Except where otherwise noted, this work is licensed under
http://creativecommons.org/licenses/by-nc-nd/3.0/

A ma famille, mes amis

Acknowledgement

Being very curious, I got passionate into doing research at the Collège de France. I had the freedom to choose my research topic and the opportunity to technically realize it, thanks to nice lab equipment, very helpful lab mates and great collaborations all around the world. I spent thrilling three years.

For having created this amazing lab and accepting me in during my PhD, I thank Jean-Marie Tarascon, my supervisor and director of the Chaire de chimie du solide et énergie. I appreciated the fact that he was always available for discussions and quite open towards trying new synthesis. I also thank Gwenaëlle Rousse, my supervisor, for teaching me crystallography, which really became a passion, and for her enthusiasm and support. I'll keep excellent memories of our refinement sessions or the FullProf and GDR schools. I spend some time in the group of Marie-Liesse Doublet, research director of CTMN lab in Montpellier, to learn about quantum chemistry with Matthieu Saubanère, associate researcher. It was quite a challenge to teach an experimentalist about theory, but they succeeded and I warmly thank both of them for their time and patience.

I thank all my lab mates for their help along these three years. I hope we can meet again in a scientific or personal context, and I wish them all the best for the future. I specially want to mention Alexis Grimaud, my office mate, with whom I had interesting scientific discussions and some afterwork beers. I also want to thank Sathiya Mariyappan for reading my manuscript and for our time sharing ideas, some of them actually turned into interesting and full studies. Antonella Iadecola is warmly acknowledged for her dedication on the beam times and for teaching me X-ray absorption spectroscopy. I also want to thank; the team working on anionic redox, Arnaud, Paul, Gaurav and Jean; Thomas for his help understanding the complex behavior of Ru in solution; Misae for having performed an amazing experimental work on the sodium ruthenates; Louis Lemarquis for his help with the gas analysis; Chunzhen Yang for testing some of my materials for water splitting; Laura, Vanessa, Jiwei and Pierre for their help with the glovebox management; and Daniel and Boris for the SEM images and the good time hiking/climbing in Fontainebleau forest.

At last, I want to thank all my collaborators: Dmitry Batuk (EMAT, Antwerp) for the splendide TEM images, Erik J. Berg (PSI, Villigen) for the OEMS mesurements, Haifeng Li (University of Chicago) and John W. Freeland (APS, Argonne) for the soft XAS experiments and discussion, Jordi Cabana (University of Chicago) for his critic corrections.

Table of Contents

Acknowledgement **I-4**

Table of Contents **I-6**

Introduction **1**

Chapter I State of the art **5**

I.1 Intercalation chemistry a wide topic including battery **5**

I.1.a Working principles of Li-ion battery 5

I.1.b Intercalation chemistry, definition and examples 6

I.1.c Evolution of cathode material for Li-ion battery 9

I.2 In the quest for high energy materials **13**

I.2.a Context and strategies: increasing the voltage or the capacity 13

I.2.b Strategies to increase the potential based on its rationalization 13

I.2.c Strategy to increase the capacity 18

I.3 Anionic redox, the theoretical understanding **21**

I.3.a Oxygen lone pairs responsible for the anionic redox 21

I.3.b Δ_{CT} and U parameters ruling the redox mechanism 22

I.3.c Strategies for the design of material showing anionic redox 24

I.3.d Electrochemical potential and reversibility of anionic redox 26

I.4 Conclusion **30**

Chapter II Exploring the limits of anionic redox in terms of capacity **33**

II.1 Introduction **33**

II.2 Synthesis, crystal structure and rationalization of the cation ordering in $Li_3M_yM'_{1-y}O_4$ compounds **35**

II.2.a Synthesis of $Li_3M_yM'_{1-y}O_4$ (M and M' being Ru, Nb, Sb, Ir, Ta) 37

II.2.b Structural characterization 38

II.2.c Rationalization of the different cation orderings using DFT calculations 56

II.2.d Partial conclusions 60

II.3 Mechanism of the electrochemical Li insertion/extraction from of $Li_3M_yM'_{1-y}O_4$ compounds **61**

II.3.a Li intercalation into the $Li_3Ru_yNb_{1-y}O_4$ 62

II.3.b Li extraction from Li_3RuO_4: degradation and charge compensation mechanisms 68

II.3.c Li extraction from $Li_3Ru_yNb_{1-y}O_4$ 78
II.3.d Li extraction from $Li_3Ru_yIr_{1-y}O_4$ 81
II.3.e Partial conclusions 86
II.4 Influence of the alkali atom on the anionic redox: the study of Na_3RuO_4 87
II.4.a Synthesis and crystal structure of Na_3RuO_4 and Na_2RuO_4 88
II.4.b Electrochemical properties of Na_3RuO_4 91
II.4.c Synthesis, structural characterization and stability of IE-Li_2RuO_4 100
II.4.d Electrochemical synthesis of Td-$NaRuO_4$ during Na removal from Na_2RuO_4 104
II.4.e Effect of the alkali on the anionic and cationic redox couples in Ru-based compounds 107
II.5 Conclusion of the chapter 109
Chapter III Unveiling different anionic redox potentials in Ni/Mn substituted Li_3TaO_4 111
III.1 Introduction 111
III.2 Synthesis, crystal structure and electrochemical signature of $Li_{1.3}Ni_{0.27}Ta_{0.43}O_2$ and $Li_{1.3}Mn_{0.4}Ta_{0.3}O_2$ 113
III.2.a Synthesis and crystal structure 113
III.2.b Electrochemical properties 115
III.3 Mechanism of Li removal in $Li_{1.3}Ni_{0.27}Ta_{0.43}O_2$ 116
III.3.a Effect of the state-of-charge 116
III.3.b X-ray absorption spectroscopy study 118
III.3.c Gas evolution 123
III.3.d Structural evolution 124
III.3.e Overall picture 126
III.4 Mechanism of Li removal in $Li_{1.3}Mn_{0.4}Ta_{0.3}O_2$ 127
III.4.a Effect of the state-of-charge 127
III.4.b X-ray absorption spectroscopy study 128
III.4.c Gas evolution 132
III.4.d Structural evolution 133
III.4.e Overall picture 134
III.5 Understanding the different anionic redox mechanisms using DFT calculations 135
III.5.a Construction and validation of structural models 135

III.5.b The band gap at the origin of the different anionic redox mechanism.....138
III.6 Conclusion of the chapter 140
Discussion and General Conclusion 143
Annexe 147
List of Figures..... 157
List of Tables 163
References..... 165

Introduction

Global warming is a major issue of the 21th century. It is caused by the high concentration of greenhouse gases, such as CO_2 or CH_4, in the atmosphere and is at the origin of the increase of the sea level, the ocean acidification and the occurrence of extreme meteorological events. Needless to say is that this will have disastrous impact on biodiversity, agriculture or health.
Fossil fuel based energy production and transportation represents 60% of the overall CO_2 emissions, hence the need to transform the way we produce and consume energy using sustainable and non-polluting technologies. Along that line, significant improvements have been made on systems, like wind turbines and solar panels, harvesting renewable energy. However, due to the intermittent nature of these energies, such systems need to be coupled to energy storage devices. Energy storage can also contribute reducing CO_2 emissions by enabling the replacement of fossil fueled cars for electric vehicles. Among the existing technologies that can store electricity, electrochemical devices and specifically Li-ion batteries show the highest specific energy and are, therefore, the preferred candidates for both grid and transportation applications.
Despite the tremendous development of Li-ion batteries in the recent years, a great amount of research is still on going because electric vehicles are limited in terms of driving distance and Li-ion batteries are too expensive to be massively used for grid applications. Two routes are currently being developed: i) decreasing the cost, and ii) increasing the performances. Concerning the second point, in the recent years, new electrode materials called Li-rich NMCs have been developed, allowing a great improvement of the performances compared to commercial materials such as the well-known $LiCoO_2$. This capacity increase is due to the intriguing participation of oxygen anions into the redox reaction. This process, called anionic redox, unfortunately comes with drawbacks which prevent the commercialization of batteries using Li-rich NMC. To alleviate such issues, fundamental understanding on anionic redox is needed, which is the aim of this work.

Li-rich NMC compounds of chemical composition $Li[Li_xM_{1-x}]O_2$ ($0 < x < 0.33$) with M a mix of Mn, Ni and Co, have a layered rocksalt structure in which the Li cations are sandwiched between layers of M cations. Anionic redox activity being triggered by x, the extra Li in the transition metal layer, to grasp further insights on this property, we studied Li “extra” rich

model materials of chemical composition $Li[Li_{0.5}M'_{0.5}]O_2$, or $Li_3M'O_4$, with M' being a transition metal. For the sake of comparison, these materials should have similar structural features than Li-rich NMC, therefore belonging to the rocksalt system, hence limiting the choice of M' to 4d and 5d transition metal. Specifically, we studied A_3MO_4 model rocksalt compounds with A being Li or Na, and M being Ru, Ir, Ta, Sb or Nb to decipher capacity and voltage aspects of anionic redox.

This work is divided into three chapters:

First, Li-ion battery principles and developments will be presented emphasizing the role of solid state chemistry. Intercalation chemistry being at the center of Li-ion battery, a broad introduction of intercalation will be given as a starting point. It will be followed by a presentation of the evolution of the cathode material over the years underlining the interests and drawbacks of anionic redox, i.e. drastically improving the capacity but causing voltage hysteresis. At the end, current theoretical understanding of anionic redox will be given together with some of the remaining questions: is anionic redox limited in terms of capacity? And can we understand better its redox potential and the origin of the voltage hysteresis?

In the second chapter, we try to assess the limit in terms of capacity of anionic redox by probing the stability of compounds showing an enhanced oxygen oxidation behavior. First, we designed such compounds among the Li_3MO_4 family (with M being a transition metal or a mix of transition metals), performed their synthesis, deeply characterized their structure and rationalized their structural evolution using DFT. In a second part, we unveiled their charge compensation mechanism using combined electrochemical and spectroscopic techniques showing anionic redox is indeed limited by the stability of the oxidized phase. In a third part, comparing Li_3RuO_4 and Na_3RuO_4, we prove that although anionic redox is equally limited in Li/Na based materials, its occurrence is affected by the size of the alkali.

The third chapter will be devoted to the study of the consequences of anionic redox on the redox potential. Specifically, we are interested into understanding the origin of the voltage hysteresis, being the difference in the average charge and discharge potentials, in compounds showing anionic redox. Comparing the charge compensation mechanism of two new

materials, based on Ni/Mn substitution in Li_3TaO_4, having different voltage hysteresis, we propose this phenomenon to be related to the charge transfer band gap of the materials.

The general conclusions at the end of this work briefly summarize the results obtained during this thesis and discuss its contribution to the solid state chemistry and battery research.

Chapter I State of the art

I.1 Intercalation chemistry a wide topic including battery

I.1.a Working principles of Li-ion battery

A Li-ion battery is an electrochemical energy storage system, i.e. it stores electrical energy by converting it into chemical energy. It relies on the reversible intercalation of Li^+ ions into two host frameworks, the positive and the negative electrodes (also called cathode and anode, respectively, in the Li-ion battery community). Li^+ being positively charged, its intercalation combines with an electron transfer, keeping the electroneutrality of the framework. Therefore, during the discharge of the battery, Li^+ and e^- leave the negative electrode material (anode) and insert into the positive one (cathode) as schematized in Figure I-1. Li^+ travels through an electrolyte, generally composed of an organic solvent and Li salt, while the e^- moves through an external circuit hence producing current. The charge of the battery happens in the reverse way. E, the specific energy, i.e. the performance of the battery, is controlled by two parameters, the capacity, C, and the voltage, V, following the equation (1):

$$E = V * C \quad (1)$$

V in volts is the difference of potentials between the two electrodes, and C in mAh/g, is proportional to the number of Li that can be inserted into the electrodes normalized by their weight.

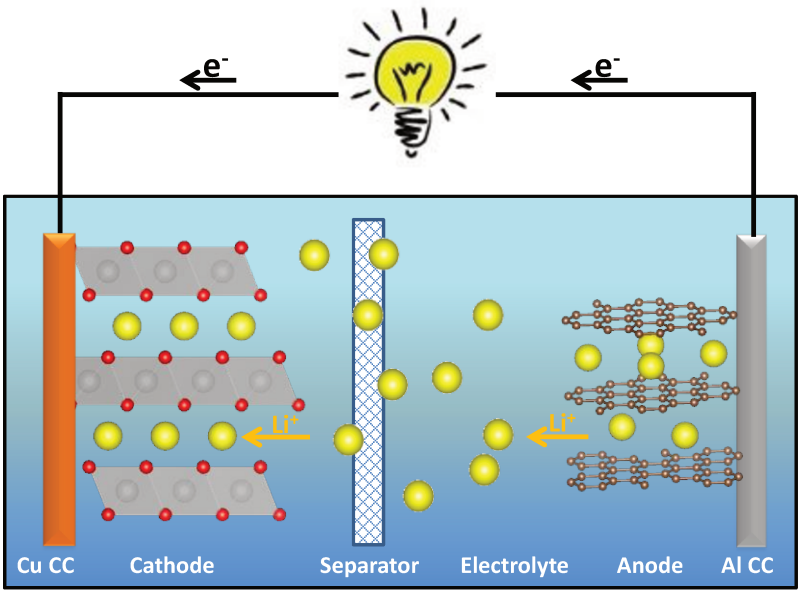

Figure I-1: Schematic of a Li-ion battery, during discharge showing the electrodes, anode and cathode, the electrolyte, the separator and the current collectors (CC) being in Al and Cu at the anode and cathode sides, respectively. The separator prevents short circuits between the two electrodes while being permeable to Li^+ ions

I.1.b Intercalation chemistry, definition and examples

As we have seen in the previous paragraph, Li-ion battery fully relies on the intercalation of Li into host frameworks (the electrodes), hence the need to define this type of chemical reactions.

I.1.b.i Definition of intercalation

Intercalation is a reversible reaction in which a guest atom or molecule, G, is inserted into a host, □Host, while preserving the structural framework according to the chemical reaction presented below, (2):

$$xG + \square Host \rightarrow G_x Host \quad (2)$$

In literature, it is also called insertion, topotactic or inclusion reactions. [1]

Intercalation chemistry has two major interests; i) it permits the storage/capture of molecules or atoms and ii) it allows the continuous modification of a property of G_xHost with x, the amount of G inserted. These two characteristics enable the use of intercalation chemistry in many different fields. Herein, we present some of the intercalation systems classified depending on their use, i.e. storage systems or property modification.

I.1.b.ii Zeolites and clays used for their storage properties

For the storage systems, the important parameters are: i) the nature of the guest, ii) the amount of guest, and iii) its diffusion, i.e. the kinetics of the intercalation process. All these parameters are related to the nature of the chemical bond between the guest and the host. For example, strong bonding will lead to lower diffusivity or the number of chemical bonds will define the number of guests in the host structure. As a consequence, host structures are developed for specific guest molecules leading to a rich variety of intercalation systems.

Zeolites have received great attention over the years for their low density, hence high porosity, allowing the uptake of various molecules in gaseous or solvated states. Their general composition is $M_{x/q}^{q+}$ $[Al_xSi_{1-x}O_2]^{x-}.nH_2O$, with M being a cation compensating the negative charge of $[Al_xSi_{1-x}O_2]^{x-}$ due to the presence of Al^{3+} ions substituting the Si^{4+}. Zeolites are 3D macromolecular structures with cavities of different sizes based on AlO_4 and SiO_4 building

block sequences, as shown in Figure I-2. The size of the cavities controls the size of the guest molecule. The Si/Al ratio controls the charge of the structure and the amount of cations therefore governing the chemical selectivity, i.e. low Si/Al ratio zeolites will trap polar molecule. Application-wise, zeolites are mainly used as detergent binders, catalyst and absorbents. [2]

Decreasing the dimensionality from 3D to 2D host structures, one falls into the clay and double layer hydroxide families. Clays form a very rich and complex family of materials, whose 2D structure relies on the building sequence of two sublayers, one being composed of $Si_2O_3(OH)_2$ with Si in tetrahedral site and the other one of $Al(OH)_6$ with Al in octahedral coordination. In Kaolinite, for instance, layers are composed of one block of each, as shown in Figure I-2.[3] These layers can be charged negatively substituting Al^{3+} by Fe^{2+}, for example, hence allowing the intercalation of cation into the interlayer space. Double layer hydroxides derive from the hydrotalcite mineral of chemical composition $Mg_6Al_2(OH)_{16}CO_3.4H_2O$. It crystalizes forming positively charged layers of edge sharing $M(OH)_6$ octahedra (M being Mg^{2+} or Al^{3+}) with H bonded to O and pointing towards the interlayer space filled with CO_3^{2-} anions and water molecules, as presented in Figure I-2. A huge amount of different double layer hydroxides can be prepared replacing Mg^{2+} by another divalent cation such as Zn^{2+}, Fe^{2+} or Co^{2+} and Al^{3+} by a trivalent Cr^{3+}, Mn^{3+} etc.[4] For both clays and double layer hydroxides, layers are weakly interacting between each other through dipole – dipole interactions. For this reason, the interlayer distance, also called van der Waals gap can be easily modulated which can lead to the insertion of huge organic ions. [5] Application wise, double layer hydroxides are nowadays extensively studied for their ability to host charged biomolecules, and serve as an encapsulating agent for drug delivery. They are also used as molecular sieves for which you can adjust the size of the capturing cavities.

I.1.b.iii Intercalation in conducting materials, a way to tune their properties

We have seen examples of materials used as molecule or ion reservoir with little concern about the evolution of the host during intercalation. In contrast, intercalation in conducting materials is often performed to tune the properties of the host structure through its

oxidation/reduction, i.e. hole/electron doping. This is done with the intercalation of a charge molecule as exemplified in equation (3):

$$xG^{n+} + Host + x * ne^{-} \rightarrow G_x^{n+}Host^{x*n-} \quad (3)$$

This strategy has first been implemented to graphite in 1841 by Schaffäutl. Graphite is a 2D material whose layers are composed of regular hexagonal network of carbon atoms, as shown in Figure I-2. It shows a high conductivity which can be drastically altered by intercalating electron dopants, such as Li or K. This discovery together with the development of X-ray diffraction measurements, allowing the characterization of the intercalated compounds, led to extensive research in this field between 1930 and 1940.[6] It permitted, for instance, the discovering of superconductivity in C_8K at 1K.[7] This research opened the door towards the study of intercalated layered compounds for their electronic property.

In the 1970th, transition metal dichalcogenides have received quite a lot of interest. Their chemical formula is MX_2, M being a transition metal such as Ti, Ta, Nb, Mo etc. and X a chalcogenide, namely, S, Se, or Te. They crystalize in a layered structure composed of MX_2 layers with the transition metal being in octahedral or prismatic coordination, as exemplified in Figure I-2. Strong covalent bonding between the metal and the chalcogenide reduces the repulsions between the layers leading to relatively small van der Walls gap, approximately 3-4 Å. Intercalation in such systems was first achieved by Rüdorff in 1959 using liquid ammonia solution of alkali.[8,9] Interestingly, this approach led to the intercalation of ammonia together with the alkali atoms showing organic molecules can be placed into the interlayer space. Along that line in 1971, Gamble et al. reported that the insertion of pyridine into these frameworks can trigger superconductivity, below 3.5K in $TaS_2(C_5H_5N)_{1/2}$.[10] This finding confirmed that interesting electronic properties can be obtained through topotactic reactions. This research is still on going, as exemplified by the study of Cava et al. on the origin of superconductivity in $TiSe_2$ intercalated with Cu ions in 2006.[11]

I.1.b.iv The place of Li-ion battery in the wide field of intercalation

In Li-ion battery, the performance is defined by the properties of the intercalation compounds in the device, since, as seen previously, the specific energy is the product between the capacity, i.e. the amount of Li that can be intercalated/removed, and the voltage, basically the work needed to extract/add an electron. Bearing this in mind, one understands that both the

ions storage behavior and the modification of the electronic properties are of primary importance because the former controls the capacity and the latter the voltage (Figure I-2). Therefore, improvements of intercalation compound for Li-ion battery is related to development in the more general field of intercalation chemistry.

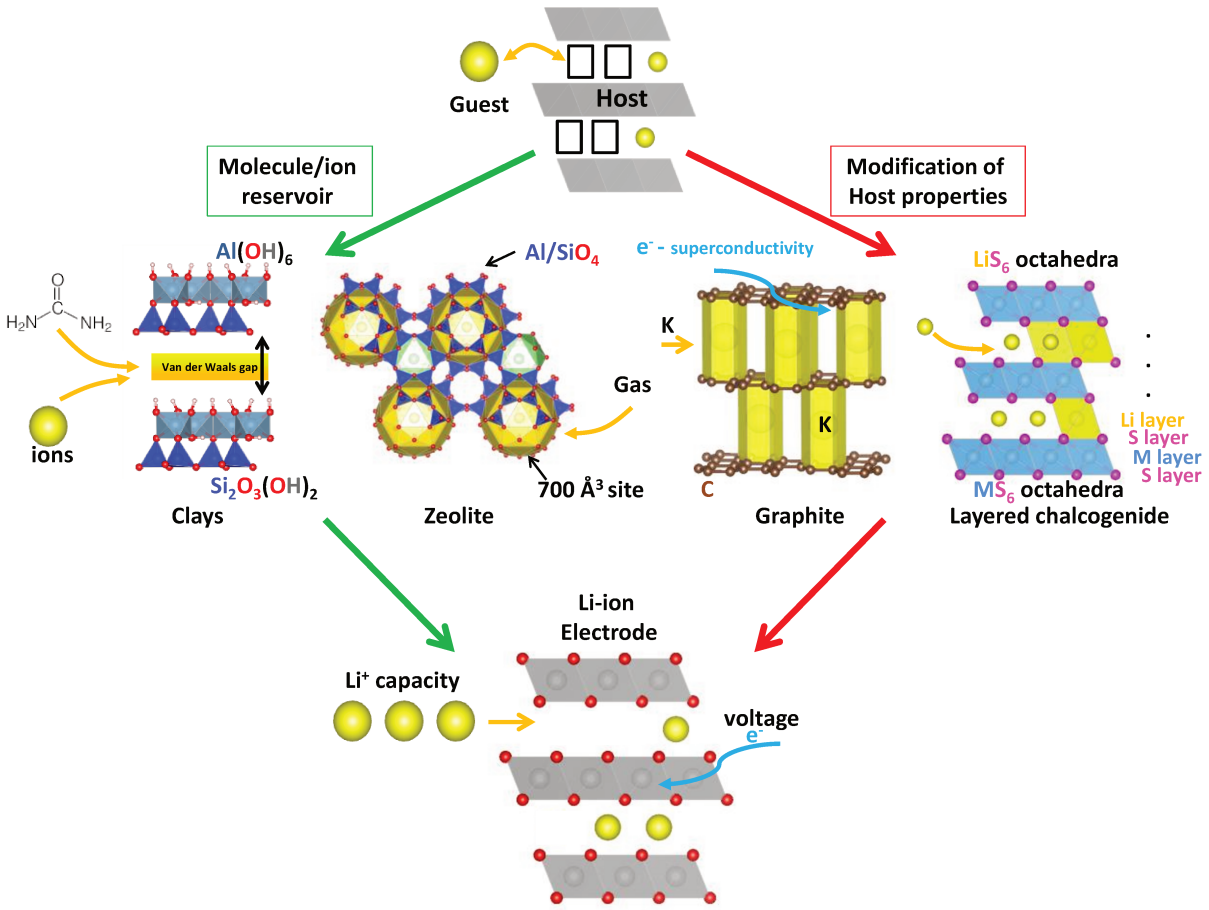

Figure I-2: Schematic of the general intercalation system (top) together with examples for ion storage systems such as clays and zeolites (middle left) and "property modification" systems, such as graphite and chalcogenides, (middle right). Li-ion electrodes combine both the properties as shown at the bottom.

I.1.c Evolution of cathode material for Li-ion battery

I.1.c.i First materials and concept of Li battery

The original concept of lithium battery was proposed in 1976 by Whittingham.[12] This battery was constituted of TiS_2 cathode and Li metal anode. Whittingham showed that Li^+ can be reversibly inserted/extracted in the layered TiS_2 at room temperature while, on the negative side, Li^+ reduce to Li metal, leading to an average potential of 2 V. The choice of TiS_2 was

motivated by its light molecular weight, low price and electronic conductivity. Moreover, Whittingham showed the charge and discharge potentials nearly superimpose proving that this system can reach a very high energy efficiency (the energy efficiency is the ratio between the specific energy in discharge and charge). Therefore, he concluded that a battery technology based on this reaction could overcome other types of electrochemical storage systems such as Na/S having lower specific energy, 330 Wh/kg compared to 480 Wh/kg for Li/TiS_2, and working at higher temperature. In the late 1980s, this research has led to the commercialization, by Moli energy, of the first battery technology based on lithium.[13] The cathode was the layered MoS_2 and the anode was constituted of a Li foil. Despite its fair specific energy and cyclability, the batteries suffered safety issues due to the formation of dendrites, causing their withdrawal from the market. Dendrites are wires of Li forming at the anode side during the Li plating, i.e. reduction of Li^+ in Li, and progressively growing through the electrolyte and separator to finally touch the cathode side. It provokes a short circuit which heats up the battery eventually leading to its explosion.

I.1.c.ii From Li battery to Li-ion or Li-polymer

To solve the issue of dendrites, two solutions were rapidly developed. First, plastic electrolyte mechanically blocking dendrites were produced leading to the development of the Li polymer technology.[14] Nowadays such strategy has been successfully implemented in electric vehicles (EV), the bluecar, developed by Bolloré. Another strategy relies on the replacement of the Li foil by an intercalation anode material operating at higher than 0 V, hence suppressing Li plating and the formation of dendrites. Such a system is called “rocking chair” or Li-ion technology because Li is only present as Li^+ ion migrating between the two electrodes.[15,16] Graphite is a material of choice for the negative electrode since it can intercalated up to x = 1 Li in Li_xC_6 leading to a specific capacity of 370 mAh/g at the very low voltage of 0.2 V.[17]

I.1.c.iii Replacement of chalcogenides by oxides having a higher potential

In the 1980th, layered oxides have been intensively studied for their electronic properties and possible applications as cathode material for Li battery.[18,19] Their chemical composition is A_xMO_2, A being an akali atom such as Li or Na, and M a transition metal. They have the

same structure as layered chalcogenides presented above with however different characteristics mainly based on the electronegativity difference between S and O, 2.6 compared to 3.5 in the Pauling scale.[20] It leads to very covalent M-S and quite ionic M-O bonds resulting in a higher charge density around the oxygen compared to sulfur. As a consequence, the electrostatic interlayer repulsion between the layers is increased in the transition metal oxides. This makes the presence of alkali ions in the interlayer space, screening the charge, mandatory for the structural stability. Practically speaking, the synthesis of such layered compounds is always performed with alkali atom and only a limited amount of cations can be removed during electrochemical extraction, directly impacting the capacity of the battery using such cathode. However, this loss is fully compensated by the higher redox voltage of layered oxides, ~3.5 V, compared to chalcogenides, ~2 V. At the end, transition metal oxides actually perform better than their chalcogenide counterparts and $LiCoO_2$ became a widely used cathode material for its high specific energy, 550 Wh/kg (140 mAh/g at 4 V).[21] Note that the theoretical capacity of $LiCoO_2$, based on the number of Li, is 275 mAh/g. However practically speaking, only 0.5 Li can be removed from $LiCoO_2$ due to the instability of the delithiated phase for the reasons mentioned above. Because of the high price and toxicity of Co, large research efforts were dedicated to finding alternative to $LiCoO_2$. $LiMnO_2$ was first investigated due to the low price and abundance of Mn. It crystalizes in an orthorhombic structure and shows a good capacity in the first cycles which rapidly decays upon further cycling.[22] It has also been synthetized as a layered compound via soft chemistry, however during Li removal, this compound suffers from irreversible phase transitions hindering its commercialization.[23,24] $LiNiO_2$ shows an specific energy competing with $LiCoO_2$, however the tendency of Li/Ni to mix in the same crystallographic site makes its synthesis as a pure layered structure difficult and damages its cycling performances.[25,26] Therefore, $LiNiO_2$ never reached the commercialization step. Interestingly, the layered transition metal oxide reached their apogee with the so called NMC, $LiNi_{0.33}Mn_{0.33}Co_{0.33}O_2$ which composition is optimal to achieve low price (low Co content), high thermal stability (presence of Mn) and high capacity (Ni^{4+}/Ni^{2+}), 200 mAh/g at 4 V in average.[27] Another successful example of layered oxide with a mix of transition metal is the $LiNi_{0.8}Co_{0.15}Al_{0.05}O_2$ (NCA).[28] Nowadays, both NCA and NMC are the most common cathode materials used in commercialized Li-ion battery.

I.1.c.iv From layered to three dimensional materials

Together with the development of 2D materials, 3D structures are also of great interest. For instance, Li^+ diffusion in spinel structures was shown to be comparable to layered structures paving the way for the discovery of cathode material having a spinel structure. Spinels, of general composition AB_2X_4 with A and B being cations and X anions, have the same anion face centered cubic close packing network than layered oxides but with the cations occupying different positions, as shown in Figure I-3. In regular spinels, A occupies tetrahedral interstices and B fills half of the octahedral positions. $LiMn_2O_4$ received particular attention for its high specific energy, 130 mAh/g at 4 V in average,[29] and despite dissolution issues which delayed its commercialization, it is now widely used.[30] Among the 3D structures, polyanionic compounds, i.e. association of a transition metal with a polyanionic ligand such as PO_4^{2-} or SO_4^{2-}, have been intensively studied. Looking for high specific energy cathode material, the research community unveiled a tremendously rich structural family with many polymorphs.[31,32] Polyanionic compounds are known for their stability during Li extraction and the most used one, $LiFePO_4$, shows excellent cyclability and perfect thermal stability together with good performances, 170 mAh/g at 3.6 V (Figure I-3).[33]

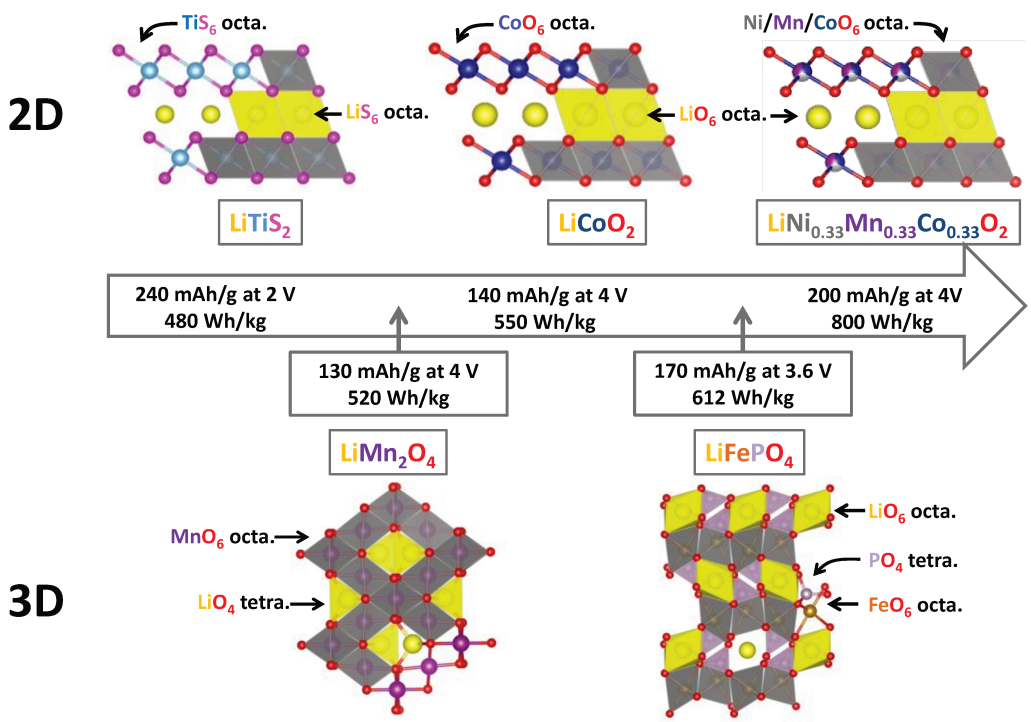

Figure I-3: Schematic showing the evolution of the specific energy of practical cathode materials with the 2D structure and 3D at the top and bottom, respectively

I.2 In the quest for high energy materials

I.2.a Context and strategies: increasing the voltage or the capacity

All the compounds listed above enabled the success of Li-ion battery and its large implementation in portable electronics. Moreover, it made the idea of having vehicles fully powered by electric energy a reality. However, to increase the market penetration of EV, the specific energy of Li-ion battery still needs to be increased.[34] The cathode material being the bottleneck, a lot of research efforts are still dedicated to improve their specific energy. Two strategies have been pursued in parallel i) increasing the voltage and ii) the capacity. In parallel to this quest towards new materials, great progress have also been made in understanding the properties of cathode materials, leading to successful rational design which will be presented below.

I.2.b Strategies to increase the potential based on its rationalization

I.2.b.i Rationalization of the potential with chemical descriptors

The thermodynamic definition of the potential, E, is related to the Gibbs energy, G, of the electrochemical reaction (4):

$$nLi + \square Host \rightarrow Li_n Host \qquad (4)$$

Given by the equation (5):

$$\Delta_r G = U_r Li_n Host - nU_r Li - U_r Host + p\Delta_r V - T\Delta_r S = -nFE \qquad (5)$$

$U_r Li_n Host$, $U_r Li$ and $U_r \square Host$ being the internal energy of the Li_nHost, Li and □Host phases while p, Δ_rV, T, Δ_rS, n, F and E are the pressure, the volume change, the temperature, the entropy change, the number of electrons exchanged, the Faraday constant and the electrochemical potential, respectively. From this equation, we can usually neglect the volume and entropy change terms as shown by Aydinol et al.[35,36] In this case, the electrochemical potential can be written as, (6):

$$E = -\frac{1}{F}\left(\frac{U_r Li_n Host - U_r \square Host}{n} - U_r Li\right) \qquad (6)$$

At this point, one can ask how to calculate or estimate the internal energy of the different phases. They can be calculated using ab initio techniques such as Density Functional Theory (DFT). It often leads to a very good estimation of the potential with however small problems

for correlated materials. Here, we will decompose this equation into terms that chemists can easily understand and tune as done by Saubanère et al. in 2014. [37]

The electrochemical reaction will be separated into different steps corresponding to different Gibbs energy variation; (7) n e^- will be removed from Li_nHost ($\Delta_r G1$) (8) then n Li^+ ion will be extracted $\Delta_r G2$) and finally (9) the n Li^+ will be reduced with the n e^- forming n Li ($\Delta_r G3$).

$$\Delta_r G1 : Li_n Host \rightarrow Li_n Host^{n+} + ne^- \quad (7)$$

$$\Delta_r G2 : Li_n Host^{n+} \rightarrow \square Host + nLi^+ \quad (8)$$

$$\Delta_r G3 : nLi^+ + ne^- \rightarrow nLi \quad (9)$$

For the first reaction (7), we can establish the corresponding Gibbs energy variation (10):

$$\Delta_r G1 = U_r Li_n Host - U_r Li_n Host^{n+} = \int_m^{m-n} \mu\, Li_n Host.dn \quad (10)$$

$\mu Li_n Host$ being the chemical potential of Li_nHost, classically defined by (11):

$$\mu = \frac{IE + A}{2} \quad (11)$$

IE and A being the ionization energy and the electronic affinity, respectively. For our study, the chemical potential will be simply defined by the IE, since it is often considered that the Fermi level is pinned at the top of the valence band and not in the middle of the band gap. Since the chemical potential of Li_nHost phase is not straightforward to estimate, we will further decompose this term. Classically the redox center, namely the atom or group of atoms from which the electron is removed during oxidation, is the metal. In this case, Figure I-4 presents a schematic explaining how the chemical potential of Li_nHost can be obtained from the ionization energy of the metal, the electrostatic interactions and the orbital overlap.

To solve equation (10), we have to integrate the chemical potential over n, the number of electrons removed. For this, one could consider the chemical potential to be constant during the removal of electrons. This approximation is roughly true when a small amount of electrons are removed from a larger amount of electrons at the Fermi levels, e.g in metals. It is frequently done in the field of battery for the sake of simplicity. However many theoreticians raised the concern about this approximation. For instance, Ceder et al. in 1997 pointed out that rigid band model, i.e. considering the electronic structure fixed during oxidation/reduction, should not represent accurately electrochemical reaction.[36]

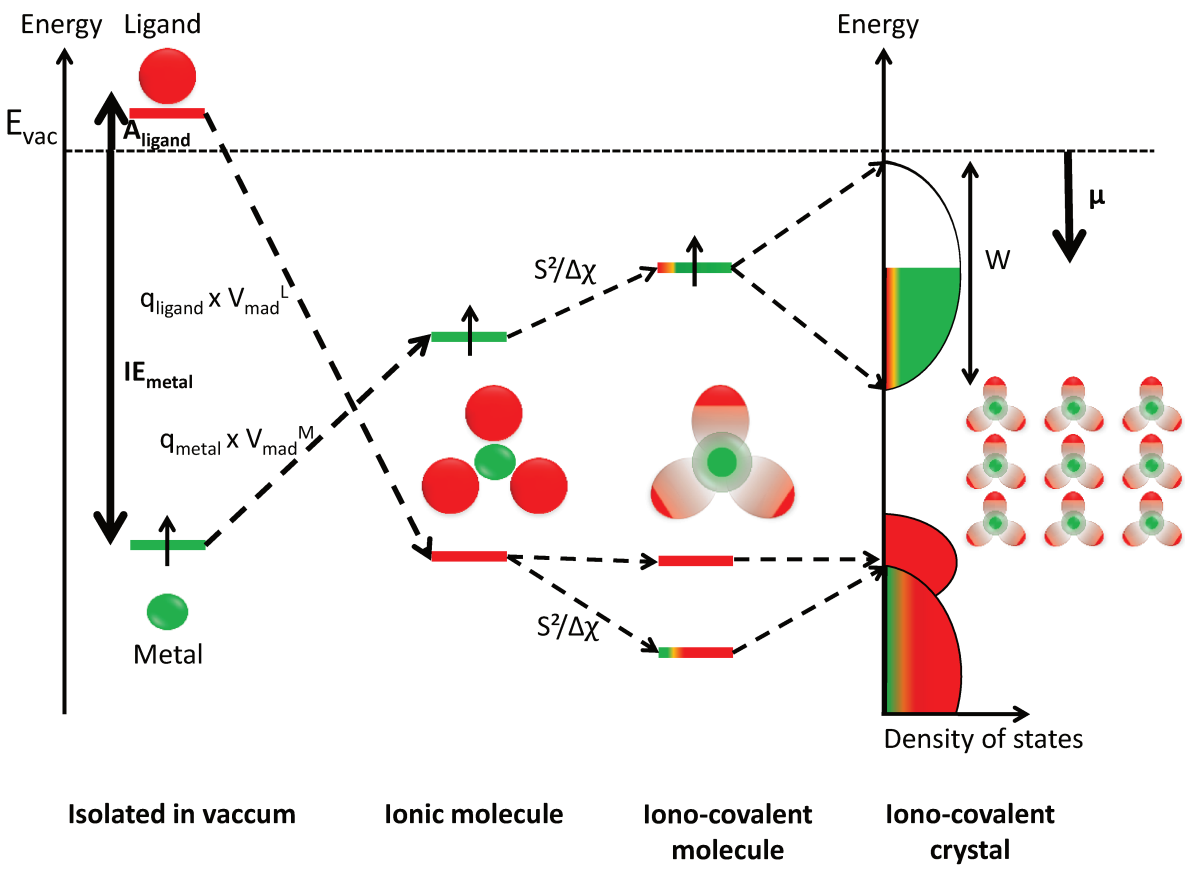

Figure I-4: Schematic representing the evolution of the chemical potential of a transition metal isolated in vaccum, or in a ionic molecule, iono-covalent molecule and iono-covalent crystal from left to right. IEmetal, Aligand, qmetal, qligand, VmadM, VmadL, $S^2/\Delta\chi$ and W are the ionization energy of the metal, the electron affinity of the ligand, the charge of the metal and the ligand, the Madelung potential on the metal and ligand site, the ratio between the orbital overlap and the difference of electronegativity, and the band width, respectively.

Therefore, Saubanère et al. proposed to take into account the evolution of the chemical potential with the number of electron, through the second order term of the Taylor series of the chemical potential with respect to the number of electrons (12):

$$\mu(n) = \mu 0 + \frac{\partial \mu}{\partial n} * n = \mu 0 + \eta * n \qquad (12)$$

η being the chemical hardness as defined by Pearson, representing the variation of the chemical potential with n.[38] The introduction of the chemical hardness is interesting because easy to use and visualize since it is classically used in chemistry through the principle known has Hard-Soft-Acid-Base (HSAB). Using equation (10) and (12), we get (13):

$$\Delta_r G1 = \mu 0 Li_n Host * n + 2 * \eta * n^2 \qquad (13)$$

Regarding the second chemical reaction (8), $\Delta_r G2$ can be expressed as follow (14):

$$\Delta_r G2 = U_r Li_n Host^{n+} - U_r Host + n * U_r Li^+ = \sum_{i=1}^{n} qLi_i^+ * V_i^{LinHost+} \quad (14)$$

$V_i^{LinHost+}$ and qLi_i^+ being the interaction potential of the Li^+ atom i in $LinHost^+$ and the charge of the Li^+ atom. The potential can usually be calculated as a Madelung potential due to the very low electronegativity of Li, i.e. always making very ionic bonds.[39]

$\Delta_r G3$ will be used as a reference for the potential following the equation (15):

$$\Delta_r G3 = -\mathrm{n} * \mathrm{F} * \mathrm{E}_{Li+/Li} \quad (15)$$

Finally, the voltage of the chemical cell can be expressed as (16):

$$V = E - \mathrm{E}_{Li+/Li} = \frac{1}{F}(\mu 0 Li_n Host + 2 * \eta * n + \sum_{i=1}^{n} qLi_i^+ * V_i^{LinHost+}) \quad (16)$$

From equation (16), one can see that to tune the potential, three parameters can be adjusted: i) the chemical potential of the Li_nHost material, ii) its hardness and iii) the Madelung potential of the Li^+ cation.

I.2.b.ii Strategies to increase the potential: playing on the transition metal or the ligand

The most common strategies to increase the potential rely on decreasing the chemical potential of Li_nHost. It can be done by increasing the ionization energy of the metal and/or the electronegativity of the ligand, as shown Figure I-5. Increasing the atomic number (Z) and the oxidation state of the metal leads to higher ionization energies, however, increasing the oxidation state of metal also decreases the theoretical capacity (less electrons can be used for the oxidation of the material). Therefore, most of the research aiming to increase the potential relies on using late transition metal such as Ni or Co instead of Fe or Mn. This trend is nicely exemplified in the olivine $LiMPO_4$ compounds with M = Fe, Mn, Co, Ni having redox potentials of 3.5, 4.1, 4.5 and 5.4 V, respectively.[33,40,41,42] Arroyo et al. showed this trend can be further extended to other polyanionic compounds.[43] In the oxides, this strategy has been implemented in $LiMn_2O_4$ spinel, for which the partial substitution of Mn by Ni considerably raises the potential, from 4 V to 4.8 V.[44] The second strategy to raise the potential is to use electronegative ligands such as O, F or XO_4 polyanions. Based on a systematic comparison between $Li_xM_2(PO_4)_3$ and $Li_xM_2(SO_4)_3$ with M being Fe or V, Goodenough proposed the

inductive effect in 1997, being that the ionicity of the M - XO_4 bond can be increased by increasing the covalency of the X – O bond, as shown Figure I-5.[45] This lead to intensive study of sulfates based material, SO_4^{2-} being the most electronegative ligand, with for instance the synthesis of $Li_2Cu_2O(SO_4)_2$ showing a redox potential of 4.7 V, highest ever reported for Cu based materials.[46] At this point, I would like to emphasize that all these materials were not only interesting for the battery field but also for other type of applications. $LiMPO_4$ olivine compounds with M = Ni and Co show an intense magnetoelectric coupling[47,48] and have been extensively studied for their anisotropic magnetic properties.[49] Moreover, tuning the chemical bonding using the inductive effect, not only impacts the chemical potential of the electrons but also their magnetic properties. Indeed, increasing the ionicity decrease the superexchange interaction impacting the Néel temperature for instance. [32]

Going back to the batteries, researchers were able to increase the specific energy of cathode materials tuning their redox potential up to 5V. However, these materials are still not used in commercialized applications because their potential overpasses the stability limit of organic electrolytes. Therefore, nowadays a large part of the research is devoted to increasing the capacity of the cathode material.

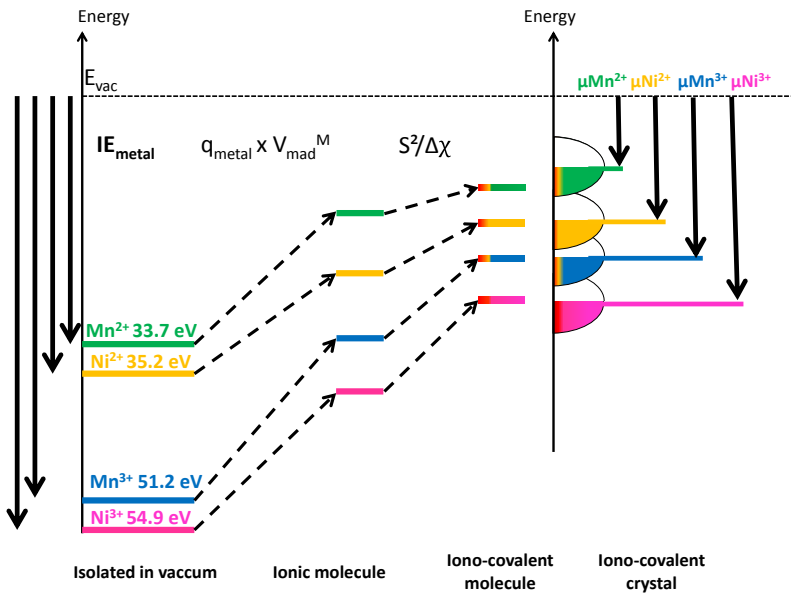

Figure I-5: Schematic showing the effect of late transition metal or high oxidation state on the chemical potential of the electron. Late transition metals have higher ionization energy, lower electrostatic interaction (larger size), and higher covalent bonding (higher electronegativity) than early transition metal, overall leading to an increased chemical potential. With the increase of the oxidation state of the metal, the electrostatic and covalent interaction increases as well (higher charge and electronegativity).

I.2.c Strategy to increase the capacity

I.2.c.i Multiple electron transfers per transition metal

In the endless quest for higher energy densities, significant amount of research is devoted to increasing the capacity of cathode material. To do so, materials having transition metal that can be oxidized/reduced more than one time, without drastic modification of the framework, are of great interest. This was shown to be possible in Nb (Nb^{5+}/Nb^{3+})[50] or Mo (Mo^{6+}/Mo^{4+}) oxides[51,52,53] but without significant improvements in terms of capacity due to the high molecular weight of such atoms. Among the 3d metals, V, Cr or Ni can achieve double electron transfers, for instance, from V^{5+} to V^{3+} in V_2O_5 compounds [Baddour 1991, Delmas 1991].[54,55] Unfortunately Cr and V based materials are toxic which makes their commercialization difficult. Ni-based compounds are among the most successful examples of multiple electron transfers. Indeed, NMC mostly relies on $Ni^{4+/}Ni^{2+}$ redox couple. Very recently, Mn has received quite a lot of attention due to the reports of Mn^{5+}/Mn^{3+} and Mn^{4+}/Mn^{2+} redox couples.[56,57,58,59]

I.2.c.ii Li-rich NMC and the origin of the extra capacity?

A family of materials, the so called Li-rich layered oxides, has attracted humongous attention in the last decade due to the high capacity of its members, up to 280 mAh/g at 3.6 V.[60,61] They have a global composition $Li_{1+x}M_{1-x}O_2$ (M being a transition metal) and show a layered structure similar to $LiCoO_2$ in which the extra Li, x, replaces some of the transition metal. Usually, Li and M order forming a honeycomb structure in which Li is surrounded by the six M. Depending on the synthesis conditions, Li-rich regions of composition Li_2MO_3, can form and the material is described as a composite, xLi_2MO_3 - $(1-x)LiMO_2$. In other cases, Li is well distributed over the particle and the compound forms a solid solution, $Li[Li_xM_{1-x}]O_2$. Lu et al. first reported a detail study of $Li[Li_{(1/3-2x/3)}Ni_xMn_{(2/3-x/3)}]O_2$.[60] They showed capacity as high as 225 mAh/g for x = 5/12, 1/3 or 1/4 with decent cycling performances. This capacity is greater than what would be expected from the oxidation of Ni^{2+} to Ni^{4+} raising the question of the nature of the redox center. Kalyani et al., studying Li_2MnO_3 end member, proposed the oxidation of Mn^{4+} to Mn^{5+}.[62] However Mn^{5+} is very rare in octahedral coordination hence leaving the origin of the capacity unclear. Tarascon et al. in 1999 achieving the full delithiation of $LiCoO_2$ proposed the oxidation of oxygen in the bulk of the material to be

responsible for the charge compensation mechanism.[63] However, this study was overlooked, and Lu proposed the following mechanism: the formation of Li_2O thanks to the diffusion of O^{2-} from the bulk to the surface during the 1st charge, leading to the formation of an oxygen deficient new phase in which the Mn^{4+}/Mn^{3+} would be activated and responsible for the extra capacity. Thackeray and co-workers in 2005 agreed on the activation of the Mn oxidation/reduction but through a different activation mechanism. They believed O^{2-} diffusion was not realistic in such material and therefore proposed that an irreversible oxidation of oxygen, following the chemical reaction $2O^{2-} \rightarrow O_2 + 4e^-$, at the surface of the material.[61] This was further confirmed by mass spectroscopy measurements in 2006 showing the presence of O_2 inside the electrochemical cell.[64] Later in 2013, Delmas and co-workers unveiled through absorption studies that $Mn^{4+/}Mn^{3+}$ is not active during the cycling of such material and proposed instead the reversible oxidation/reduction of oxygen in the bulk of the material to be responsible for the charge compensation.[65] This was experimentally demonstrated in model system in the same period by Sathiya et al.[66] This discovery raised a tremendous amount of research trying to understand better this anionic redox and take profit of it.

A part from studying the charge compensation mechanism, a lot of efforts have been directed towards the optimization of the performances of Li-rich compounds leading to the identification of the best chemical compositions: $Li_{1.2}Ni_{0.13}Mn_{0.54}Co_{0.13}O_2$ showing 280 mAh/g at 3.6 V. Moreover, surface stabilization strategies have been implemented to limit the O_2 release and its related surface reconstruction.[67] Despite these upgrades, Li-rich NMC still suffers several issues such as i) voltage decay, ii) layered to spinel transformation[68], iii) slow kinetics and iv) voltage hysteresis.[69,70]

I.2.c.iii Using model compounds to understand anionic redox

To improve the performances of Li-rich NMC, their evolution during cycling should be better understood. This material being very complex due to the presence of multiple elements, Tarascon and co-workers proposed the study of model compounds, like Li_2RuO_3 or Li_2IrO_3. The interest of such compounds is twofold, i) they show a very similar electrochemical signature, hence a similar redox mechanism, compared to Li-rich NMC, ii) they are easier to study due to their chemical simplicity, indeed Ru or Ir are the only redox active elements. Thanks to this approach, the first direct evidence of anionic redox in $Li_2Ru_{1-y}Sn_yO_3$ system

was given using complementary X-ray Photoemission Spectroscopy (XPS) and Electron Paramagnetic Resonance (EPR) techniques.[66] From XPS studies, O species with higher binding energy are observed, corresponding to oxygen atoms having a low electronic density, hence being oxidized.[71] EPR is sensitive to paramagnetic center and was used to detect the presence of O – O species having unpaired electrons.[72] Overall, from these findings combined to DFT calculations, it is proposed that oxidation of oxygen results in the formation of peroxo-like species having O – O bonds of 2.4 Å. In 2015, studying Li_2IrO_3, Mc Calla et al. confirmed the formation of the peroxo-like species through their direct visualization by High Resolution Transmission Electron Microscopy (HRTEM) coupled to neutron diffraction.[73] Recently, these model compounds have been used again to assess the kinetic of the anionic redox. Studying $Li_2Ru_{0.75}Sn_{0.25}O_3$, Assat et al. have shown that anionic redox is a kinetically limited process explaining the poor rate capability of Li-rich materials.[74] Moreover, anionic redox is also accompanied by hysteresis, i.e. charge and discharge happen at different potential, being detrimental for the energy efficiency of the Li-ion battery.[75] At this point, I would like to emphasize that the study of these model compounds have enabled a deep understanding of anionic redox, hence showing, once again, the importance of fundamental studies.

I.2.c.iv From model compounds to practical systems

These findings have served as platform to study anionic redox in practical systems having 3d transition metal, and recently thanks to hard XPS (being sensitive to the bulk), O K-edge X-ray Absorption Spectroscopy (XAS) and Resonant Inelastic X-ray Scattering (RIXS) direct evidence of anionic redox was given for Li-rich NMC.[76,69,70] Going further than probing the presence of anionic redox, these technics can be used to obtain more information on the nature of the oxidized oxygen species. Along that line, Bruce and co-workers performing RIXS experiments on Li-rich NMC proposed the formation of localized holes on oxygen atoms upon charge without formation of peroxides (O – O distance of 1.5 Å).[76] In the same period, Yabuuchi and co-workers proposed the formation of O_2^-, the superoxide, in the early state-of-charge of $Li_{1.3}Nb_{0.3}Fe_{0.4}O_2$ compounds while confirming the formation of localized hole for $Li_{1.3}Nb_{03}Mn_{0.4}O_2$.[77] The difference between the two systems is proposed to be nested in the band gap. $Li_{1.3}Nb_{0.3}Fe_{0.4}O_2$ having a low band gap allows the oxidized oxygen (valence band) to donate its electron to Fe (conduction band), leading to the formation of a highly

oxidized species, O_2^-, which evolves toward O_2 gas formation. In $Li_{1.3}Nb_{03}Mn_{0.4}O_2$, the band gap is too large for this donation, and therefore the electron hole stays localized. I personally don't think the claim for the superoxide formation is correct, because I believe the Soft X-ray Absorption Spectroscopy (SXAS) data were wrongly interpreted, however, the band gap theory is quite interesting.

Overall, in only a few years, thanks to combined study of model and practical materials, the understanding of anionic redox progressed tremendously. However, practical issues of anionic redox material, namely the kinetic and hysteresis limits, still exist preventing their commercialization. Therefore more understanding is still needed to propose strategies tackling these issues. In the next part, we'll review the current understanding of anionic redox and highlight the remaining challenges.

I.3 Anionic redox, the theoretical understanding

I.3.a Oxygen lone pairs responsible for the anionic redox

A crucial question concerning anionic redox regards the nature of the electronic states involved in the anionic redox? This can be nicely understood using a simple Lewis representation of O. Oxide ions, O^{2-}, has 4 doublets, 1 with 2s and 3 with 2p electronic configurations (Figure I-6). The 2s levels being nearly core levels, they are not considered for the chemical bonding. When oxygen is bonded to a metal, one of the three 2p doublets will interact with the 3d orbitals of the cation leading to the formation of bonding (M-O) and antibonding (M-O)* states. Antibonding levels are high in energy and are typically involved during cationic redox. (M-O) bonding levels are low in energy and crucial for the stability of the chemical bond, therefore anionic redox cannot come from such states. Interestingly, up to now, anionic redox has only been observed in compounds having an O/M ratio higher than two. In this case, O is bonded to less than 3 metals hence leaving free one of the 2p oxygen doublets. Such states are usually called lone pairs, while in the battery field; they have been given other names such as "orphan state" or "unhybridized levels" etc. They are responsible for the extra capacity observed during anionic redox as demonstrated by Seo et al.[78,79] Confirming this finding, Ben Yahia et al. used the Electron Localisation Function, ELF,[80,81] to directly visualize the decrease of the lone pair density during Li extraction from various compounds showing anionic redox.[82] At this point, I should emphasize that playing with the

O/M ratio, i.e. going from $LiMO_2$, to Li_2MO_3 and Li_4MO_5, one can tune the number of lone pairs, 0, 1 and 2 per oxygen atoms, respectively. A question remains; how is the capacity of anionic redox affected by the density of lone pairs? Giving clues to answer this intriguing question is one of the aspects of this work.

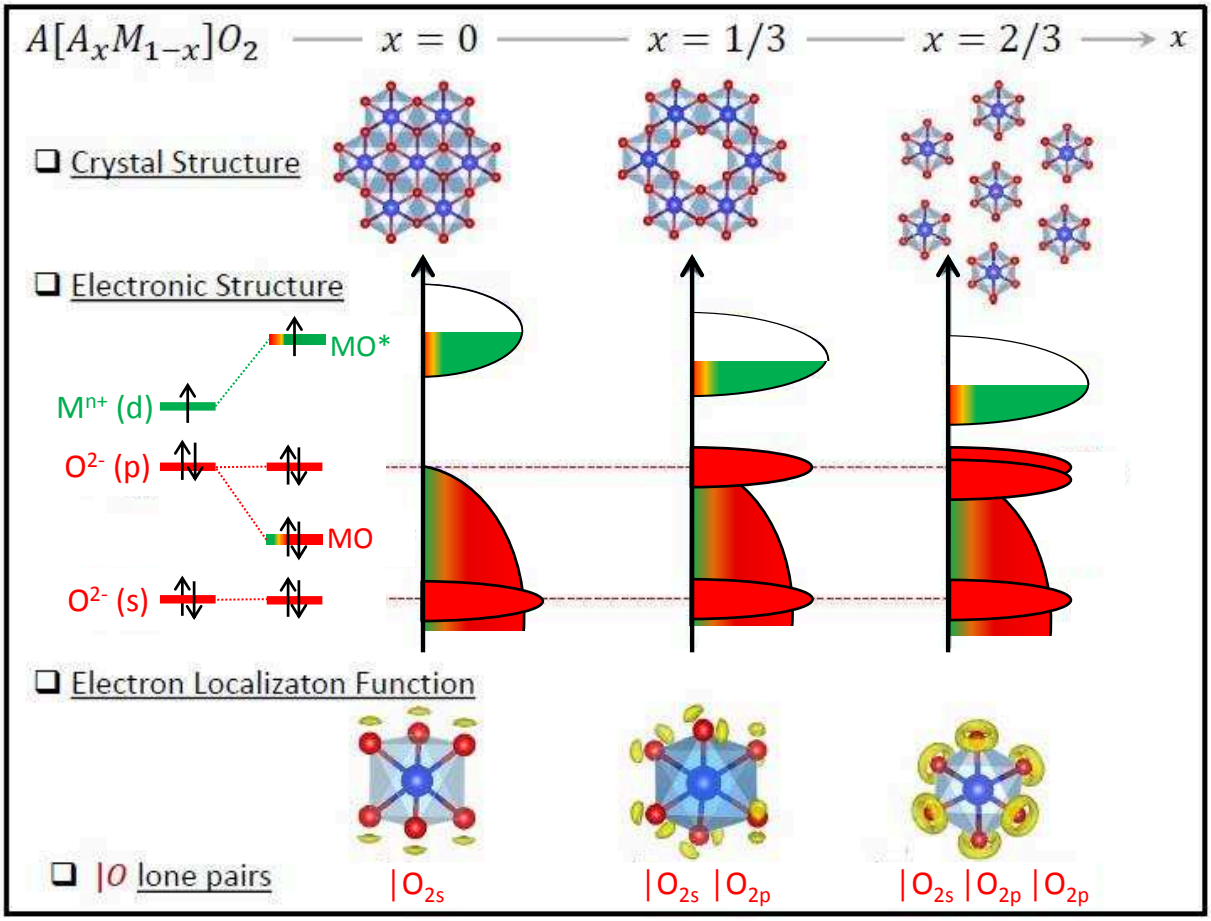

Figure I-6: Schematic representation of the electronic structures for $LiMO_2$ (x = 0), Li_2MO_3 (x = 1/3) and Li_5MO_6 (x = 2/3) where the $|O_{2s}$ and $|O_{2p}$ lone-pair states are highlighted in red bands. Electron Localization function (ELF) computed within the DFT framework are shown (ELF iso-value 0.72) for the fully ordered layered $LiCoO_2$ (x=0), Li_2IrO_3 (x=1/3)and Li_5IrO_6 phases (x=2/3). Adapted from ref[82].

I.3.b Δ_{CT} and U parameters ruling the redox mechanism

Before going further in the theoretical understanding of anionic redox, I need to introduce some concept of solid state chemistry that will complete the introduction of the electronic structure of transition metal oxides or chalcogenides started in **I.2.b.i.** Most of the following concepts have been developed in the 1980th by Zaanen and co-workers.[83] Schematics are presented in Figure I-7. The charge transfer Δ_{CT} is the energy corresponding to the charge

fluctuation $d^n \rightarrow d^{n+1}L$ (L corresponding to a ligand hole) or the difference of chemical potential between the empty (M-X)* levels and the filled X 2p band. U is the energy associated to $2*d^n \rightarrow d^{n+1} + d^{n-1}$. It is the coulombic repulsions between two electrons, of opposite spin, occupying the same orbital.[84] The effect of the coulomb interaction is to split the (M-X)* levels into upper Hubbard band (UHB) and lower Hubbard band (LHB), the latter being filled with a majority of up spin, while the former is empty with an important density of down spin holes. Being proportional to the inverse of the orbital size, this term is of great importance when the orbitals are spatially localized, e.g. in 3d metals compared to 4d and 5d. Moreover, it increases going from left to right in the periodic table due to the orbital contraction. Zaanen, Sawatzky and Allen proposed a classification of the oxides using U and Δ_{CT}, which main features are;

- if $U << \Delta_{CT}$ called Mott-Hubbard regime (MH), the Fermi level is at the top of the LHB

- if $U \approx \Delta_{CT}$ the intermediate regime, both LHB and ligand 2p bands are at the Fermi level

- if $U >> \Delta_{CT}$ the charge transfer regime (CT), the Fermi level lies at the top of the ligand 2p band with the LHB being lower in energy.

- if $\Delta_{CT} < 0$ negative charge Transfer (CT) regime, holes are created into the ligand band. In that case, Δ_{CT} is taken between the filled (M-X)* and the empty L band. It corresponds to the $d^{n+1}L \rightarrow d^n$ charge fluctuation.

In terms of redox reactions, in oxidation, i.e. electron removal, cationic redox will be observed for oxides in the Mott-Hubbard regime since the Fermi level is composed of (M-X)* levels having an important metallic character. Anionic redox will be activated for compounds in the Charge-transfer or negative charge transfer regime because oxygen lone pairs are at the Fermi level. In the case of the intermediate regime, both oxygen and transition metal will be oxidized. Having explained the theoretical representation, now we will see how these regimes can be achieved experimentally.

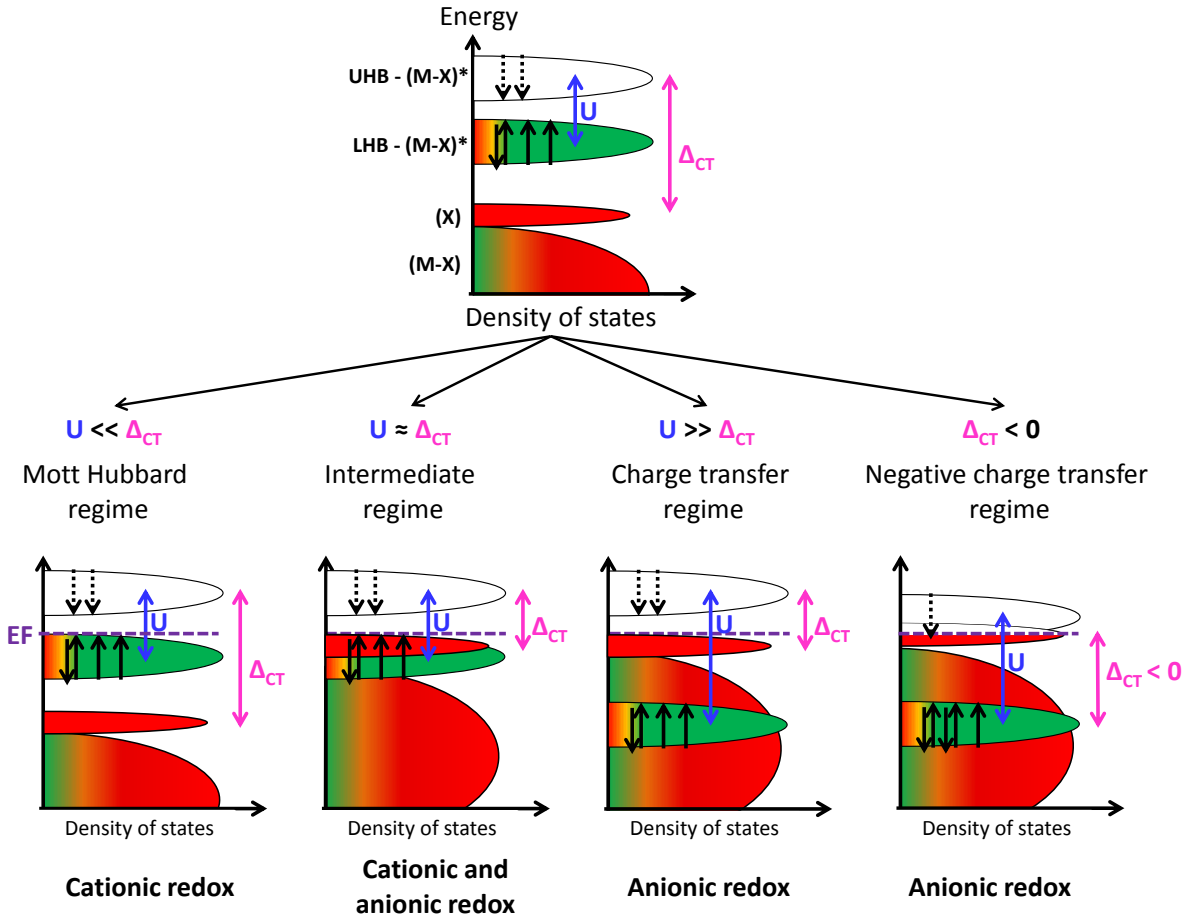

Figure I-7: Schematic presenting U and Δ_{CT} together with the different electronic regimes that can be achieved depending on the relative value of U and Δ_{CT}. UHB, LHB, (M-X)*, (M-X), (X) and EF stand for Upper Hubbard band, Lower Hubbard band, M-X antibonding and bonding states, X lone pairs and EF Fermi level.

I.3.c Strategies for the design of material showing anionic redox

I.3.c.i First rules given by Rouxel studying the chalcogenides

In the 1990th, Rouxel gave the first design principles to tune the electronic structure of the compounds from a Mott-Hubbard regime all the way to a negative charge transfer regime.[85,86] This gave rise to the ligand-hole chemistry. Looking into the crystal chemistry of different transition metal chalcogenides, Rouxel showed that a negative CT regime ($\Delta_{CT} < 0$) can be triggered playing on the chemical composition: on one hand, by decreasing the electronegativity of the ligand, i.e. going from S to Se and Te, hence raising the level of the 2p band and on the other hand, going from early transition metal (Ti, V) to late transition metals (Fe, Co, Ni), lowering the energy of the (M-X)*. Moreover, he showed that holes on

chalcogenides lead to the formation of X–X bonds for which the bond length is as short as X is oxidized. This is perfectly exemplified looking into the structure of the MX_2. Early transition metal crystallize in layered structure while late transition metal form pyrite structure in which S – S bonds of 2.2 Å are observed, as presented in Figure I-8. At this point, one can wonder if negative charge transfer can be achieved in oxides since oxygen electronegativity is much higher than sulfur. In 1991, Mizokawa et al. reported the study of $NaCuO_2$ being a negative charge transfer compound showing this regime can be achieved.[87]

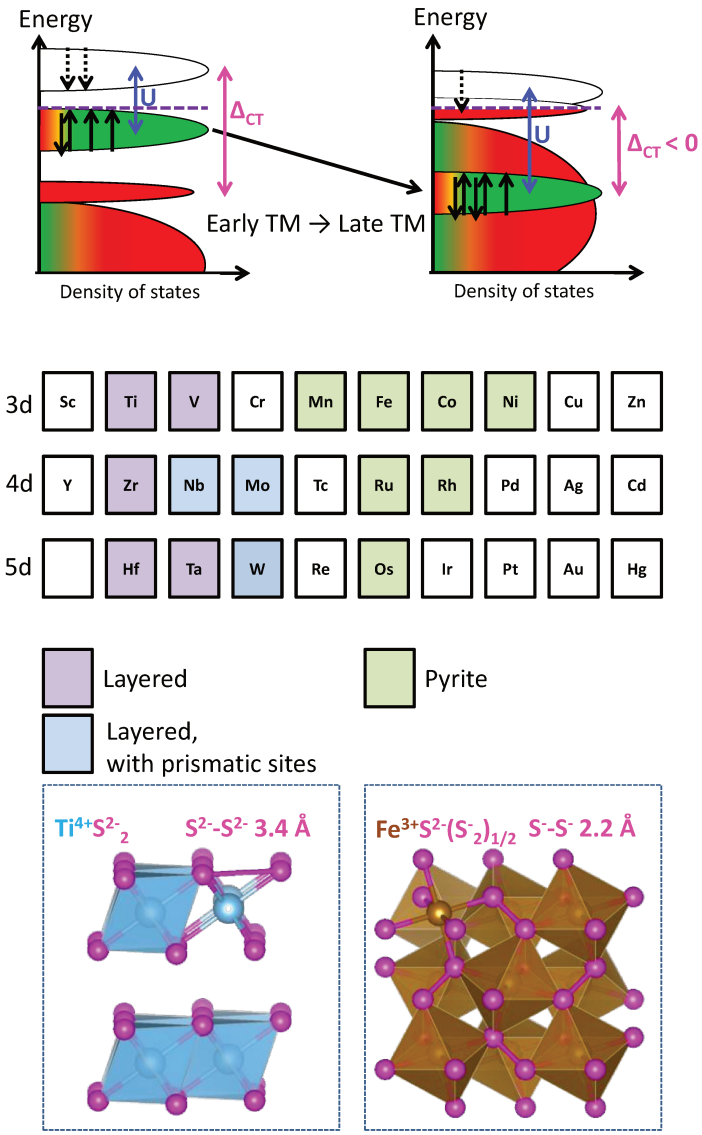

Figure I-8: Schematic presenting the evolution from a MH to a negative charge transfer regime in MS_2 going from early to late transition metals (TM). This is exemplified by the structural transformation from a layered structure to a pyrite structure having S – S bonds of 3.4 and 2.2 Å, respectively.

I.3.c.ii Electrostatic destabilization of lone pairs

Along with the chemical composition, the destabilization of the lone pair is also a strategy to trigger anionic redox. The lone pair chemical potential is only sensitive to electrostatic interactions since these states are not involved into chemical bonds. Therefore, decreasing the electrostatic potential increases the chemical potential of the lone pairs. This is typically what happens when Li^+ or a transition metal are removed from the surrounding of oxygen through electrochemical extraction/migration. Therefore, during oxidation, anionic redox can be triggered dynamically.

I.3.d Electrochemical potential and reversibility of anionic redox

Experimentally speaking, anionic redox potential in layered oxide ranges between 4 and 4.5 V which is much higher than in sulfur based chalcogenides (~2 V). Bearing in mind the correlation between the redox potential and the chemical potential of the electron in the pristine phase, the chemical hardness of the electron and the Madelung potential of the Li^+ ions established in section **I.2.b.i**, we can easily understand the observed potentials. Indeed, the Li^+ Madelung potential and the chemical potential of the electrons are higher and lower, respectively, in the oxides due to the more ionic M-O bonds compared to M-S bonds. Moreover, the chemical hardness of oxygen is much higher than sulfur.

Apart from raising the electrochemical potential, the high hardness of oxygen leads to the destabilization of the compounds during oxidation. This will undoubtedly cause electronic/structural reorganizations which control the reversibility of the anionic redox, namely the possibility to reduce oxidized oxygen species at a similar potential than their oxidation. Experimentally, different type of transformations were proposed, namely the formation of delocalized holes on oxygen states in covalent systems,[88] oxygen localized holes in Mn-rich compounds[76] and superoxide formation in Fe based material[77]. Experimentally, while the delocalized and localized holes lead to a fair reversibility, the formation of superoxide leads to O_2 release, hence poor reversibility. Despite its crucial importance, understanding the nature of the oxidized oxygen species and hence the difference between oxidation and reduction potential is still in its early stage.

Ben Yahia et al. have been theoretically investigating the nature of the oxidized species and the impacts on the electrochemical properties.[82] Covalent and ionic compounds were separated since they show different properties towards anionic redox.

For covalent compounds, reversible anionic redox can be achieved when the oxide is in the intermediate regime because the ligand hole will be delocalized over an O – O bond of 2 – 2.5 Å in interaction with metal orbitals via a reductive coupling mechanism (Figure I-9). In details, during oxidation, the electrostatic destabilization of the lone pair will happen concomitantly with the lowering of the (M-O)*. At one point, (M-O)* and lone pair levels will be at the same energy and thanks to a deformation of the lattice will interact through a reductive coupling mechanism. This leads to the formation of M-(O-O) states which causes the disappearance of one of the lone pairs as exemplified by the ELF functions presented in Figure I-9.

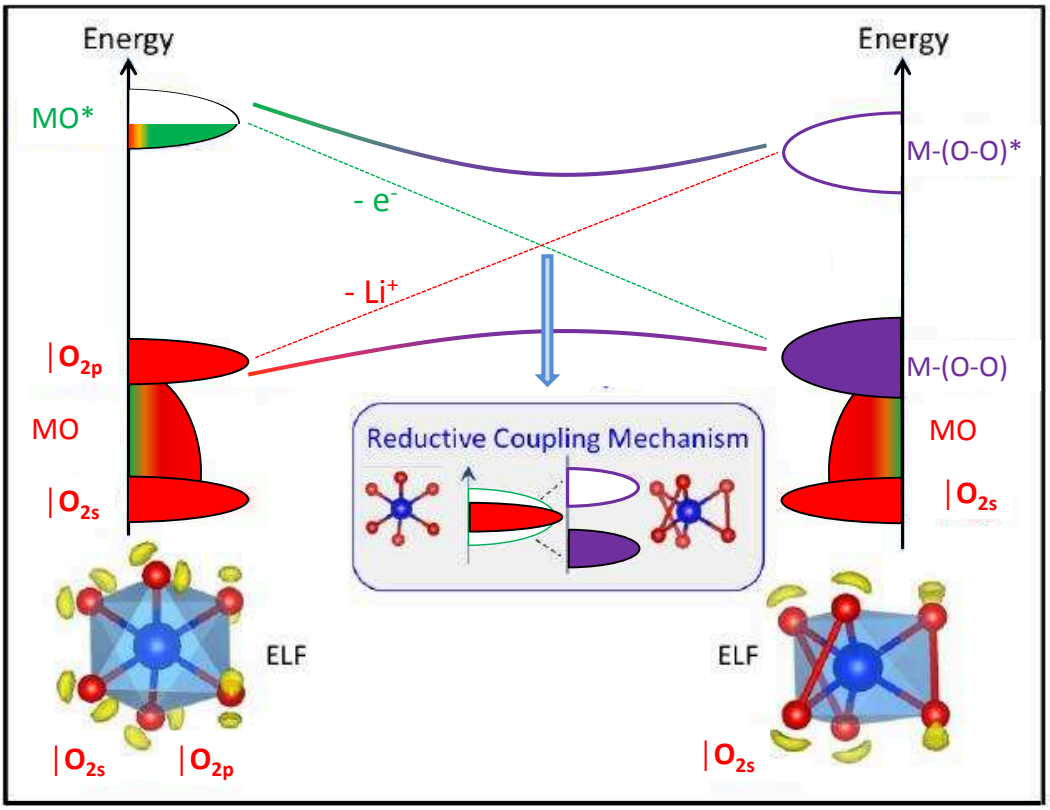

Figure I-9: Dynamics of Li-removal in strongly covalent compounds. The electrostatic stabilization (resp. destabilization) of the (M-O)* antibonding states (resp. lone pairs) upon e- (resp. Li+) removal is shown by the dashed lines. The reductive coupling mechanism, shown in the blue inset, lifts the electronic degeneracy into M-(O-O) bonding and antibonding bands represented in pink. This electron depletion of the anions is illustrated on the Li2-yIrO3 electrode at y = 0 (bottom left) and y = 2 (bottom right) showing that the formation of short O-O bonds ("peroxo-like" species) comes along with the loss of one O2p lone-pair. Adapted from Mouna et al.[82]

In this case, oxygen can be reduced during the subsequent discharge, with however small hysteresis linked to the structural transformation of the anionic lattice. If the oxide lies in the CT regime, i.e. in the absence of (M-O)* states, the oxidation of the hard oxygen atoms will lead to the creation of short O – O bonds that will be more prone to degassing.

For ionic compounds, oxygen lone pairs will not be able to interact with the transition metal. Therefore its oxidation will lead to the formation of peroxo-like species having discrete energy levels corresponding to the σ, π, π* and σ* levels. The more oxygen is oxidized, the shorter the O – O distance will become, as it can be observed moving from O_2^-, to O_2^{2-} and O_2 having bond distance of 1.8, 1.5 and 1.2 Å. Moreover, the energy between the σ, π, π* and σ* will depend on the O – O distance, i.e. the smaller is O – O the more the σ, π, π* and σ* will be separated apart from each other. The behavior of the oxidized oxygen will depend on the relative energy between the σ*, π* and Δ, labeled as Δ_{CT}, $\Delta^{\sigma}_{o\text{-}o}$ and $\Delta^{\pi}_{o\text{-}o}$, respectively, in Figure I-10.

- If $\Delta^{\sigma}_{o\text{-}o} < \Delta_{CT}$, oxygen oxidation happens with slight distortion of the oxygen lattice. The reduction is made without drastic hysteresis. In Figure I-10, this case is represented from the pristine, left, to 1. This is the case of the localized hole in Mn-based material.

- if $\Delta^{\sigma}_{o\text{-}o} > \Delta_{CT}$, the electrons from the σ* will flow towards the transition metal empty states, leading to the formation of O_2^{2-} species and the reduction of the transition metal. This case is exemplified in Figure I-10 between 1 and 2. The formed peroxide species will reduce at very low potential and the metal reduction will likely happen before during the charge. Such effect is called band inversion. Practically speaking, this is close to case of $Li_{1.3}Nb_{0.3}Fe_{0.4}O_2$.

- if $\Delta^{\pi}_{o\text{-}o} > \Delta_{CT}$, O_2 is formed and degases together with the reduction of the transition metal.

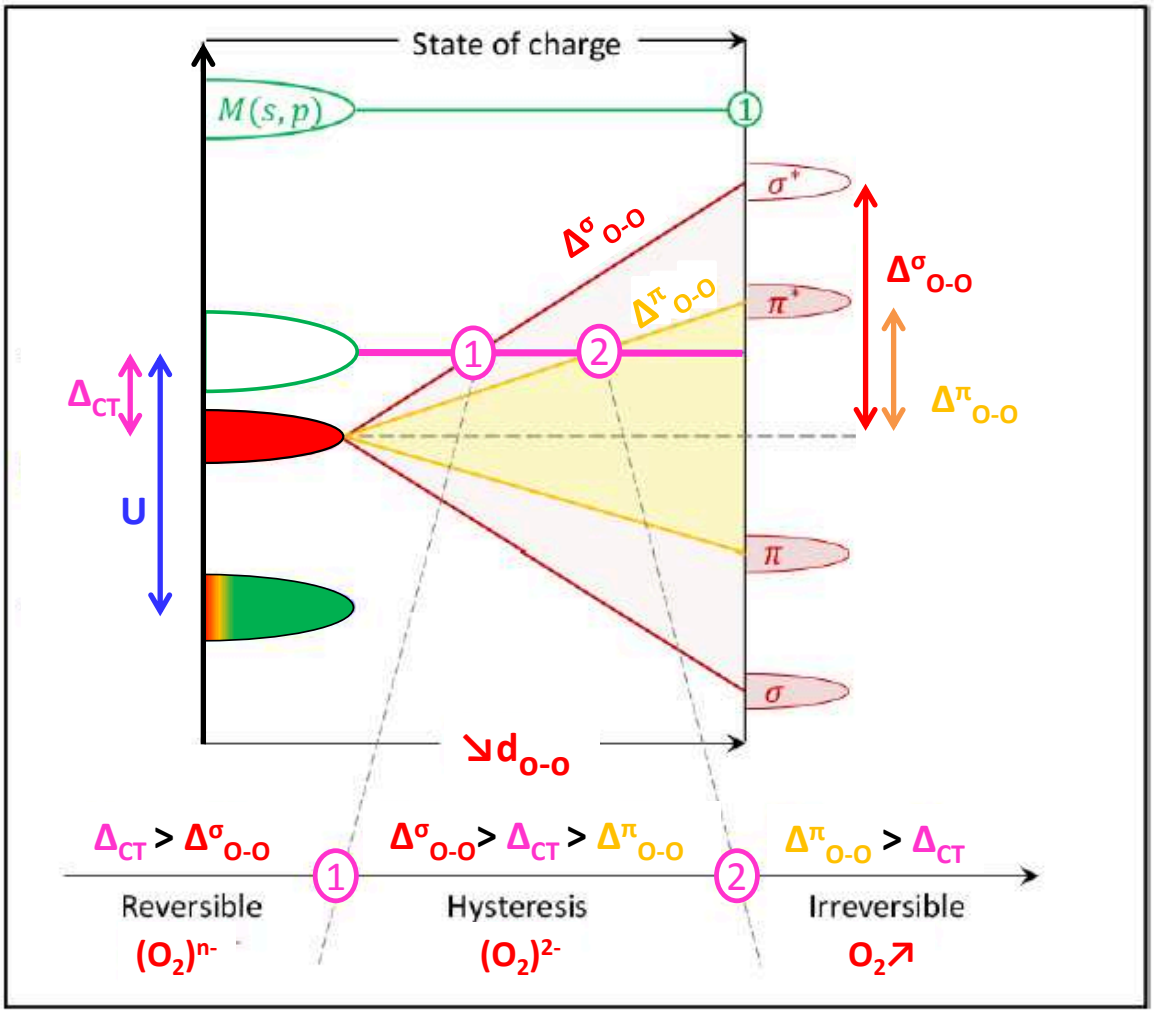

Figure I-10: Dynamics of the oxidation process in compounds being in the charge transfer regime. The splitting of the O2p narrow band into discrete σ, π, π* and σ* levels is highlighted by the red and yellow lines, as a function of the decreasing O-O distance (bottom horizontal axis) and the increasing oxidation state of the $(O\text{-}O)^{n-}$ species (top horizontal axis). The different domains of anionic activity are represented by the intervals delimited by (1) and (2)

This classification of the redox mechanism fits nicely with the available experimental facts; however, it still needs to be challenged with a wider range of material and composition. In this work, we will provide new examples focusing on Mn and Ni based compounds.

I.4 Conclusion

In this chapter, the evolution of the Li-ion battery cathode materials over the years has been presented together with theoretical findings rationalizing their performances. It is highlighted that state of art cathode needs to combine many characteristics such as; crystallographic sites and diffusion pathways for Li, electronic conduction, high electrochemical potential, stability versus Li removal and of course low cost, price and toxicity. To produce materials having all these qualities, a very precise design needs to be performed. This can only be done if the structure-property relationships are understood and mastered hence showing the need to develop the fundamental understanding of cathode materials. As a personal opinion, I think that this close relation between fundamental science and application is crucial for further battery developments.

Anionic redox activity comes with huge benefits in terms of capacity but also important drawbacks, voltage decay or potential hysteresis, and owing the complexity of this property, fundamental research is highly needed to design practical materials relying on oxygen oxidation. The use of model materials, the development of characterization techniques and the proposition of theoretical models have already paved the way, however, some questions still remain opened, i) what is the limit in terms of capacity of anionic redox? and ii) can anionic redox potential be understood and predicted ?

To answer the first question, Li "extra" rich materials have been recently studied such as Li_5FeO_4 by Zhan et al. or the Li_3IrO_4 by our group in 2017.[89,90] Both materials decompose on oxidation before the removal of all the lithium atoms suggesting anionic redox capacity is indeed limited by the stability of the oxidized compounds. In this work, we propose to assess the influence of crystal structure and chemical composition on the limit of anionic redox through a detailed study binary compounds of chemical composition: $A_3M_yM'_{1-y}O_4$ rocksalt family (A being Li or Na and M and M', Ru, Ir, Nb, Sb or Ta).

Regarding the second question on the redox potential, Assat et al. and Gent et al. showed that anionic redox comes with a potential hysteresis in Li-rich NMC, being an important drawback to the commercialization of this material.[69,70] Gent proposed cation migrations to explain this hysteresis and this lead should definitely be investigated deeper. From a theoretical point of

view, Ben Yahia et al. proposed the hysteresis to be related to the nature of the oxidized oxygen species as detailed in **I.3.d**.[82] Herein, we designed model compounds $Li_{1.3}Mn_{0.3}Ta_{0.4}O_2$ and $Li_{1.3}Ni_{0.27}Ta_{0.43}O_2$, substituting Ta by Mn or Ni in Li_3TaO_4, having very different voltage hysteresis, namely less than 1V and more then 2V, respectively, to further understand the relation between hysteresis and oxygen redox

.

Chapter II Exploring the limits of anionic redox in terms of capacity

II.1 Introduction

Anionic redox, being the oxidation/reduction of oxygen atoms, is an interesting property to increase the specific energy of Li-ion battery cathode materials. Indeed, moving from classical layered rocksalt NMC to Li-rich NMC, the capacity could be increased from 200 mAh/g to 290 mAh/g, thanks to the removal of 0.3 e^- per oxygen in the Li-rich NMC. Considering the fact that the electrochemical reaction oxidizing O^{2-} into O^- and O enlists 1 and 2 e^-, respectively, we can expect the capacity based on anionic redox to be even superior to what is achieved in today's Li-rich NMC. This observation leads to one important question: what is the limit of anionic redox in terms of capacity? To answer this question, we need to design materials having enhanced anionic redox activity. As detailed in **I.3.a**, oxygen lone pairs are the electronic states involved during anionic redox, hence the need to increase the density of these levels.[78] This can be done playing with the atomic oxygen/metal (O/M) ratio. Indeed, at high O/M ratio, less oxygen is bonded to metal and therefore more non-bonding oxygen states, or lone pairs, are present in the material.[79] This finding has led to the study of "Li extra rich" materials such as Li_5FeO_4 or Li_3IrO_4.[89,90] In both cases, anionic redox was shown to participate to the charge compensation mechanism but leads to the decomposition of the material. These preliminary results clearly indicate that the anionic redox capacity is indeed limited by the stability of the oxidized compounds. In this chapter, we propose a more detailed analysis of this limit by i) using a wider range of transition metal, ii) different structures and iii) changing the nature alkali ion from Li to Na.

We thus embarked into designing binary systems of chemical composition $Li_3M_yM'_{1-y}O_4$, with M and M' being transition metals, and compare some of these compounds with their Na counterparts. To do so, the first step is to choose the transition metals M and M'. The choice is restricted by the following criteria, i) composition should be A_3MO_4, with A^+ and M^{5+} being the alkali and the metal, respectively, and ii) the structure should be a derivative of the rocksalt structure, hence all cations should be octahedrally coordinated. These two conditions prevent the use of 3d transition metals since they are found in tetrahedral coordination in the

5+ oxidation state. Therefore, we have chosen the following 4d and 5d transition metals: Nb^{5+} ($4d^0$), Ru^{5+} ($4d^3$), Sb^{5+} ($4d^{10}$), Ta^{5+} ($5d^0$) and Ir^{5+} ($5d^4$), that have different d orbital filling and hence are expected to have different chemistries. Turning to the structural requirements, the Li_3MO_4 family possesses a rich crystal chemistry based on different cation orderings depending on the nature of the transition metal, M, and hence provides a fertile ground to assess the influence of the crystallographic structure on the anionic redox.

This chapter will be composed of three parts. First, the synthesis of compounds among the series $Li_3M_yM'_{1-y}O_4$ for M and M' being Nb, Ru, Sb, Ta or Ir, will be presented together with their detailed structural characterization and the rationalization of their crystal structure using DFT calculations. Second, their electrochemical properties and charge compensation mechanisms will be assessed. Third, Na_3RuO_4 will be compared to Li_3RuO_4 to probe the influence of the alkali atom over the anionic redox mechanism.

This chapter refers to already published data. [91,92,93]

II.2 Synthesis, crystal structure and rationalization of the cation ordering in $Li_3M_yM'_{1-y}O_4$ compounds

The end members; Li_3NbO_4 (I -4 3 m), Li_3RuO_4 (P 2/a), Li_3SbO_4 (P 2/c), Li_3IrO_4 (R -3 m) and Li_3TaO_4 (α, β, γ polymorph, P 2/n, C 2/c, F m -3 m respectively) have already been reported.[94,95,96,90,97,98] All crystalize in a rocksalt type structure having the following characteristics: i) all cations are octahedrally coordinated by anions and so are the anions by the cations, ii) anions are close-packed (FCC stacking) and all octahedral interstices are occupied with cations, and iii) MO_6 octahedra are connected by their edges.[99] However, their crystal structure differs by the Li/M ordering leading a rich crystal chemistry based on different metallic frameworks as presented in Figure II-1. For instance, Li_3NbO_4 is composed of tetramers of NbO_6 octahedra while in Li_3RuO_4, RuO_6 are forming infinite chains along one crystallographic direction. We have been able to synthesized, via ceramic methods, a multitude of new members among the $Li_3M_yM'_{1-y}O_4$ series. Detailed structural characterization including long range, local environment and defect analysis showed that all compounds also crystallize in a rocksalt structure with variety of different cation orderings which will be rationalized using DFT calculations.

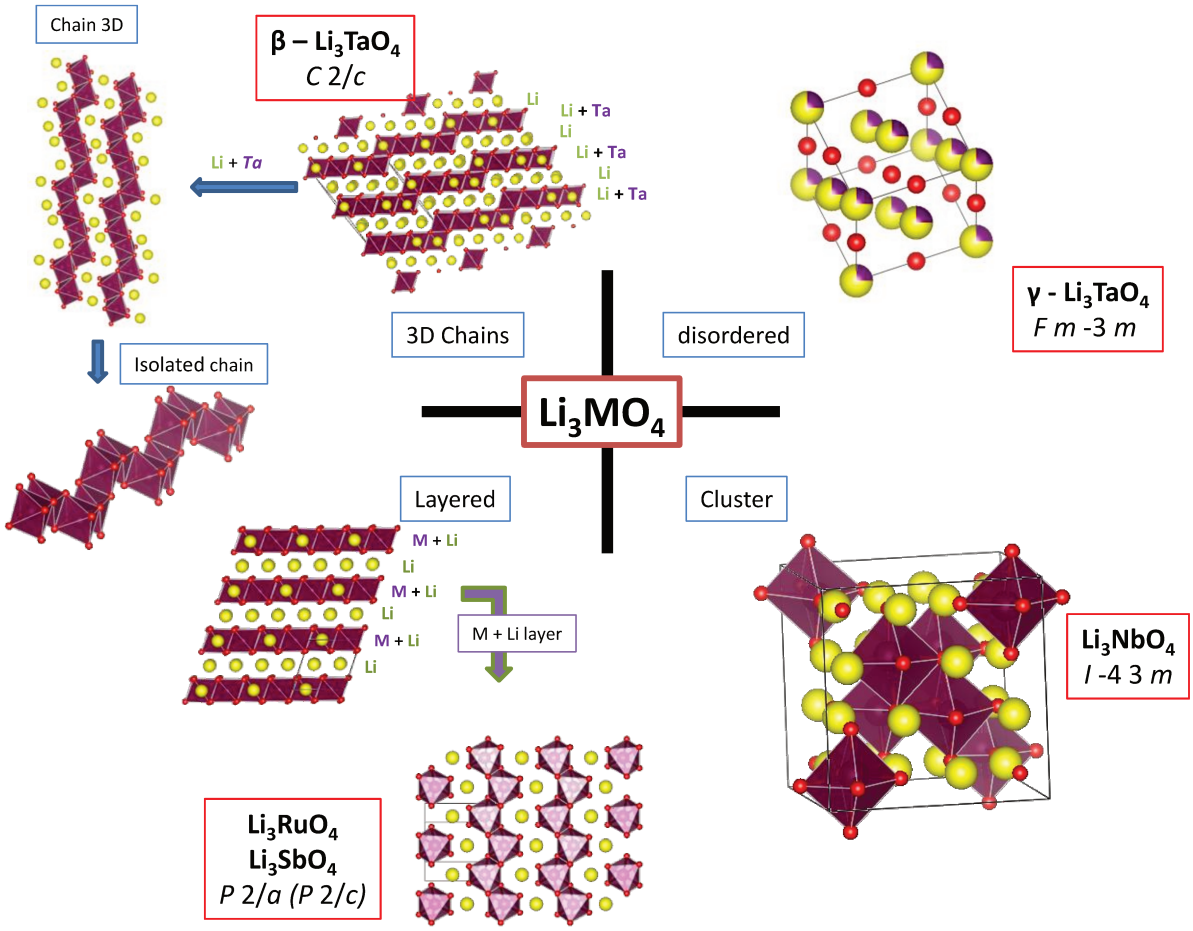

Figure II-1: Schematic presenting the structure of some Li_3MO_4 compounds with M being Nb, Ru, Sb and Ta. All are rocksalt with different Li/M ordering.

II.2.a Synthesis of $Li_3M_yM'_{1-y}O_4$ (M and M' being Ru, Nb, Sb, Ir, Ta)

Among the possible cation combinations, we focused on $Li_3Ru_yNb_{1-y}O_4$, $Li_3Ru_ySb_{1-y}O_4$, $Li_3Ru_yIr_{1-y}O_4$, $Li_3Sb_yNb_{1-y}O_4$ for which samples for y = 0, 0.25 (or 0.3), 0.5, 0.75 (or 0.7) and 1 have been prepared, so as to get a representative view of the phase diagrams. $Li_3Ru_{0.5}Ta_{0.5}O_4$ has also been synthetized. Pure phase could be obtained for nearly all the compositions using classical solid-state synthesis from metallic or oxide precursors, Nb_2O_5 (Sigma-Aldrich 99.9%), RuO_2 (Alfa Aesar, 99.9%), Sb_2O_3 (Alfa Aesar, 99.998%), Ta_2O_5 (Alfa Aesar, 99.85%), Ir black (Alfa Aesar 99.9%) with 10% excess Li_2CO_3 (Sigma Aldrich, 99%). The reactants were mixed using a mortar and pestle before grinding in a planetary ball-mill using a zirconia set for 1 hour at 600 rpm. Grinding is a crucial step in order to have a homogenous mixing of the transition metal precursor and therefore limit the phase segregation. Moreover, zirconia set is compulsory due to the hardness of Nb_2O_5 preventing the use of stainless steel vial and balls. Ground powders were fired for 24 h at 900°C in air in alumina crucible. Then, the samples were ground again, using a mortar and pestle, and re-fired at 900°C – 1000°C, with the exception of members of the $Li_3Ru_yIr_{1-y}O_4$ series which suffer from reduction upon prolonged heating. This step was repeated until pure phases were obtained. Heat treatment conditions for each sample are reported in Table II-1.

Composition	Heat treatment sequence
$Li_3Ru_yIr_{1-y}O_4$ for $0 \leq y \leq 1$	900°C – 24h
$Li_3Ru_{0.7}Sb_{0.3}O_4$	900°C -24h *2
$Li_3Ru_{0.5}Sb_{0.5}O_4$	900°C -24h *2
$Li_3Ru_{0.3}Sb_{0.7}O_4$	900°C -24h *2
Li_3SbO_4	900°C -24h + 1000°C – 24h *3
$Li_3Sb_{0.7}Nb_{0.3}O_4$	900°C -24h + 1000°C – 24h *3
$Li_3Sb_{0.5}Nb_{0.5}O_4$	900°C -24h + 1000°C – 24h *3
$Li_3Sb_{0.3}Nb_{0.7}O_4$	900°C -24h + 1000°C – 24h *4
Li_3NbO_4	900°C -24h + 1000°C – 24h
$Li_3Ru_{0.1}Nb_{0.9}O_4$	900°C – 24h * 2 + 1000°C – 24h *4
$Li_3Ru_{0.3}Nb_{0.7}O_4$	900°C – 24h * 3 + 1000°C – 24h *2
$Li_3Ru_{0.5}Nb_{0.5}O_4$	900°C – 24h * 2
$Li_3Ru_{0.7}Nb_{0.3}O_4$	900°C – 24h
$Li_3Ru_{0.5}Ta_{0.5}O_4$	900°C – 24h +900°C – 24h

Table II-1: Synthesis conditions. All heat treatment were made under air.

II.2.b Structural characterization

II.2.b.i Long range structure via complementary neutron and X-ray diffraction

The structural determination was performed using synchrotron X-ray powder and neutron powder diffractions, called hereafter SXRD and NPD, respectively, for $Li_3Ru_ySb_{1-y}O_4$, $Li_3Ru_yNb_{1-y}O_4$, and $Li_3Sb_yNb_{1-y}O_4$ systems. SXRD was performed using the mailing service of the 11-BM beamline in APS while NPD was done on D1B beamline at ILL, with the help of Mrs. Vivian Nassif. Coupling these two techniques allows the accurate determination of the atomic positions of heavy (Ru, Sb and Nb) and light (Li and O) elements with X-rays and neutron, respectively (Z_{Li} = 3 and b_{Li} = -1.90 fm, Z_{Ru} = 44 and b_{Ru} = 7.03 fm, Z_{Sb} = 51 and b_{Sb} = 5.57 fm, Z_{Nb} = 41 and b_{Nb} = 7.05 fm, z_o = 8 and b_o = 5.803 fm).

One should note that Nb and Ru are hard to distinguish since both have nearly the same electron densities and neutron scattering lengths. For $Li_3Ru_yIr_{1-y}O_4$ with y = 1, 0.75, 0.5, 0.25 and 0 and $Li_3Ru_{0.5}Ta_{0.5}O_4$, conventional XRD was used.

Structures of $Li_3Ru_yIr_{1-y}O_4$ for y = 0, 0.25, 0.5, 0.75 and 1.

First the crystal structure of members among the series $Li_3Ru_yIr_{1-y}O_4$ will be presented. The XRD patterns of the obtained compounds are shown in Figure II-2. Li_3RuO_4 can be described in the P 2/a space group with a volume per formula unit of 71.79 $Å^3$ while Li_3IrO_4 has been recently reported to crystallize in R -3 m with a volume per formula unit of 72.77 $Å^3$. Both are layered rocksalt derivatives composed of LiO_6 and $(M_{0.5}Li_{0.5})O_6$ layers (M being Ru or Ir) with the only difference being nested in the way the Li is arranged with respect to M within the $(M_{0.5}Li_{0.5})O_6$ layers. In Li_3RuO_4, Li and Ru are ordered in zig-zag chains, while in Li_3IrO_4, Li and Ir are randomly distributed within the layers. Regarding the intermediate compositions, $Li_3Ru_{0.25}Ir_{0.75}O_4$ and $Li_3Ru_{0.5}Ir_{0.5}O_4$ show the same pattern as Li_3IrO_4 while $Li_3Ru_{0.75}Ir_{0.25}O_4$ pattern is similar to the one of Li_3RuO_4. Accordingly, $Li_3Ru_{0.75}Ir_{0.25}O_4$ was satisfactorily refined using the structural model of Li_3RuO_4 (P 2/a) while introducing a slight Li/M cation mixing in the $(M_{0.5}Li_{0.5})O_6$ layers (Table II-2). Rietveld refinement of $Li_3Ru_{0.25}Ir_{0.75}O_4$ and $Li_3Ru_{0.5}Ir_{0.5}O_4$ using Li_3IrO_4 (R -3 m) structural model led to a decent fit, which could however be improved using the structural model of Li_3RuO_4 with a total disordering between Li and M in the transition metal layer, as it can be seen in Figure II-3. The main difference between the R -3 m and the P 2/a models is nested in the oxygen stacking

which is slightly distorted in the latter due to the β angle. Across the series, the volume per formula unit increases from 71.97 Å^3 to 72.24 Å^3 and 72.55 Å^3 for y = 0.75, 0.5 and 0.25, respectively, which is fully consistent with the slightly larger ionic radii of Ir (0.57 Å) compared to Ru (0.56 Å).[100] Overall, through the $Li_3Ru_yIr_{1-y}O_4$ phase diagram, a phase transition from a perfectly ordered layered structure to a disordered layered structure is unveiled.

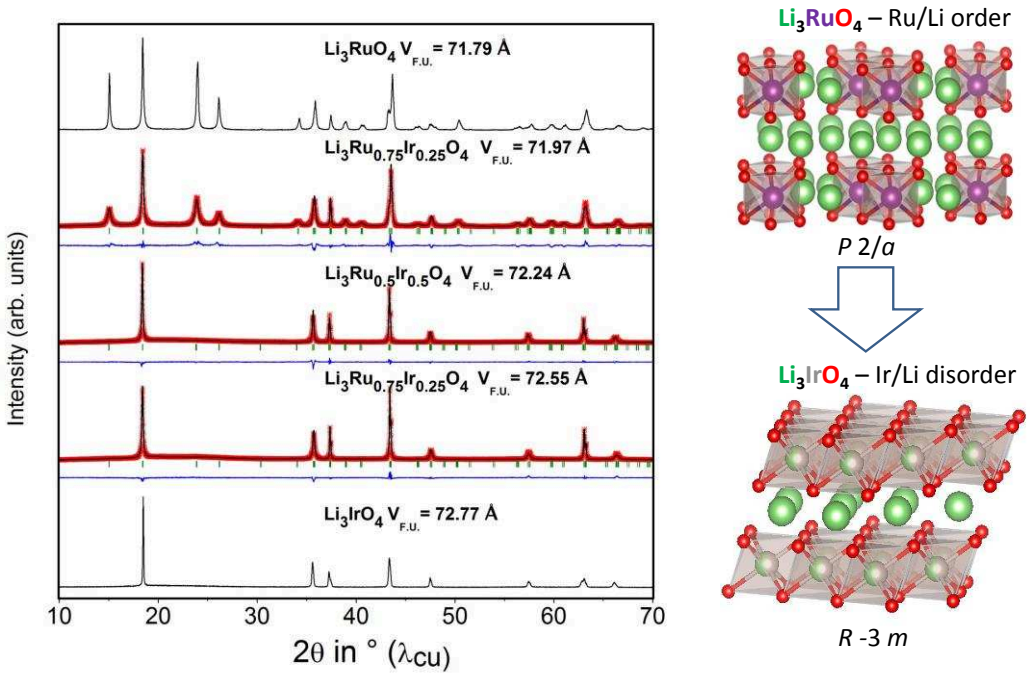

Figure II-2: XRD patterns and Rietveld refinements of compounds among the solid solution $Li_3Ru_yIr_{1-y}O_4$ for y = 1, 0.75, 0.5, 0.25 and 0 from top to bottom together with the structures of Li_3RuO_4 and Li_3IrO_4 with a fully ordered and partially ordered rocksalt structure, respectively. Li, Ru, Ir and O are in green, gray, purple and red, respectively. The red crosses, black continuous line and bottom blue line represent the observed, calculated, and difference patterns respectively. Vertical green tick bars are the Bragg positions.

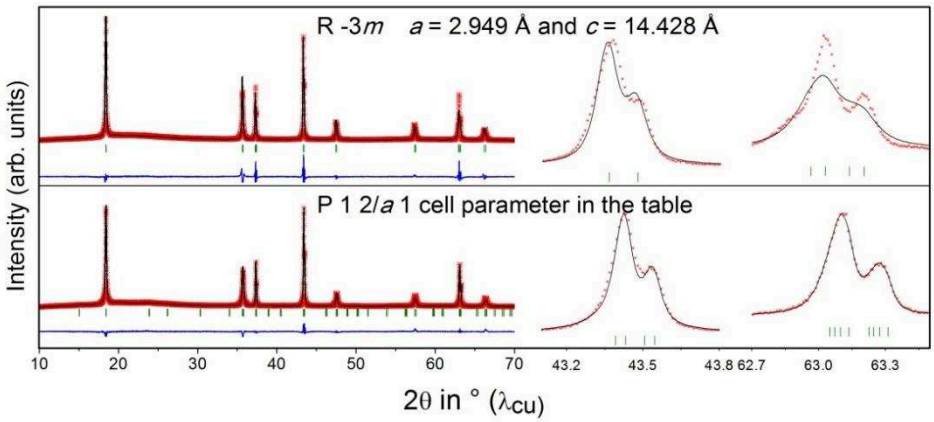

Figure II-3: Rietveld refinement of $Li_3Ru_{0.5}Ir_{0.5}O_4$ using the structural model of Li_3IrO_4 described in R -3m (top) and the P 1 2/a 1 structural model of Li_3RuO_4 (bottom) together with zooms emphasizing the better fit using the structural model of Li_3RuO_4.

$Li_3Ru_{0.75}Ir_{0.25}O_4$ – $R_{bragg\ XRD}$ =7.25 %				
P 1 2/a 1	a = 5.10576(11) Å b = 5.87070(13) Å	c = 5.10066(12) Å β = 109.703(15)°	Z = 2	V/Z = 71.969 Å^3
$Li_3Ru_{0.5}Ir_{0.5}O_4$ – $R_{bragg\ XRD}$ = 7.63 %				
P 1 2/a 1	a = 5.1052(9) Å b = 5.8856(8) Å	c = 5.10077(7) Å β = 109.495(12) °	Z = 2	V/Z = 72.24 Å^3
$Li_3Ru_{0.25}Ir_{0.75}O_4$ – $R_{bragg\ XRD}$ = 9.03 %				
P 1 2/a 1	a = 5.11825 (5) Å b = 5.89270 (4) Å	c = 5.10494 (5) Å β = 109.536(7)°	Z = 2	V/Z = 72.552 Å^3

Atom	Wyckoff position	x	y	z	B_{iso} (Å²)	occupancy
O1	4g	0.037(17) 0.027(3) 0.028(4)	0.6413(12) 0.628(3) 0.627(3)	0.7685(17) 0.744(3) 0.770(5)	0.7	1
O2	4g	0.522(2) 0.512(5) 0.491(5)	0.1163(13) 0.111(3) 0.112(2)	0.2270(17) 0.231(3) 0.247(5)	0.7	1
Li1/Ru1/Ir1	2e	¾	0.612	0	1.0	0.88/0.08/0.04 0.5/0.25/0.25 0.50/0.12/0.38
Li2	2f	¾	0.870	½	1.0	1
Li3	2f	¾	0.386	½	1.0	1
Ru4/Ir4/Li4	2e	¾	0.8655(3) 0.8751(11) 0.8750(7)	0	1.0	0.66/0.22/0.12 0.25/0.25/0.5 0.12/0.38/0.50

Table II-2: Crystallographic data for $Li_3Ru_{0.75}Ir_{0.25}O_4$, $Li_3Ru_{0.5}Ir_{0.5}O_4$, and $Li_3Ru_{0.25}Ir_{0.75}O_4$ in red, blue and green letters, respectively. B_{iso} and Li position in black were not refined. Note that P 1 2/a 1 space group, unique axis b, with a $\beta < 120°$ is not a standard description. However, we used this description since it is the way Li_3RuO_4 as reported. Li_3SbO_4, isostructural to Li_3RuO_4 has been reported in P 2/c with the same cell metrics, in that case being a standard description.

Structure of $Li_3Ru_ySb_{1-y}O_4$, $Li_3Ru_yNb_{1-y}O_4$, and $Li_3Sb_yNb_{1-y}O_4$ for y= 0, 0.3, 0.5, 0.7, 1.

SXRD patterns of compounds among the $Li_3Ru_ySb_{1-y}O_4$ family, shown in Figure II-4a, are similar but with Bragg peaks gradually shifted to lower angle when the Sb content increases, indicating a solid-solution behavior. One should note in Figure II-4b that, for some compositions, a few reflections show very peculiar peak shape which indicates the presence of a complex microstructure. For Li_3SbO_4, this peculiar peak shape can be reproduced by introducing in the Rietveld refinement three Li_3SbO_4 phases with slightly different cell parameters (Figure II-4c). This distribution of cell parameters may be due to inhomogeneous composition within the sample and/or severe strain effects. For the $Li_3Ru_yNb_{1-y}O_4$ and $Li_3Sb_yNb_{1-y}O_4$, the patterns and hence the crystal structures change substantially with y (Figure II-5a-b). All diffractograms could be indexed with known structures; $Li_3Ru_{0.7}Nb_{0.3}O_4$, $Li_3Ru_{0.5}Nb_{0.5}O_4$ and $Li_3Ru_{0.5}Ta_{0.5}O_4$ crystallize in the same structure as Ag_3RuO_4.[101] $Li_3Ru_{0.3}Nb_{0.7}O_4$ and $Li_3Sb_{0.3}Nb_{0.7}O_4$ are isostructural to β-Li_3TaO_4. $Li_3Sb_{0.5}Nb_{0.5}O_4$ adopts the structure of α–Li_3TaO_4 and $Li_3Sb_{0.7}Nb_{0.3}O_4$ resembles Li_3SbO_4.

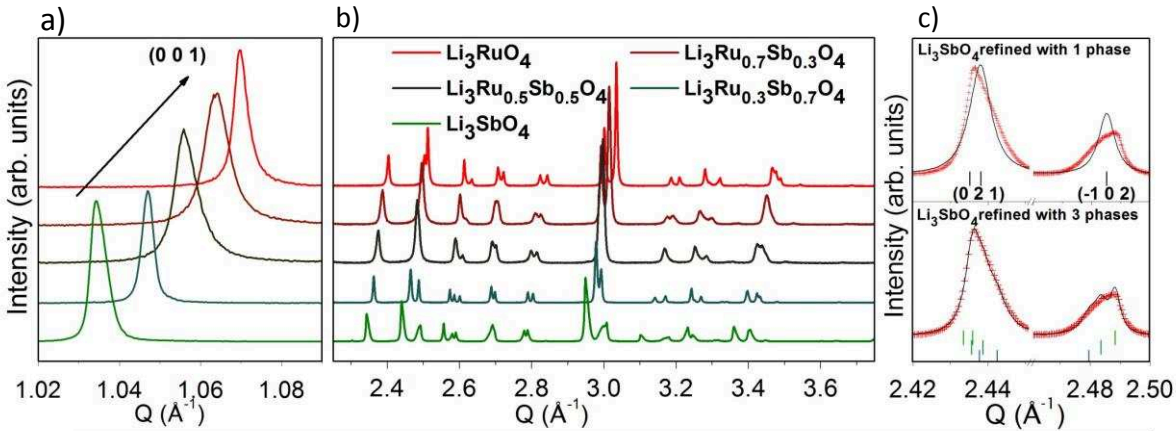

Figure II-4: SXRD patterns (λ = 0.414562 Å) for the $Li_3Ru_ySb_{1-y}O_4$ samples with y = 1, 0.7, 0.5, 0.3, and 0, at different regions of Q; a) around the (001) reflection and b) from 0.8 $Å^{-1}$ to 3.750 $Å^{-1}$. c) Rietveld refinement of Li_3SbO_4 SXRD pattern using one phase (top) or three phases with the structural model of Li_3SbO_4 but slightly different cell parameters (bottom). The red crosses and black continuous line represent the observed and calculated patterns, respectively. Vertical tick bars are the Bragg positions.

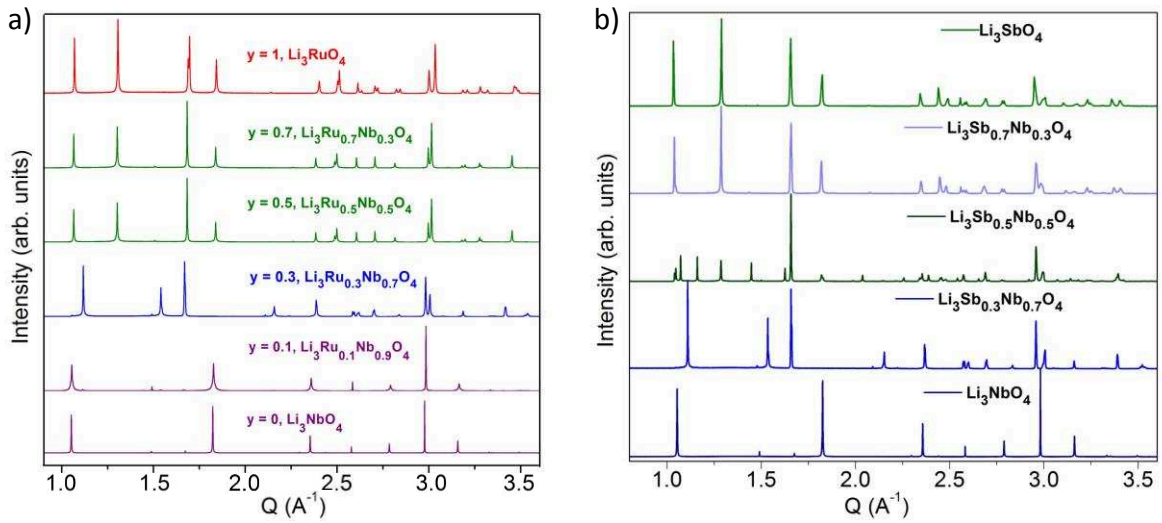

Figure II-5: Synchrotron X-ray diffraction patterns (λ = 0.414562 Å) for a) the $Li_3Ru_yNb_{1-y}O_4$ samples with y = 1, 0.7, 0.5, 0.3, 0.1 and 0 and b) the $Li_3Nb_ySb_{1-y}O_4$ samples with y = 1, 0.7, 0.5, 0.3, and 0.

Overall, all structures are rocksalt derivatives and differ in their cation orderings, as emphasized on Figure II-6 in which only the transition metal cations are shown. This representation of the metallic framework highlights the Ru, Sb and Nb connecting modes. For the $Li_3Ru_ySb_{1-y}O_4$ system, the same metallic framework is found over the whole diagram, and consists of zig-zag (Ru, Sb)O_6 edge-sharing chains. The $Li_3Ru_yNb_{1-y}O_4$ system is more complex. As the niobium content increases, the arrangement of the M-M bonds transforms from [RuO_6] zig-zag chains in Li_3RuO_4 to [MO_6] spiral chains in $Li_3Ru_yNb_{1-y}O_4$ for y = 0.7 and y = 0.5, then to jagged [MO_6] chains in $Li_3Ru_{0.3}Nb_{0.7}O_4$, and finally to clusters of four [MO_6] in $Li_3Ru_{0.1}Nb_{0.9}O_4$ and Li_3NbO_4. In the $Li_3Sb_yNb_{1-y}O_4$, the zig-zag chains arrangement is observed for y = 1 and 0.75, then it evolve into [MO_6] “eight”-shaped chains in $Li_3Sb_{0.5}Nb_{0.5}O_4$, then to jagged [MO_6] chains in $Li_3Sb_{0.3}Nb_{0.7}O_4$, and finally to clusters of four [MO_6] in Li_3NbO_4. At this point, one should note the following trends: i) structures containing Nb^{5+} show a rich diversity, ii) compounds without Nb adopt the same structure.

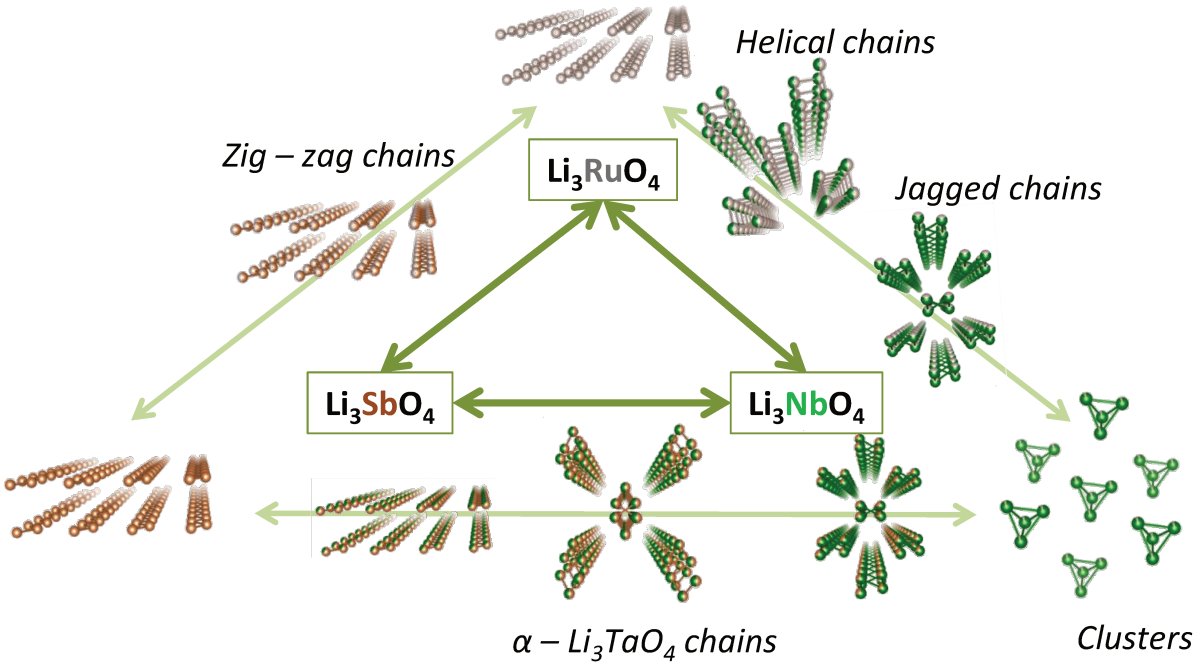

Figure II-6: Schematic of the structures of the $Li_3Ru_yNb_{1-y}O_4$, $Li_3Ru_ySb_{1-y}O_4$, and $Li_3Sb_yNb_{1-y}O_4$ for y = 1, 0.7, 0.5, 0.3, and 0. For each composition only the metallic framework, M-M bonds with M = Nb, Sb or Ru, are shown.

Following the goal of understanding the structural evolution and, ideally, finding a chemical descriptor, we performed combined Rietveld refinements of SXRD and NPD patterns on each compound to retrieve precise structural parameters. We should emphasize that for all the systems, no ordering was found between Ru/Sb/Nb atoms. Therefore, they share the same crystallographic sites with the partial occupancy being defined by the chemical formula.

All compositions of the $Li_3Ru_ySb_{1-y}O_4$ system (y = 1, 0.7, 0.5, 0.3, and 0) were satisfactorily refined with the structural model of Li_3SbO_4 (Figure II-7a), crystallizing in P 2/c space group, with the atomic positions given in Table II-3. The volume variation with Ru/Sb content follows Vegard's law (Figure II-7b), while cell parameters present a nonlinear evolution with the composition, as can be expected from an anisotropic structure (Figure II-7c). We now focus on the $Li_3Sb_yNb_{1-y}O_4$ and $Li_3Ru_yNb_{1-y}O_4$ systems (y = 0, 0.3, 0.5, 0.7, 1). Good Rietveld refinements on combined SXRD and NPD patterns were obtained for all compositions using one of the following structural models: Li_3SbO_4, α–Li_3TaO_4, and β–Li_3TaO_4 and Ag_3RuO_4 (Figure II-8). From Table II-4 to Table II-7 giving the space group, cell parameters, and atomics positions obtained by refinement, it can be seen that, for most of the mixed compositions, a partial disordering between Ru/Sb/Nb and Li was considered, greatly improving the fit.

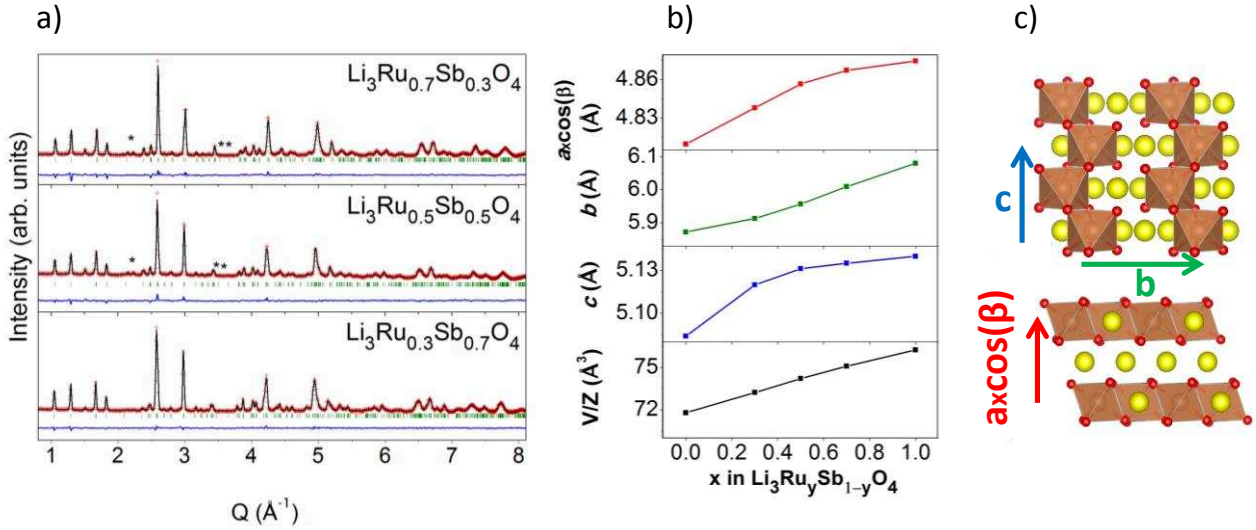

Figure II-7: a) Rietveld refinement of neutron diffraction patterns (λ = 1.29 Å) for $Li_3Ru_{0.7}Sb_{0.3}O_4$, $Li_3Ru_{0.5}Sb_{0.5}O_4$ and $Li_3Ru_{0.3}Sb_{0.7}O_4$ performed using the structural model of Li_3SbO_4 having a zig-zag chains structure. The red crosses, black continuous line and bottom blue line represent the observed, calculated, and difference patterns respectively. Vertical green tick bars are the Bragg positions. Li_2CO_3 was added as a secondary phase (marked with *). b) and c) Evolution of interlayer distance axcos(β), interchain distance b, c parameter and V/Z in red, green, blue, and black respectively along the solid solution together with two representations of the structure highlighting the reported distances. Error bars are included within the symbol size. Li, Sb and O are in yellow, orange and red, respectively

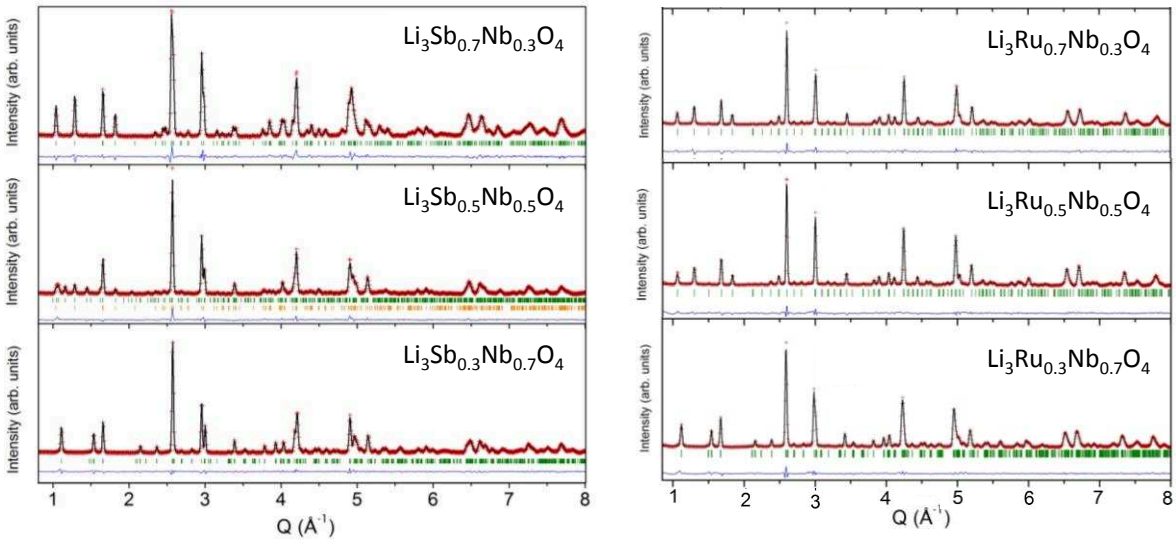

Figure II-8: Rietveld refinement of NPD patterns (λ = 1.29 Å) for $Li_3Sb_{0.7}Nb_{0.3}O_4$, $Li_3Sb_{0.5}Nb_{0.5}O_4$ and $Li_3Sb_{0.3}Nb_{0.7}O_4$ and $Li_3Ru_{0.7}Nb_{0.3}O_4$, $Li_3Ru_{0.5}Nb_{0.5}O_4$ and $Li_3Ru_{0.3}Nb_{0.7}O_4$ on the left and right side, respectively. The red crosses, black continuous line and bottom blue line represent the observed, calculated, and difference patterns respectively. Vertical green tick bars are the Bragg positions. Second phase for $Li_3Sb_{0.5}Nb_{0.5}O_4$ pattern is fitted with $Li_3Sb_{0.7}Nb_{0.3}O_4$ model

$Li_3Ru_{0.7}Sb_{0.3}O_4$ – Zig-zag chains $R_{bragg\ neutrons}$ = 6.07%. $R_{bragg\ SXRD}$ = 4.67%				
P 1 2/c 1	a = 5.14770(9) Å c = 5.12039(10) Å	b = 5.91378(11)Å β = 109.9749(14)°	Z = 2	V/Z = 73.25 Å^3
$Li_3Ru_{0.5}Sb_{0.5}O_4$ – Zig-zag chains $R_{bragg\ neutrons}$ = 6.92%. $R_{bragg\ SXRD}$ = 5.74%				
P 1 2/c 1	a = 5.16212(5) Å c = 5.13165(5) Å	b = 5.95672(6)Å β = 109.815(7)°	Z = 2	V/Z = 74.22 Å^3
$Li_3Ru_{0.3}Sb_{0.7}O_4$ – Zig-zag chains $R_{bragg\ neutrons}$ = 4.07%. $R_{bragg\ SXRD}$ = 4.47%				
P 1 2/c 1	a = 5.16436(5) Å c = 5.13490(5) Å	b = 6.00957(6)Å β = 109.535(8)°	Z = 2	V/Z = 75.09 Å^3

Atom	Wyckoff position	x	y	z	B_{iso} (Å²)	occupancy
O1	4g	0.2265(8) 0.2234(8) 0.2222(7)	0.1122(7) 0.1113(6) 0.1059(4)	0.0047(9) 0.0022(9) -0.0013(9)	0.41(2) 0.41(2) 0.463(13)	1
O2	4g	-0.2434(7) -0.2442(7) -0.2454(6)	0.3641(7) 0.3618(6) 0.3607(6)	0.0226(8) 0.0258(8) 0.0215(8)	0.26(2) 0.26(2) 0.46(2)	1
Ru1/Sb1	2e	0	0.1402(4) 0.1407(3) 0.1431(3)	¼	0.405(16) 0.485(16) 0.276(3)	0.7/0.3 0.5/0.5 0.3/0.7
Li1	2e	0	0.617(4) 0.602(2) 0.608(3)	¼	1.03(8) 1.20(7) 1.078(7)	1
Li2	2f	½	0.146(5) 0.135(5) 0.141(4)	¼	1.03(8) 1.20(7) 1.078(7)	1
Li3	2f	½	0.390(3) 0.395(3) 0.409(2)	¼	1.03(8) 1.20(7) 1.078(7)	1

Table II-3: Crystallographic table for $Li_3Ru_{0.7}Sb_{0.3}O_4$, $Li_3Ru_{0.5}Sb_{0.5}O_4$ and $Li_3Ru_{0.3}Sb_{0.7}O_4$ in red, blue and green obtained by refinement of combined SXRD and NPD patterns. Note that the reported compounds are isostructural to Li_3RuO_4, reported in P 1 2/a 1.

$Li_3Sb_{0.7}Nb_{0.3}O_4$ - Zig – zag chains $R_{bragg\ neutrons}$ = 3.51%. $R_{bragg\ SXRD}$ = 5.73%						
P 1 2/c 1	a = 5.18099(6) Å c = 5.15324(5) Å	b = 6.05403(6) Å β = 109.338(7)°		Z = 2		V/Z = 76.258 Å^3
Atom	Wyckoff position	x	y	z	B_{iso} (Å²)	Occupancy
O1	4g	0.2234(6)	0.1059(4)	0.0013(7)	0.19(3)	1
O2	4g	-0.2467(6)	0.3612(4)	0.0237(6)	0.28(3)	1
Sb1/Nb1	2e	0	0.14751(19)	¼	0.41(9)	0.7/0.3
Li2	2e	0	0.618(2)	¼	1.12(8)	1
Li3	2f	½	0.133(3)	¼	1.12(8)	1
Li4	2f	½	0.4141(15)	¼	1.12(8)	1

Table II-4: Crystallographic data for $Li_3Sb_{0.7}Nb_{0.3}O_4$ obtained by refinement of combined SXRD and NPD patterns

$Li_3Sb_{0.5}Nb_{0.5}O_4$ - α-Li_3TaO_4 - $R_{bragg\ neutrons}$ = 1.63%. $R_{bragg\ SXRD}$ = 7.19%						
P 2/n	a = 6.02691(4) Å c = 12.96630(10) Å	b = 6.00699(4) Å β = 103.533(5)°		Z = 6		V/Z = 76.06 Å^3
Atom	Wyckoff position	x	y	z	B_{iso} (Å²)	Occupancy
O1	4g	0.0029(18)	0.1318(19)	0.2589(13)	0.78(4)	1
O2	4g	0.4901(18)	0.3776(18)	0.7460(13)	0.78(4)	1
O3	4g	0.1745(18)	0.3501(18)	0.0769(11)	0.78(4)	1
O4	4g	0.655(2)	0.359(2)	0.09307(11)	0.78(4)	1
O5	4g	0.6946(17)	0.112(2)	0.5888(11)	0.78(4)	1
O6	4g	0.148(2)	0.107(2)	0.5739(10)	0.78(4)	1
Sb1/Nb1/Li1	2f	1/4	0.600(6)	3/4	0.767(14)	0.40/0.40/0.2
Sb2/Nb2/Li2	4g	0.3938(3)	0.1231(4)	0.0828(2)	0.767(14)	0.45/0.45/0.1
Li3/Sb3/Nb3	2e	3/4	0.131(2)	3/4	0.91(9)	0.8/0.1/0.1
Li4/Sb4/Nb4	4g	0.451(2)	0.405(3)	0.5781(14)	0.91(9)	0.9/0.05/0.05
Li5	4g	-0.084(5)	0.117(6)	0.091(3)	0.91(9)	1
Li6	2e	1/4	0.361(8)	1/4	0.91(9)	1
Li7	2f	1/4	0.144(7)	3/4	0.91(9)	1
Li8	4g	0.601(5)	0.349(5)	-0.078(4)	0.91(9)	1

Table II-5: Crystallographic data for $Li_3Sb_{0.5}Nb_{0.5}O_4$ obtained by refinement of combined SXRD and NPD patterns.

$Li_3Sb_{0.3}Nb_{0.7}O_4$ - jagged chains - $R_{bragg\ neutrons}$ = 1.52%. $R_{bragg\ SXRD}$ = 16.68%						
C 2/c	a = 8.50754(6) Å c = 9.37868(7) Å	b = 8.51140(5) Å β = 116.7354(5)°		Z = 8	V/Z = 75.82 Å^3	
Atom	Wyckoff position	x	y	z	Biso (Å²)	Occupancy
O1	8f	0.1673(11)	-0.1256(10)	0.3615(10)	0.59(14)	1
O2	8f	0.9483(9)	-0.1070(8)	0.8887(9)	0.59(14)	1
O3	8f	0.4358(4)	-0.1378(6)	0.8840(9)	0.59(14)	1
O4	8f	0.6916(2)	-0.1295(8)	0.3670(7)	0.59(14)	1
Nb1/Sb1/Li1	8f	0.0775(2)	-0.1385(2)	0.1241(3)	0.486(16)	0.66/0.28/0.06
Li2	8f	0.326(3)	-0.108(3)	0.626(2)	1.27(4)	1
Li3/Nb2/Sb2	8f	0.543(2)	-0.123(2)	0.124(2)	1.27(4)	0.94/0.04/0.02
Li4	8f	0.827(3)	-0.119(3)	0.6433(19)	1.27(4)	1

Table II-6: Crystallographic data for $Li_3Sb_{0.3}Nb_{0.7}O_4$ obtained by refinement of combined SXRD and NPD patterns. Note that the relatively large $R_{bragg\ SXRD}$ is due to peculiar peak shapes which could not be totally taken into account using anisotropic strain models as implemented in Fullprof.

$Li_3Ru_{0.3}Nb_{0.7}O_4$ – Jagged chains - $R_{Bragg\ neutrons}$ = 4.05%, $R_{Bragg\ SXRD}$ = 7.64%						
C 1 2/c 1	a = 8.425(1) Å b = 8.428(1) Å	c = 9.343(1) Å β = 116.503(7)		Z = 8	V/Z = 74.2Å^3	
Atom	Wyckoff position	x	y	z	B_{iso} (Å²)	occupancy
O1	8f	0.1722(12)	-0.1234(14)	0.3607(12)	0.72(18)	1
O2	8f	0.4382(15)	-0.1415(12)	0.8846(12)	1.09(19)	1
O3	8f	0.6959(12)	-0.1273(13)	0.3722(11)	0.27(15)	1
O4	8f	0.9460(10)	-0.1144(11)	0.8895(11)	0.27(15)	1
Ru1/Nb1/Li1	8f	0.0778(3)	-0.1383(2)	0.1247(3)	0.21(2)	0.28/0.64/0.08
Li2/Ru2/Nb2	8f	0.5483(18)	-0.1224(19)	0.126(2)	1.09(4)	0.92/0.02/0.06
Li3	8f	0.321(4)	-0.120(4)	0.627(4)	1.09(4)	1
Li4	8f	0.816(3)	-0.124(3)	0.631(3)	1.09(4)	1

Table II-7: Crystallographic data for $Li_3Ru_{0.3}Nb_{0.7}O_4$ obtained by refinement of combined SXRD and NPD patterns.

$Li_3Ru_{0.7}Nb_{0.3}O_4$ – Helical chain - $R_{Bragg\ neutrons}$ = 5.31%, $R_{Bragg\ SXRD}$ = 8.95%						
P 4_1 2 2		a = 5.8940(2) Å c = 8.3854(4) Å		Z = 4	V/Z = 72.75 Å^3	
$Li_3Ru_{0.5}Nb_{0.5}O_4$ – Helical chain - $R_{Bragg\ neutrons}$ = 5.66%, $R_{Bragg\ SXRD}$ = 9.41%,						
P 4_1 2 2		a = 5.9176(7) Å c = 8.3937(8) Å		Z = 4	V/Z = 73.48 Å^3	
Atom	Wyckoff position	x	y	z	B_{iso} (Å²)	Occupancy
O1	8d	0.2367(5) 0.2371(5)	0.4896(7) 0.4905(8)	0.5039(3) 0.5053(4)	0.79(4) 0.92(3)	1
O2	8d	0.2406(5) 0.2417(5)	0.9933(7) 0.9927(7)	0.0136(3) 0.0129(4)	0.41(3) 0.53(4)	1
Ru1/Nb1/Li1	4a	0	0.26921(17) 0.27185(16)	½	0.065(14) 0.150(14)	0.66/0.28/0.06 0.455/0.455/0.09
Li2/Ru2/Nb2	4b	0.2689(13) 0.2592(12)	1/2	¾	0.70(5) 0.90(4)	0.94/0.05/0.01 0.91/0.045/0.045
Li3	4a	0	0.754(2) 0.747(2)	½	0.70(5) 0.90(4)	1
Li4	4b	0.246(2) 0.252(2)	1/2	¼	0.70(5) 0.90(4)	1

Table II-8: Crystallographic data for $Li_3Ru_{0.7}Nb_{0.3}O_4$ and $Li_3Ru_{0.5}Nb_{0.5}O_4$ in blue and green, respectively obtained by refinement of combined SXRD and NPD patterns.

Searching for a chemical parameter explaining the structural evolution, we plotted in Figure II-9a-b-d the variation of the volume per formula unit, V/Z, the average M – O distance and average distortion coefficient of the MO_6 octahedra (Figure II-9 caption for formula), respectively. The M – O distances grow upon going from Ru-rich, to Sb-rich, and to Nb-rich compounds, in agreement with the ionic radius of each element, i.e. 0.56 Å, 0.60 Å, and 0.64 Å for Ru^{5+}, Sb^{5+}, and Nb^{5+}, respectively.[100] Interestingly, the cell volume doesn't follow this trend since it is the highest for Li_3SbO_4, despite the smaller ionic radius of Sb^{5+} compared to Nb^{5+}. Moreover, the distortion coefficient stays roughly constant in the $Li_3Ru_ySb_{1-y}O_4$

diagram while it grows as soon as Nb^{5+} is added to the composition, in correlation with the structural evolution, hence suggesting the importance of this parameter. The high value of the distortion coefficient of the MO_6 octahedra is due to the displacement of the cation inside the octahedron, which will be called off-centering from here onward. It is triggered by the presence of two different oxygen atoms, O1 and O2, in the MO_6 octahedron, such that M tends to move towards the oxygen atom which is depleted in charge. [102] It is worth mentioning that the distortion deduced from diffraction analysis is averaged over the metallic atoms since they all share the same crystallographic site, hence the need to go for a chemical sensitive technique to probe the distortion associated with the different transition metals.

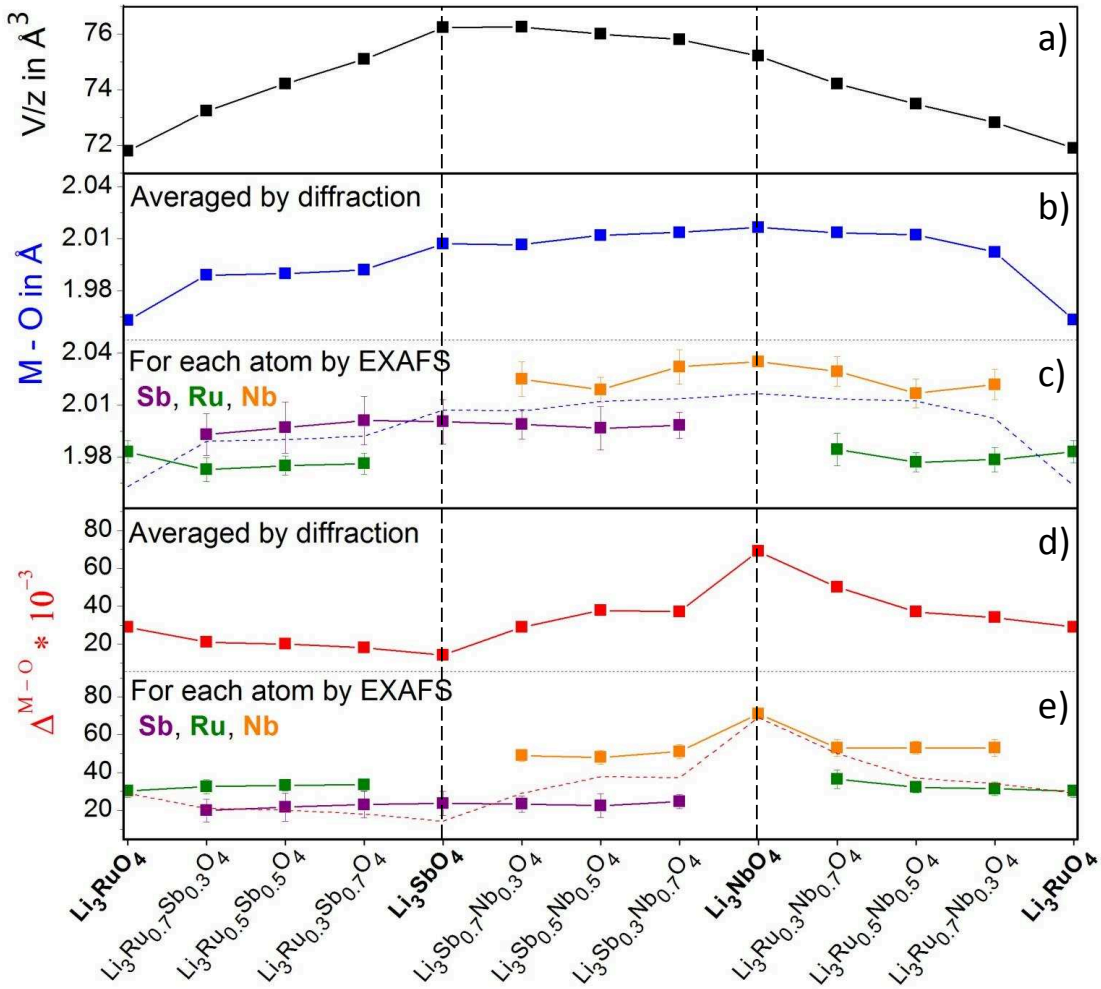

Figure II-9: a) Volume/Z variation among the phase diagrams. b) and d) show the variation of the average M – O distance and distortion coefficient around the M atoms, respectively, as obtained by Rietveld refinement. c) and e) show the average M – O bond lenghts and distortion coefficient for each metallic atom (Ru in green, Nb in orange and Sb in purple), respectively, obtained by EXAFS analysis. Dashed line stand for the M – O and distortion coefficient obtained by Rietveld refinement. Distortion coefficient is calculated according the formula : $\Delta^{M-O} = \frac{1}{6}\sum_{i=1}^{6}\left[\frac{d_i - \langle d \rangle}{\langle d \rangle}\right]^2$

II.2.b.ii Local scale structure investigated by EXAFS

Since X-ray absorption spectroscopy is a site-sensitive and local technique, we can access directly the evolution of distortion around RuO_6, SbO_6, and NbO_6 in the different compounds. Therefore, hard XAS experiments at the Ru, Sb, and Nb K-edges were performed on the ROCK beamline at Soleil synchrotron with the help of Antonella Iadecola, and the EXAFS oscillations were analyzed. The magnitude of the Fourier transform $|\chi(k)\ k^2|$ of the EXAFS oscillations (Figure II-10, points) represents the atomic distribution around the Ru, Sb, and Nb atoms, where the first peak corresponds to the MO_6 octahedron (first shell). Fits for all compositions are reported as solid lines in Figure II-10 and the obtained results are summarized in Table II-9. Figure II-9c-e shows the average M – O bond lengths and the distortion coefficient obtained by refining the 1st coordination shell around each metallic atom for all compositions. One should note that the agreement between the M – O bond length and distortion obtained by diffraction (dashed line) and EXAFS (plain line) is quite satisfactory. For a given atom, M – O distances and their associated distortion are almost constant over the phase diagram (Ru – O = 1.978(3) Å, Sb – O = 1.997(2) Å, and Nb – O = 2.025(5) Å; $\Delta RuO_6 = 33(1)x10^{-3}$, $\Delta SbO_6 = 23(1)x10^{-3}$, and $\Delta NbO_6 = 54(4)x10^{-3}$). Note that off-centering is higher, in the case of d^0 cations, such as Nb^{5+} compared to Ru or Sb, because of a second order Jahn-Teller effect (SOJT).[103] A second order Jahn-Teller effect is a structural distortion allowing the splitting of two quasi-degenerated states, one filled and one empty, resulting in a lowering of the overall energy of the system. In the case of d^0 cations in octahedral configuration, the antibonding t_{2g} empty-states mix with the bonding t_{1u} filled-states breaking by the same the Oh symmetry through the displacement of metallic atom along the C4 or C3 axis of the octahedron. Overall, distortion coefficient increases when Nb is added to the composition because of the SOJT which seems to be related to the structural evolution.

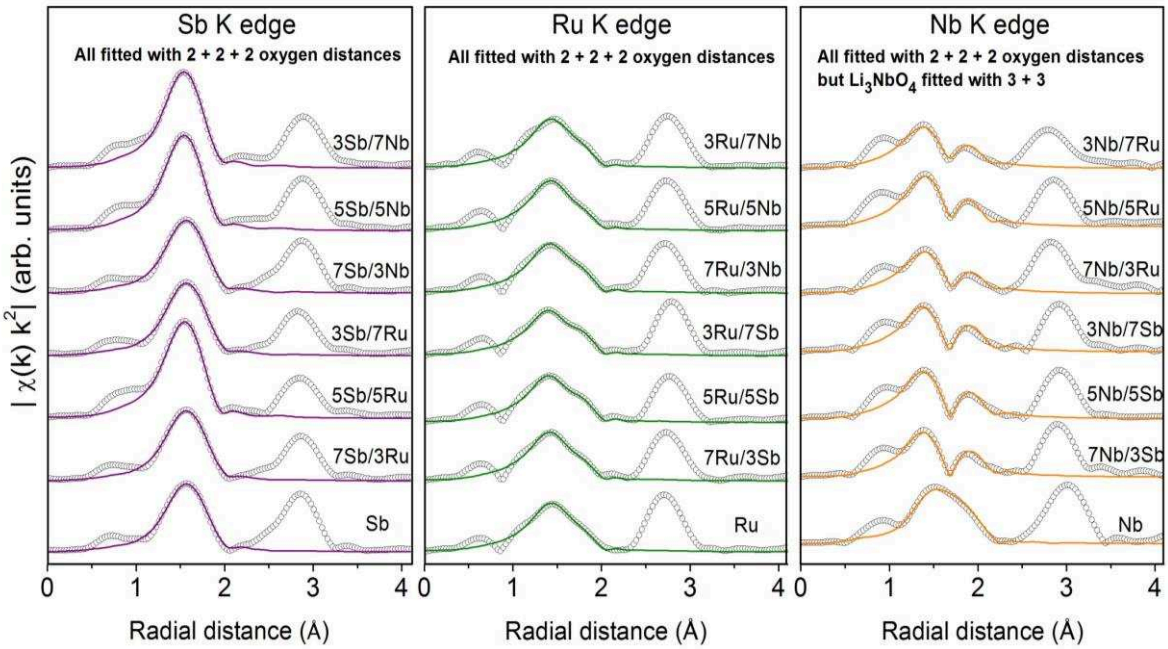

Figure II-10: Magnitude of the Fourier transforms of the EXAFS oscillations extracted at the Sb K-edge, Ru K-edge, and Nb K-edge for the left, middle and right panel respectively. The solid lines represent the model fitting for the M-O shell.

Nb - K edge E0 = 8											
	CN	d	CN	d	CN	d	Average d	Distortion $*10^3$	error	Sig$*10^3$	R$*10^3$
Li_3NbO_4	3	1.891	3	2.180			2.036	72	1.5	3	6
$Li_3Nb_{0.7}Ru_{0.3}O_4$	2	1.887	2	2.016	2	2.185	2.029	51	3.7	4	15
$Li_3Nb_{0.5}Ru_{0.5}O_4$	2	1.882	2	2.005	2	2.163	2.017	48	3.7	3	19
$Li_3Nb_{0.3}Ru_{0.7}O_4$	2	1.879	2	2.014	2	2.173	2.022	49	3.9	4	24
$Li_3Sb_{0.3}Nb_{0.7}O_4$	2	1.878	2	2.025	2	2.194	2.032	53	4.4	2	16
$Li_3Sb_{0.5}Nb_{0.5}O_4$	2	1.869	2	2.0083	2	2.179	2.019	53	3.4	2	6
$Li_3Sb_{0.7}Nb_{0.3}O_4$	2	1.870	2	2.0177	2	2.187	2.025	54	4.8	2	16
Ru - K edge E0 = -2											
	CN	d	CN	d	CN	d	Average d	Distortion $*10^3$	error	Sig	Rfactor
Li_3RuO_4	2	1.893	2	1.988	2	2.067	1.983	30	3.6	3	9
$Li_3Sb_{0.3}Ru_{0.7}O_4$	2	1.878	2	1.970	2	2.069	1.9728	32	3.2	3	12
$Li_3Sb_{0.5}Ru_{0.5}O_4$	2	1.876	2	1.976	2	2.072	1.975	33	3.1	2	8
$Li_3Sb_{0.7}Ru_{0.3}O_4$	2	1.877	2	1.977	2	2.074	1.976	33	2.8	2	8
$Li_3Ru_{0.7}Nb_{0.3}O_4$	2	1.883	2	1.979	2	2.073	1.978	32	3.9	2	14
$Li_3Ru_{0.5}Nb_{0.5}O_4$	2	1.884	2	1.973	2	2.072	1.977	32	3.1	3	5
$Li_3Ru_{0.3}Nb_{0.7}O_4$	2	1.891	2	1.984	2	2.077	1.984	31	5.4	3	18
Sb - K edge E0 =9											
	CN	d	CN	d	CN	d	Average d	Distortion $*10^3$	error	Sig	Rfactor
Li_3SbO_4	2	2.000	2	1.930	2	2.071	2.000	24	5.0	2	8
$Li_3Sb_{0.7}Ru_{0.3}O_4$	2	1.999	2	1.933	2	2.070	2.001	23	5.1	2	5
$Li_3Sb_{0.5}Ru_{0.5}O_4$	2	1.996	2	1.932	2	2.062	1.997	22	7.2	2	6
$Li_3Sb_{0.3}Ru_{0.7}O_4$	2	1.995	2	1.9334	2	2.050	1.993	20	5.8	2	6
$Li_3Sb_{0.7}Nb_{0.3}O_4$	2	1.99692	2	1.93129	2	2.069	1.999	23	3.8	1	2
$Li_3Sb_{0.5}Nb_{0.5}O_4$	2	1.99348	2	1.92905	2	2.064	1.996	23	5.8	1	4
$Li_3Sb_{0.3}Nb_{0.7}O_4$	2	1.99497	2	1.92769	2	2.072	1.998	25	3.3	1	3

Table II-9: Structural parameters obtained by fitting the EXAFS oscillations for all compositions for the M-O bonds. CN, d, Average d, distortion and sig stand for Coordination Number, M-O distance in Å, Average M-O distance in Å, distortion coefficient calculated according to the formula of the Figure II-9 caption and the Debye-Waller factor in Å². The difference energy threshold, E0, and the amplitude reduction factor (S_0^2) are fixed during fit. S_0^2 was taken equal to 1 for all analysis.

II.2.b.iii Defect analysis by combined SXRD and TEM

Further exploiting the structural results, we will now focus on the presence/nature of defects in the materials. In part **II.2.c.i,** we mentioned that the introduction of Li/M (M being a mix of Nb, Ru and Sb) intersite mixing into the structural model of many of the intermediate compounds drastically improves the Rietveld refinement. This is exemplified for $Li_3Ru_{0.5}Nb_{0.5}O_4$ as shown in Figure II-11a. To assess the presence of cation disorder, HRTEM has been performed at the University of Antwerp by Dmitry Batuk. Figure II-11b shows HAADF-STEM images of $Li_3Ru_{0.5}Nb_{0.5}O_4$ along the [100] direction emphasizing the structure of the helical chains. Figure II-11c shows a region of the crystal showing numerous defects consisting in cooperative Ru/Nb displacement.

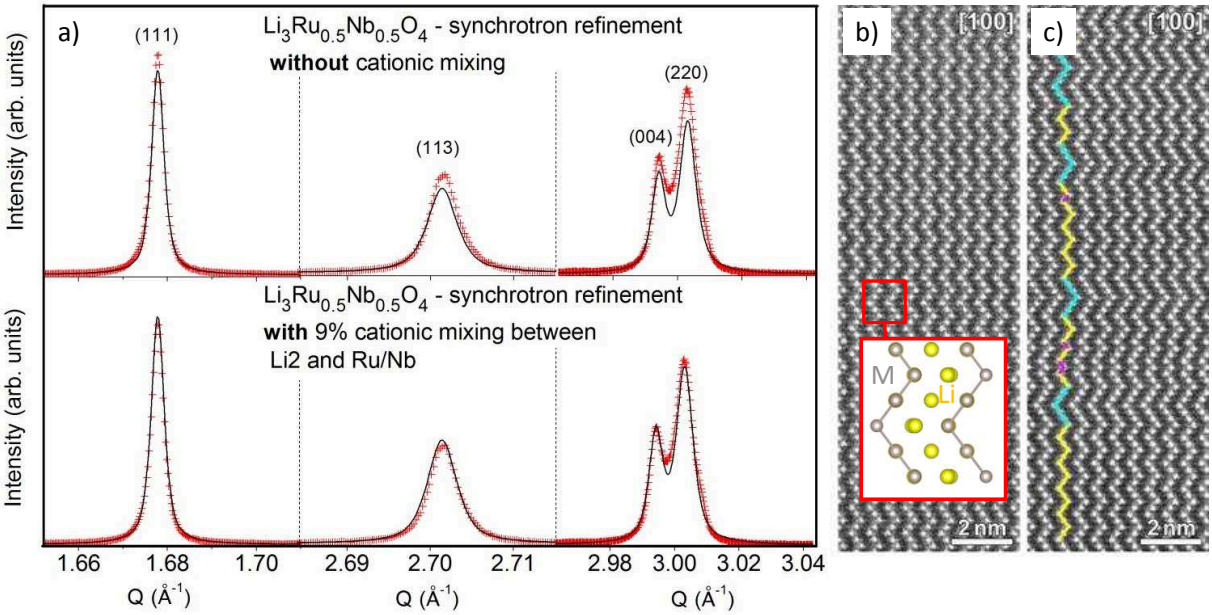

Figure II-11: a) Rietveld refinement of the SXRD pattern (λ = 0.414562 Å) of $Li_3Ru_{0.5}Nb_{0.5}O_4$ without considering Li2 and Ru/Nb cationic mixing (top) and with the 9% mixing (bottom). (c) typical HAADF-STEM images of the $Li_3Ru_{0.5}Nb_{0.5}O_4$ compound along [100] direction with a view of the structure. [100] image in c) is from a crystal containing numerous cooperative defects in the cation ordering pattern, which are visible as variations in the length of the corresponding «straight» fragments of the (Ru,Nb) atomic columns (yellow: 3, as in a regular structure ; cyan : 4 and magenta : 2).

Another type of defect has been encountered in these samples, namely antiphase boundaries, as exemplified for $Li_3Ru_{0.1}Nb_{0.9}O_4$ (I -4 3 m). A striking aspect of the SXRD pattern of $Li_3Ru_{0.1}Nb_{0.9}O_4$ is the very strong anisotropic peak broadening (Figure II-12a). It is well known that the most common sources of peak broadening are either the submicrometric size

of coherent domains (following Sherrer equation) or the presence of microstrain (lattice parameter fluctuations from one crystallite to another). In the present case, all our attempts to fit the peak broadening using classical models of anisotropic size and/or strain effects failed. Therefore a detailed analysis of the relation between indexation and peak shape was carried out. It appeared that some peaks, namely those corresponding to NaCl rocksalt subcell a_{NaCl} = a/2, are very sharp while the others - superstructure peaks due to ordering between Li and Ru/Nb - are very broad with a pronounced Lorentzian shape. In the light of this observation, anisotropic broadening of the peaks was taken into account using a selective broadening depending on hkl indices: All peaks that arise from the rocksalt subcell (whose lattice parameter is a_{NaCl} = a/2 where a is the actual lattice parameter of $Li_3Ru_{0.1}Nb_{0.9}O_4$), i.e. that comply the condition "h/2, k/2 and l/2 integer and same parity", were kept sharp, and all others were broadened. This resulted in a great improvement of the fit, as can be seen in (Figure II-12b). By implementing this broadening depending on hkl indices into the refinement, the average size of coherent domains can be estimated to be around 45 nm.

TEM analysis of the $Li_3Ru_{0.1}Nb_{0.9}O_4$ material confirms the presence of numerous domains with sizes comparable to the average value estimated from SXRD refinement. High resolution HAADF-STEM data (Figure II-12c-e) reveal that these domains are antiphase domains, separated by antiphase boundaries (APB). The positions of the cation columns across an APB are consistent with the basic rocksalt structure indicating that the APBs leave the anionic sublattice unchanged, but create discontinuity in the pattern of cation ordering. There are two types of APBs in the material, and their atomic arrangement can be derived directly from the [001] and [011] HAADF-STEM images (Figure II-12c-d-e). The APBs of type 1 shift one domain with respect to another over a/4 and introduce a 90° rotation of the structure. The APBs of type 2 shift the domains over a/2 and do not change the orientation of the tetrahedral $(NbO_6)_4$ units. Within the domains, the structure preserves perfect cation ordering (Li and Ru/Nb), so that no actual local antisite defects were observed.

Our XRD and TEM results unambiguously demonstrate that while the material maintains its rocksalt structure on large coherent domains, the ordering between the cations (Li and Ru/Nb) suffers from the presence of small coherent domains. This is fully consistent with the broadening of the superstructure peaks while subcell peaks remain sharp as it is illustrated in Figure II-12f. As a conclusion, the presence of antiphase boundaries together with the average size of the antiphase domains can be deduced from the analysis of the XRD pattern. Note that a similar approach has been recently reported for $LiNi_{0.5}Mn_{1.5}O_4$ spinel derivative.[104]

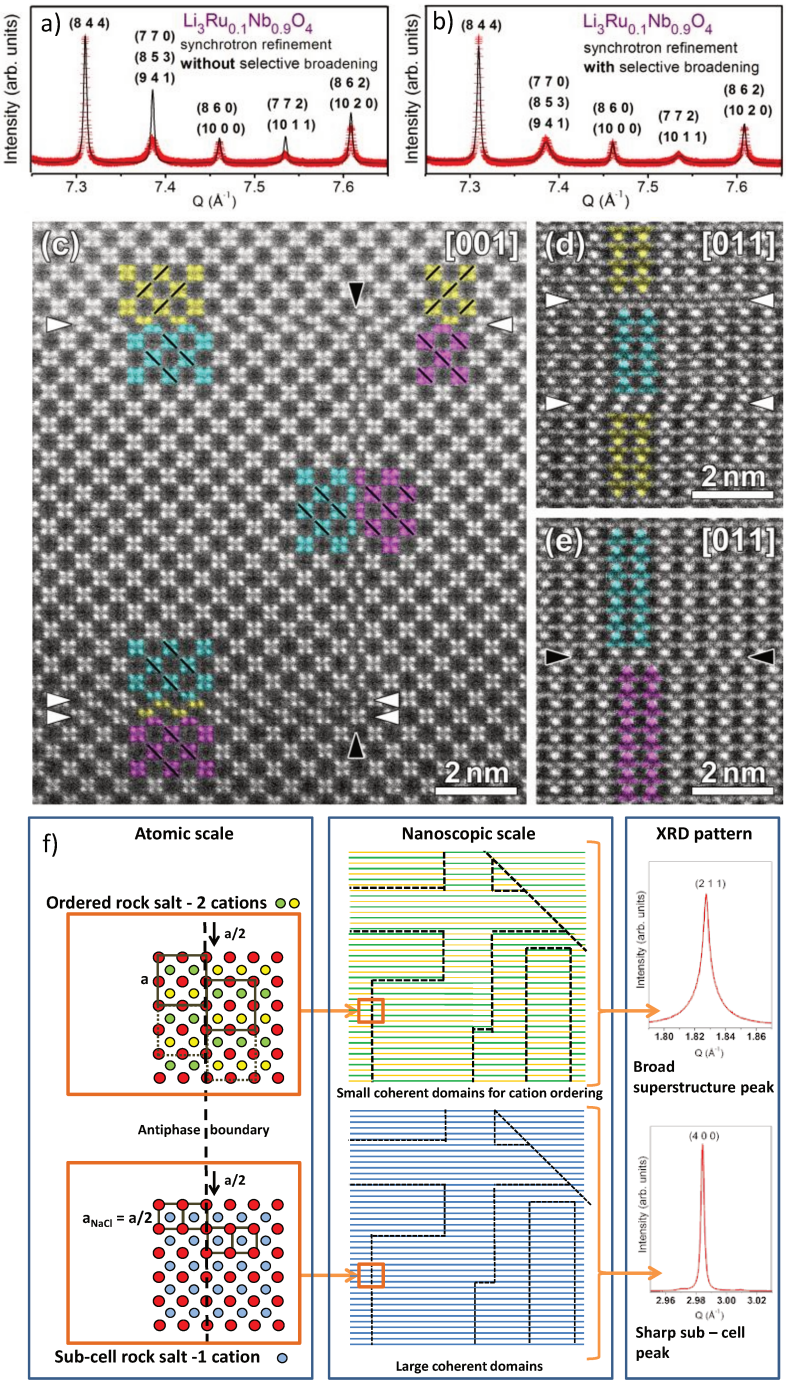

Figure II-12: Rietveld refinement of SXRD pattern of $Li_3Ru_{0.1}Nb_{0.9}O_4$ without and with selective broadening of the reflections (a) and (b), respectively. (c-e) HAADF-STEM images of $Li_3Ru_{0.1}Nb_{0.9}O_4$ confirming that the structure is based on tetrahedral units of $(Ru,Nb)O_6$ octahedra and revealing two types of APBs in the material. APB of type 1 and type 2 are marked with white and black arrowheads, respectively. Colored squares highlight translations of the structural domains across the phase boundary, while the black dotted lines show that the $(NbO_6)_4$ tetrahedra are rotated across the boundary. f) scheme representing the effect of the antiphase boundaries on the cation ordering for two different rocksalt structures, one with two ordered cations (top) and one with one cation only (bottom), at the atomic scale (left) and at the nanoscopic scale (middle). The right panel shows the effect of the antiphase domains on the XRD peak shapes.

II.2.c Rationalization of the different cation orderings using DFT calculations

We unveiled a rich crystal chemistry in the $Li_3M_yM'_{1-y}O_4$ system (with M and M' being Ru, Sb and Nb) enlisting five rocksalt structures which differs by their cationic Li/(M or M') arrangement. At this point, it is tempting to search for indicators explaining the structural evolution. With this in mind, DFT calculations were performed with the help of Matthieu Saubanère and Marie-Liesse Doublet from the Institut Charles Gerhardt in Montpellier. Amongst the considered indicators, three retained our attention: 1) electrostatic interactions, 2) the presence of a d^0 element, and 3) the off-centering of M in the MO_6 octahedron.

Owing to the high electronegativity of oxygen, many oxide structures possess strongly ionic bonds and, therefore, their structural packing can be explained by simple electrostatic effects. Pursuing this direction, structural models for Li_3RuO_4, Li_3SbO_4, and Li_3NbO_4 with different structures were obtained by relaxing the ions through DFT. Then, Madelung electrostatic energies were calculated using formal charges and Bader charges,[105] as presented in Figure II-13a. Among the three systems explored, the zig-zag-chains structure is the most stable in terms of minimizing electrostatic interactions and turns out to be the one experimentally adopted by Li_3SbO_4 and Li_3RuO_4. However, Li_3NbO_4 escapes this logic since it does not crystallize in the zig-zag chains structure. To see if the ground state for Li_3NbO_4 can be retrieved using a more sophisticated method, DFT energy calculations were considered and presented in Figure II-13a. With DFT, the most stable structure for Li_3NbO_4 is the clusters structure, in agreement with experiments. Applying this methodology to Li_3RuO_4, one can notice that all the different structures, i.e. zig-zag chains, helical chains, α–Li_3TaO_4 chains, and jagged chains, are very close in energy (less than 14 meV per atom). This indicates that Li_3RuO_4 could be obtained in a disordered rocksalt structure, in agreement with our experimental data since this compound can indeed be synthetized partially disordered Figure II-13b via short annealing times at 700°C. Interestingly, Li_3SbO_4 cannot be synthetized in a disordered rocksalt structure.[96] Such a difference might be due to the higher ionicity of the Sb – O bond compared to the Ru – O bond, which enhances the importance of electrostatic interactions towards the phase stability, hence stabilizing the zig-zag-chains structure for Li_3SbO_4. This theory is further supported considering the $Li_3Ru_yIr_{1-y}O_4$ phase diagram in which the structure transforms from a fully ordered compound (Li_3RuO_4) to a partially disordered one (Li_3IrO_4), when Ir, forming very covalent Ir – O bonds, is added to the

composition. Overall, electrostatic energy considerations can explain the structure for Li_3RuO_4 and Li_3SbO_4, but fail for Li_3NbO_4.

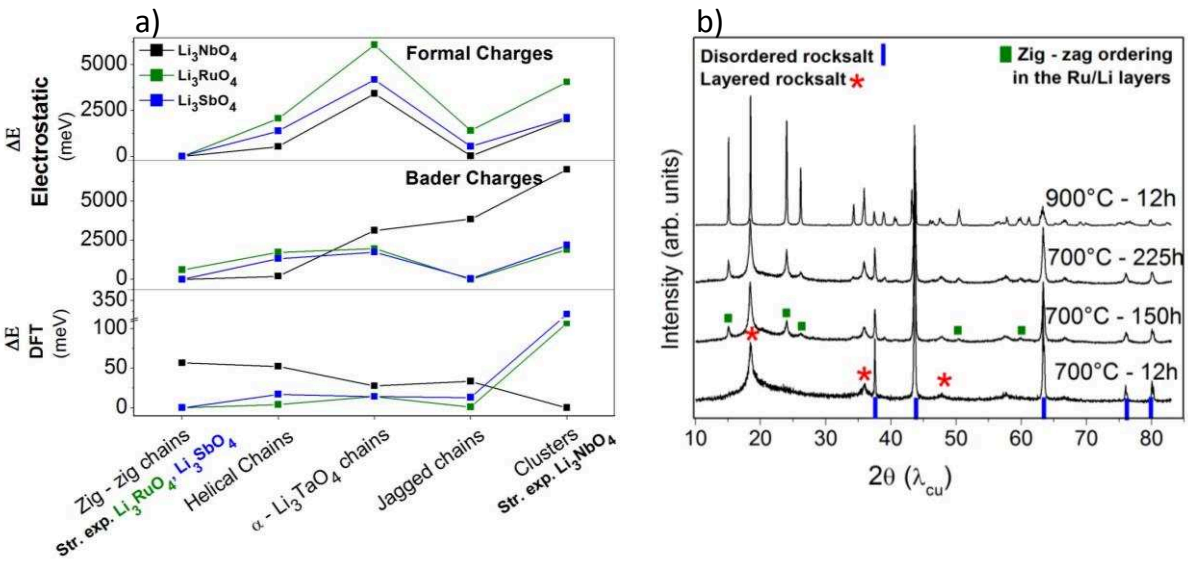

Figure II-13: a) Difference of electrostatic energies (ΔE electrostatics), calculated using formal charges or Bader charges and DFT energies (ΔE DFT) with the ground state for Li_3NbO_4, Li_3RuO_4 and Li_3SbO_4 in the different structures obtained in the $Li_3(Ru,Nb,Sb)O_4$ binary system. b) XRD patterns of Li_3RuO_4 synthetized at different temperatures and for different times. When synthetized at 700°C – 12h, it crystallizes in a disordered rocksalt structure with a partial layered ordering between the Ru and Li, then going at higher temperature or longer time, the superstructure peaks corresponding to the Ru/Li ordering inside the Ru/Li layers appear.

While exploring the Nb-based binary phases, we could observe that the addition of Nb rapidly triggers structural transitions, suggesting an eventual effect of having an empty d shell (d^0-metal). To further probe this hypothesis, we embarked into a comparison with another d^0 element, Ta^{5+}. Li_3TaO_4 crystallizes in two polymorphs: α-Li_3TaO_4 which is isostructural to $Li_3Sb_{0.5}Nb_{0.5}O_4$ or $Li_3Ru_{0.3}Nb_{0.7}O_4$, and β-Li_3TaO_4 which possesses a structure alike $Li_3Sb_{0.3}Nb_{0.7}O_4$. Both structures are not stable ones considering electrostatic interactions only. Thus we synthetized $Li_3Ru_{0.5}Ta_{0.5}O_4$ crystallizing in the same structure as $Li_3Ru_{0.5}Nb_{0.5}O_4$, which is different from the d^0-free $Li_3Ru_{0.5}Sb_{0.5}O_4$, supporting the fact that there might be a correlation between structure and d-metals having empty d shells (d^0). However, being a d^0 cation is not the only factor explaining the structure, since Li_3NbO_4 and Li_3TaO_4, both containing d^0, show different cationic arrangements. This was an impetus to look for a property of d^0 elements that could explain the structural evolution.

Within this context, we should recall that d^0 compounds are prone to second order Jahn-Teller effect displacing the M from the center of the MO_6 octahedron. Interestingly, we have seen from the structural analysis that the distortion coefficient varies when the structures evolve (Figure II-9e). All together, these two effects point towards the importance that such distortion could have on the structural evolution. How can the displacement of the cation lead to different long range structures? We explored the effect of the distortion in zig-zag chains and clusters structures on the oxygen charges. For this, a set of structures with different cation off-centerings was constructed and distortion coefficients and Bader charges were calculated. We found that the metal off-centering changes the charge distribution among the oxygen atoms of the MO_6 octahedron. In the specific case of Li_3MO_4 structures, two different types of oxygen atoms, labelled O1 and O2, are present. The displacement of M, being always shifted towards O1, translates into the increase of the charge in O1 by δ_{O1} and a decrease in the charge of O2 by δ_{O2} as illustrated in Figure II-14a (δ_{O1} being negative since the oxygen charge is negative and δ_{O2} positive for the same reason). Moreover, the difference between δ_{O2} and δ_{O1} increases when the distortion gets more severe (right panel of Figure II-14a). To evaluate the charge difference for a specific composition of metals, we determine the off-centering associated to each of the Sb^{5+}, Nb^{5+}, Ta^{5+}, and Ru^{5+} ions. For this, zig-zag, helical, α–Li_3TaO_4, jagged chains, and clusters structures for Li_3SbO_4, Li_3RuO_4, Li_3TaO_4, and Li_3NbO_4 were relaxed by DFT, and the resulting distortion coefficients are shown in Figure II-14b. We could demonstrate that each cation presents distinct off-centerings associated to distortion coefficient values of 23 x 10^{-3}, 33 x 10^{-3}, 45 x 10^{-3}, and 54 x 10^{-3} for Sb^{5+}, Ru^{5+}, Ta^{5+}, and Nb^{5+}, respectively. It is worth mentioning that these values are in agreement with those experimentally obtained. As the difference in charge (δ_{O2} - δ_{O1}) scales with the distortion coefficient (right panel of Figure II-14a), δ_{O2} - δ_{O1} will be higher in NbO_6, than in TaO_6, RuO_6, and finally SbO_6. Obviously, when considering the overall structure, these MO_6 octahedra will try to order so that their specific charge distribution is stabilized. An adequate way to estimate this stabilization is to compare the difference between the O1 and O2 Madelung site potentials for each structure. O site potentials and their difference have been calculated for the zig-zag, helical, α–Li_3TaO_4, jagged chains and clusters structure for Li_3RuO_4, Li_3SbO_4, Li_3TaO_4 and Li_3NbO_4. The average values obtained among the four compositions are shown in Figure II-14c. From this figure, one can see that the difference is the largest for the clusters structure, then for the jagged, α–Li_3TaO_4, zig-zag, and finally the helical chains structures. This suggests that clusters structure, which shows the largest O site

potentials difference, should stabilize highly distorted NbO_6 octahedra (having the largest difference δ_{O2} - δ_{O1}). Note that this is in agreement with the crystallization of Li_3NbO_4 in a clusters structure. Following this reasoning, α–Li_3TaO_4 and jagged chains structures should stabilize TaO_6 octahedra, which is once again the case. Finally, Li_3SbO_6 and Li_3RuO_4 crystallize in the zig-zag chain, because Ru^{5+} and Sb^{5+} induce a weak charge density difference between O1 and O2.

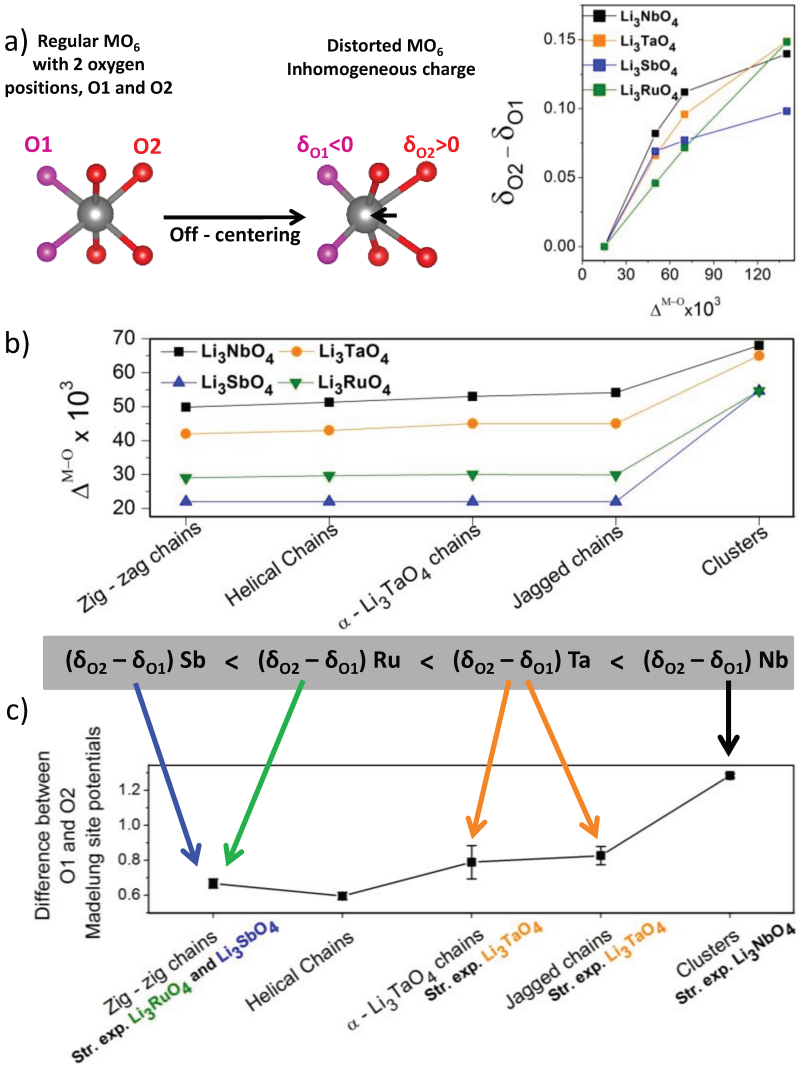

Figure II-14: Schematic of the charge distribution evolution in the MO_6 octahedron with the displacement of the M atoms (M = Ru, Nb, Sb or Ta), together with the evolution of the Bader charge difference δ_{O2} - δ_{O1} with the amplitude of the distortion, δ_{O2} and δ_{O1} being the charge lost by O2 and gained by O1, respectively. Charges were calculated for Li_3NbO_4, Li_3RuO_4, Li_3SbO_4, and Li_3TaO_4 in the zig –zag structure with different displacement values. b) Distortion coefficient Δ^{M-O} obtained from Li_3NbO_4, Li_3RuO_4, Li_3SbO_4 and Li_3TaO_4 converged through DFT in the zig-zag chains, helical chains, α–Li_3TaO_4, jagged chains and clusters structures. The obtained values match with the experimental values obtained for Nb^{5+}, Ru^{5+} and Sb^{5+}. c) Average difference Madelung site potentials between O1 and O2 calculated for undistorted zig-zag chains, helical chains, α–Li_3TaO_4, jagged chains and clusters structures for Li_3NbO_4, Li_3RuO_4, Li_3SbO_4 and Li_3TaO_4.

Overall, we have demonstrated that Li_3SbO_4 and Li_3RuO_4 crystallize in the zig-zag chain because it minimizes the electrostatic interactions. However for compounds having d^0 metals (Li_3TaO_4 and Li_3NbO_4), such electrostatic interactions are overruled by the second order Jahn-Teller effect which is accompanied by displacement of the cations out of the octahedron center. While Li_3NbO_4 crystallizes in the clusters structure, Li_3TaO_4 forms in the α–Li_3TaO_4 structure or in the jagged chains structures due to lower displacement values for Ta^{5+} compared to Nb^{5+}.[103] For $Li_3M_yM'_{1-y}O_4$ (M and M' being Ru, Sb, Ta or Nb), the average distortion coefficient Δ^{M-O} can be used to predict the structure: for Δ^{M-O} varying between 20 x 10^{-3} and 30 x 10^{-3}, zig-zag chains will be preferred, while helical and jagged chains have a greater chance to be found for Δ^{M-O} ranging from 37.5 x 10^{-3} to 42 x 10^{-3} and 43 x 10^{-3} to 48 x 10^{-3}, respectively. Beyond these values, clusters structure is more likely to be formed.

II.2.d Partial conclusions

We have synthetized new compounds $Li_3Ru_yNb_{1-y}O_4$, $Li_3Ru_ySb_{1-y}O_4$, $Li_3Ru_yIr_{1-y}O_4$, $Li_3Sb_yNb_{1-y}O_4$, for y = 0, 0.25 (or 0.3), 0.5, 0.75 (or 0.7) and 1, showing a rich crystal chemistry based on rocksalt structures with different cation orderings depending on the transition metal. Thorough structural characterization combining SXRD and TEM unveiled the presence of cooperative cation ordering defects and antiphase boundaries. Combining long range characterization, diffraction, and local probe, EXAFS, we could also show a direct relation between the structure and the distortion of the MO_6 octahedra caused by the displacement of the d^0 cation from the center of the polyhedral due to the second order Jahn-Teller effect (SOJT). Through DFT calculations, we unveiled that the SOJT leads to in inhomogeneous charge distribution in the MO_6 octahedron which is compensated electrostatically by the specific long range orderings. At the end, we propose the mean deviation of the M – O distances in the MO_6 octahedra as a simple parameter to predict the cation ordering into Li_3MO_4. Going further, I wonder if molecular dynamics could be used to look for new cation ordering taking the MO_6 octahedron with different charge distribution as a building block.

II.3 Mechanism of the electrochemical Li insertion/extraction from of $Li_3M_yM'_{1-y}O_4$ compounds

In this part, we will perform the electrochemical characterization of members of the $Li_3M_yM'_{1-y}O_4$ system (M and M' being Ru, Nb, Ir, Ta or Sb) in order to assess the presence of anionic redox and its limit in terms of capacity. The study will encompass: i) Li_3RuO_4 as a model system, ii) compounds among the $Li_3Ru_yNb_{1-y}O_4$ ($0 < y < 1$) series for their rich structural evolution and electronic conductivity and iii) $Li_3Ru_yIr_{1-y}O_4$ ($0 < y < 1$) series that will be compared to the already reported end member Li_3IrO_4. Through this section we will focus on the structural stability and charge compensation mechanism during Li removal and uptake, i.e. oxidation and reduction, of the phases as summarized Table II-10.

	Li_3RuO_4	$Li_3Ru_yNb_{1-y}O_4$	$Li_3Ru_yIr_{1-y}O_4$	$Li_3Ru_ySb_{1-y}O_4$	$Li_3Sb_yNb_{1-y}O_4$
Li insertion $Li_3MO_4 \rightarrow Li_{3+x}MO_4$	√	√	X	X	X
Li extraction $Li_3MO_4 \rightarrow Li_{3-x}MO_4$	√	√	√	X	X

Table II-10: Summary of the systems which electrochemical properties will be studied (marked with a green tick).

II.3.a Li intercalation into the $Li_3Ru_yNb_{1-y}O_4$

The $Li_3Ru_yNb_{1-y}O_4$ phases (Figure II-15) shows the cycling performances between 4 and 1 V of cells started on reduction, i.e. Li insertion. Cutoff voltages were fixed above 1 V to limit conversion reaction. All of the cells, with the exception the one containing $Li_3Ru_{0.1}Nb_{0.9}O_4$, show interesting reversible capacities. Indeed capacities of 1.6 Li, 1.4 Li, 0.8 Li and 0.5 Li are measured for Li_3RuO_4, $Li_3Ru_{0.7}Nb_{0.3}O_4$, $Li_3Ru_{0.5}Nb_{0.5}O_4$ and $Li_3Ru_{0.3}Nb_{0.7}O_4$ as positive material, respectively. This reduction in capacity with the increasing Nb content is indicative of its electrochemical transparency. Additionally, for most compositions except for Li_3RuO_4, the reduction occurs via two redox processes of similar capacity and with a number of Li exchanged during each process equal to the ruthenium content. This is well illustrated with $Li_3Ru_{0.7}Nb_{0.3}O_4$ which uptakes 0.7 lithium atoms on the first process and 0.7 on the second one suggesting that the two plateaus are associated with the reduction of Ru^{5+} to Ru^{4+} and of Ru^{4+} to Ru^{3+}, respectively. These two redox processes are also confirmed by the corresponding derivative dQ/dV plots in the right side of Figure II-15. Moreover, these plots

show a broadening of the peaks between the first and fifth cycle, which is more pronounced for the Ru-rich samples and indicative of Li-driven structural modifications. To better understand the science underpinning these electrochemical properties, in situ XRD measurements were performed and presented for Li_3RuO_4 and $Li_3Ru_{0.5}Nb_{0.5}O_4$ in the next paragraphs.

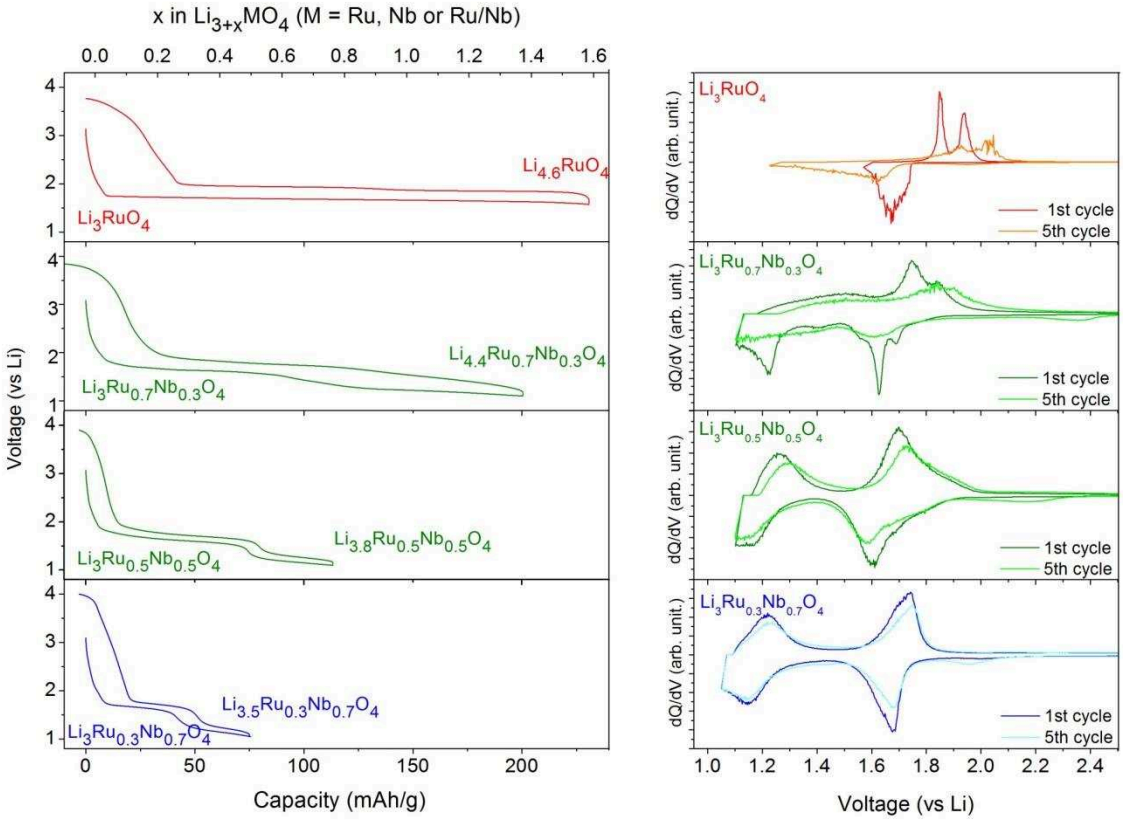

Figure II-15: Electrochemical behavior of Li_3RuO_4, $Li_3Ru_{0.7}Nb_{0.3}O_4$, $Li_3Ru_{0.5}Nb_{0.5}O_4$ and $Li_3Ru_{0.3}Nb_{0.7}O_4$ starting on discharge. (a) Voltage versus composition curves for the 1st cycle at C/10 with cutoff voltages of 1.40 V, 1.10 V, 1.05 V and 1.00 V b) Derivative dQ/dV curves for the 1st and 5th cycle.

The lithiation–delithiation mechanism in Li_3RuO_4 was first examined by operando X-ray diffraction. During the cell discharge, we initially observe (Figure II-16) a progressive disappearance of the pristine phase to the expense of a new phase which becomes single phase at x = 1 (Li_4RuO_4). Upon further Li insertion, this phase disappears and a new one is formed, and becomes single phase at x = 1.6 ($Li_{4.6}RuO_4$). The two reduced phases Li_4RuO_4 and $Li_{4.6}RuO_4$ were both indexed with the same space group P 2/a as the pristine phase but with the increased lattice parameters ([a = 5.25 Å, b = 5.99 Å, c = 5.41 Å and β = 113.66°] and [a = 5.46 Å, b = 6.19 Å, c = 5.06 Å and β = 90.58°], respectively). The strong decrease in the β angle corresponds to a change in the oxygen stacking from ABCABC (O3 type) to ABAB.[18] As all octahedral positions are occupied in pristine Li_3RuO_4, the additional Li ions in the reduced compounds likely sit in tetrahedral positions. Combined X-ray and neutron refinements indicate that the $Li_{4.6}RuO_4$ structure consists in a T1-layered structure in which extra Li occupies tetrahedral positions, while maintaining chains of lithium and ruthenium in the metal layer (Table II-11).[26] Upon subsequent oxidation, the structural sequence proceeds with the pristine phase being fully recovered at the end of charge. However a few peaks do not recover their full initial intensity, which is most likely related to the emergence of staking faults associated with the gliding of the transition metal layers upon transformation from the O3 structure in the pristine phase to the T1 structure of the fully reduced $Li_{4.6}RuO_4$ phase.

$Li_{4.6}RuO_4$ - $R_{Bragg\ neutrons}$ = 6.49%, $R_{Bragg\ SXRD}$ = 38.89%						
P 1 2/a 1	a = 5.4611(5) Å b = 6.1899(6) Å		c = 5.0572(3) Å β = 90.585(9)°		Z = 2	V/Z = 85.49 Å^3
Atom	Wyckoff position	x	y	z	B_{iso} (Å²)	occupancy
O1	4g	-0.59	0.13	-0.77	1.0	1.0
O2	4g	-0.60	0.64	-0.76	1.0	1.0
Ru1/Li1	2e	0.25	0.8915(19)	0	1.0	0.716(4)/0.292(4)
Li2/Ru2	2e	0.75	0.62	0	1.0	0.716(4)/0.292(4)
Li3	4g	0.45	0.12	-0.33	1.0	1.0
Li4	4g	0.44	0.61	-0.36	1.0	1.0

Table II-11: Crystallographic data for $Li_{4.6}RuO_4$. Li positions were chosen in the center of the tetrahedral interstices. Note that the R_{Bragg} for the synchrotron is quite high due to very peculiar peak shape which could not be taken into account using anisotropic strain models. For the same reason, only the ruthenium positions were refined.

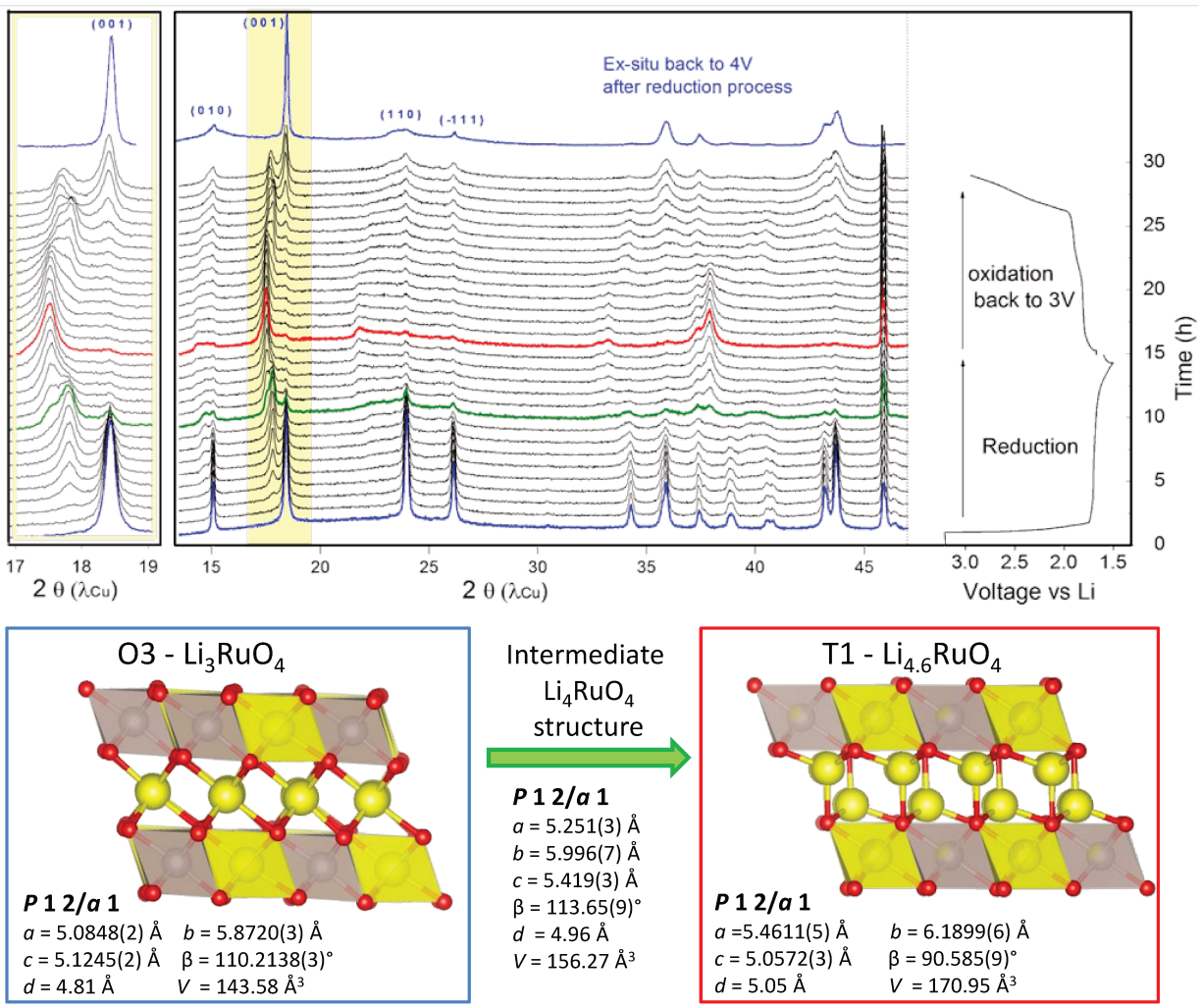

Figure II-16: Operando XRD patterns during the reduction of Li_3RuO_4, with the corresponding galvanostatic curve. The compound is discharged at C/10 using a 1.5 V cutoff voltage on reduction and 3 V on subsequent oxidation; the XRD patterns are taken at intervals of 1 hour. The bottom part presents the structure of the pristine (left) and fully reduced (right) phases. Cell parameters, a, b, c, and β, interlayer distance d and cell volume V are given for the pristine, the intermediate and the fully reduced compounds.

The structural consequence of Li insertion into $Li_3Ru_{0.5}Nb_{0.5}O_4$ is interesting since it doesn't crystallize in a classical layered structure. Both reduction processes, corresponding to the insertion of 0.5 and 0.3 Li, respectively, occur via solid-solution mechanisms as it can be seen by the progressive shifting of the Bragg reflection in Figure II-17. The first reduced phase $Li_{3.5}Ru_{0.5}Nb_{0.5}O_4$ was refined in the same space group as the parent phase (P 4_1 2 2), with however larger cell parameters (a = 5.9744(5) Å and c =8.5302(7) Å) giving a larger cell volume of 76.12 $Å^3$ per formula unit, compared to 73.48 $Å^3$ in the pristine. In contrast, the fully reduced $Li_{3.8}Ru_{0.5}Nb_{0.5}O_4$ phase could only be refined considering a monoclinic distortion from P 4_1 2 2 to a P 1 1 2_1 space group with a = 6.077(1) Å, b = 6.0202(9) Å, c = 8.857(2) Å, γ = 95.255(19)°, and a cell volume of 84.49 $Å^3$ per unit formula. Owing to the peculiar peak shape and broadening of some reflections, we could not refine O or Li positions. Nevertheless, in light of our previous finding for the fully reduced $Li_{4.6}RuO_4$ phase, namely the presence of Li in tetrahedral sites, it is very likely that the same occurs for the fully reduced $Li_{3.8}Ru_{0.5}Nb_{0.5}O_4$ phase. Therefore, we propose a model in which some octahedral sites of the pristine structure are emptied to put twice the number of Li in tetrahedral sites, see Figure II-17. The choice of the occupied tetrahedral site has been done using bond valence energy landscape approaches Table II-12.

$Li_4Ru_{0.5}Nb_{0.5}O_4$													
P 1 1 2_1		a =6.077(1) Å b = 6.0202(9) Å					c = 8.857(2) Å γ = 95.255(19)°				Z = 4		$V_{/unit}$ = 85.49 $Å^3$
Atom	position	x	y	z	B_{iso}	Occupancy	Atom	position	x	y	z	B_{iso}	Occupancy
O1	2a	0.263	0.509	0.260	1.0	1.000	Ru2/Nb2	2a	0.698	0.016	0.539	1.0	0.5/0.5
O2	2a	0.991	0.763	0.510	1.0	1.000	Li1	2a	0.500	0.253	0.255	1.0	1.000
O3	2a	0.737	0.509	0.250	1.0	1.000	Li2	2a	0.247	0.000	0.505	1.0	1.000
O4	2a	0.009	0.763	0.000	1.0	1.000	Li3	2a	0.248	0.500	0.005	1.0	1.000
O5	2a	0.742	0.992	0.268	1.0	1.000	Li4	2a	0.000	0.748	0.255	1.0	1.000
O6	2a	0.493	0.758	0.018	1.0	1.000	LiT1	2a	0.750	0.250	0.130	1.0	1.000
O7	2a	0.742	0.007	0.742	1.0	1.000	LiT2	2a	0.750	0.750	0.900	1.0	1.000
O8	2a	0.507	0.758	0.492	1.0	1.000	LiT3	2a	0.000	0.500	0.110	1.0	1.000
Ru1/Nb1	2a	0.500	0.708	0.292	1.0	0.5/0.5	LiT4	2a	0.000	0.500	0.400	1.0	1.000

Table II-12: Proposed structural model for $Li_4Ru_{0.5}Nb_{0.5}O_4$

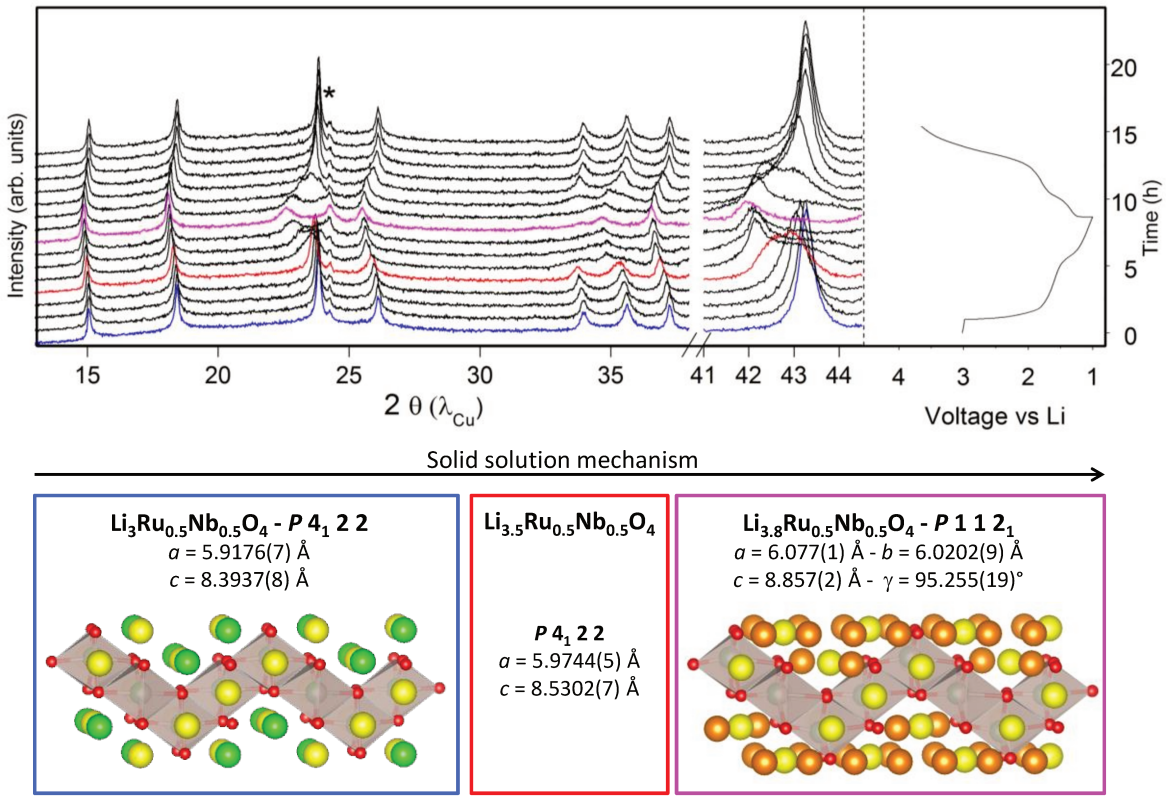

Figure II-17: In the top panel is presented the operando XRD patterns during the reduction of $Li_3Ru_{0.5}Nb_{0.5}O_4$ with the corresponding galvanostatic curve. Cell parameters and space groups for the pristine (blue), intermediate (red) and fully reduced (pink) are given in the bottom panel together with their structural models. Yellow, green and orange balls represent Li in octahedral, Li in octahedral which are no longer present in the discharge sample and Li in tetrahedral sites. Gray octahedra are $(Ru/Nb)O_6$. * peak from the Be window.

II.3.b Li extraction from Li_3RuO_4: degradation and charge compensation mechanisms

II.3.b.i Electrochemical properties and structural evolution

From Figure II-18, it can be seen that nearly three lithium atoms per formula unit can be extracted from the material below 4 V in a single process with the subsequent discharge showing a sloppy profile during the "reinsertion" of 2.5 Li down to 1.5 V. The "S" shape is preserved on subsequent cycles while the capacity rapidly decays. The origin of such degradation could be nested in structural modification of the material during cycling, dissolution of the active material, since a black deposit is observed on the separator and anode after the 1st charge, or gas release. All these aspects are investigated in the next paragraphs.

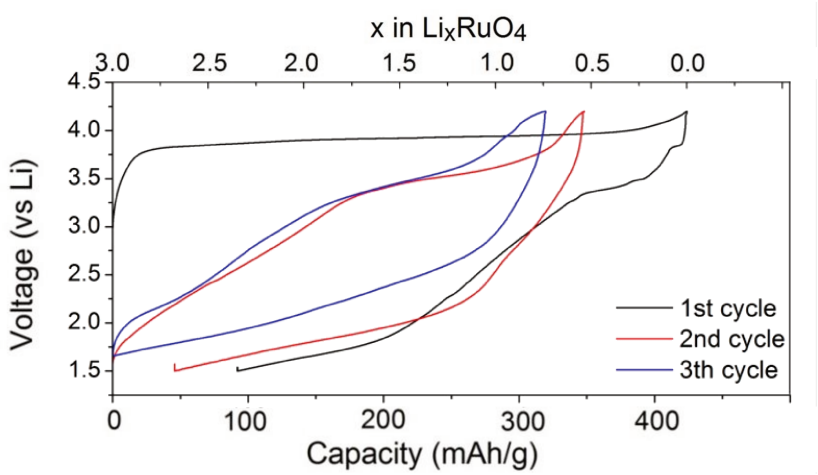

Figure II-18: 1st, 2nd and 3rd galvanostatic cycles for Li_3RuO_4 at C/10 with 4.2 V – 1.5 V cutoff voltages

From the evolution of the patterns during charge (Figure II-19), no new peaks or peak shifting are observed. Moreover, it can be seen that the peak intensity is nearly the same between the pristine and Li_2RuO_4 (left panel Figure II-19) , suggesting a topotactic removal of the 1st Li. In contrast it drastically decreases upon further oxidation showing the amorphization of the active material. No crystallization is observed during the subsequent discharge. This finding shows the different charge and discharge structural pathways, hence explaining the different voltage-composition curves.

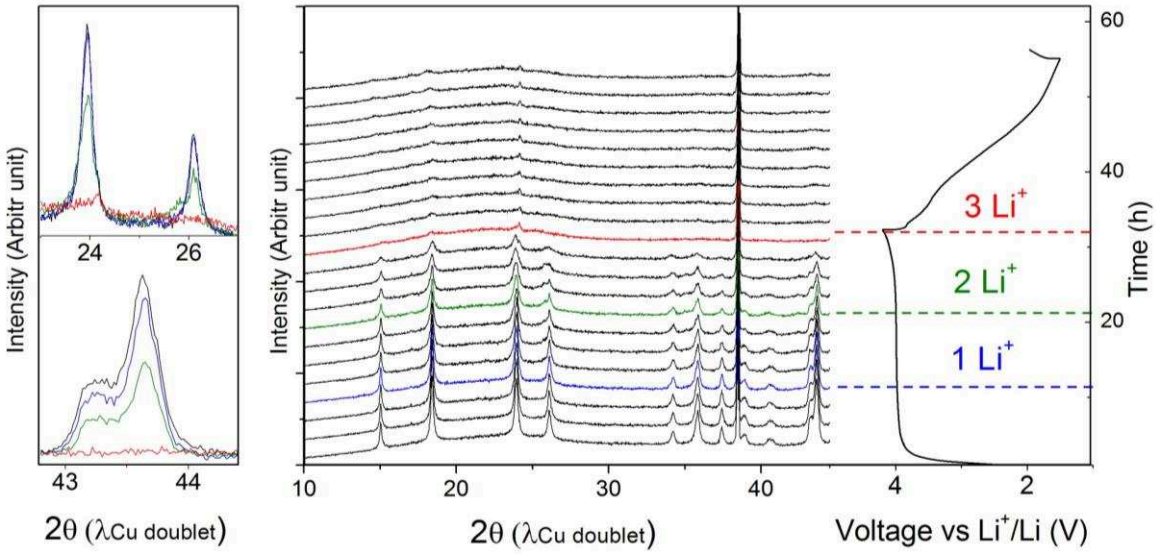

Figure II-19: In the middle panel are presented the XRD patterns collected during the charge and subsequent discharge of Li_3RuO_4 operando. On the left side, specific patterns of the pristine, after the extraction of 1, 2 and 3 Li are shown in black, blue, green and red, respectively. On the right side the associated galvanostatic curve at C/10.

II.3.b.ii Ru dissolution probed by EDX and UV-visible spectroscopy

We performed SEM-EDX measurements on the Li counter electrode after the first electrochemical oxidation of Li_3RuO_4. Results unveil the presence of Ru, as it can be seen Figure II-20, showing the dissolution of some Ru ions/species in the electrolyte upon charge.

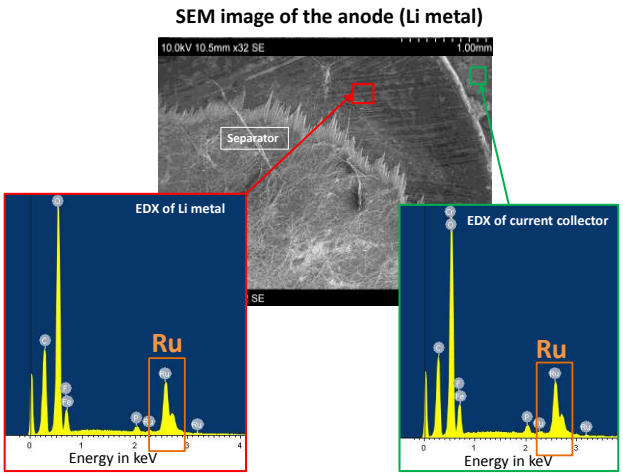

Figure II-20: SEM image of the Li counter electrode with separator and current collector together with the EDX spectra obtained on the Li metal and current collector, in the top, left and right panels respectively. Orange square highlights the presence of Ru

To quantify the amount of dissolution, we measured the active material mass loss by simply weighing electrodes, made self-standing using PTFE, before and after the charge (Figure II-21d). We found that dissolution starts after the removal of the 1st Li and reaches 35% after the removal of three lithium atoms from Li_3RuO_4. Accordingly, the electrochemical data are systematically renormalized based on the active material loss. Operando UV-visible absorption spectroscopy was performed on the electrolyte to characterize the soluble ruthenium species formed during charge. From the results, presented in Figure II-21a-b-c, no change can be observed in the UV-visible spectra during the extraction of the first Li from Li_3RuO_4, in agreement with the XRD and mass loss results. Upon further oxidation from Li_2RuO_4 to $Li_{0.3}RuO_4$, the absorbed intensity grows rapidly. Two features can be seen on the UV-visible spectra. First, there is an increase of the absorbance in ultra violet region, which is typically due to light scattering caused by the presence of particles in the electrolyte (Rayleigh scattering). Particles can also be spotted visually in the cell forming a black deposit at the bottom of the UV-visible cuvette (Inset Figure II-21a). Second, two pairs of broad peaks can be observed at 310-360 nm and 340-500 nm, the former being ascribed to RuO_4/RuO_4^- and the latter to RuO_4^{2-}.[106] Therefore, from operando UV-visible spectroscopy, we could provide evidence for the formation of RuO_4/RuO_4^- soluble species in the electrolyte, together with the appearance of particles and RuO_4^{2-}. Note that similar observations were done in cells using LP100 (1M $LiPF_6$ dissolved in 1/1/3 EC/PC/DMC), LP30 (1M $LiPF_6$ dissolved in 1/1 EC/DMC) or PC containing 1M of $LiClO_4$ electrolytes.

Being powerful oxidizing agents, RuO_4 and RuO_4^- might chemically react with the electrolyte.[107] To assess this hypothesis, we added LP100 onto $KRuO_4$ (K^+, RuO_4^-) powder and monitored the evolution of the obtained solution by UV-visible spectroscopy (Figure II-22). The formation of RuO_4^- species is initially observed together with the appearance of particles. Then, the UV-visible signal associated to RuO_4^- disappears while the amount of particles precipitating in the solution increases. Similar observations were made with RuO_4. To assess if the chemical reaction of RuO_4/RuO_4^- with the electrolyte can lead to gas evolution, mass spectrometry measurements were performed. To do so, $KRuO_4$ and LP100 were mixed in the air-tight argon filled reaction vial, after mixing and letting the reaction proceed 24 h, the gas composition inside the reaction tube was measured by Mass spectroscopy which revealed the presence of CO_2. Altogether, these results demonstrate the partial decomposition of the Li_2RuO_4 upon further oxidation, in RuO_4/RuO_4^- species that

further chemically react with the carbonate constituents of the LP100 electrolyte to form insoluble amorphous RuO_x particles and CO_2 gas (see scheme in Figure II-21e).

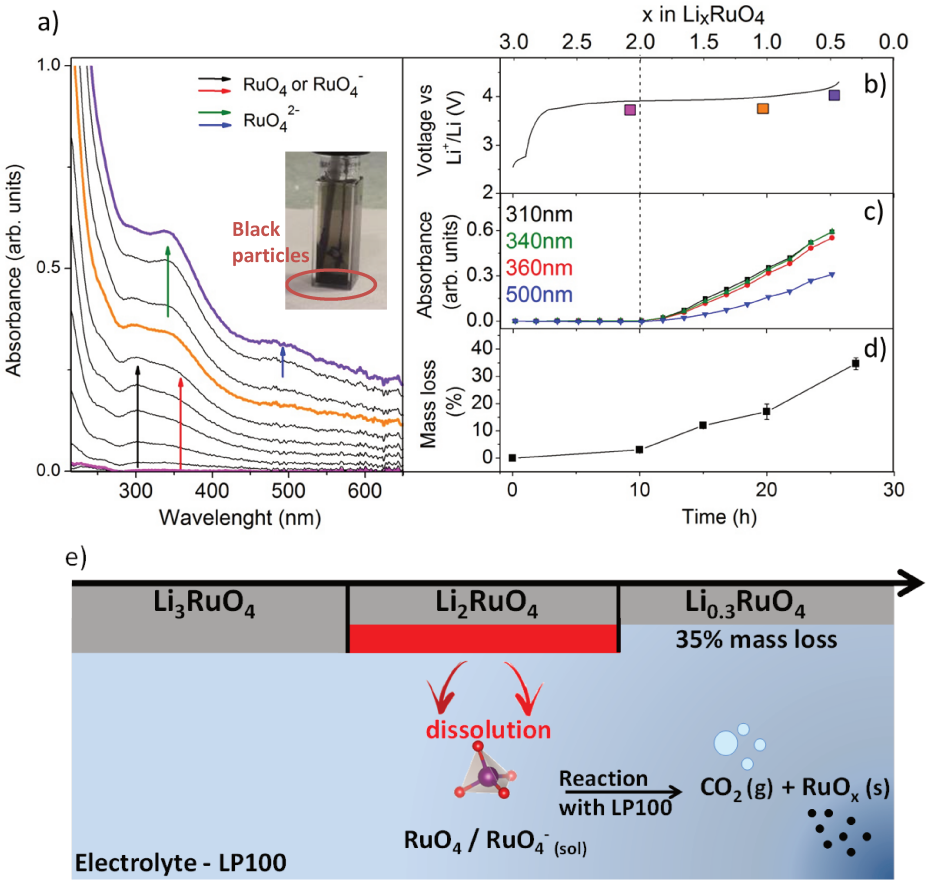

Figure II-21: Operando UV-visible during the charge of Li_3RuO_4 vs Li. a) Evolution of the UV-visible spectra highlighting the 310 nm, 360 nm, 340 nm and 500 nm absorbance wavelengths corresponding to RuO_4/RuO_4^- and RuO_4^{2-} species. b) and c) show the galvanostatic curve, C/10, together with the evolution of the absorbance of 310 nm, 360 nm, 340 nm and 500 nm. d) Average active material mass loss during charge determined ex situ using PTFE film electrodes in Swagelock type cells. e) Schematics summarizing the dissolution process during the oxidation of Li_3RuO_4.

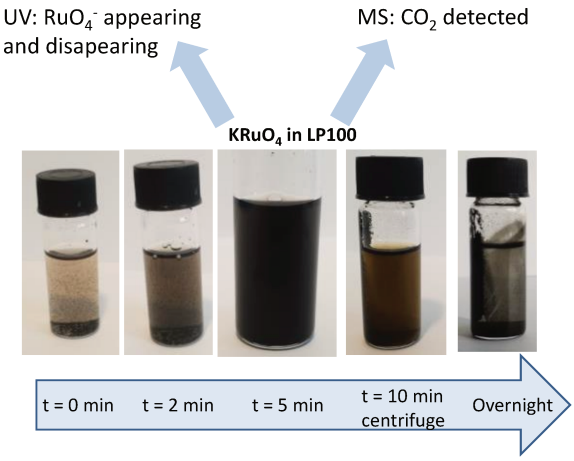

Figure II-22: Reaction vials showing the evolution with time of a $KRuO_4$ and LP100 mixture. RuO_4^- appears, turning the solution green-brownish, as monitored by UV-visible, together with the formation of particle. With time, more particle forms in the solution while the RuO_4^- progressively disappears until the solution turns transparent again. CO_2 evolution was detected by Mass Spectrometry (MS) during the reaction.

II.3.b.iii Gas evolution measurements

Gas formation, O_2 specifically, is a well-known degradation mechanism for compounds showing anionic redox[108]; therefore Online Electrochemical Mass Spectroscopy (OEMS) was performed by Erik J. Berg at PSI. From Figure II-23a, it can be seen that gas evolution starts after the removal of 0.5 Li with the formation of CO_2 and progresses constantly until $Li_{0.3}RuO_4$, leading to a cumulated release of 0.2 moles of CO_2 per mole of Li_3RuO_4. Pushing the oxidation process beyond $Li_{0.3}RuO_4$ results in drastic increase of the CO_2 release which comes along with the production of O_2 gas but in much smaller amount (20 times less), hence the need to limit our cycling between Li_3RuO_4 and $Li_{0.3}RuO_4$. Pressure cell measurements carried out in this composition range confirm a relatively low gas evolution during the first cycle (Figure II-23b). To account for this gas release three contributions should be considered: i) surface Li_2CO_3 decomposition at the beginning of charge,[109] ii) reaction of RuO_4/RuO_4^- with LP100 after the removal of the first Li and iii) surface reactivity of charged Li_xRuO_4. Assessing the exact contribution of each of these mechanisms is not trivial; however the second process is believed to be the most important source of gas release, keeping in mind that 35% of the electrode dissolves into RuO_4/RuO_4^-.

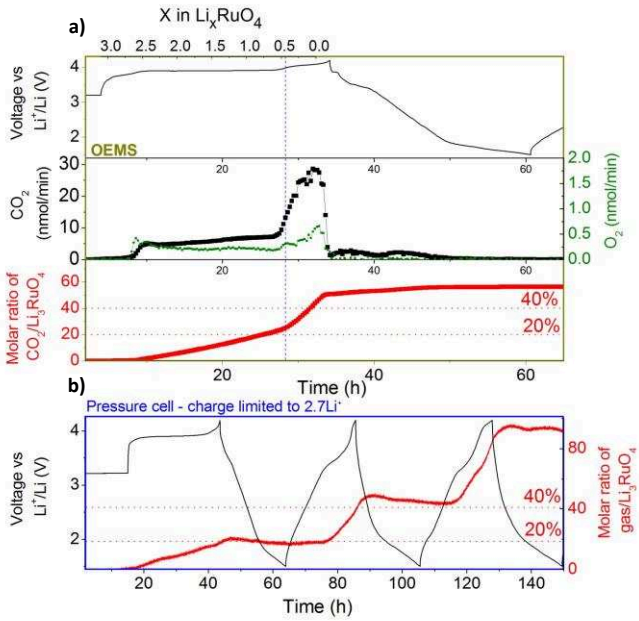

Figure II-23: OEMS measurements on Li_3RuO_4 during galvanostatic cycling, C/10. a) Galvanostatic cycle, CO_2 and O_2 production rate, and integrated number of moles of CO_2 over the moles of active material are presented on the top, middle and bottom panel respectively. b) Pressure cell measurement limiting the charge before the massive gas release, e.g. at $Li_{0.3}RuO_4$ composition.

Overall, the capacity decay is associated to the dissolution of the cathode material, while the sloppy profile observed during discharge is likely caused by the amorphization of the compound.

II.3.b.iv XAS and XPS measurements for Li_3RuO_4

Having established the degradation mechanisms, we now turn to the study of the charge compensation mechanism in the electrode by XAS, performed on the ROCK beamline at Soleil Synchrotron, and XPS, done by Dominique Foix at the University of Pau.

Operando XAS measurements at Ru K-edge are performed on a cell initially started on discharge to assess the participation of Ru (Figure II-24). During Li intercalation in Li_3RuO_4 (process 1 on the curve), there is a clear shift of the edge position towards lower energy indicative of the Ru reduction from 5+ to 3.5+ since 1.5 Li can be intercalated into Li_3RuO_4. This process is fully reversible since 1.5 Li can be removed from $Li_{4.5}RuO_4$ to restore Li_3RuO_4 (process 2). In contrast, when Li_3RuO_4 is oxidized (process 3) the shift of Ru K-edge XAS spectra is small, but shows the appearance of a pre-edge peak, indicative of a non-centrosymmetric environment around Ru. For the discharge processes 4 and 5, the pre-edge peak disappears and the edge position shifts continuously to lower energy, showing the reduction of Ru.

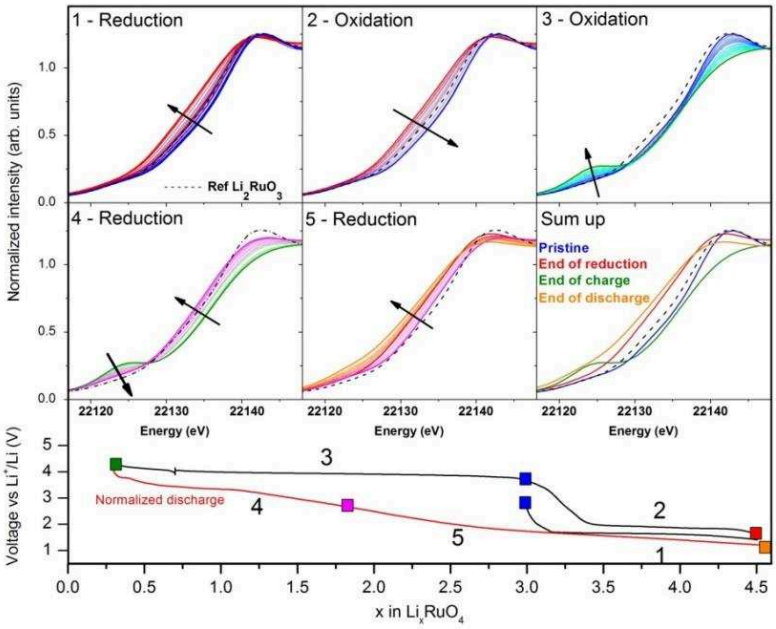

Figure II-24: Operando Ru K-edge XANES spectra for Li_3RuO_4. The XANES spectra for different regions of the galvanostatic curve, C/5, are presented together with the electrochemical data.

To better exploit the data, Principal Component Analysis (PCA) combined to Multivariate Curve Resolution-Alternating Least Squares (MCR-ALS) has been carried out for all the collected XAS spectra.[110,111] We find that seven components are necessary to describe the complex evolution of the spectra (Figure II-25a). The oxidation state of the Ru in the different components is determined using the reduction of Li_3RuO_4 → $Li_{4.5}RuO_4$ and K_2RuO_4 as references (Figure II-25b). The XANES and the fit of the Fourier Transforms of the EXAFS oscillations of the principal components, giving access to the Ru-O and Ru-Ru distances, are reported in Figure II-26 and Table II-13. Each process, namely the reduction (process 1 and 2), the charge (process 3) and the discharge (process 4 and 5) will be described separately for clarity reasons.

Three components are needed to describe the spectral evolution during the reduction process: the 1st component (C1) corresponds to the pristine material, the 2nd component (C2) corresponds to Ru^{4+} and the 3rd component (C3) corresponds to $Ru^{3.5+}$. In agreement with Ru reduction, the average Ru-O bond lengths increase from 1.98 Å to 2.02 Å and 2.06 Å for C1, C2 and C3, respectively. Concerning the Ru – Ru distances, the appearance of short Ru – Ru distance of 2.7 Å is observed during the reduction. Such Ru – Ru dimerization has been observed in other compounds with Ru^{4+}.[112] This process is reversible since the oxidation from $Li_{4.5}RuO_4$ to Li_3RuO_4 nearly follows the reverse transformation.

Turning to the oxidation of Li_3RuO_4, it can be described with only two components: the pristine (C1) and fully charged component (C4) whose concentration reaches 100% at the end of charge. At this point, one should note that the dissolved RuO_4/RuO_4^- species have little influence on the spectra since their contribution could not be spotted through the PCA analysis. This is attributed to the dispersion of the soluble species inside the cell, diluting their concentration in the beam. The Ru oxidation state of C4 corresponds to $Ru^{5.4+}$. In C4, Ru adopts a highly distorted environment composed of 1 short, 3 medium and 2 long Ru – O distances of 1.72 Å, 1.91 Å and 2.07 Å, respectively. The distortion of the RuO_6 local environment is confirmed by the presence of the pre-edge peak in the XANES region of the spectra. Unlike the intense pre-peak in K_2RuO_4 and Na_2RuO_4 ascribed to the tetrahedral and trigonal bipyramid geometry of the Ru coordination shell (Figure II-26b), the lower intensity of the C4 pre-peak suggests that the end of charge compound keeps its octahedral coordination, consistent with EXAFS fitting. For the reduction part (process 4 and 5), four components are needed: C4, C5, C6 and C7 which corresponds to $Ru^{5.4+}$, $Ru^{4.7+}$, $Ru^{3.6+}$ and

$Ru^{2.8+}$, respectively. In terms of Ru – O distances, the average distance in C5, C6 and C7 are 1.93 Å, 2.03 Å and 2.07 Å, respectively, consistent with their respective oxidation states. Again, short Ru – Ru distances of 2.6 Å are observed in these components.

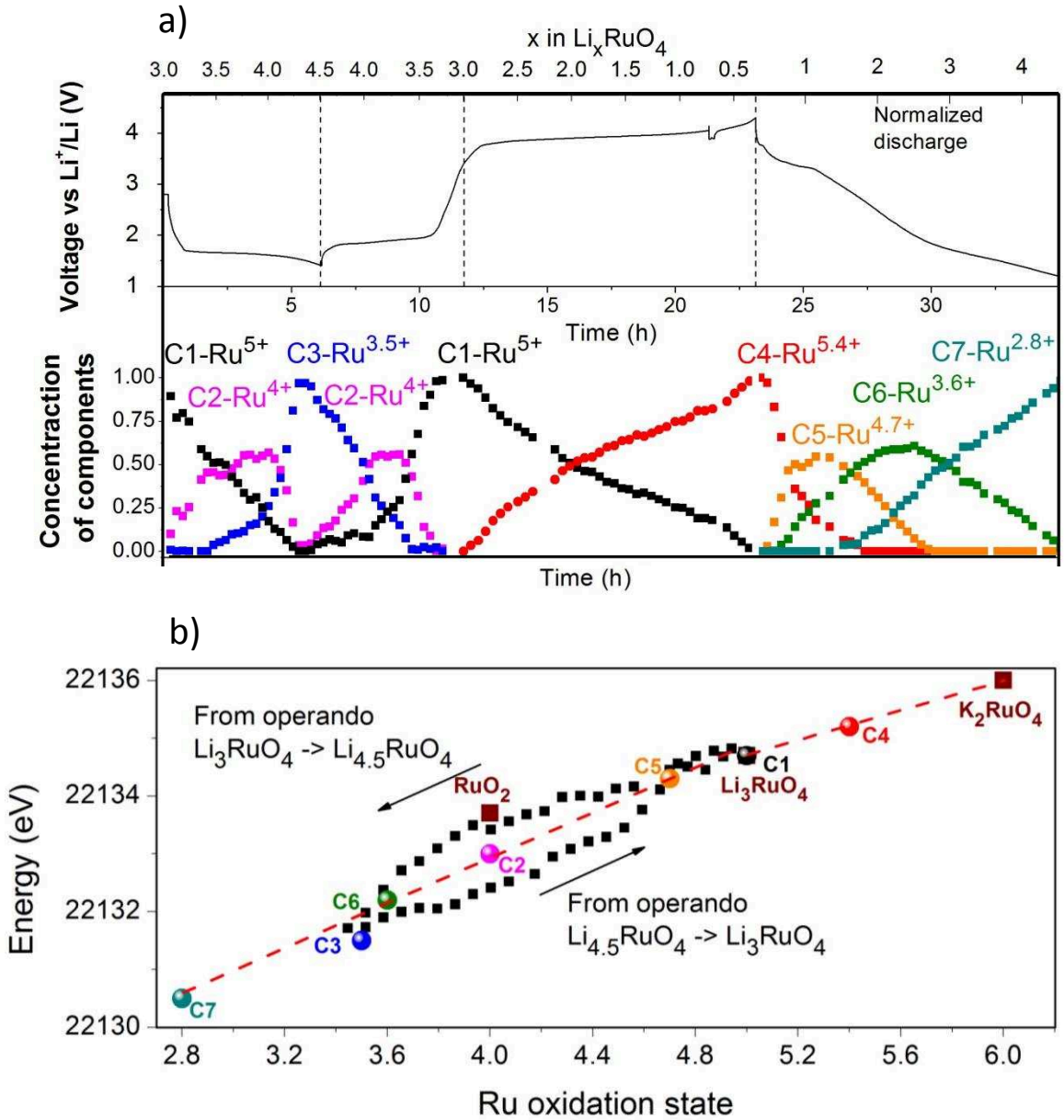

Figure II-25: Results from the a) Galvanostatic curve of Li_3RuO_4, C/5, together with the evolution of the concentration of principal components during cycling obtained by PCA and MCR-ALS analysis on the operando XAS of Li_3RuO_4. Black, magenta, blue, red, orange, green and cyan squares corresponds to the concentration of component from C1 to C7, respectively. b) Edge position at 0.6 of the edge jump plotted versus the oxidation state of Ru. Experimental points taken during the reduction process of Li_3RuO_4, i.e. $Li_3RuO_4 \rightarrow Li_{4.5}RuO_4$, and the subsequent charge, $Li_{4.5}RuO_4 \rightarrow Li_3RuO_4$ are shown in black. Reference samples RuO_2, K_2RuO_4 and Li_3RuO_4 are shown in wine. The oxidation state of the chemical species obtained by PCA analysis is obtained assuming a linear relationship between the edge position and the oxidation state.

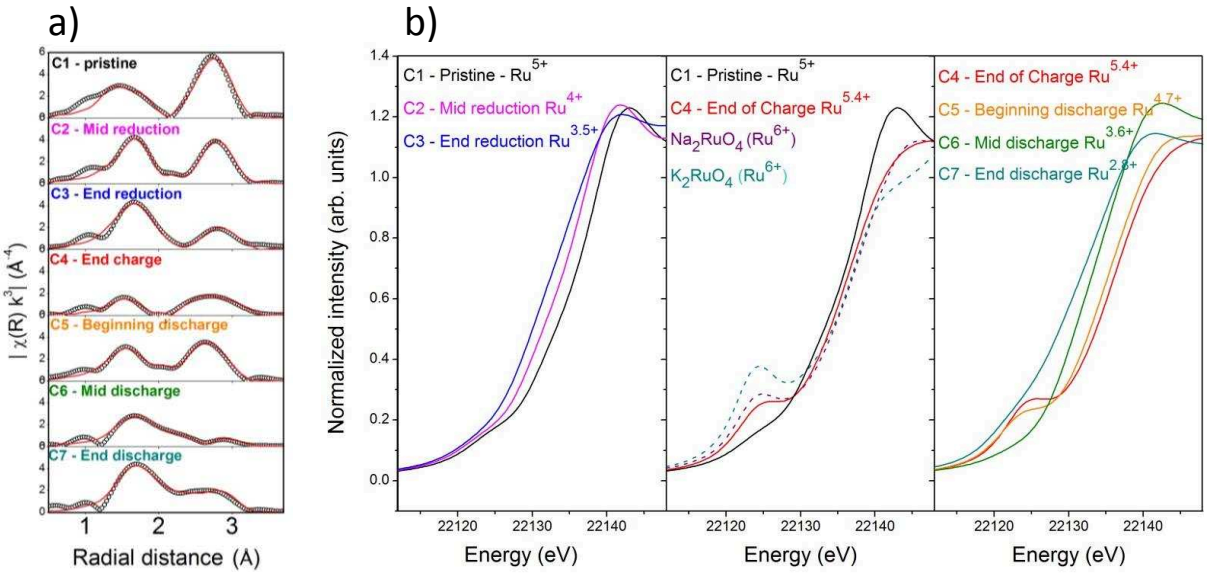

Figure II-26: a) Magnitude of the Fourier transforms (dotted line) and fit (plain line) of the k^3-weighted EXAFS oscillations of the MCR-ALS components. b) XANES spectra of the principal components obtained through MCR-ALS together with reference samples Na_2RuO_4 and K_2RuO_4 that have both Ru^{6+} oxidation state but in bipyramid (RuO_5) and tetrahedral (RuO_4) coordination, respectively.

	First coordination shell: Ru – O distances								Second coordination shell: Ru – Ru distances					
Component	**CN**	**d_{Ru-O}**	**$\sigma*10^3$**	**CN**	**d_{Ru-O}**	**$\sigma*10^3$**	**CN**	**d_{Ru-O}**	**$\sigma*10^3$**	**Avg. d_{Ru-O}**	**CN**	**d_{Ru-Ru}**	**$\sigma*10^3$**	**CN**	**d_{Ru-Ru}**	**$\sigma*10^3$**	**Avg. d_{Ru-Ru}**	**$R*10^3$**
C1 - pristine	2	1.886(9)	2.5	2	1.982(6)	2.5	2	2.07(1)	2.5	1.98	2	3.08(1)	4				3.08	21
C2 – Mid reduction	2	1.93(1)	4.4	4	2.063(5)	3.5				2.02	1.7	3.099(4)	4	0.3	2.66(1)	4	3.04	8.4
C3 - End reduction	2	1.97(1)	3.3	4	2.101(3)	3.4				2.06	1.6	3.144(8)	7	0.4	2.69(2)	7	3.053	14
C4 - End charge	1	1.72(1)	2.6	3	1.91(3)	4.0	2	2.072(2)	6.2	1.90	1	3.04(1)	3	1	3.159(9)	3	3.10	9
C5 – Beginning discharge	2	1.86(2)	5.2	4	1.968(5)	5.2				1.93	1	3.06(2)	4	0.5 0.5	2.738(2) 2.536(3)	4 4	2.84	7
C6 – Mid discharge	2	1.931(8)	2.4	4	2.053(4)	2.2				2.01	1	3.088(9)	3	1	2.54(1)	6	2.81	16
C7 - End of discharge	6	2.06(4)	9.3							2.07	1	3.12(2)	9	1	2.61(1)	8	2.87	21

Table II-13: Local structure obtained by fitting the EXAFS oscillations for the PCA components for the Ru-O bonds and Ru-Ru bonds. CN stands for Coordination Number; d the distances are given in Å, σ the Debye-Waller factors in Å², Avg. d, the Average distances in Å. The difference energy threshold, E0, and the amplitude reduction factor (S_0^2) are fixed during fit. S_0^2 was taken equal to 1 for all analysis.

So in short, Operando Ru K-edge XAS spectra on Li_3RuO_4 confirm the cationic redox, $Ru^{5+} \rightarrow Ru^{3.5+}$ for Li insertion into Li_3RuO_4 and suggest the participation of oxygen in the charge compensation mechanism. This is confirmed by XPS analysis, carried out on ex situ samples, focusing on the O1s spectrum in which we note the appearance of an extra component at 530.5 eV for the oxidized samples that was previously assigned to peroxo-like species (Figure II-27).[71]

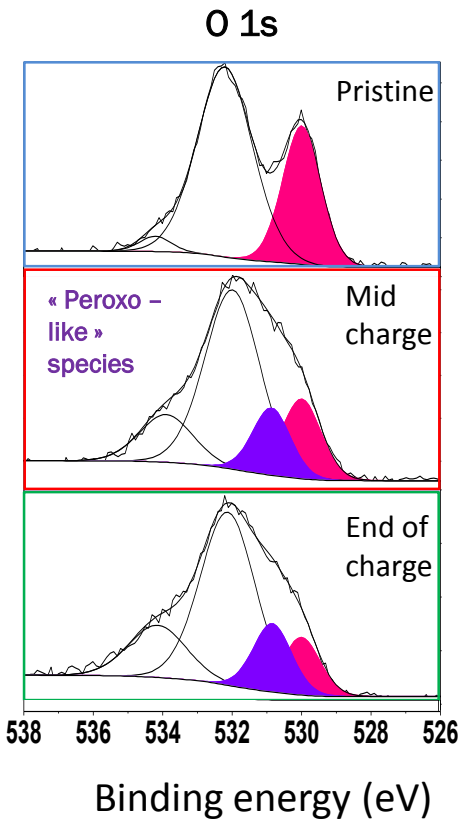

Figure II-27: O1s XPS spectra performed on ex situ samples of Li_3RuO_4. Pristine sample corresponds to Li_3RuO_4, mid charge to $Li_{1.5}RuO_4$, end of charge to "$Li_{0.3}RuO_4$". Pink and purple regions correspond to the O^{2-} and oxidized oxygen species, respectively. Peak at 532 eV correspond the surface species. From the mid charge, an extra contribution is found corresponding to the peroxo species. It is still present in the end of charge sample.

Overall, regarding the charge of Li_3RuO_4, we have shown that both cationic and anionic redox processes are responsible for the charge compensation mechanism. The cationic redox enlists the formation of the RuO_4/RuO_4^- and the oxidation of $Ru^{5+} \rightarrow Ru^{5.4+}$ making a total of 1.1 e^- (see Annexe for details). Given that 2.7 Li^+ (2.7 e^-) are extracted from Li_3RuO_4, by simple subtraction, we find that the participation of the anionic redox is 1.6 e^-. During the discharge, 4.2 Li^+/e^- reacts with $Li_{0.3}RuO_4$ out of which 2.6 e^- are attributed to the cationic reduction of $Ru^{5.4+} \rightarrow Ru^{2.8+}$, hence making a total of 1.6 e^- for the anionic redox. Also not fully accurate, this calculation strongly suggests a decent reversibility for the oxygen activity in this material, despite its partial dissolution. At this point, we will try to assess the role of chemical substitution and structure in $Li_3Ru_yM_{1-y}O_4$ on the Ru dissolution.

II.3.c Li extraction from $Li_3Ru_yNb_{1-y}O_4$

The electrochemical performances on oxidation of compounds among the $Li_3Ru_yNb_{1-y}O_4$ series are obtained by cycling the cells at C/10 between 4 or 4.5 and 1.5 V. Figure II-29a shows that similar electrochemical signatures are observed for all $Li_3Ru_yNb_{1-y}O_4$ compounds, but with, however, the amount of Li removed from the 4 V plateau which decreases with increasing Nb substitution. Bearing in mind that these compounds have different crystallographic structures, it can be concluded that the structure don't drastically influence the electrochemical properties. Upon cycling, as exemplified in Figure II-29b for $Li_3Ru_{0.5}Nb_{0.5}O_4$, capacity decay is observed together with the charge-discharge curves becoming featureless, reminding us the case of Li_3RuO_4. Operando XRD revealed the amorphization of all the compounds during oxidation (shown for $Li_3Ru_{0.5}Nb_{0.5}O_4$ in Figure II-28). Moreover, when recovering the separator and anode after cycling, a black deposit is observed suggesting Ru dissolution is also happening during the oxidation of compounds among the $Li_3Ru_yNb_{1-y}O_4$ series.

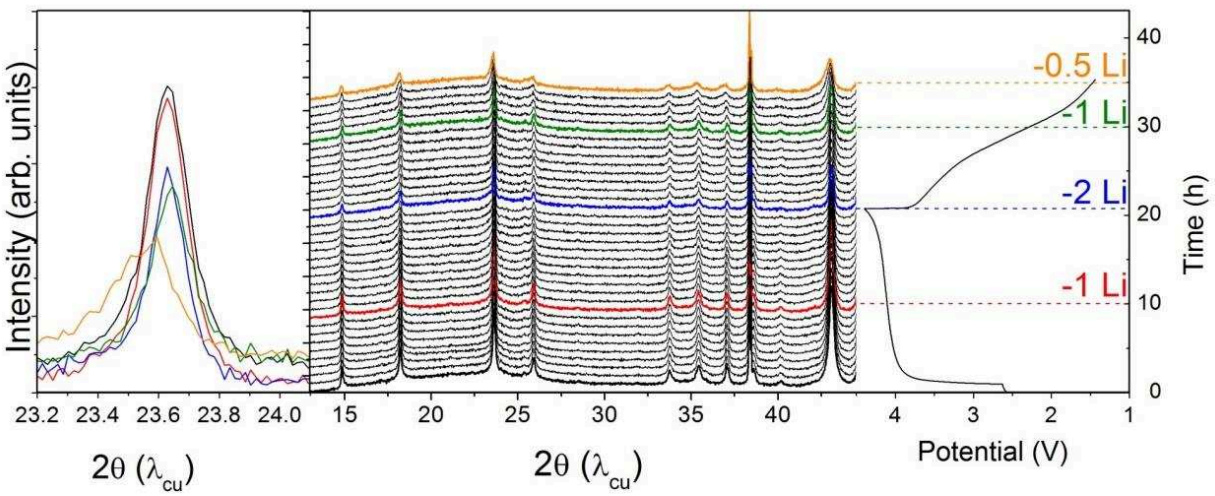

Figure II-28: In the middle panel are presented the XRD patterns collected during the charge and subsequent discharge of $Li_3Ru_{0.5}Nb_{0.5}O_4$ Operando. On the left side, specific patterns of the pristine, after the extraction of 1, 2 Li and reinsertion of 1 Li and 0.5 Li are shown in black, red, blue, green and orange, respectively. On the right side the associated galvanostatic curve, C/10.

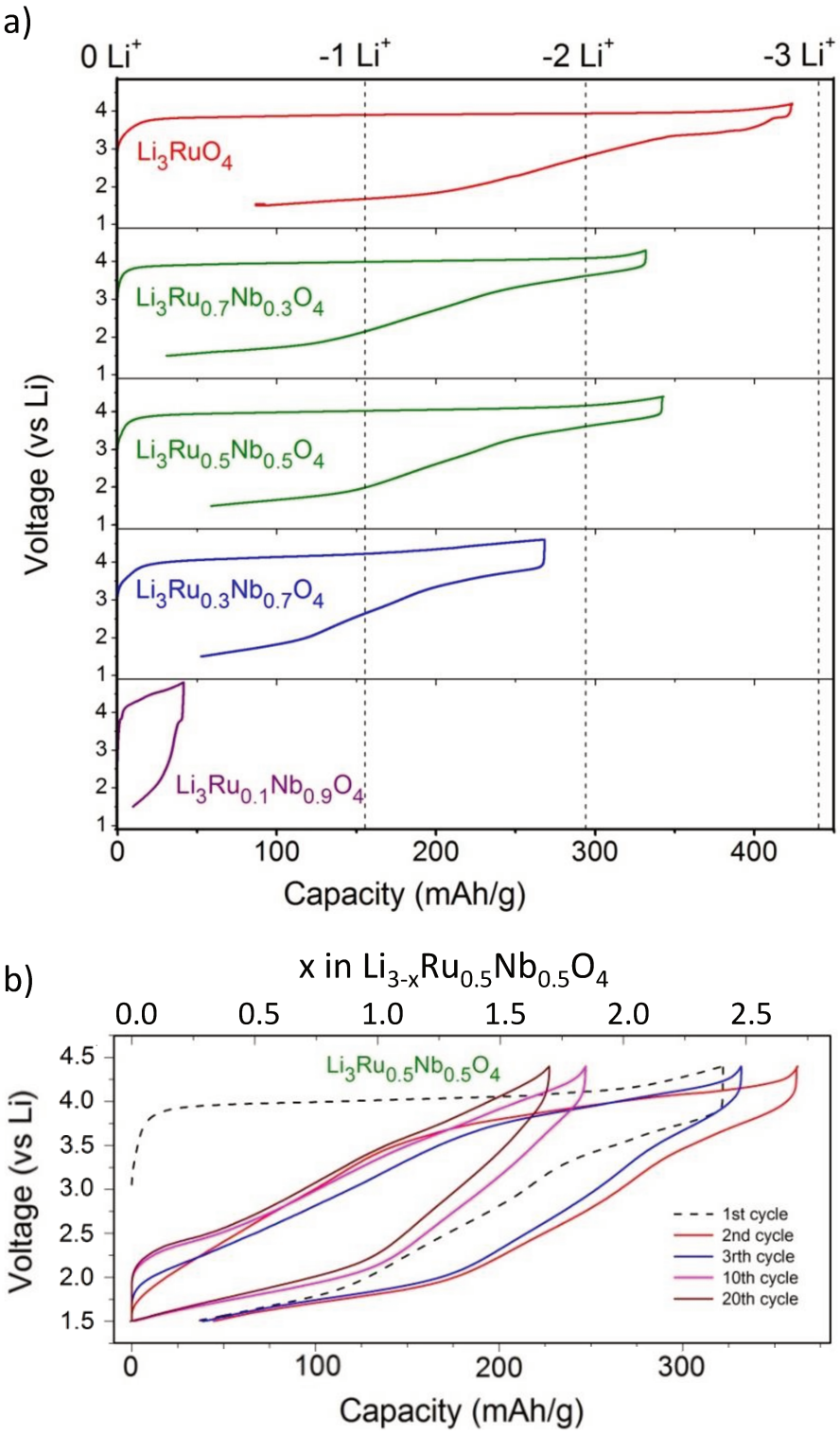

Figure II-29: a) First cycle upon oxidation at C/10 of all the compounds among the $Li_3Ru_yNb_{1-y}O_4$ series for y = 1, 0.7, 0.5, 0.3, 0.1 from the top to the bottom. b) Cycling performances for $Li_3Ru_{0.5}Nb_{0.5}O_4$ cycled at C/10 with 4.4 V – 1.5 V cutoff voltages.

Operando XAS has been performed on $Li_3Ru_{0.5}Nb_{0.5}O_4$ at the Ru K-edge. The XANES evolution during the 1st cycle is shown in Figure II-30. Since a higher polarization was obtained in the XAS cell compared to normal Swagelock, cutoff voltages were raised from 4.5 – 1.5 V to 5 – 1 V. Such enlargement of the sweeping potentials led to electrolyte oxidation/reduction at the very end of charge/discharge, explaining the absence of spectral evolution during the last part of discharge. Despite these issues, the data can be used for qualitative interpretation since it matches with spectra realized on ex situ samples. During oxidation (process 1), the edge position only slightly shifts towards higher energy and a pre-edge clearly appears. During reduction (processes 2 and 3), the Ru K-edge moves towards low energy showing that ruthenium oxidation state is decreasing. Overall, the spectra of the pristine, end of charge and end of discharge for Li_3RuO_4 and $Li_3Ru_{0.5}Nb_{0.5}O_4$ are nearly similar showing the charge compensation in both compounds is very similar despite the presence of Nb and the different crystallographic structure.

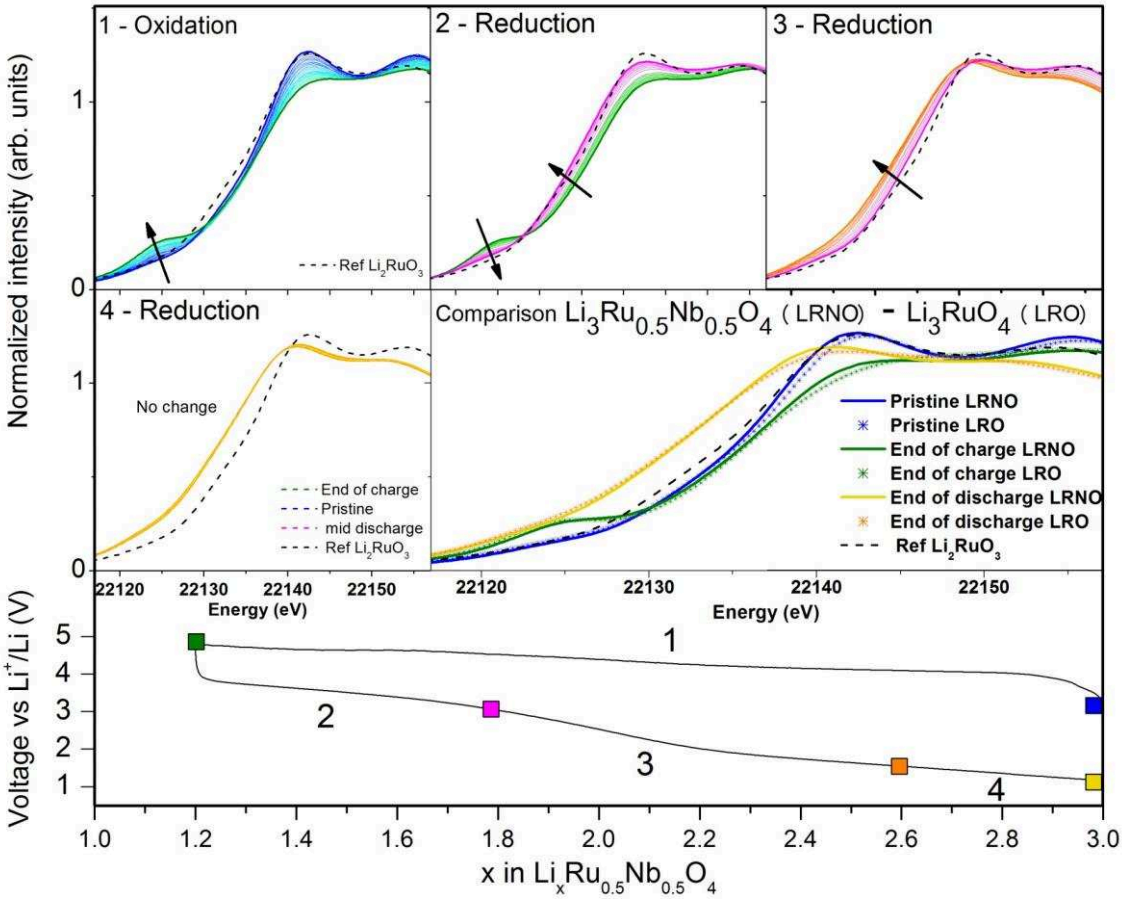

Figure II-30: Operando Ru K-edge XANES spectra for $Li_3Ru_{0.5}Nb_{0.5}O_4$. The XANES spectra for different regions of the galvanostatic curve are presented together with the electrochemical data, C/5, and a comparison of the spectra between $Li_3Ru_{0.5}Nb_{0.5}O_4$ and Li_3RuO_4.

Overall, Nb substitution and structural change has nearly no effect on the charge compensation mechanism and on the dissolution issue which plagues the electrochemical properties of these phases. How to alleviate this issue? Some hope remains in the use of Ir as substitute to Ru since Li_3IrO_4 has been shown to be stable against dissolution, hence our interest into studying the $Li_3Ru_yIr_{1-y}O_4$ phases.

II.3.d Li extraction from $Li_3Ru_yIr_{1-y}O_4$

Electrochemical properties for the 1st cycle of the $Li_3Ru_yIr_{1-y}O_4$ members (Figure II-32a) show similar behaviors irrespective of y: nearly 3 Li can be extracted up to 4.8 V, while 2 Li can be re-inserted down to 2 V. Interestingly, whatever the amount of Ir, no black deposit is observed on the separator after the disassembly of the cell. Operando UV-visible experiments carried out on $Li_3Ru_{0.5}Ir_{0.5}O_4$ shown in Figure II-31 confirmed the absence of metal dissolution, hence demonstrating the benefit of the Ir substitution for preventing electrode dissolution.

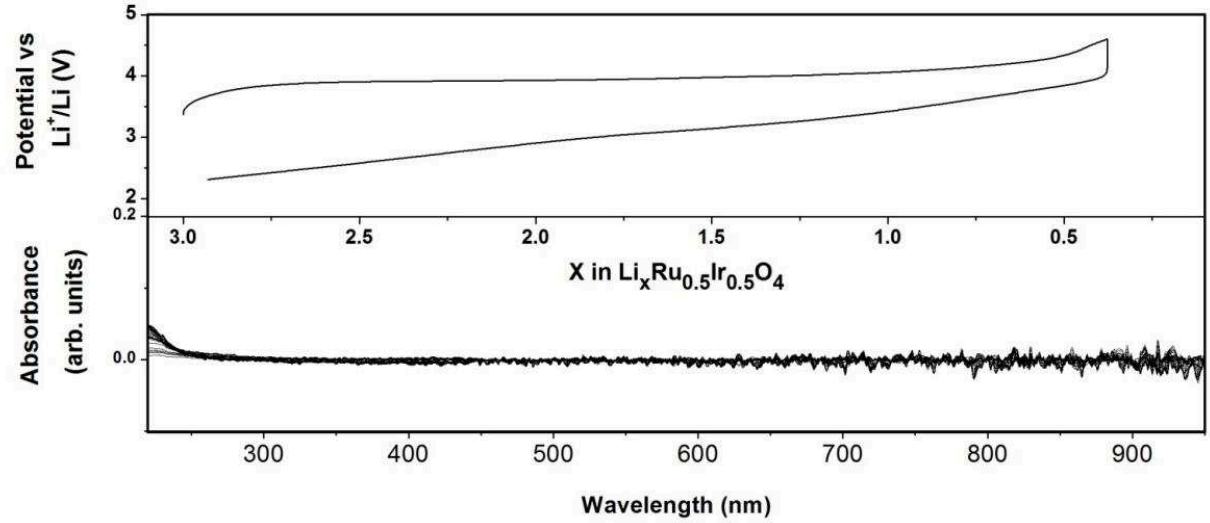

Figure II-31: Operando UV-visible spectroscopy for $Li_3Ru_{0.5}Ir_{0.5}O_4$. No sign of Ru dissolution is shown. Electrochemical cycle done at C/10.

However, gas pressure measurements during cycling (see Figure II-32b) show that while Li_3RuO_4 gas evolution is rather small during delithiation, once Ir is added to the chemical composition, it increases dramatically up to $6x10^{-3}$ bar/mg. By converting pressure to moles, it corresponds to a molar ratio between the gas and the active material of 50%. Interestingly, the onset of this gas release is correlated to the content of Ir in the material as it occurs at x =

2.4, 1.8, 1.4 and 1 in $Li_xRu_yIr_{1-y}O_4$ for y = 0.75, 0.5, 0.25 and 1, respectively. Moreover, we note that the amount is Li extracted before gas release is twice the amount of Ir. As for Li_3IrO_4, if we assume all O atoms from CO_2/O_2 come from the material, one can deduce, independently of y, a 25% oxygen loss from the material leading to a $Ru_yIr_{1-y}O_3$ composition at the very end of charge.[90]

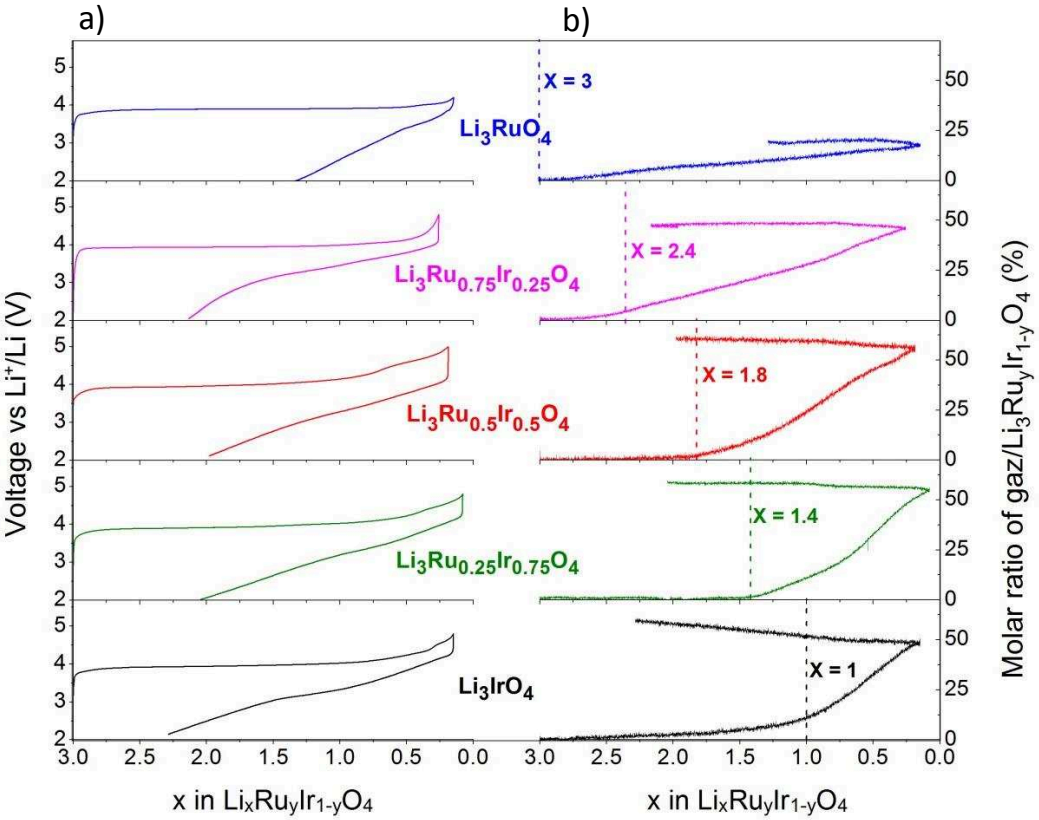

Figure II-32: a) 1st cycle of galvanostatic cycling, C/10, and b) molar ratio of the gas/active material evolution inside the cell for compounds among the solid solution $Li_3Ru_yIr_{1-y}O_4$ for y = 1, 0.75, 0.5, 0.25 and 0 from top to bottom, at the left and right side, respectively. Dash lines indicate the gas pressure increase threshold.

To check the impact of gas release on the material structure, operando XRD was conducted on each composition and the results are presented in Figure II-33 for $Li_3Ru_{0.5}Ir_{0.5}O_4$. Upon oxidation of $Li_3Ru_{0.5}Ir_{0.5}O_4$, we observe the growth of a new set of peaks, starting after the removal of 0.3 Li, as emphasized in the inset in Figure II-33a. They can be ascribed to a new Li poor phase coexisting with the pristine one and having a similar structure with however larger cell parameters, a = 2.965 Å and c = 14.525 Å compared to a = 2.945 Å and c = 14.425 Å (described in R -3 m space group), giving a volume per formula unit of 73.81 $Å^3$ compared to 72.24 $Å^3$ (Figure II-33b). The growth of the cell parameters is likely due to the increased electrostatic repulsions between the oxygen layers which are less efficiently screened upon Li

extraction. After x = 1.6 in $Li_xRu_{0.5}Ir_{0.5}O_4$, further oxidation leads to a drastic broadening and shift of the peaks corresponding to the new phase suggesting its amorphization. For $Li_3Ru_{0.25}Ir_{0.75}O_4$, a biphasic process between the pristine structure and a new phase with larger cell parameters and volume per unit formula, i.e. 72.55 $Å^3$ and 74.53 $Å^3$, respectively, is also observed from the beginning of charge up to x = 1.3. It is followed by the amorphization of this new phase upon further oxidation. For $Li_3Ru_{0.75}Ir_{0.25}O_4$, the loss of crystallinity is also observed at the beginning of charge. Overall, it can be observed that the onset of gas release upon oxidation from the $Li_3Ru_yIr_{1-y}O_4$ members is associated with the amorphization of an intermediate Li-poor phase.

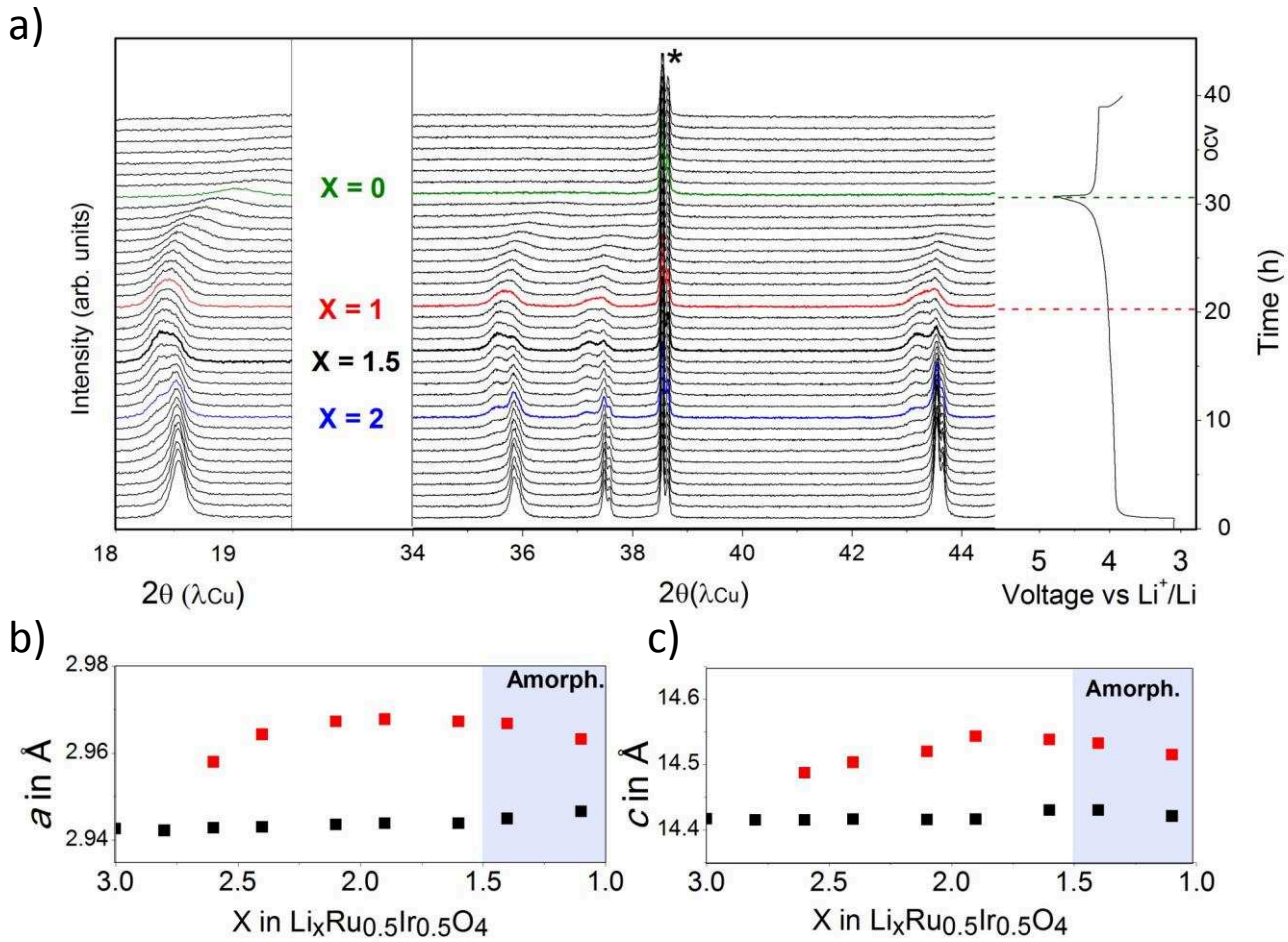

Figure II-33: Operando XRD for $Li_3Ru_{0.5}Ir_{0.5}O_4$ during the 1st charge. a) show the XRD patterns in 18-19.5°and 34-44.5° range and the galvanostatic curve, C/10, from left to right. * peak comes from the cell b) and c) present the evolution of the a and c cell parameter (fit in R-3m) during the charge obtained with Rietveld refinement for both phases.

Next, first-principles DFT calculations were performed to address the origin of the decomposition of Li_xRuO_4 which shows limited O_2 release and does not stabilize RuO_3 at the end of charge compared to Li_xIrO_4. The phase stability diagrams are computed for Li_xRuO_4 and Li_xIrO_4 (Figure II-34). It can be seen that both electrodes should undergo an equivalent structural phase transition converting the metal oxide framework from condensed chains of edge-shared MO_6 octahedra (Oh) into disconnected MO_4 tetrahedra (Td), at x = 1 for Ru and x = 0 for Ir. In the case of Li_3IrO_4, the reaction enthalpy computed for the O_2 release mechanism is negative in $LiIrO_4$ and IrO_4 showing that these compounds will never form. In contrast, the Li_xRuO_4 phase, consisting in an opened framework of tetrahedra, is predicted to be stable vs. O_2 release down to x = 0 but might behave as a salt for which the $(Ru^{Td}O_4)^-$ ionic species are prone to dissolution in the electrolyte. These results correlate perfectly with the experimental data since tetrahedral RuO_4^- species have been indeed detected by UV-visible spectroscopy, proving the structural transition mentioned above is possible in this system. Hence, we could bypass the oxygen instability in the Ru-based electrode to the expense of chemical dissolution problems.

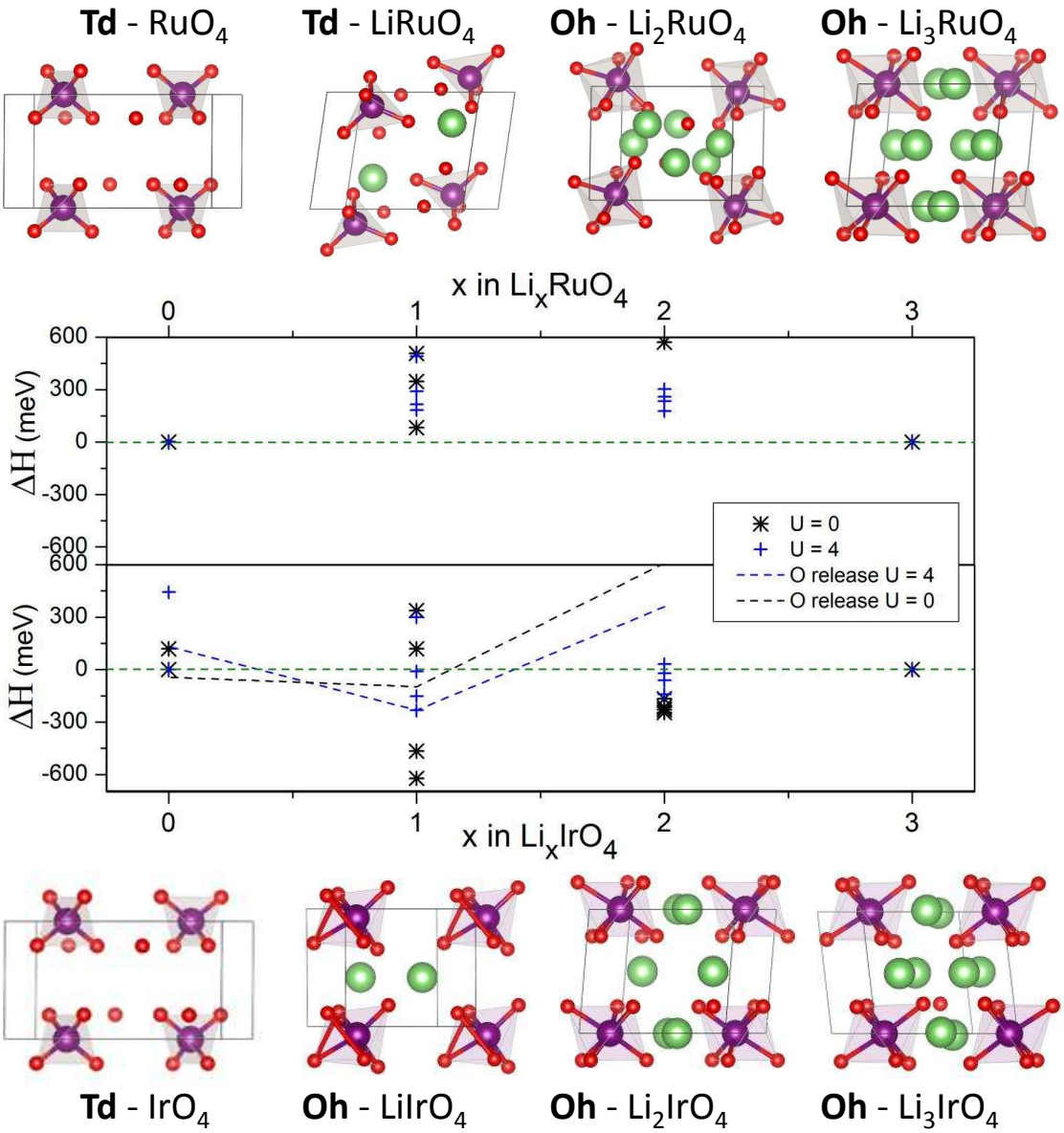

Figure II-34: Most stable crystallographic structures and convex hull for Li_xRuO_4 (top) and Li_xIrO_4 (bottom). DFT+U phase stability diagram computed at different U values (in eV) as a function of the lithium content x. Symbols represent the formation energy of Li_xMO_4 (M = Ru, Ir) compared to the reference energy of the direct $Li_3MO_4 \rightarrow MO_4 + 3$ Li transformation, taken as the reference energy (horizontal plain line). Negative values of ΔH show that a single phase with intermediate Li compositions can be achieved electrochemically, which is the case in Li_xIrO_4. Most stable relaxed structures for each delithiation stage are represented on the top/bottom of the diagram with the M coordination, either octahedral (Oh) or tetrahedral (Td). Reaction enthalpies for O_2 gas release show that all Li_xRuO_4 compositions are stable versus decomposition (not shown here) while Li_xIrO_4 are prone to decomposition in $Li_xIrO_3 + ½ O_2$ (dashed lines) at low Li content.

II.3.e Partial conclusions

In the first part, we show that Li can be intercalated into $Li_3Ru_yNb_{1-y}O_4$ for y = 1, 0.75, 0.5 and 0.25, with minor structural changes, i.e. gliding of layers or unit cell distortion, while the charge compensation mechanism enlists the reduction of $Ru^{5+} \rightarrow Ru^{3+}$.

In a second part, we unveiled the participation of oxygen in the charge compensation mechanism of Li_3RuO_4 via complementary XAS and XPS measurements, summarized in Figure II-35. Moreover, we show that anionic redox is limited by cationic redox, through the formation of high Ru oxidation state species namely RuO_4/RuO_4^- having Ru 8+ and 7+, respectively, which dissolve into the electrolyte leading to irreversible electrochemical properties. Similar behavior is observed in $Li_3Ru_yNb_{1-y}O_4$ showing that both the structure and the Nb doping are ineffective to stabilize the cathode material upon oxidation. Interestingly, Ru dissolution can be inhibited as soon as Ir is added to the composition, as exemplified in $Li_3Ru_yIr_{1-y}O_4$ compounds. However, it leads to a drastic increase of gas evolution due to the oxidative decomposition of an intermediate Li-poor phase. Overall, the capacity of anionic redox is limited to the exchange of $2e^-$ in Li_3IrO_4, by the destabilization of the oxidized oxygen species leading to O_2 release, and $1e^-$ in Li_3RuO_4, prior the emergence of Ru dissolution caused by cationic oxidation. Interestingly, the existence of Na_2RuO_4 (Ru^{6+}) shows high oxidation state of Ru can be stabilized in solid state,[113] hence our interest to study the electrochemical performances of Na_3RuO_4.

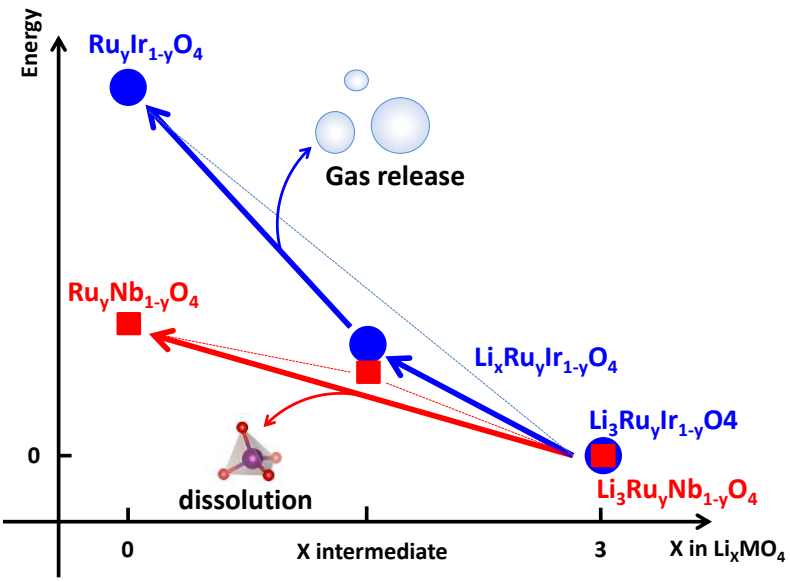

Figure II-35: Scheme explaining the impact of the stability of the MO_4 end member with respect to the formation of intermediates and O_2 gas release.

II.4 Influence of the alkali atom on the anionic redox: the study of Na_3RuO_4

Na-ion batteries could also benefit from the oxygen redox activity; however, research in this direction is still in its early stage. It is parted between two types of compounds i) Na-rich model compounds such as Na_2RuO_3[114,115] or Na_2IrO_3[116] and ii) Na deficient compounds such as P2-type $Na_{2/3}[Mg_x(Zn_x)Mn_{1-x}]O_2$ [117,118]. Concerning the Na-rich compounds, recent studies have shown that Na_2RuO_3 behaves differently than Li_2RuO_3 in terms of structure and electrochemical properties, while both show anionic activity.[115] This highlights that all our learning about anionic redox activity in Li-based compounds cannot blindly be extrapolated to Na ones, thus, the importance of carrying comparative studies. Along that line, we studied the electrochemical properties of Na_3RuO_4 in order to i) get insights on the different charge compensation mechanism triggered by the use of Na rather than Li, and ii) assess the limit of stability of Na-rich materials during oxidation.

This study has been done in collaboration with Misae Otoyama, a PhD student from the graduate school of Engineering of Osaka, while she was visiting the lab during 6 month.

II.4.a Synthesis and crystal structure of Na_3RuO_4 and Na_2RuO_4

Na_3RuO_4 was prepared by classical solid state synthesis. More specifically, pure Na_3RuO_4 phase was obtained by heating RuO_2 (Alfa Aesar, 99.9%) with 10% excess NaOH (Alfa Aesar, 98%) at 750°C in air for 40 hours and then at 540°C under flowing O_2 for 8 hours. These conditions differ from those reported in the literature (500°C under O_2 during 18 h followed by 650°C under N_2 during 18 h)[119] that we found to give samples having always Na_2RuO_3 as second phase. The structure of Na_3RuO_4 was characterized using Rietveld refinement of SXRD pattern, which were measured on the 11-BM beamline at APS (Figure II-36a and Table II-14). The refinement was performed with the structural model reported by Regan et al.[119] Na_3RuO_4 crystalizes in C 2/m space group with cell parameters a = 11.022(63) Å, b = 12.796(58) Å, c = 5.7009(4) Å and β = 109.919(22)°. Its structure can be described as a layered structure with alternated NaO_6 and $Na_{0.5}Ru_{0.5}O_6$ layers with the Ru framework forming isolated tetramers of edge sharing RuO_6 octahedra in the $Na_{0.5}Ru_{0.5}O_6$ layer (Figure II-36a).

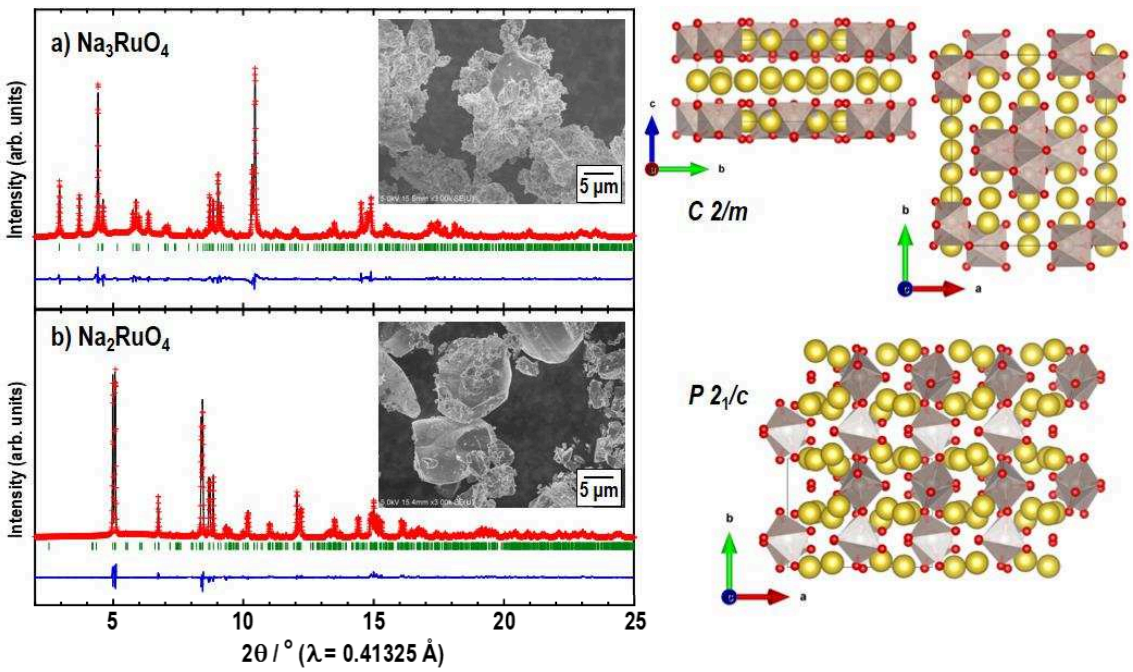

Figure II-36: Rietveld refinement of the SXRD patterns (λ = 0.41325 Å) for a) Na_3RuO_4 and b) Na_2RuO_4 together with SEM images. The structures of Na_3RuO_4 and Na_2RuO_4 are shown, top and bottom, respectively. Na, Ru and O are shown in yellow, gray and red, respectively.

Single phase Na_2RuO_4 was also prepared by placing a hand ground mixture of RuO_2 and 10% excess Na_2CO_3 (Sigma-Aldrich, anhydrous, 99.95-100.05%) in an alumina boat that was heated at 650°C for 20 hours under flowing O_2. Heating and cooling steps were done at a rate of 2°C/min. Rietveld refinement of the SXRD patterns using the previously reported structure gave good fit (Table II-15). [113,120] Na_2RuO_4 adopts a P 2_1/c space group with cell parameters a = 10.7107(7) Å, b = 7.0356(7) Å, c = 10.8735(4) Å and β = 119.181(37)°. Its crystal structure can be described has isolated chains of vertex sharing RuO_5 trigonal bipyramid running along the b-axis (Figure II-36b).

At this point, I want to emphasize that the structure of Na_3RuO_4, consisting in Ru plaquettes, is quite different from the one of Li_3RuO_4, having zig-zag chains of Ru. Moreover, Na_3NbO_4, with Nb^{5+} being d^0, is isostructural to Na_3RuO_4,[121] which implies that the competition between electrostatic interaction and SOJT detailed in Chapter II.2 is overruled by the presence of Na. These observations further show the large influence of the alkali atom on the crystal chemistry and the delicate balance ruling the crystal structure of this type of compounds.

Na_3RuO_4 - $R_{Bragg\ SXRD}$ = 5.17%						
C 2/m	a = 11.02263(13) Å c = 5.70094(7) Å	b = 12.79658(15) Å β = 109.9192(7)°		Z = 8	V/Z = 94.505 Å^3	
Atom	Wyckoff position	x	y	z	B_{iso} (Å²)	occupancy
O1	4i	0.1146(13)	0	0.209(3)	0.63(8)	1
O2	8j	0.1012(8)	0.2307(7)	0.2202(16)	0.63(8)	1
O3	4i	0.1546(12)	1/2	0.186(2)	0.63(8)	1
O4	8j	0.0984(8)	0.1092(6)	0.8298(17)	0.63(8)	1
O5	8j	0.1455(9)	0.3878(6)	0.766(2)	0.63(8)	1
Na1/Ru1	4g	0	0.3781(5)	0	1.01(6)	0.85/0.15
Na2	4e	1/4	0.25000	0	1.01(6)	1
Na3	8j	0.2370(6)	0.1202(4)	0.5358(10)	1.01(6)	1
Na4	2c	0	0	1/2	1.01(6)	1
Na5	4h	0	0.2549(7)	1/2	1.01(6)	1
Na6	2d	0	1/2	1/2	1.01(6)	1
Ru7	4g	0	0.12791(18)	0	0.495(14)	1
Ru8/Na8	4i	0.2532(3)	0	0.0237(5)	0.495(14)	0.85/0.15

Table II-14: Crystallographic data for Na_3RuO_4.

II.4.b Electrochemical properties of Na_3RuO_4

The voltage-composition profile for a Na_3RuO_4/Na half-cell, shown in Figure II-37a, reveals the presence of a staircase-like trace on charge with the appearance of 3 plateaus at 3, 3.5 and 4.6 V that nearly correspond to removal of 1, 2 and 3 Na, respectively. A drastically different profile is observed on the following discharge with namely a sharp potential fall followed by an S-type curve centered around ~1 V while the amount of Na is nearly fully recovered on discharge. Moreover, cycling the cell over the full capacity leads to a rapid decay of the performances, which can be improved by limiting the state-of-charge (SOC) after the removal of 2 or 1 Na as presented in Figure II-37b-c-d.

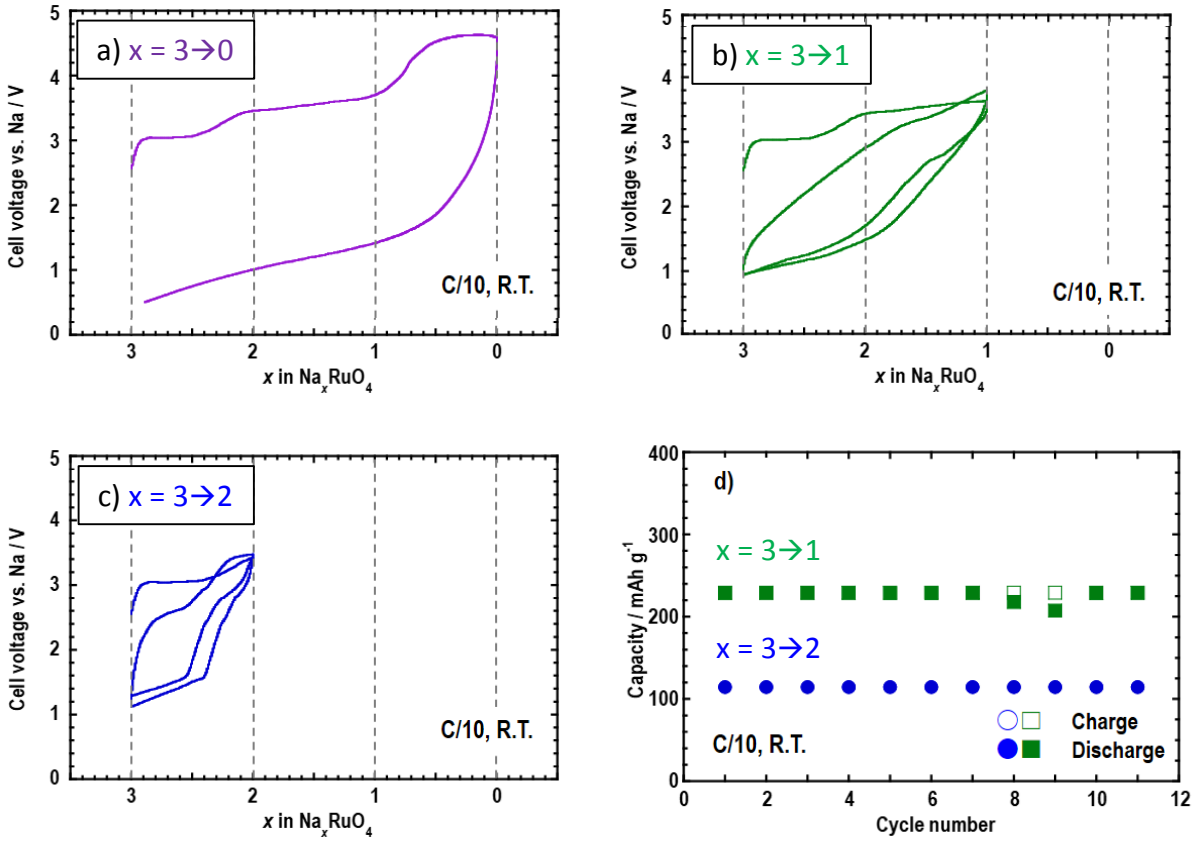

Figure II-37: The 1st and 2nd galvanostatic curves of Na cells with Na_3RuO_4 cycled between a) x = 3→0, b) 3→1 and c) 3→2. d) Cycle performance of the cells with x = 3→1 (green square) and x = 3→2 (blue circle) in Na_xRuO_4.

Na_3RuO_4 having a very different electrochemical signature compared to Li_3RuO_4, Operando XRD has been performed (Figure II-38a). Upon charge, there is initially the progressive disappearance of the Na_3RuO_4 peaks to the expense of new ones corresponding to a new phase that becomes the main phase after removal of 1 Na. This new phase, having a similar XRD pattern than Na_2RuO_4 made by solid state method, is denoted hereafter EX-Na_2RuO_4 (EX stands for electrochemically made). Further oxidation leads to a solid solution process between x = 2 and x = 1 in Na_xRuO_4, as deduced from the progressive shift of the Bragg reflections. The compound obtained after the release of 2 Na is called hereafter EX-$NaRuO_4$. Finally, the removal of the last Na leads to an amorphous material whose crystallinity is not regained during the subsequent discharge. To solve the structure of EX-Na_2RuO_4 and EX-$NaRuO_4$, ex situ SXRD patterns were collected and are presented in Figure II-38b-c together with the results of the Rietveld refinements. EX-Na_2RuO_4 is similar to Na_2RuO_4 synthetized by solid state method with however slightly larger cell parameters leading to a larger unit cell volume 89.84 $Å^3$ vs. 89.39 $Å^3$ (Table II-15), and broader peaks suggesting the presence of microstrain or small crystallite size due to electrochemical grinding (inset Figure II-38b). Concerning EX-$NaRuO_4$, it is likely formed through a topotactic Na removal from EX-Na_2RuO_4 as revealed by the solid solution mechanism observed in the operando XRD. Therefore, its SXRD pattern was refined using the structural model of Na_2RuO_4 with larger a and c parameters, a = 11.019(4) Å, and c = 11.077(3) Å compared to a = 10.7107(7) Å and c = 10.8735(4) Å and smaller b parameter, b = 6.7911(11) Å compared to b = 7.0356(7) Å while the β angle remains similar. Despite the broadness of the peaks pertaining to EX-$NaRuO_4$ together with minute traces of an impurity phase, the proposed model gives a decent fit without refining any atomic positions suggesting the Ru framework is conserved during Na removal. Concerning the Na occupancy, we propose by simulating the XRD of different Na vacancy configuration that the Na2 and Na3 site in Na_2RuO_4 are empty in EX-$NaRuO_4$. The increase of a and c parameters in EX-$NaRuO_4$ is attributed to the increase of the electrostatic interactions between the RuO_5 chains unscreened by Na removal. Note that the contraction of the b parameter causes the shortening of the Ru – Ru distances, as it will be discussed later.

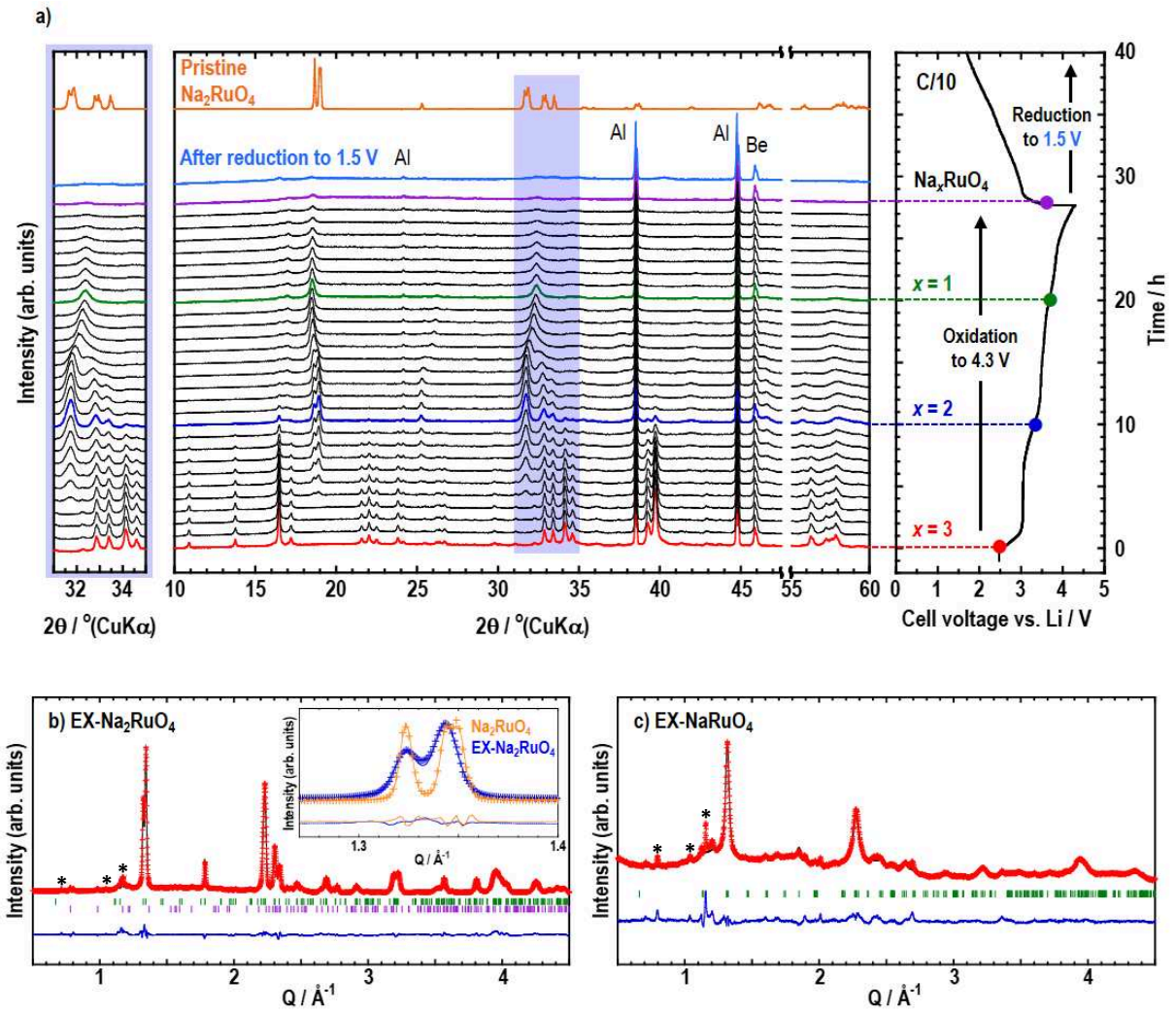

Figure II-38: a) Operando XRD patterns during the oxidation and reduction of Na_3RuO_4 and the corresponding charge-discharge curve. The XRD patterns were collected every one hour. The left part shows the enlarged XRD patterns of the 31~35° region highlighted in blue. An XRD pattern of pristine Na_2RuO_4 synthesized by solid state method is shown in orange at the top of figure a) as a reference. Rietveld refinement of the SXRD patterns of b) EX-Na_2RuO_4 and c) EX-$NaRuO_4$. Second phase in b) is Na_3RuO_4 present in very small amount. The red crosses, black continuous line and bottom blue line represent the observed, calculated, and difference patterns, respectively. Vertical green and purple tick bars are the Bragg positions. The inset figure b) shows enlarged synchrotron XRD patterns of Na_2RuO_4 and EX-Na_2RuO_4. The impurity peaks in EX-Na_2RuO_4 and EX-$NaRuO_4$ are highlighted with asterisks.

Na_2RuO_4 $R_{bragg\ SXRD}$ = 5.25% **(prepared by solid state synthesis)** **EX-Na_2RuO_4** – $R_{bragg\ SXRD}$ = 9.04% **EX-NaRuO4** – $R_{bragg\ SXRD}$ = 22.7%			
P 2_1/c	a = 10.71077(6) Å c = 10.87354(6) Å	b = 7.03567(4) Å β = 119.1813(3)°	V/Z = 89.425 Å^3
P 2_1/c	a = 10.748(8) Å c = 10.907(6) Å	b = 7.045(3) Å β = 119.48(6)°	V/Z = 89.84 Å^3
P 2_1/c	a = 11.019(4) Å c = 11.077(3) Å	b = 6.7911(11) Å β = 120.5(2)°	V/Z = 89.25 Å^3

Atom	Wyckoff position	x	y	z	B_{iso}(Å^2)	Occupancy
O1	4e	0.1629(18)	0.166(3)	0.3856(19)	1.49(7)	1
		0.1629	0.166	0.3856	1.49	1
		0.1629	0.166	0.3856	1.49	1
O2	4e	0.4855(17)	0.638(2)	0.3901(17)	1.49(7)	1
		0.4855	0.638	0.3901	1.49	1
		0.4855	0.638	0.3901	1.49	1
O3	4e	0.3229(18)	0.2431(19)	0.2355(15)	1.49(7)	1
		0.3229	0.2431	0.2355	1.49	1
		0.3229	0.2431	0.2355	1.49	1
O4	4e	0.0088(16)	0.309(2)	0.0856(16)	1.49(7)	1
		0.0088	0.309	0.0856	1.49	1
		0.0088	0.309	0.0856	1.49	1
O5	4e	0.1643(17)	0.7285(19)	0.2412(17)	1.49(7)	1
		0.1643	0.7285	0.2412	1.49	1
		0.1643	0.7285	0.2412	1.49	1
O6	4e	0.3451(17)	0.669(3)	0.5975(18)	1.49(7)	1
		0.3451	0.669	0.5975	1.49	1
		0.3451	0.669	0.5975	1.49	1
O7	4e	0.4777(14)	0.013(3)	0.6562(17)	1.49(7)	1
		0.4777	0.013	0.6562	1.49	1
		0.4777	0.013	0.6562	1.49	1
O8	4e	0.0517(15)	0.490(2)	0.3452(17)	1.49(7)	1

		0.0517	0.490	0.3452	1.49	1
		0.0517	0.490	0.3452	1.49	1
		0.3098(15)	0.4599(16)	0.4126(18)	3.14(8)	1
Na1	4e	0.3098	0.4599	0.4126	3.14	1
		0.3098	0.4599	0.4126	3.14	1
		0.3549(14)	0.5634(16)	0.9093(16)	3.14(8)	1
Na2	4e	0.3549	0.5634	0.9093	3.14	1
		0.3549	0.5634	0.9093	3.14	**0**
		0.1953(15)	0.509(2)	0.0932(17)	3.14(8)	1
Na3	4e	0.1953	0.509	0.0932	3.14	1
		0.1953	0.509	0.0932	3.14	**0**
		0.1528(14)	0.002(2)	0.0920(15)	3.14(8)	1
Na4	4e	0.1528	0.002	0.0920	3.14	1
		0.1528	0.002	0.0920	3.14	1
		0.5005(4)	0.2450(4)	0.2519(4)	0.416(7)	1
Ru1	4e	0.5032(9)	0.2562(14)	0.2522(11)	0.416	1
		0.5032	0.2562	0.2522	0.416	1
		0.0002(4)	0.2350(3)	0.2488(4)	0.416(7)	1
Ru2	4e	-0.0013(9)	0.2451(7)	0.2565(9)	0.416	1
		-0.0013	0.2451	0.2565	0.416	1

Table II-15: Crystallographic data for Na_2RuO_4 (prepared by solid state method), EX-Na_2RuO_4 and EX-$NaRuO_4$. All positions and B_{iso} factors were refined for Na_2RuO_4. For EX-Na_2RuO_4 all positions and B_{iso} were taken equal to Na_2RuO_4 except for the Ru positions which were refined freely. For EX-$NaRuO_4$, all positions and B_{iso} were taken equal as in EX-Na_2RuO_4.

To grasp a better insight into the charge compensation mechanism for Na_3RuO_4, ex situ Ru K-edge XAS was performed on the ROCK beamline of Soleil synchrotron. The samples were prepared at different state-of-charge, namely, after the removal of 0, 1, 2 and 3 Na, identified as Na_3RuO_4, EX-Na_2RuO_4, EX-$NaRuO_4$ and "RuO_4", respectively. For sake of completion, the sample obtained at the end of subsequent discharge till 1.2 V was also studied. XANES spectra and EXAFS results of the Ru K-edge are presented in Figure II-39a-b and Figure II-39c-d-e-f-g, respectively. Ruthenium has a 5+ oxidation state in pristine Na_3RuO_4. Upon oxidation (Figure II-39a), there is first a shift of the edge position towards higher energy which after the removal of the first Na neatly superimposes with the one of Na_2RuO_4 and K_2RuO_4, hence implying the presence of Ru^{6+}.[122] Moreover, the pre-edge features of EX-Na_2RuO_4 and Na_2RuO_4 are very similar indicating similar Ru environment. The removal of additional Na from EX-Na_2RuO_4 to EX-$NaRuO_4$ does not produce noticeable changes on the edge position (Figure II-39b), while it is shifting towards lower energy upon further oxidation, implying Ru oxidation state (+6) stays constant between x = 2 and x = 1 and reduces to 5+ from x = 1 to x = 0. Lastly, the Ru K-edge position shifts to very low energy for the fully discharged sample implying its reduction to Ru^{3+}, as deduced using energy/oxidation state calibration in II.3.b.iv, and showing the irreversibility of the charge compensation mechanism.

As an attempt to access the Ru – O and Ru – Ru distances, we analyzed the EXAFS region of the spectra. The obtained distances are reported in Figure II-39c and Table II-16. For Na_3RuO_4, they are found to match perfectly with those of the reported crystal structure. For both Na_2RuO_4 and EX-Na_2RuO_4, the same environment is found, composed of 3 short and 2 long Ru – O distances and 2 Ru – Ru distances of 1.778 Å, 1.983 Å, and 3.512 Å, respectively. In contrast, the Debye Waller factors for EX-Na_2RuO_4 are greater than for Na_2RuO_4 suggesting the latter to be more crystallized, in perfect agreement with the SXRD data. For EX-$NaRuO_4$, 2 short, 2 medium and 1 long Ru – O distances are found with 1.753, 1.920 and 2.072 Å bond lengths, respectively, confirming Ru keeps a five-fold coordination. Two different Ru – Ru distances are found at 3.013 Å and 3.139 Å, making an average Ru – Ru distance of 3.076 Å which is substantially smaller than in Na_2RuO_4 (3.506 Å). Such a shortening was observed in SXRD by the decrease of the b axis. Lastly, it is worth mentioning that EXAFS analysis wasn't performed on the "RuO_4" or on the discharge samples due to the weak signal/noise ratio.

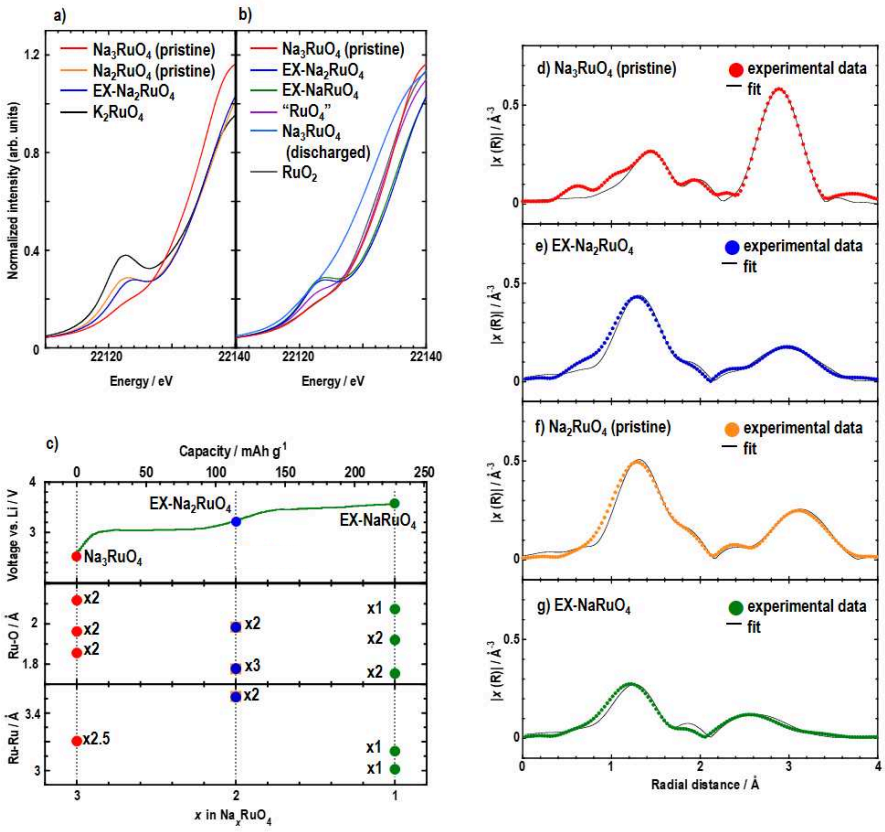

Figure II-39: a) and b) Ru K-edge XANES spectra of Na_3RuO_4, Na_2RuO_4, EX-Na_2RuO_4, EX-$NaRuO_4$, "RuO_4" and discharged Na_3RuO_4 (removed 3 Na then discharged to 1.2 V). Ru K-edge XANES spectra of K_2RuO_4 and RuO_2 are shown in a) and b), respectively as references.[122] c) Ru-O and Ru-Ru distances and coordination numbers in Na_3RuO_4, Na_2RuO_4, EX-Na_2RuO_4 and EX-$NaRuO_4$ obtained from EXAFS analysis. Galvanostatic curve of Na_3RuO_4 is shown on top. Magnitude of the Fourier transforms of the k^2-weighted EXAFS oscillations with their fit, dot and plain lines, respectively for d) Na_3RuO_4, e) EX-Na_2RuO_4, f) Na_2RuO_4 and g) EX-$NaRuO_4$.

	Ru K-edge E0 = -8													
	Ru - O shell								Ru - Ru shell					
	CN	d	CN	d	CN	d	Av. d	$\sigma*10^3$	CN	d	CN	d	$\sigma*10^3$	$R*10^3$
Na_3RuO_4	2	1.855(5)	2	1.962(6)	2	2.117(5)	1.978	3.2	2.5	3.209(5)			4.4	9
Na_2RuO_4	3	1.776(2)	2	1.984(3)			1.859	1.7	2	3.516(8)			4.3	5
EX-Na_2RuO_4	3	1.778(7)	2	1.983(6)			1.859	3.3	2	3.511(4)			8.2	7
EX-$NaRuO_4$	1	1.74(2)	2	1.78(2)	2	1.96(2)	1.84	4.3	1	3.01(2)	1	3.12(3)	5.6	29

Table II-16: Structural parameters obtained by fitting the EXAFS oscillations. CN, d, Av. d, σ stand for Coordination Number, distance in Å, Average distance in Å, and the Debye-Waller factor in Å². The difference energy threshold, E0, and the amplitude reduction factor (S_0^2) are fixed during fit. S_0^2 was taken equal to 1 for all analysis.

Having shown the irreversible nature of the redox process, especially at high SOC (Figure II-37), and bearing in mind the case of Li_3RuO_4, we have performed operando UV-visible measurements to assess possible Ru dissolution (Figure II-40). During the removal of the first Na, the UV-visible spectra show nearly no change, but upon further oxidation there is an increase of the background together the appearance of an absorbance at low wavelength (~200 nm). This feature, whose intensity varies roughly in $1/\lambda^4$ has been previously ascribed, in II.3.b.ii, to the formation of particles in the solution, which can be visually seen in the UV-visible cell. Lastly, towards the end of charge, new features at 310 nm and 380 nm appear in the UV-visible spectra. They are indicative of the presence of RuO_4/RuO_4^-, both species having the same absorption wavelengths [106]. Turning back to the observed particles, we have previously shown that the reaction of RuO_4/RuO_4^- with the electrolyte could lead to the formation of precipitate together with gas release.

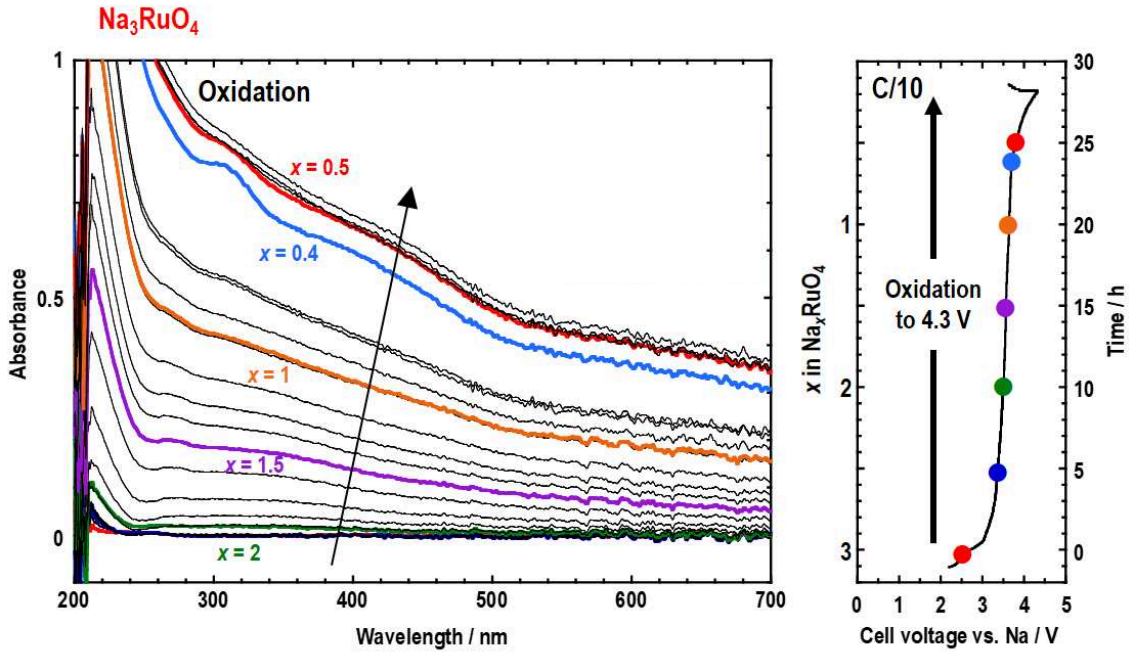

Figure II-40: Operando UV-visible spectra of Na_3RuO_4 during the oxidation and the corresponding charge curve. Note that the charge doesn't show exactly the same profile as in a standard electrochemical cell. We attribute this difference to the absence of pressure applied on the electrode in the UV-visible cell. The UV-visible spectra were collected every one hour

To confirm the occurrence of this mechanism, we have performed gas pressure measurements during the oxidation/reduction of Na_3RuO_4 (Figure II-41). We found that the gas pressure increases from 3.5 V (e.g. removal of 1.2 Na) until the end of charge and remains constant during the following discharge. By reconciling the UV-visible spectroscopy and gas pressure

analysis results, we propose that the dissolution of Ru under the form of RuO_4/RuO_4^- starts at x = 2 with the rate of dissolution being lower than the RuO_4/RuO_4^- reaction rate, explaining the absence of the 310 and 380 nm feature but the presence of the particle between x = 2 and x = 1. When oxidation is pushed further x = 1, the rate of dissolution increases leading to the appearance of the RuO_4/RuO_4^- spectra, hence explaining part of our capacity fade.

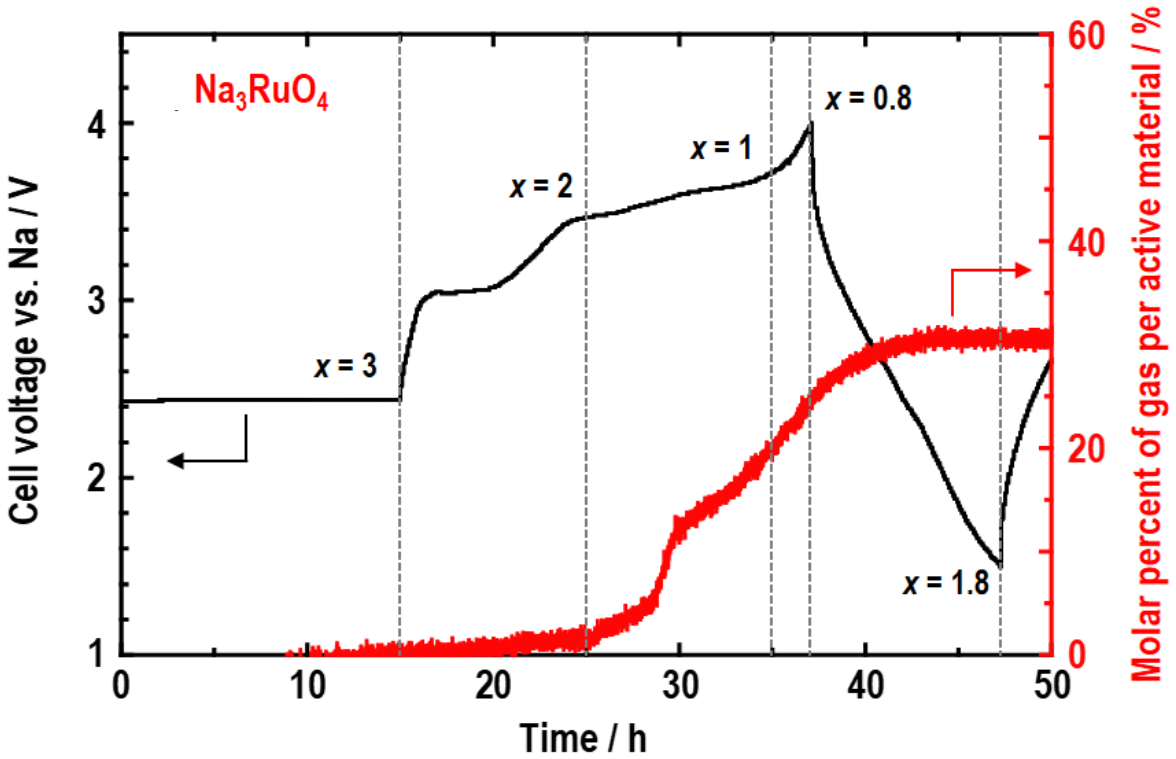

Figure II-41: Gas pressure measurement of the cell using pristine Na_3RuO_4 operated at C/10. 15 hours OCV period was performed before starting charge. Black curve is a charge-discharge curve. Red curve is molar ratio gas per active material.

Altogether, operando UV-visible and ex situ XAS showed that the removal of Na from Na_3RuO_4 initially enlists the oxidation of Ru^{5+} to Ru^{6+}. Further oxidation causes structural evolution proving Na is being removed from the material but without Ru oxidation, hence indirectly suggesting the participation of the anionic redox. This process comes concomitantly with a partial dissolution of the active material via the formation of RuO_4/RuO_4^- species leading to the appearance of particles and gas. Towards the very end of the charge a reduction of Ru back to 5+ is observed, indicative of the degradation of the material. Whatever, the complexity of the oxidation mechanism beyond the removal of one Na, this study unambiguously reveals the possibility of reaching Ru^{6+} in Na_2RuO_4 while $Ru^{5.4+}$ cannot be out

passed upon oxidation of Li_3RuO_4. At this stage, a legitimate question regards why Li_2RuO_4 with a similar structure and Ru oxidation state as in Na_2RuO_4 could not be formed during the electrochemical oxidation of Li_3RuO_4? To answer this question, we have synthetized Li_2RuO_4 by ion exchange from Na_2RuO_4, called hereafter IE-Li_2RuO_4 (Figure II-42), and tried to assess its stability. It will be followed by the investigation of the electrochemical properties of Na_2RuO_4, bearing in mind its slight difference, with EX-Na_2RuO_4, in terms of microstructure.

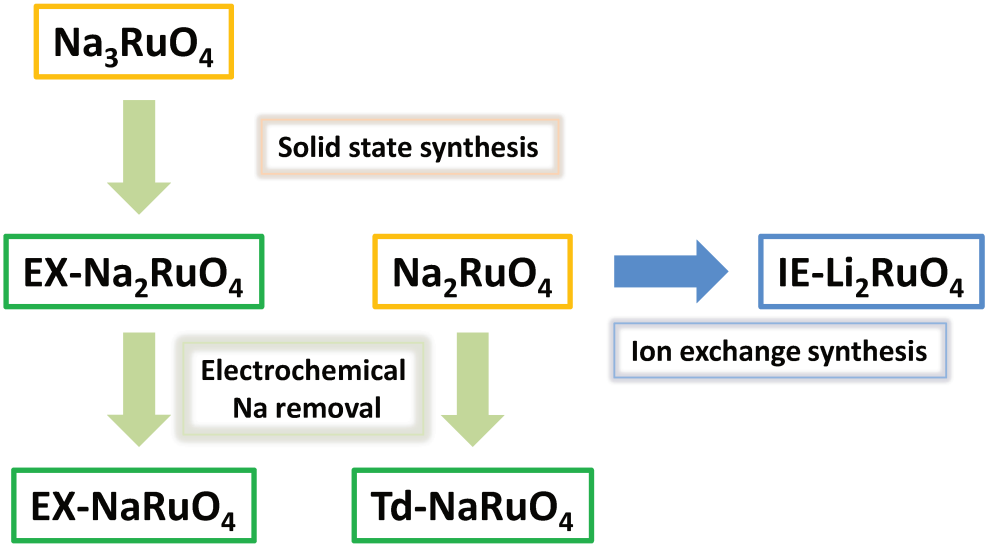

Figure II-42: Schematics summarizing the investigated compounds and their synthesis.

II.4.c Synthesis, structural characterization and stability of IE-Li_2RuO_4

Successful ion exchange was performed via solvent based method consisting in adding LiCl (Alfa Aesar, anhydrous, 98+%) and Na_2RuO_4, in a 1 : 6 molar ratio, to an acetonitrile solution (ACROS Organics, 99.9%) that was stirred at 70°C on a hotplate. After six days of reaction, centrifugation of the solution and repeated washings with dimethyl sulfoxide and acetonitrile to remove the NaCl and residuals of LiCl, respectively, IE-Li_2RuO_4 is produced as deduced from EDX and ICP analysis (Figure II-43b). It is worth mentioning that acetonitrile is a solvent of choice for this experiment, because it maintains the reaction temperature below its ebullition T_{eb}~80°C and moreover solubilizes very well LiCl (1.10 mg/mL) but not NaCl (0.00197 mg/mL),[123] hence driving the chemical equilibrium towards the Na to Li ion exchange. Regarding the structure of IE-Li_2RuO_4, a decent fit of the SXRD pattern was obtained via Rietveld refinement using a structural model similar to Na_2RuO_4 (Figure II-43a and Table II-17), i.e. space group P $2_1/c$, with smaller cell parameters a = 9.938(8) Å, b =

6.888(7) Å, c = 9.982(9) Å and β = 120.281(16)° giving a reduced volume per unit formula for IE-Li_2RuO_4, 74.39 Å, compared to Na_2RuO_4, 89.39 Å. This results show ion exchange follows a topotactic reaction, however due to the poor crystallinity only Ru position were refined. In order to increase the crystallinity of the obtained IE-Li_2RuO_4, heat treatments were performed but all trials resulted in the decomposition of the phase. This was confirmed by DSC experiment revealing features as low as 110°C (Figure II-43c).

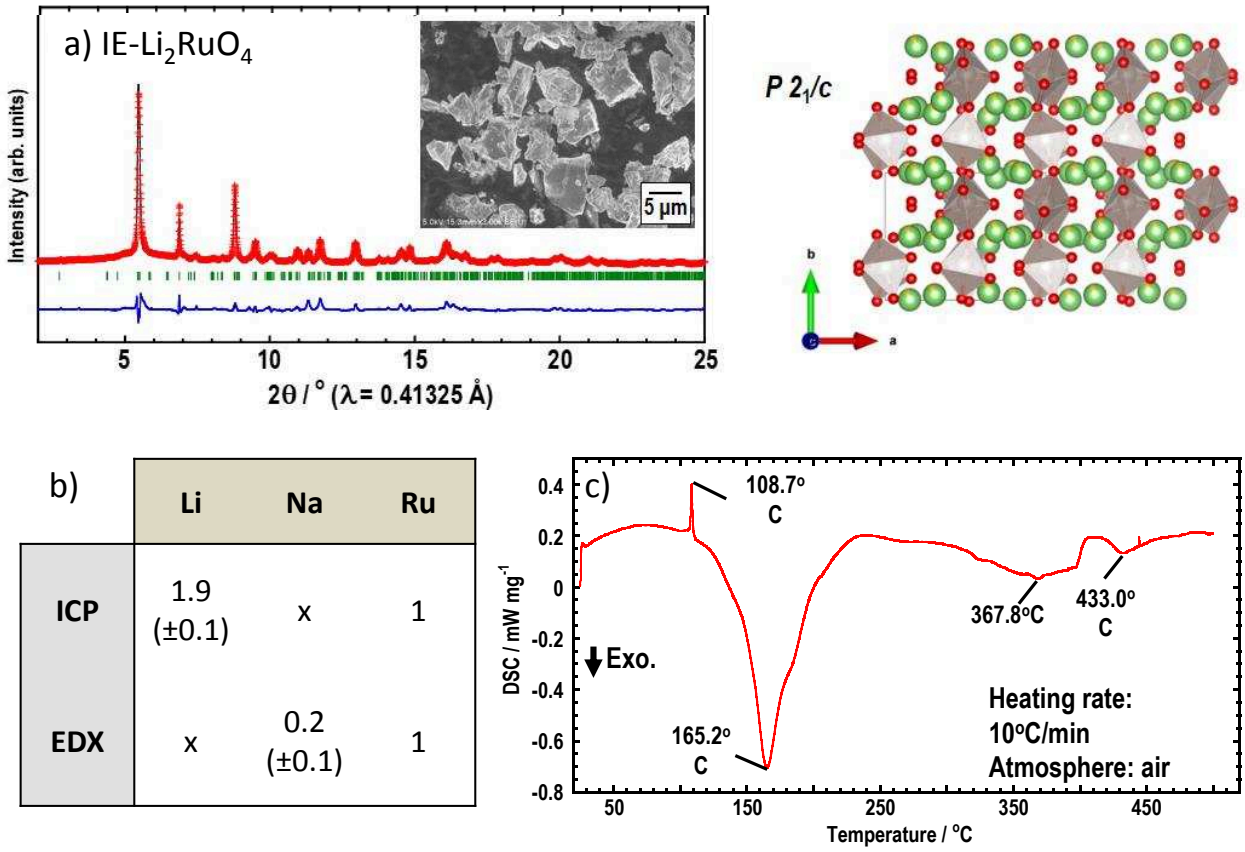

b)

	Li	Na	Ru
ICP	1.9 (±0.1)	x	1
EDX	x	0.2 (±0.1)	1

Figure II-43: a) Rietveld refinement of the SXRD pattern (λ = 0.41325 Å) with SEM image and structure of IE-Li_2RuO_4. b) Table showing the elemental analysis performed on IE-Li_2RuO_4. Traces of remaining Na were found by EDX. Note that Na quantification was not performed by ICP due to the utilization of NaOCl in the dissolution process. c) DSC of IE-Li_2RuO_4 under air.

IE-Li_2RuO_4 - $R_{bragg\ SXRD}$ = 18.5%						
P 2_1/c	a = 9.938(8) Å c = 9.982(9) Å		b = 6.888(7) Å β = 119.45(5)°			V/Z = 74.39 Å^3
Atom	Wyckoff position	x	y	z	B_{iso}(Å^2)	Occupancy
O1	4e	0.16269	0.16667	0.3851	1.591	1
O2	4e	0.48583	0.6379	0.39039	1.591	1
O3	4e	0.32270	0.24357	0.23524	1.591	1
O4	4e	0.00892	0.30828	0.08577	1.591	1
O5	4e	0.16404	0.72809	0.24100	1.591	1
O6	4e	0.34487	0.66910	0.59708	1.591	1
O7	4e	0.47751	0.01151	0.65630	1.591	1
O8	4e	0.05139	0.48941	0.34525	1.591	1
Li1/Na1	4e	0.30790	0.45999	0.41234	2.121	0.9/0.1
Li2/Na2	4e	0.35507	0.56367	0.90861	2.121	0.9/0.1
Li3/Na3	4e	0.19344	0.50972	0.09307	2.121	0.9/0.1
Li4/Na4	4e	0.15263	0.00207	0.09179	2.121	0.9/0.1
Ru1	4e	0.492(2)	0.2303(16)	0.247(2)	1.734	1
Ru2	4e	0.001(2)	0.241(3)	0.251(2)	1.734	1

Table II-17: Crystallographic data for IE-Li_2RuO_4. Note that $Li_{1.8}Na_{0.2}RuO_4$ composition was considered for the Rietveld analysis in agreement with the elemental analysis.

To further grasp insights into the local structure and oxidation state of Ru in IE-Li_2RuO_4, we performed Ru K-edge measurements. Figure II-44a shows that the Ru K-edge position for IE-Li_2RuO_4 is between Na_2RuO_4 and Na_3RuO_4, and nearly at the same position as $Li_{0.3}RuO_4$ (cf. II.3.b.iv) proving Ru oxidation state is 5.4+ in IE-Li_2RuO_4. The reduction of Ru during ion exchange from Na to Li implies that an internal redox occurred, likely resulting in the oxidation of the oxygen centers as in $Li_{0.3}RuO_4$. From the analysis of the EXAFS spectra for IE-Li_2RuO_4 (Figure II-44b-c Table II-18), we could deduce that Ru is six fold coordinated, rather than fivefold as in Na_2RuO_4, with 2 short, 2 medium and 2 long Ru – O distances of 1.782, 1.928 and 2.030 Å, respectively. The change from five to six-fold coordination is in agreement with diminution of the pre-edge intensity in going from Na_2RuO_4 to IE-Li_2RuO_4.

Moreover, from EXAFS analysis of the Ru – Ru distances we identified the presence of three different distances of 3.06, 3.44 and 3.75 Å with coordination numbers of 0.6, 0.8 and 0.6, respectively. Notice that Ru – Ru distances of 3 and 3.7 Å are typical for edge sharing and vertex sharing RuO_6 octahedra, hence comforting our local structural assignments.

Gathering SXRD and XAS analysis, we propose the structure of Li_2RuO_4 to be composed of chains of RuO_6 having an average Ru-Ru distance of 3.4 Å with the presence of Ru dimers leading the formation of the short and long Ru-Ru distance of 3 Å and 3.7 Å, respectively. All our attempts to spot the dimerization on the SXRD pattern failed, suggesting their random distribution along the chains. Note that no reliable information on the oxygen positions can be extracted from diffraction due to their weak participation in the SXRD pattern (z_{Ru} = 44 and z_o = 8) and the broadness of the Bragg reflections.

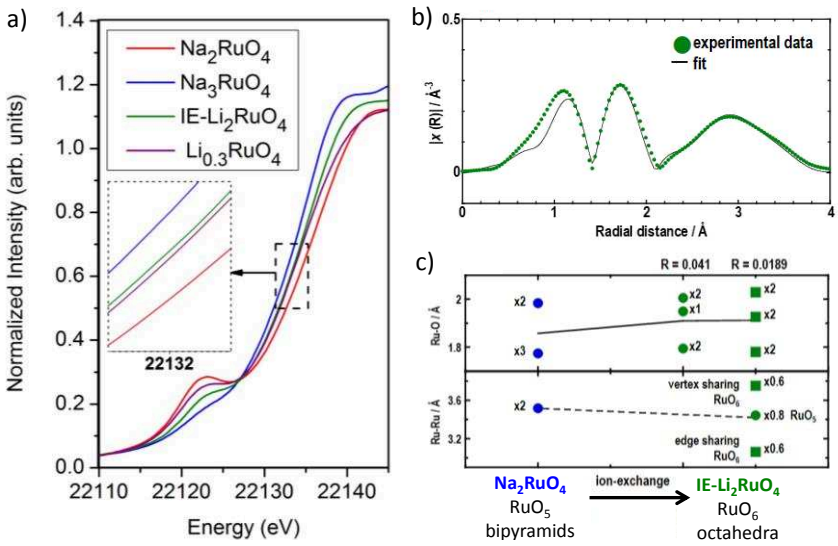

Figure II-44: a) Ru K-edge XANES spectra of Na_3RuO_4, IE-Li_2RuO_4, Na_2RuO_4 and $Li_{0.3}RuO_4$ (cf II.3.b.iv). b) Magnitude of the Fourier transforms of the k^2-weighted EXAFS oscillations of the IE-Li_2RuO_4 spectra with their fit, dot and plain lines, respectively. c) Ru-O and Ru-Ru distances and coordination numbers of Na_2RuO_4 and IE-Li_2RuO_4 obtained from EXAFS analysis. Black solid and broken lines show average Ru-O and Ru-Ru distances, respectively.

Li_2RuO_4 - EXAFS - Ru K-edge E0 = -8							
Ru - O shell							
CN	d_{Ru-O}	CN	d_{Ru-O}	CN	d_{Ru-O}	Av. d	$\sigma*10^3$
2	1.781(4)	2	1.937(6)	2	2.030(5)	1.91	1.6
Ru - Ru shell							
CN	d_{Ru-Ru}	CN	d_{Ru-Ru}	CN	d_{Ru-Ru}	$\sigma*10^3$	$R*10^3$
0.6	3.06(2)	0.8	3.44(2)	0.6	3.75(3)	5.1	13

Table II-18: Structural parameters obtained by fitting the EXAFS oscillations. CN, d, Av. d, σ stand for Coordination Number, distance in Å, Average distance in Å, and the Debye-Waller factor in Å². The difference

energy threshold, E0, and the amplitude reduction factor (S_0^2) are fixed during fit. S_0^2 was taken equal to 1 for all analysis.

In spite of these structural insights, the origin of the difference in the low structural stability of IE-Li_2RuO_4 with respect to Na_2RuO_4 and K_2RuO_4 that can be prepared by ceramic processes at T ≥ 650°C remains unclear. Bearing in mind that both Na and K phases contain Ru^{6+} which is 5-fold coordinated and 4-fold coordinated, respectively, while Ru of lower valence is 6-fold coordinated, we could deduce that the stability issue most likely originates from a complex balance between alkali size, coordination number and charge.

II.4.d Electrochemical synthesis of Td-$NaRuO_4$ during Na removal from Na_2RuO_4

For sake a completion, we compared the electrochemical performance of ceramic Na_2RuO_4 and electrochemically made EX-Na_2RuO_4 which are alike structural-wise. Surprisingly, their behavior drastically differs with the removal of 2 Na occuring via a single plateau for Na_2RuO_4 (Figure II-45a) as compared to two voltages plateau for EX-Na_2RuO_4 with the first one associated to the formation EX-$NaRuO_4$ (Figure II-45b). Tracking the structural changes during the removal of Na in Na_2RuO_4, Operando XRD, shown in Figure II-45c, reveals after removal of 0.5 Na, the appearance of extra peaks located at 18.6° and 28.4° which disappears upon oxidation leading to a featureless pattern. Decent Rietveld refinement of the extra peaks was obtained using the structural model of $KRuO_4$ (Figure II-45d), crystallizing in I 4_1/a space group, with Na replacing K and using smaller cell parameters (a = 5.2449(9) Å, c = 12.1160(4) Å compared to a = 5.6105(5) Å, c = 12.959(1) Å).[124] In light of the results of the refinement, this new phase, called hereafter Td-$NaRuO_4$, contains Ru and Na in tetrahedral and seven-fold coordinations, respectively. (Figure II-45e and Table II-19). Interestingly, the ruthenium oxidation state, in $KRuO_4$, was determined to be 7+ via magnetic mesurements. In the case of Td-$NaRuO_4$, due to its structural similarity with $KRuO_4$, we make the hypothesis that the ruthenium oxidation state is also 7+, however, XAS measurements should definitely be performed to confirm this assumption.

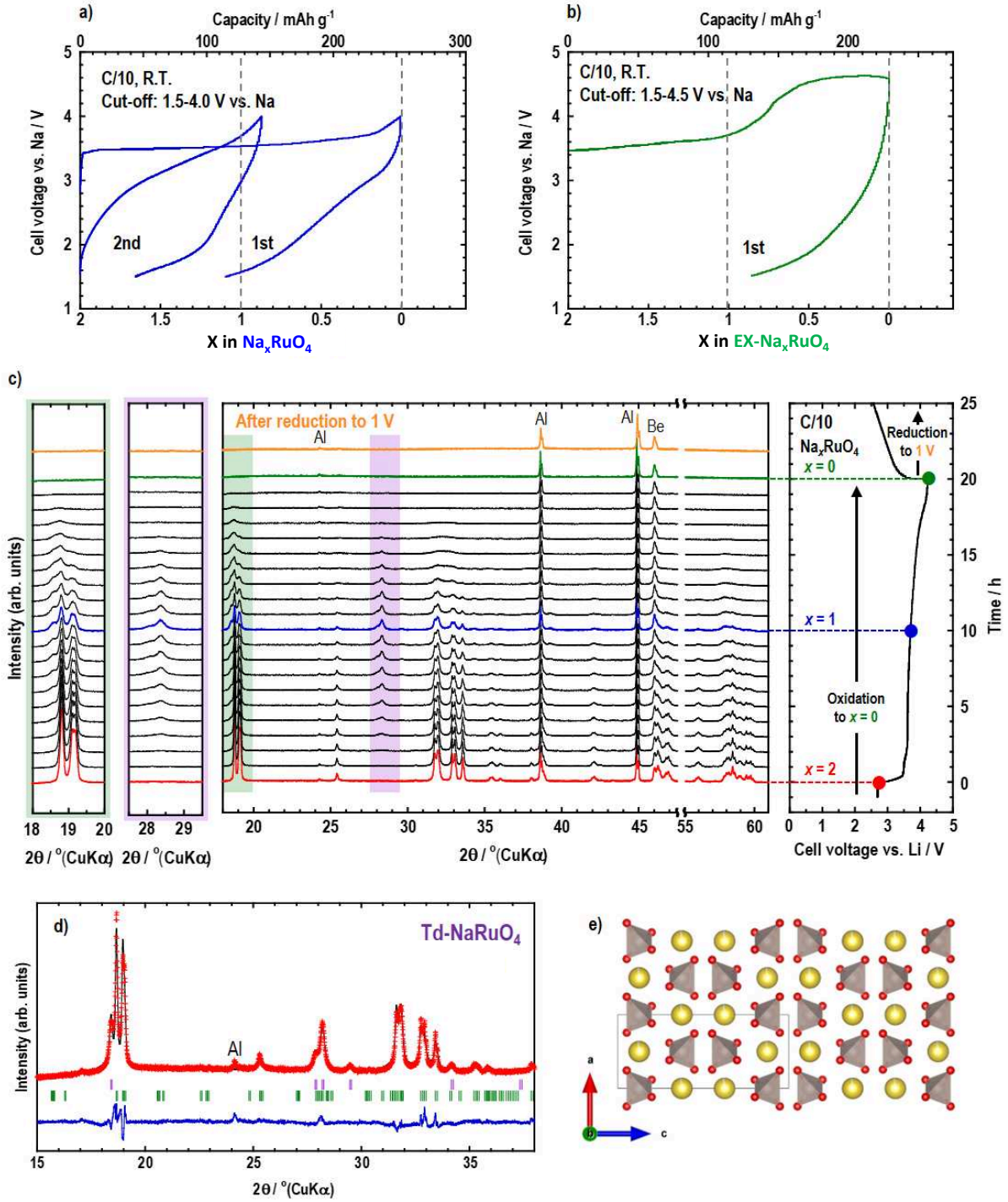

Figure II-45: Charge-discharge curves of the Na cells with a) Na_2RuO_4 and b) EX-Na_2RuO_4 operated at room temperature with C/10 rate. c) shows operando XRD patterns of Na_2RuO_4 during the oxidation and reduction processes and the corresponding charge-discharge curves. XRD patterns were collected every one hour. The left parts are enlarged XRD patterns of 18~20° and 27.5~29.5° regions highlighted in green and purple, respectively. d) Ex situ XRD pattern of the x = 1 compound in Na_xRuO_4. The red crosses, black continuous line and bottom blue line represent the observed, calculated, and difference patterns, respectively. Vertical green and purple tick bars are the Bragg positions for Td-$NaRuO_4$ and Na_2RuO_4, respectively. e) Structure of Td-$NaRuO_4$.

Td-NaRuO$_4$- R$_{bragg}$ = 8.83%						
I 4_1/a	a = 5.2449(9) Å		c = 12.1160(4) Å			V/Z = 83.33 Å^3
Atom	Wyckoff position	x	y	z	B_{iso}(Å^2)	Occupancy
O1	16f	0.117	0.006	0.198	1.000	1
Na1	4b	0	1/4	5/8	1.200	1
Ru1	4a	0	1/4	1/8	0.600	1

Table II-19: Crystallographic data for Td-NaRuO$_4$. B_{iso} and atomic positions were not refined.

Interestingly, we could never fully isolate Td-NaRuO$_4$ whose appearance upon Na removal was found to be postponed towards the end of charge with increasing the cycling rate and whose proportion decays over hours when the charging current is stopped. This suggests that its growth most likely enlists a dissolution-precipitation process with saturation concentration threshold that could explain its time and rate formation dependence. This solution path does not come as a total surprise since the only report on Td-NaRuO$_4$ synthesis mentions a solution of RuO$_4$ in which concentrated NaOH was added.[125] At this stage, in absence of structural differences between both phases, we believe that the different mechanistic of Na removal which is topotactic for EX-Na$_2$RuO$_4$ and enlists a solution path for Na$_2$RuO$_4$, is nested in the sizes and crystallinity differences between both materials with the EX-Na$_2$RuO$_4$ being the most faulted and divided.

II.4.e Effect of the alkali on the anionic and cationic redox couples in Ru-based compounds

We have studied the electrochemical redox mechanism of Na_3RuO_4 which enlists the formation of EX-Na_2RuO_4 having Ru^{6+} and, upon further oxidation, the presence of anionic redox in EX-$NaRuO_4$, together with the dissolution of the active material. Moreover, during the Na removal from Na_2RuO_4 we could observe the presence of a new phase, Td-$NaRuO_4$, isostructural to $KRuO_4$ having Ru^{7+}. Therefore, the Na_xRuO_4 ($0 < x \leq 3$) phase diagram appears to be very rich enlisting compounds having Ru in the 5+, 6+ and 7+ oxidation state in octahedral, bipyramid or tetrahedral environment. Our previous study of the Li_xRuO_4 ($0 < x \leq 3$) system, in **II.3.c**, combined with IE-Li_2RuO_4, shows in contrast, less diversity since it only gathers compounds having mostly RuO_6 coordination with 5+ or 5.3+. It is also worth recalling that previous investigations of the K_xRuO_4 phase diagram have revealed the existence of the K_2RuO_4 and $KRuO_4$ phases having a Ru oxidation state of 6+ and 7+, respectively with both showing Ru in a tetrahedral environment.[124,122] From the compilation of the aforementioned $Li(Na)(K)_xRuO_4$ phase diagrams, a trend seems to emerged; the smaller is the alkali, i) the higher is the coordination of Ru and ii) the lower is the oxidation state of Ru.

The first part of this trend doesn't come as a surprise considering the tremendous amount of work dealing with physical pressure-driven phase transitions. Commonly, it shows that applying pressure, hence reducing the cell volume, leads to structural transitions increasing the coordination of the highest charged cation (e.g. from apex tetrahedral to edge-shared octahedrons). This is exemplified by the pressure-induced wurtzite to rocksalt phase transition in CdSe associated to a switch from tetrahedral to octahedral environment for the Cd atoms.[126,127] Equally, closer examples regard i) NaCl which goes, under pressure, from a rocksalt to a CsCl-type structure, with Na having octahedral and cubic coordination, respectively,[128] and ii) the pressure induced transformation of quartz into Stishovite, having Si in tetrahedral and octahedral environment, respectively.[129] In our case, the applied pressure is of chemical nature, since moving from K to Li, the unit cell size of the A_xRuO_4 compounds is reduced hence leading to the stabilization of RuO_6 compared to RuO_4.

To better quantify the second part of the trend enlisting the link between the size of the alkali and the oxidation state of Ru, convex hull diagram of the Na_xRuO_4 system was computed through DFT calculations. From the relative energies (Figure II-46), it can be seen that Ru^{5+},

Ru^{6+} and Ru^{7+} are stabilized in octahedral, trigonal pyramid and tetrahedral environment, respectively. This most likely nested in the electronic configuration of the metal cation, since Ru^{5+} (d^3) will prefer an octahedral environment while Ru^{6+} (d^2) or Ru^{7+} (d^1) will be more stable in a tetrahedron or a trigonal bipyramid.

Overall, we showed that the competition between cationic and anionic redox drastically depends on the alkali atoms, therefore, emphasizing the difficulties of transposing the knowledge of anionic redox from Li to Na based materials.

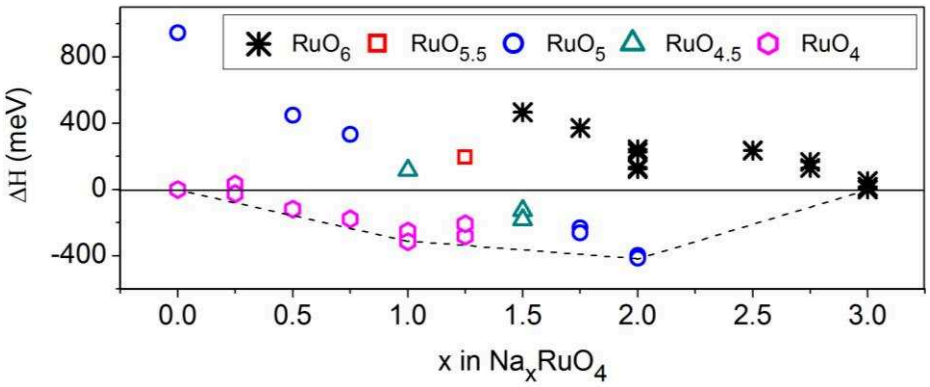

Figure II-46: Convex Hull for the Na_xRuO_4 system. Symbols represent the formation energy of Na_xRuO_4 compared to the reference energy of the direct Na_3RuO_4 to RuO_4 + 3 Na transformation, taken as the reference energy (horizontal plain line). Negative values of ΔH show that a single phase with intermediate Na compositions can be achieved electrochemically. Thermodynamic reaction pathway is highlighted in dot lines. Black cross, red squares, blue circle, green triangle and pink hexagon stand for structures presenting octahedra (RuO_6), a mix of octahedra and trigonal bipyramids ($RuO_{5.5}$), trigonal bipyramids (RuO_5), a mix of trigonal bipyramids and tetrahedral ($RuO_{4.5}$) and tetrahedral (RuO_4), respectively.

II.5 Conclusion of the chapter

In this chapter, we presented a strategy to probe the limit in terms of capacity of anionic redox. It relied on the design and study of compounds among the A_3MO_4 family (A being Li or Na and M being a mix of Ru, Nb, Sb, Ir, Ta and Sb) having an elevated O/M ratio and hence a high density of oxygen lone pairs. As a first step, we successfully synthetized a batch of compounds, carefully determined their structure and developed a theoretical framework to understand their rich structural diversity. In a second part, we turned to the study of their electrochemical properties and found that anionic redox is limited in the $Li_3Ru_yIr_{1-y}O_4$ compounds, after the removal of 2 e^- per Ir atom, by the destabilization of the oxidized oxygen species leading to massive gas release. In contrast, in the Li_3RuO_4 compounds, no O_2 evolution is observed suggesting that the oxidized oxygen species remain stable. However, drastic capacity fade is observed due to the formation and dissolution in the electrolyte of RuO_4/RuO_4^- species having high oxidation state of Ru, 8+ and 7+, respectively, showing that anionic redox can be limited by cationic redox. To tackle the dissolution problem, one strategy is to stabilize the high oxidation state of Ru in solid state. This can be done increasing the size of the alkali ion as shown by the electrochemical formation of Na_2RuO_4 and $NaRuO_4$ having Ru^{6+} and Ru^{7+}, respectively. Practically speaking, dissolution is still observed during Na removal from Na_3RuO_4 therefore a more radical and interesting method would be to use superconcentrated electrolyte or even solid state electrolyte.

As a perspective, we would like to discuss how our findings on model materials can be useful to design practical materials. Mn-based compounds are the most successful cathode materials showing anionic redox. Bearing in mind the established size-coordination-valence correlation (II.4.e) together with the similarities between Ru and Mn in terms of feasible oxidation states and coordinations, we decided to further investigate Mn-based compounds. As a first step, we plotted the energy landscape diagram as a function of the oxidation state for various compounds issued from the Materials Project.[130] We found (Figure II-47) that Li based compounds with high oxidation states are less stable (blue curve) because of a large decomposition energy, greater than Na-based and K-based compounds (black and red curves, respectively). This observation suggests that high oxidation states should be favored in Mn-based materials containing large alkali, hence limiting the chances of having anionic redox activity. Comparing these findings to literature, $Na_2Mn_3O_7$ [131,132] and $Na_{2/3}[Mg_{0.28}Mn_{0.72}]O_2$ [117]

have been studied and no sign of Mn oxidation has been found implying that the critical unit cell size for Mn oxidation has yet not been reached, setting an interesting path for further study.

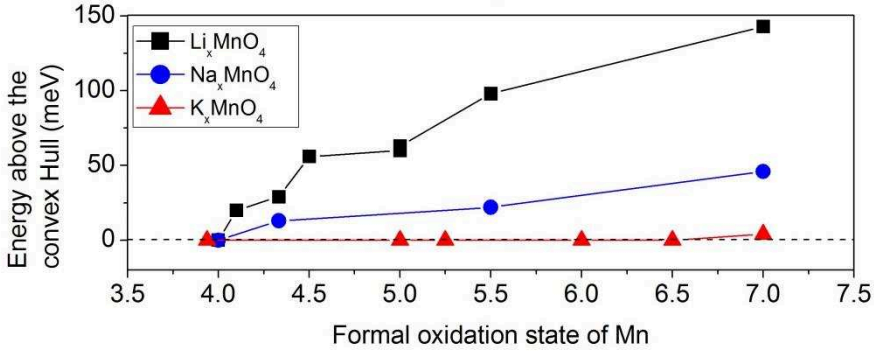

Figure II-47: Energy above the convex hull of the most stable structure depending on the oxidation state. Black, blue and red line stand for Li_xMnO_4, Na_xMnO_4 and K_xMnO_4 systems, respectively.

Chapter III Unveiling different anionic redox potentials in Ni/Mn substituted Li_3TaO_4

III.1 Introduction

Cumulating cationic and anionic redox processes, being the oxidation/reduction of the cation and the anion, respectively, allows a great improvement of the specific energy of Li-ion battery. However, materials showing anionic redox, like Li-rich NMC, are still not used in commercial applications because they suffer from voltage decay, kinetic limitation and voltage hysteresis.[69,70] To tackle these issues and design better positive electrode materials, we need to provide a better understanding of this new phenomenon. In this chapter, we will focus on the voltage hysteresis problem which is the most pronounced in Li-rich disordered rocksalt compounds.

Li-rich disordered rocksalt oxides (DRS) are attractive because they show tremendous capacity, 300 mAh/g for $Li_{1.3}Mn_{0.4}Ti_{0.3}O_2$ and 250 mAh/g for $Li_{1.2}Ni_{0.33}Ti_{0.33}Mo_{0.13}O_2$ compared to commercialized materials $LiNi_{0.33}Mn_{0.33}Co_{0.33}O_2$ (200 mAh/g).[133,77,134,135] Both $Li_{1.3}Mn_{0.4}Ti_{0.3}O_2$ and $Li_{1.2}Ni_{0.33}Ti_{0.33}Mo_{0.13}O_2$ capacities are the result of combined cationic and anionic redox processes. Application-wise, $Li_{1.2}Ni_{0.33}Ti_{0.33}Mo_{0.13}O_2$ shows less interesting properties compared to $Li_{1.3}Mn_{0.4}Ti_{0.3}O_2$ mostly because of poor energy efficiency due to a strong voltage hysteresis. Indeed, while both compounds have similar redox potentials in oxidation, Ni-based compounds show a lower averaged reduction potential of 3 V, compared to 3.2 V in the Mn-based one, due to a sudden drop of voltage from 3.5 to 1.5 V in the middle of discharge. Interestingly, this phenomenon which can be observed in many Ni-based rocksalt (Table III-1), but never in Mn-based compounds, has been investigated in only two studies. Lee et al. attributed this phenomena to the formation of a Li – poor layer at the surface of the material during charge, impeding Li diffusion in $Li_{1.2}Ni_{0.33}Ti_{0.33}Mo_{0.13}O_2$ [135] while Zhao et al. proposed the reduction of Mn/Mo due to oxygen release in $Li_{1.2}Ni_{0.4}Mn_{0.2}Mo_{0.2}O_2$.[136]

Composition	Potential drop in discharge	Proposed origin	Ref.
$Li_{1.33}Ni_{0.33}W_{0.33}O_2$	2 V	Not explored	Kumakura et al. [137]
$Li_{1.3}Ni_{0.27}Nb_{0.43}O_2$	2 V	Not explored	Yabuuchi et al. [133]
$Li_{1.2}Ni_{0.33}Ti_{0.33}Mo_{0.16}O_2$	1.5 V	Kinetic limitation - formation of densified surface	Lee et al. [135]
$Li_{1.33}Ni_{0.33}Mo_{0.33}O_2$	1.9 V	Not explored	Yabuuchi et al. [138]
$Li_{1.05}Ni_{0.5}Ti_{0.3}Nb_{0.15}O_2$	1.8 V	Not explored	Colin et al.[139]
$Li_{1.2}Ni_{0.4}Mn_{0.2}Mo_{0.2}O_2$	2V	Mn or Mo reduction triggered by oxygen release	Zhao et al. [136]

Table III-1: Composition, observed potential drop during discharge and the origin of such feature for reported Ni-based compounds.

To check the validity of these hypotheses, we propose a detailed comparison of two new Ni and Mn-based DRS model systems. To favor the cation disordering, d^0 elements such as Ti^{4+}, Nb^{5+} or Mo^{6+} are added to the chemical composition, based on early work by Urban et al.[140] Herein, we propose to use Ta^{5+} as d^0 element and, by substituting Ta for Ni or Mn in Li_3TaO_4, prepared the two phases $Li_{1.3}Ni_{0.27}Ta_{0.43}O_2$ (LNTO) and $Li_{1.3}Mn_{0.4}Ta_{0.3}O_2$ (LMTO). We compare their electrochemical properties with the aim to i) assess the origin of the different discharge potentials between Mn-based and Ni-based compounds, and ii) probe the role of Ta^{5+} ($5d^0$) substitution in the overall redox processes, compared to Nb^{5+} and Mo^{6+} ($4d^0$), or Ti^{4+} ($3d^0$).

This chapter will be divided as follow: we first briefly describe the synthesis of these compounds together with their general electrochemistry prior to present the mechanism of the Li-removal/uptake in $Li_{1.3}Ni_{0.27}Ta_{0.43}O_2$ and $Li_{1.3}Mn_{0.4}Ta_{0.3}O_2$, separately, as determined by complementary operando XAS, OEMS and XRD. Then, we will engage into a theoretical approach focusing on the charge transfer band gap in these materials.

III.2 Synthesis, crystal structure and electrochemical signature of $Li_{1.3}Ni_{0.27}Ta_{0.43}O_2$ and $Li_{1.3}Mn_{0.4}Ta_{0.3}O_2$

III.2.a Synthesis and crystal structure

Classical solid state synthesis from the oxide precursors, NiO (green, Sigma-Aldrich 99%), Mn_2O_3 (Sigma-Aldrich, 99.9%), Ta_2O_5 (Alfa Aesar, 99.85%) and with 10% excess Li_2CO_3 (Sigma Aldrich, 99%), was employed to prepare the $Li_{1.3}Ni_{0.27}Ta_{0.43}O_2$ and $Li_{1.3}Mn_{0.4}Ta_{0.3}O_2$ phases.The composition were chosen so that the Li content is similar in both compounds, with Ni, Mn and Ta being at the 2+, 3+ and 5+ oxidation states, respectively. The reactants were mixed using mortar and pestle before grinding in a planetary ball mill using a zirconia set for 1 hour at 600 rpm for the $Li_{1.3}Ni_{0.27}Ta_{0.43}O_2$ precursors and 12 hours at 600 rpm for $Li_{1.3}Mn_{0.4}Ta_{0.3}O_2$ precursors. Intimate mixing was necessary to prevent the formation of $LiMnO_2$ during the subsequent heat treatment. The powders were fired for 24 h at 900°C in air for $Li_{1.3}Ni_{0.27}Ta_{0.43}O_2$ and under argon flux for $Li_{1.3}Mn_{0.4}Ta_{0.3}O_2$. The structure of these new compounds was determined by XRD coupled to NPD whose Rietveld refinements are presented in Figure III-1 and the resulting crystallographic data in Table III-2. XRD and NPD are complementary here since they provide different contrast between the atoms (Z_{Li} = 3 and b_{Li} = -1.90 fm, Z_{Mn} = 25 and b_{Mn} = -3.73 fm, Z_{Ni} = 28 and b_{Ni} = 10.3 fm, and Z_{Ta} = 73 and b_{Ta} = 6.91 fm). Neutron diffraction was measured on D1B beamline at the ILL with a wavelength of λ = 1.29 Å. Both compounds crystalize in F m -3 m space group with cell parameters a = 4.1990(10) Å and a = 4.1975(11) Å for LNTO and LMTO, respectively. Their structure is a rocksalt structure with all the cations randomly distributed over the 4a Wyckoff position as it can be seen on the schematic Figure III-1.

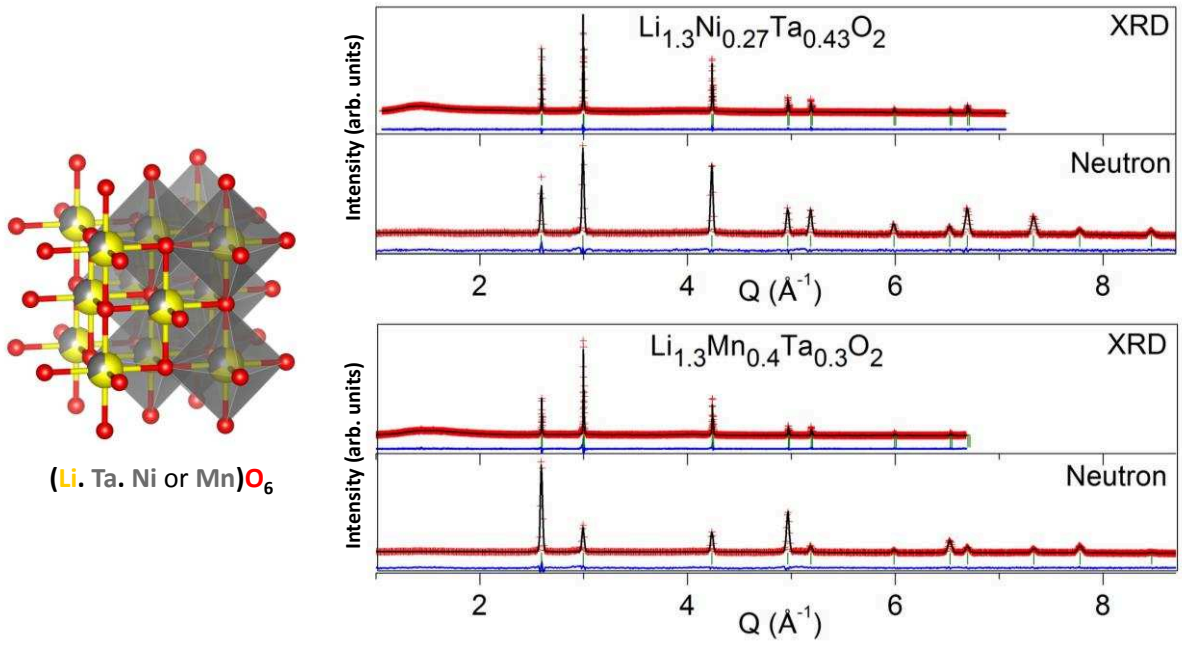

Figure III-1: Rietveld refinement of XRD ($\lambda_{cu} \approx 1.54$ Å) and NPD ($\lambda \approx 1.29$ Å) patterns of $Li_{1.3}Ni_{0.27}Ta_{0.43}O_2$ and $Li_{1.3}Mn_{0.4}Ta_{0.3}O_2$, on top and bottom, respectively, together with a representation of the structural model. The red crosses, black continuous line and bottom blue line represent the observed, calculated, and difference patterns respectively. Vertical green tick bars are the Bragg positions

$Li_{1.3}Ni_{0.27}Ta_{0.43}O_2$ – $R_{Bragg\ neutrons}$ = 5.23% $R_{Bragg\ XRD}$ = 5.70%						
F m -3 m	a = 4.1990(10) Å		Z = 2		V/Z = 36.96 Å^3	
$Li_{1.3}Mn_{0.4}Ta_{0.3}O_2$ – $R_{Bragg\ neutrons}$ = 3.99% $R_{Bragg\ XRD}$ = 6.40%						
F m -3 m	a = 4.1975(11) Å		Z = 2		V/Z = 36.88 Å^3	
Atom	Wyckoff position	x	y	z	B_{iso} (Å²)	occupancy
O	4b	$\frac{1}{2}$	$\frac{1}{2}$	$\frac{1}{2}$	0.91(3) 1.5(3)	1
Li/Ni/Ta Li/Mn/Ta	4a	0	0	0	0.57(5) 1.73(13)	0.65/0.135/0.215 0.65/0.2/0.15

Table III-2: Crystallographic data for $Li_{1.3}Ni_{0.27}Ta_{0.43}O_2$ and $Li_{1.3}Mn_{0.4}Ta_{0.3}O_2$.

III.2.b Electrochemical properties

The electrochemical behavior of LNTO and LMTO as cathode for Li-ion battery was investigated. The 1st, 2nd and 10th cycles for each compound are presented in Figure III-2. LNTO and LMTO show discharge capacities of 220 mAh/g and 180 mAh/g, respectively. They correspond to the extraction/insertion of 1.1 Li for LNTO and 0.9 Li for LMTO. Although the capacity of LNTO is higher than LMTO, the Ni-based compound shows a lower discharge potential since only 0.25 Li are inserted above 3 V compared to 0.6 Li for LMTO. Moreover, comparing the charge and discharge potentials of the 2nd cycle, one can clearly see a stronger voltage hysteresis for LNTO, i.e. charge happens at 4 V while most of the discharge is centered around 1.5 V, compared to LMTO. This low average voltage and high hysteresis has been observed in other Ni-based disordered rocksalt compounds and it is detrimental for the specific energy and energy efficiency, hence the need to understand its origin. Is it related to diffusion issues, cationic vs. anionic redox competition, or Li-driven structural changes? To answer these questions, complementary operando XAS, OEMS and XRD measurements were performed.

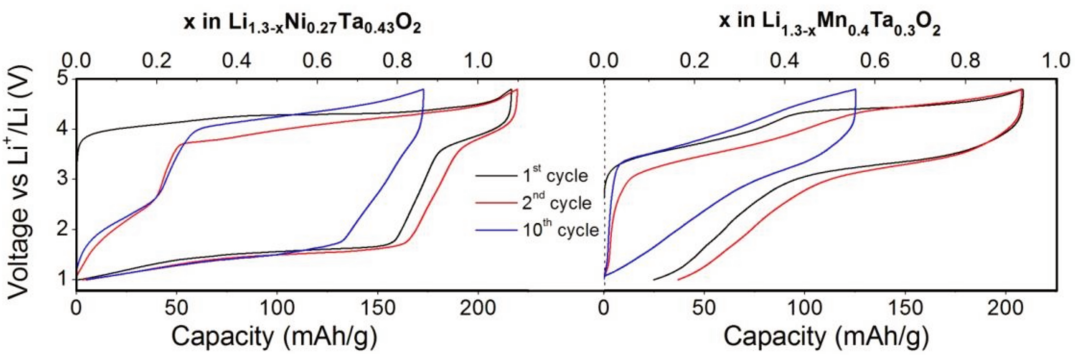

Figure III-2: shows the 1st, 2nd and 10th cycles, at C/20, of $Li_{1.3}Ni_{0.27}Ta_{0.43}O_2$ and $Li_{1.3}Mn_{0.4}Ta_{0.3}O_2$, respectively. x values for $Li_xNi_{0.3}Ta_{0.4}O_2$ and $Li_xMn_{0.4}Ta_{0.3}O_2$ are given for the 1st charge.

III.3 Mechanism of Li removal in $Li_{1.3}Ni_{0.27}Ta_{0.43}O_2$

III.3.a Effect of the state-of-charge

The voltage-composition curve for LNTO shows 6 distinct processes: 3 in charge and 3 in discharge, hereafter called CN1, CN2, CN3, DN4, DN5 and DN6, as highlighted in Figure III-3a, (C, D and N stand for "Charge", "Discharge" and "Nickel", respectively). Upon charge, CN1, CN2, and CN3 happen at 4 V, 4.3 V and 4.5 V as deduced from the dQ/dV curve and account for the extraction of 0.3, 0.4 and 0.4 Li, respectively. Upon discharge, the processes DN4, DN5, and DN6 occur at 3.8 V, 1.7 V and 1.3 V and correspond to the insertion of 0.25, 0.5 and 0.3 Li, respectively. Concerning the 2nd charge, a new redox process can be seen centered around 1.7 V. Its capacity scales with the capacity of DN6, hence showing their correlation in Figure III-4, however its origin is not yet understood.

Next, to determine the corresponding oxidation-reduction processes, several cells were made and oxidized to reach different SOC prior to be discharged to 1.5 V (Figure III-3b-c). Interestingly, when charging over CN1, the reduction curve is mainly composed of DN4 implying the link between both. Moreover, DN5 appears when further charging, hence showing a clear connection between CN2-CN3 and DN5 with however a large voltage difference between the charge and discharge processes. Worth mentioning is that the capacity of DN4 decreases with increasing SOC and this trend is even more severe at 55°C. Lastly, despite strong polarization observed during DN5 on the GITT curve (Figure III-3d) equilibrium potential in discharge do not reach the ones in charge implying that the observed voltage difference is not only kinetic but also enlists a thermodynamic limitation. Thus, could such an effect be related to a peculiar charge compensation mechanism having sluggish kinetics associated with the anionic redox species as previously reported in Li-rich materials?

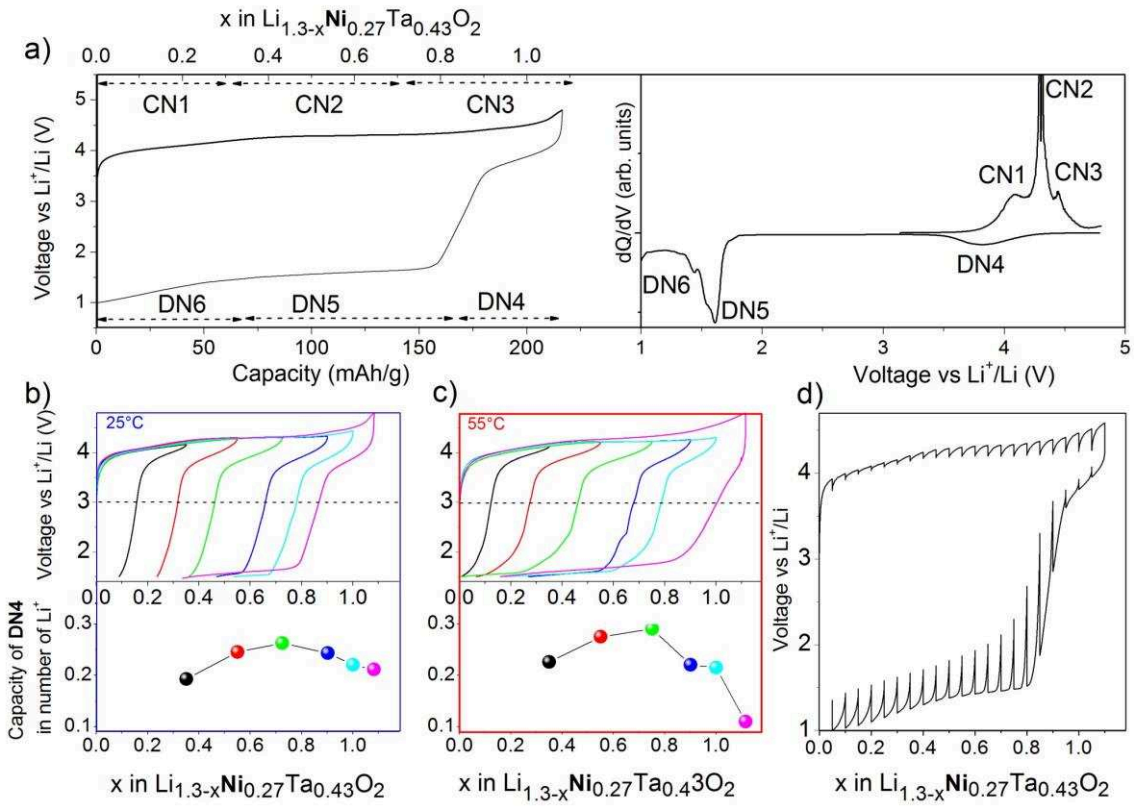

Figure III-3: a) Voltage-composition curve of the 1st galvanostatic cycle, C/20, and its dQ/dV profile, on the left and right panel respectively. b) and c) voltage-composition curve of the 1st cycle with different state-of-charge (top) together with the capacity of the DN4 (>3 V) depending on the SOC (bottom) at 25°C and 55°C. d) GITT measurement performed on the 1st cycle of LNTO at C/20 with 5 hours rest every hour.

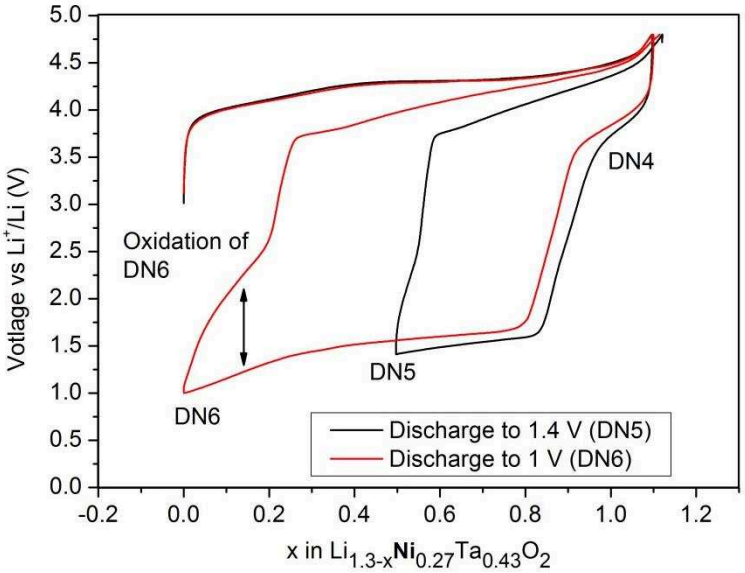

Figure III-4: Voltage composition curve of the galvanostatic cycling, C/20, of LNTO realized at different depths of discharge, namely 1.2 V and 1 V in black and red, respectively. After reducing to 1 V, in the 2nd charge a new oxidation process can be observed centered ~1.7 V showing it corresponds to the oxidation of the species reduced during DN6.

III.3.b X-ray absorption spectroscopy study

To determine the evolution of Ni, Ta, and O oxidation states during cycling, we used operando Ni K-edge, ex situ Ta L_3-edge and O K-edge XAS, as presented below. Hard XAS was measured on ROCK beamline at Soleil Synchrotron with the help of Antonella Iadecola. Soft XAS was measured on the ID-4-C beamline at APS, with the help of Haifeng Li, Jordi Cabana and John W. Freeland.

First, we monitor the variation of Ni oxidation state by exploiting, operando, the Ni K-edge position during the electrochemical cycling that we compare with standards, namely NiO (Ni^{2+}) and $LiNiO_2$ (Ni^{3+}) as presented in Figure III-5 and Figure III-6a. The Ni oxidation state is close to 2+ in the pristine compound and increases up to nearly 3+ during the first part of charge (CN1 and CN2), corresponding to the extraction of 0.5 Li. Bearing in mind the chemical composition, $Li_{1.3}Ni_{0.27}Ta_{0.43}O_2$, this implies that Ni is not the only redox active element during CN1 and CN2. Upon further charging, there is a reduction of Ni whose oxidation state becomes nearly equal to 2.5+ at the end of charge, as determined assuming a linear correlation between the edge position and the oxidation state using NiO and $LiNiO_2$ as references. During DN4, the oxidation state of Ni converts back to ≈2+ and stays constant during DN5 and DN6.

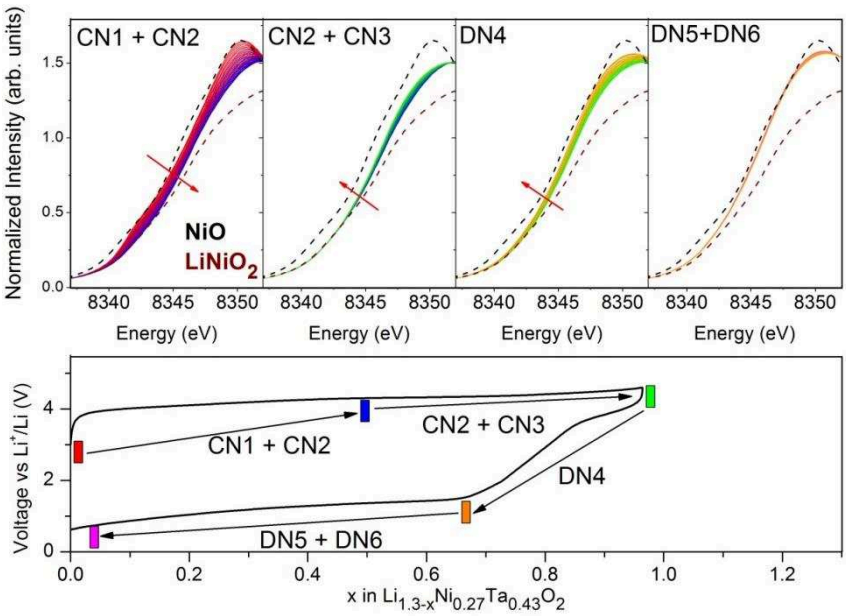

Figure III-5: Variation of the Ni K-edge measured operando during the 1st charge and discharge of $Li_{1.3}Ni_{0.27}Ta_{0.43}O_2$ (top) together with the galvanostatic cycling, at C/20 (bottom). The data has been divided in four parts CN1+CN2, CN2+CN3, DN4 and DN5+DN6. Black and wine dot lines stand for NiO and $LiNiO_2$ spectra, respectively. The edge position of Ni K-edge XAS spectra of materials containing Ni^{4+} is located at much higher energy than $LiNiO_2$, excluding the presence of Ni^{4+} during Li removal from LNTO.

The XAS spectra evolution during the electrochemical cycle was further exploited using Principal Component Analysis (PCA) combined to Multivariate Curve Resolution-Alternating Least Squares (MCR-ALS). Three components were identified and both their concentration evolution and their corresponding EXAFS were analyzed and presented in Figure III-6b-c and Table III-3. The 1st and 2nd components correspond to the pristine material and the phase having solely Ni^{3+}, respectively. The 3rd component appears in the middle of the charge, end of CN2. Its concentration increases gradually up to 60% at the end of DN4 and stays constant during the rest of the discharge. In this component, Ni is in the same oxidation state than in the pristine, ≈2+, as determined from their edge position, Figure III-7a, and their EXAFS signal showing similar Ni-O environments, 6 Ni – O distances of 2.048 and 2.068 Å, respectively, as opposed to a distorted Jahn –Teller environment, composed of 4 short and 2 long Ni – O distances of 1.940 and 2.111 Å, for the 2nd component. The main difference between the pristine and the 3rd component is nested in the Ni-M environment. Indeed, the values obtained for the Ni – Ni distances, the Ni – Ta distances and the related Debye-Waller factors are higher in the 3rd component indicating a higher atomic disorder of the end of discharge compound compared to the pristine. Note that Ni K-edge data measured on ex situ samples are consistent with the operando data as presented in Figure III-7b.

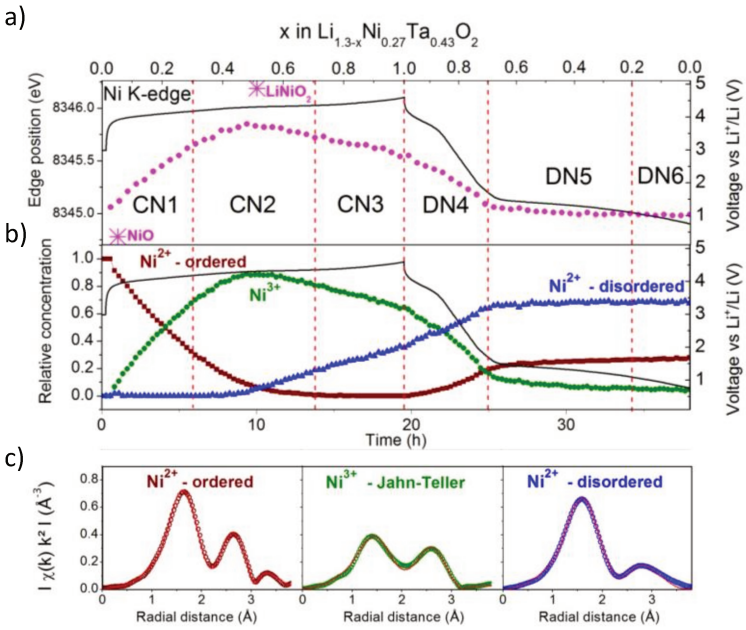

Figure III-6: a) Evolution of the Ni K-edge energy position (pink) during operando measurement for the 1st cycle of LNTO together with the voltage-composition curve, C/20 (black). b) Component concentration evolution obtained by MCR-ALS during operando measurement, in brown, green, and blue, together with the voltage-composition curve in black. c) Fit of the magnitude of the Fourier transforms performed on the reconstructed spectra of the three components.

MCR-ALS components	1st shell Ni - O					2nd shell Ni – Ni			2nd shell Ni - Ta			
	CN	dNi-O	CN	dNi-O	$\sigma*10^3$	CN	dNi-Ni	$\sigma*10^3$	CN	dNi-Ta	$\sigma*10^3$	$R*10^3$
Ni^{2+} Ordered	6	2.068(2)	-	-	9.2(1.1)	1.8	2.988(7)	6.9(6)	2.4	3.04(2)	12.1(1.1)	7
Ni^{3+} Jahn-Teller	4	1.940(3)	2	2.111(15)	11.2(1.5)	1.8	2.958(6)	9.6(1.3)	2.4	3.22(3)	21(2)	4
Ni^{2+} Disordered	6	2.0483(19)	-	-	11.5(1.1)	1.8	3.021(17)	17(2)	2.4	3.25(4)	17.2(1.9)	2

Table III-3: Structural parameters obtained by fitting the Ni K-edge EXAFS oscillations of the reconstructed components from the operando measurements on LNTO. CN, d, and σ stand for Coordination Number, distance in Å and the Debye-Waller factor in Å². The difference energy threshold, E0, and the amplitude reduction factor (S_0^2) are fixed during fit. S_0^2 was taken equal to 1 for all analysis.

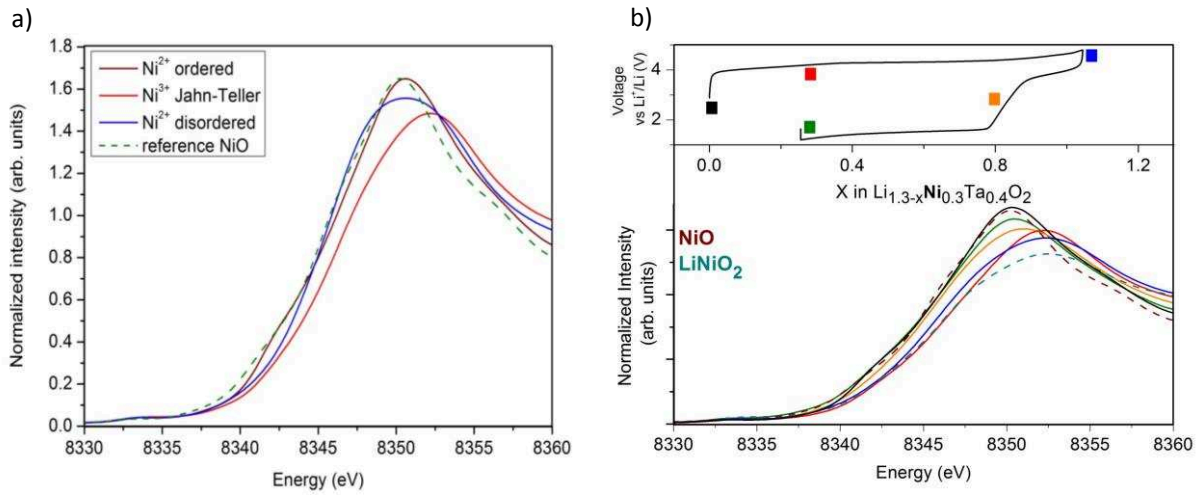

Figure III-7: a) Ni K-edge XANES spectra of the reconstructed components in brown, red and blue. NiO is shown as reference in dotted green line. b) On the top, voltage-composition curve of LNTO, C/20, with squares indicating the composition of the prepared ex situ samples, namely the pristine, x = 0.3 (end of CN1, 4.2 V), x = 1.1 (end of CN3, 4.8 V), x = 0.85 (DN4, 3 V) and x = 0.3 (end of DN5, 1.2 V), in black, red, blue, magenta and green, respectively. On the bottom, Ni K-edge XANES spectra of the ex situ samples.

Ta L_3-edge and O K-edge measurements were performed on ex situ samples recovered from $Li_{1.3}Ni_{0.27}Ta_{0.43}O_2$/Li cells stopped at various states of charge; after CN1 (4.2 V and x = 0.3), after CN2 (4.5 V and x = 0.7), and after CN3 (4.8 V and x = 1.1), and discharge, in DN4 (3V and x = 0.85) and after DN5 (1.2 V and x = 0.3).

Concerning Ta, for all samples the edge position is similar to the one in Ta_2O_5, spotted from the maximum of the first derivative of the normalized intensity (Figure III-8a) showing Ta stays in the 5+ oxidation state during cycling. However, the white line shape and intensity changes show evolution of the Ta environment during Li removal/uptake. To better assess

these changes, analysis of EXAFS oscillations was carried out (Figure III-8b-c). It shows that while the average Ta – O and Ta – M (M being Ni and Ta) distances stay roughly constant during the Li removal/uptake, approximately 1.95 Å and 3.1 Å, the distortion coefficient of the TaO_6 octahedron, calculated from the mean deviation of Ta-O bond lengths, changes substantially. From these results, we concluded that Ta is not oxidized/reduced during the electrochemical cycling but suffers from modification of its coordination shell, which is highly distorted at the end of charge (CN3) and at the beginning of discharge (DN4).

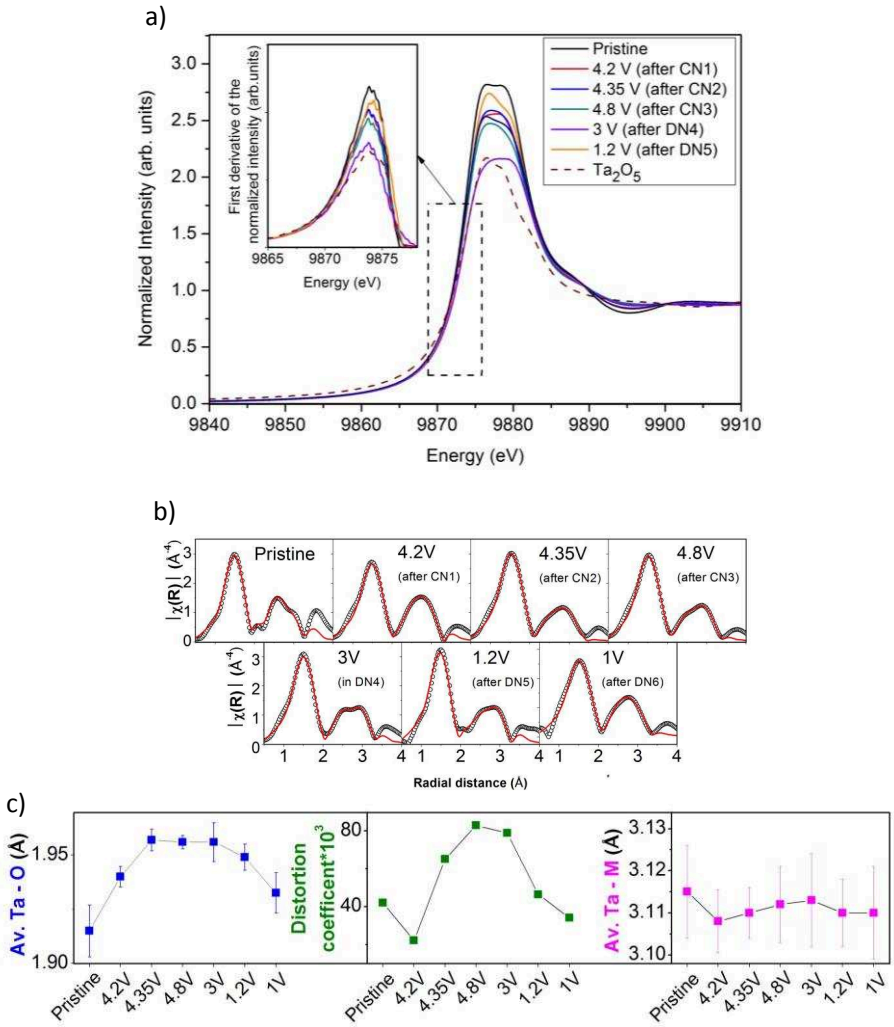

Figure III-8: a) Ex situ Ta L_3-edge XANES spectra together with its first derivative curve for ex situ samples along the galvanostatic cycling of LNTO. Comparing all spectra, changes can be seen in the while line intensity and shape but not in the edge position as emphasized in the derivative plot. These results suggest that Ta keeps its 5+ oxidation state but suffers changes in its local environment during Li removal/uptake. b) Magnitude of the Fourier transforms of the Ta L_3-edge EXAFS oscillations on ex situ LNTO with the solid representing the model fitting. c) From left to right, average Ta-O bond lengths, distortion coefficients of TaO_6 and average Ta – M bond lengths as extracted from the EXAFS fitting. Distortion coefficient is calculated according the formula: $\Delta^{M-O} = \frac{1}{6}\sum_{i=1}^{6}\left[\frac{d_i - <d>}{<d>}\right]$

Altogether, the previous findings dealing with the Ni and Ta redox during the 1st cycle lead us to hypothesize that anionic redox is responsible for the charge compensation mechanism during CN2, CN3 and DN5. To prove this hypothesis, we analyzed the pre-edge features (525 – 532 eV) of the O K-edge spectra (Figure III-9a). Two main features at 526.5 eV and 530 eV can be observed. They correspond to electronic transitions from O 1s into hybridized oxygen 2p states with nd cations. Using O pDOS computed via DFT calculations (Figure III-9b), we show that the 526.5 eV feature corresponds to Ni-O states which appears solely in presence of Ni^{3+}, while the 530 eV signal is reminiscent of both Ni-O and Ta-O states. By subtracting the pristine from the ex situ spectra (Figure III-9a bottom) we highlight its evolution during the 1st cycle which is mainly centered at 526.5 eV and 528.7 eV. The 526.5 eV feature intensity is maximum after CN1 and decreases during CN2, CN3 and DN4 directly following the presence of Ni^{3+} in agreement with DFT calculations. The second feature at higher energy (528.7 eV) which appears during CN2 and increases during CN3, clearly suggest the removal of some electronic density on the oxygen atoms. Since neither Ni nor Ta is active in this region of the charge, the presence of the 528.7 eV is a direct evidence of anionic redox. Interestingly, the 528.7 eV signal remains constant during DN4 and fully disappears in DN5 as expected.

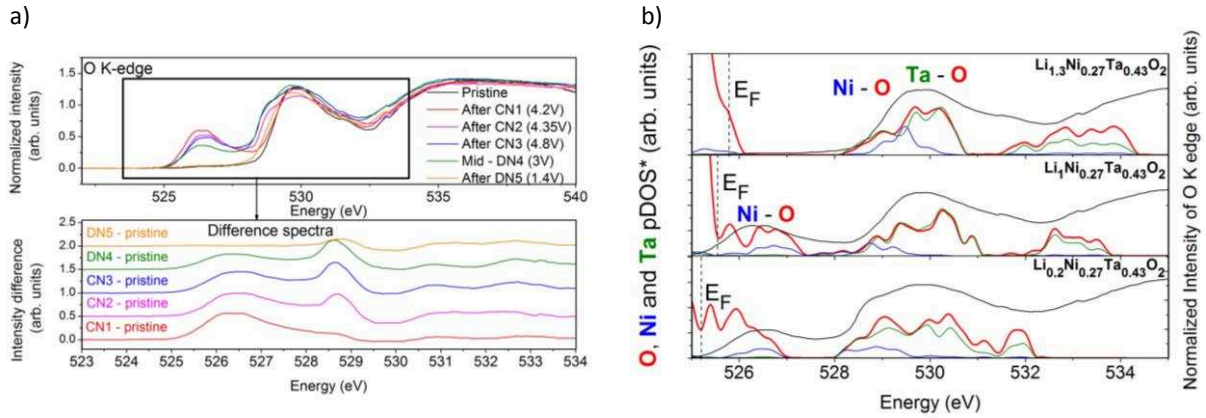

Figure III-9: a) O K-edge XAS spectra, acquired in total fluorescence mode (TFY), for ex situ samples for LNTO during the charge and discharge, together with the difference spectra between the pristine and the spectra of the ex situ samples in the bottom panel. b) Comparison of the TFY O K edge data (black) at various state-of-charge with the empty O, Ni and Ta pDOS in red, blue and green, respectively. Note that the intensity of the Ni and Ta pDOS has been modified for graphical purposes. Note that oxidized oxygen states may not appear at the correct energy on the pDOS due to the valence shift of the O1s states.

Overall, using various spectroscopy techniques, we have shown that Ni oxidation/reduction happens at ≈ 3.9 V with limited polarization ≈ 100 mV while anionic redox occurs at 4.2 V in charge and 1.5 V in discharge, clearly implying that anionic redox is responsible for the large voltage hysteresis observed in LNTO. To better understand the characteristics of anionic redox in LNTO, namely the stability of the oxidized oxygen species towards O_2 release, gas analyses were performed and are presented in the next part.

III.3.c Gas evolution

OEMS experiments were performed, by Erik J. Berg at PSI, to test the stability of the phase against O_2 release. The results, presented in Figure III-10, show initially no gas evolution upon oxidation. In contrast, there is a copious amount of CO_2 and O_2 produced inside the cell as soon as we reach the CN3 process. Interestingly, this gas production is concomitant with the partial reduction of Ni^{3+} suggesting that a fraction of the released oxygen atoms in CO_2 and O_2 molecules come from the bulk of the material. Bearing in mind previous work, by Luo et al., showing that both oxygen atoms to form O_2 come from the material in Li-rich NMC,[76] our findings suggest O – O pair formation occurs in LNTO during charge. Note that there is no gas evolution during discharge implying that the formed O_2 gas molecules do not reduce, which is surprising bearing in mind the reduction of O_2 at 2.2 V in in Li – O_2 battery systems. To confirm these findings, an electrode is charged up to 4.8 V, then removed from the electrochemical cell, washed, and discharged in a fresh cell down to 1 V. The obtained discharge curve, presented in Figure III-11, is exactly similar to the normal discharge, i.e for an electrode charged and discharged in the same cell, confirming the gas formed during charge do not reduce. Thus we confirm that DN5 process corresponds to the reduction of the oxidized oxygen species from the bulk of the material.

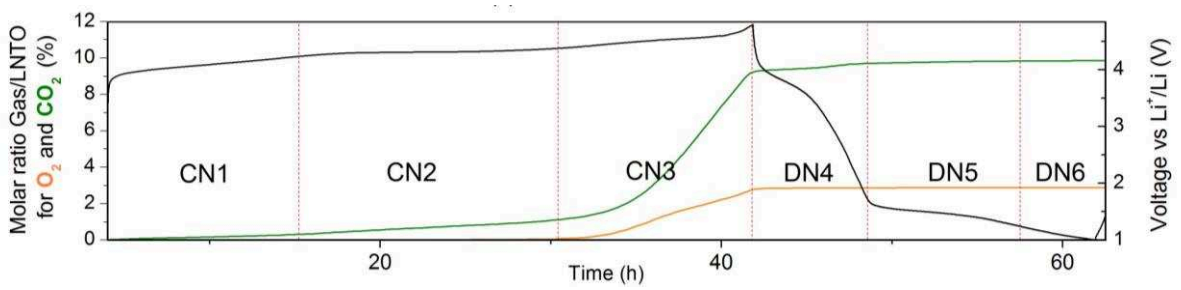

Figure III-10: Molar ratio of O_2/LNTO and CO_2/LNTO measured via mass spectrometry during galvanostatic cycling together with the voltage-composition curve, in orange, green and black, respectively. Note that the rate for the charge was C/40 and C/20 for the discharge.

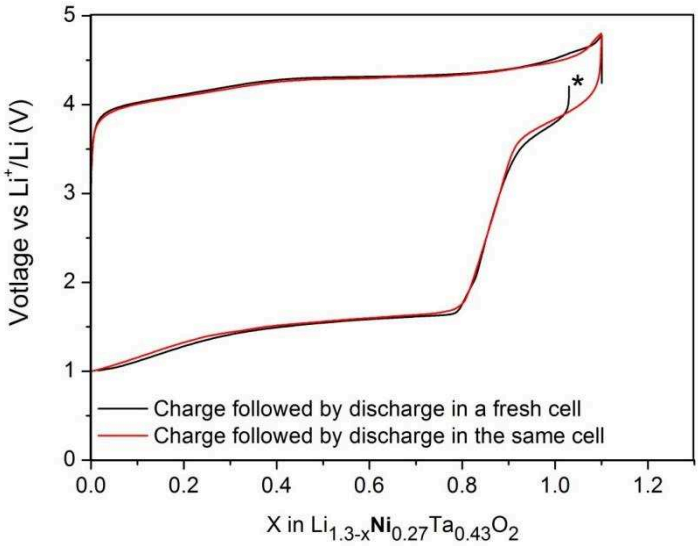

Figure III-11: Voltage-composition curve, C/20, for LNTO with the charge and discharge performed in the same cell, in red, and charge and discharge performed in different fresh cell in black. This experiment indicates that the reduction features observed in LNTO do not come from the reduction of species formed during the oxidation (gas or dissolved species). * small self-discharge is observed.

III.3.d Structural evolution

To check whether the release of oxygen at high potential is associated to structural changes, we performed operando X-ray diffraction. Figure III-12a-b-c-d presents the electrochemical cycle and the Rietveld refinements of the XRD patterns. At this point, we recall that the pristine LNTO crystallizes in a cubic space group F m -3 m, with therefore one cell parameter, a. During process CN1, the cell parameter decreases gradually which is consistent with Ni oxidation ($Ni^{2+} \rightarrow Ni^{3+}$), then stays constant through the CN2 process during which oxygen is oxidized but not released from the material. In the middle of CN3 process, when O_2 leaves the material, the appearance of a shoulder peak can be seen in XRD pattern in Figure III-12c. It can be indexed with an extra phase having the same space group as the pristine, with however smaller cell parameter, 4.148 Å compared to 4.1990(10) Å. The chemical composition of this new phase, now called “high voltage phase”, couldn’t be estimated due the overlap between its peaks and the pristine ones. During discharge, the cell parameters of both phases decrease and convert back to that of the pristine material with however a larger peak width indicative for the presence of strain, consistent with the XAS data. Finally, at the end of discharge, another shoulder peak is observed as it can be seen in Figure III-12d. We attribute this peak shape to the formation of a third phase during DN6 crystalizing in F m -3 m with a = 4.225 Å.

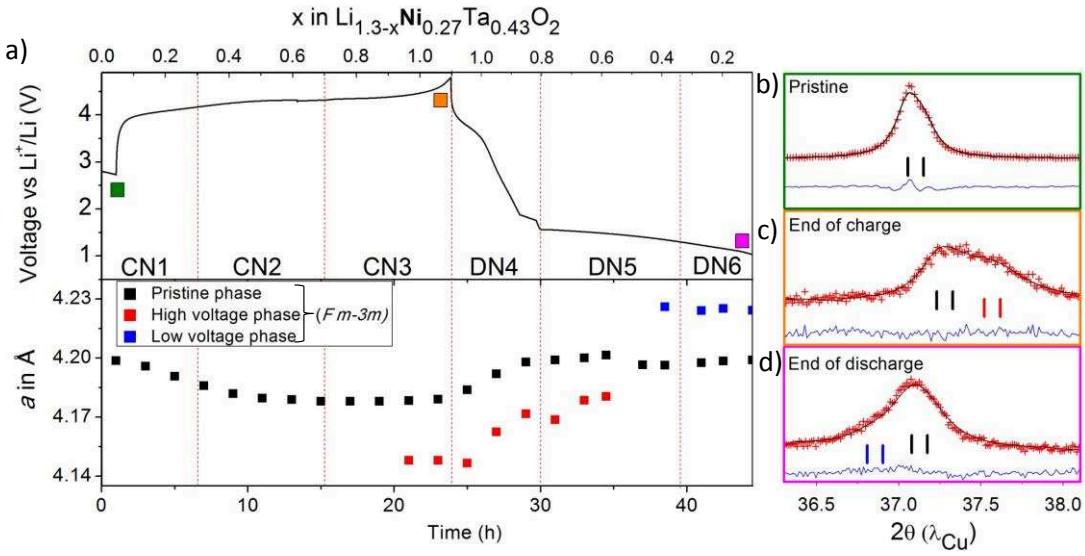

Figure III-12: a) Voltage-composition curve of the galvanostatic cycling, C/20, during operando XRD measurement together with the cell parameter variation extracted from the patterns using Rietveld refinement. Black, red, and blue dots correspond to the cell parameters of the different phases. b-c-d) Rietveld refinement of specific patterns of the operando experiment. The red crosses, black continuous line and bottom blue line represent the observed, calculated, and difference patterns respectively. Vertical green tick bars are the Bragg positions.

III.3.e Overall picture

Altogether these data provide an accurate description of the material's evolution during the first charge that can be schematically summarized in Figure III-13. During CN1, 0.3 Li is extracted thanks to the oxidation of mainly Ni^{2+} to ~$Ni^{2.7+}$ causing the decrease of the unit cell parameter together with a small contribution of anionic redox. Upon further oxidation, the removal of the 0.4 extracted Li (CN2) is associated with the oxidation of oxygen with a minor contribution of Ni oxidation from ~$Ni^{2.7+}$ to Ni^{3+}. Lastly, when the oxidation is pushed further, oxidation of the oxygen species leads to the departure of O_2 from the material responsible for the reduction of Ni^{3+} to ~$Ni^{2.5+}$ and the formation of the high voltage phase having a smaller cell parameter. Such a phase could correspond to a densified structure as proposed by Lee et al.[135] Upon discharge, there is at high potential (i.e. process DN4) the uptake of 0.25 Li, corresponding the reduction of ~$Ni^{2.5+}$ in Ni^{2+}, prior to the appearance of the potential jump corresponding to the reduction of the oxidized oxygen species which occurs through a highly polarized process. To further understand the relationship between the potential drop and anionic redox, a similar study was performed on $Li_{1.3}Mn_{0.4}Ta_{0.3}O_2$ which shows less hysteresis compared to its Ni counterpart.

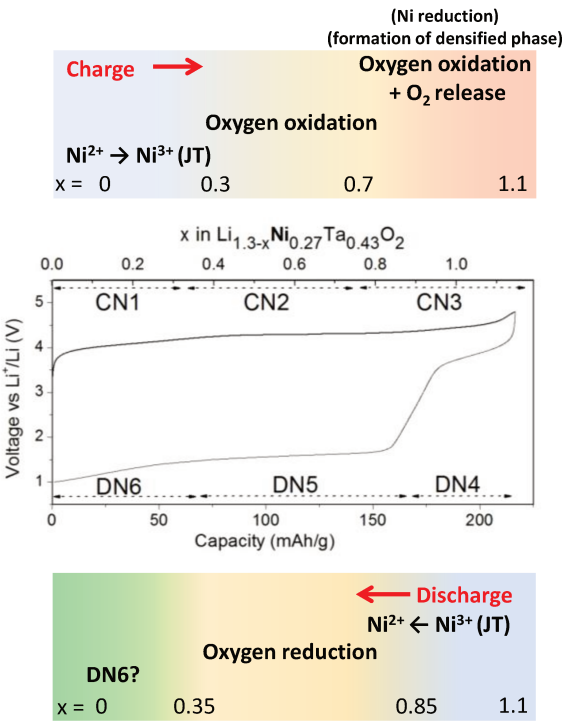

Figure III-13: Schematics presenting the charge compensation mechanism in $Li_{1.3}Ni_{0.27}Ta_{0.43}O_2$. The compensation during DN6 is marked as "DN6?" because still unclear.

III.4 Mechanism of Li removal in $Li_{1.3}Mn_{0.4}Ta_{0.3}O_2$

III.4.a Effect of the state-of-charge

The voltage-composition curve for $Li_{1.3}Mn_{0.4}Ta_{0.3}O_2$ is shown in Figure III-14a together with its dQ/dV profile. Two oxidation peaks at 3.7 V (CM1) and 4.5 V (CM2) can be observed corresponding to the removal 0.4 and 0.5 Li, respectively, and two reduction peaks, one well pronounced at 3.4 V (DM3) and another one (DM4) spread in voltage (3-1 V) corresponding to the insertion of 0.6 and 0.2 Li. Following the same procedure as for the Ni-based compound, we could deduce that both CM1 and CM2 are merged into DM3 in discharge showing the irreversibility of the redox chemistry (Figure III-14b). Moreover note that DM4 appears only after charging at high SOC, hence its straight correlation with CM2. By comparison with the voltage-composition profile for the Ni-based compound, we note that the abrupt potential jump upon reduction is replaced in the Mn-phase by a smoother decay and a lower polarization as deduced from GITT measurements in Figure III-14c.

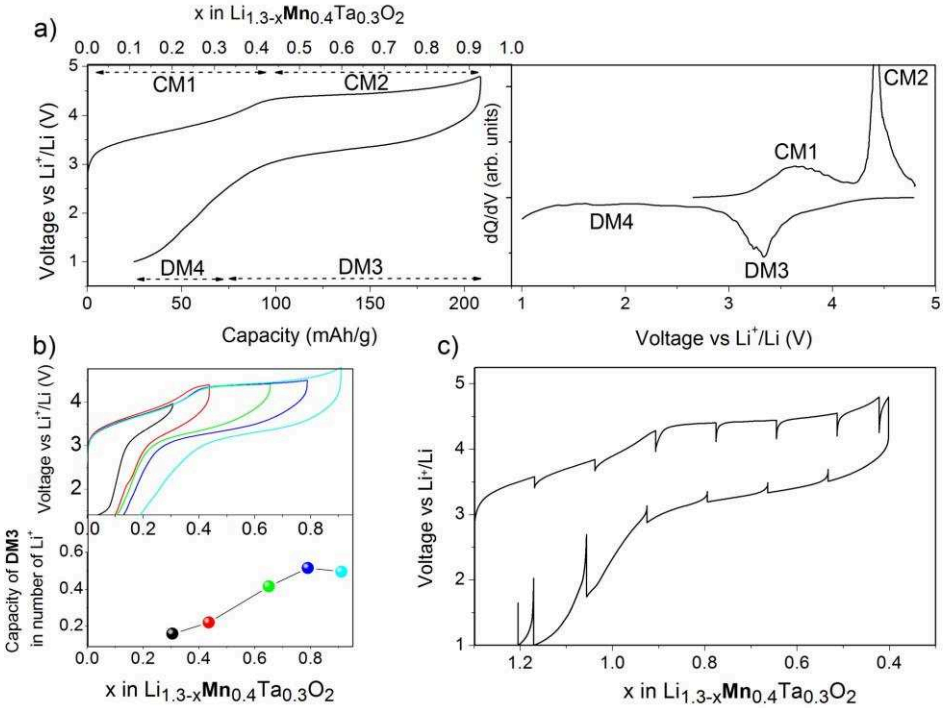

Figure III-14: a) Voltage-composition curve of the 1st galvanostatic cycle of LMTO, at C/20, together with its dQ/dV profile emphasizing the CM1, CM2, DM3 and DM4 processes. b) 1st galvanostatic cycle at different SOC together with the discharge capacity, in number of Li, of DM3 (>3 V) in the bottom panel. c) GITT of the 1st cycle of LMTO at C/20 with 5 hours rest every 3 hours.

III.4.b X-ray absorption spectroscopy study

Operando XAS was performed to access the charge compensation mechanism in $Li_{1.3}Mn_{0.4}Ta_{0.3}O_2$. Following the Mn K-edge position during operando measurement and comparing it with the reference spectra of Mn_2O_3 (Mn^{3+}) and Mn_2O_4 (Mn^{4+}), (Figure III-15a-c), it can be concluded that Mn is 3+ in the pristine material, oxidizes to Mn^{4+} during the first part of the charge (CM1) and remains as such afterwards (CM2). On discharge, Mn^{4+} is continuously reduced back to Mn^{3+} through the DM3 and DM4 processes. A similar trend is obtained from ex situ measurements confirming the reproducibility of the operando data (Figure III-15b).

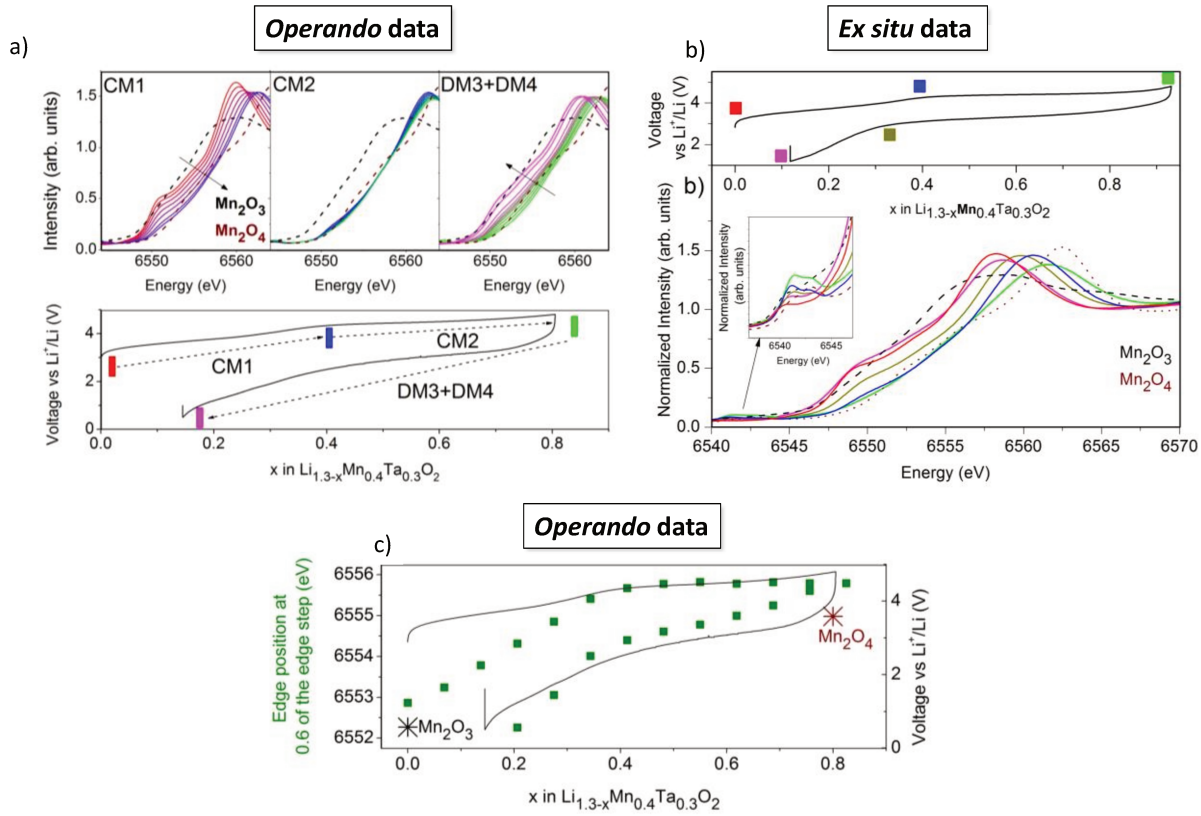

Figure III-15: a) Variation of the Mn K-edge measured operando during the 1st charge and discharge of $Li_{1.3}Mn_{0.4}Ta_{0.3}O_2$ (top) together with the galvanostatic cycling, C/20 (bottom). The data has been divided in three parts called CM1, CM2 and DM3+DM4. Only 1 spectra over 5 is shown for reasons of clarity. b) Ex situ Mn K-edge XANES spectra acquired for samples along the voltage composition curve, C/20, of LMTO marked as squares, bottom and top respectively. Black and wine dotted lines stand for Mn_2O_3 and Mn_2O_4 spectra respectively. c) Evolution of the Mn K-edge position taken at 0.6 of the edge step, in green, together with the voltage composition curve, in black.

The data were further exploited using PCA coupled to MCR-ALS analysis. Seven components were needed to describe the evolution of Mn oxidation state and environment during Li removal/insertion. The evolution of the concentrations of the reconstructed components together with the XANES and the analysis of their EXAFS oscillations are presented in Figure III-16a-b-c and in Table III-4. In the pristine compound, Mn^{3+} sits in a Jahn-Teller distorted environment, with 4 short (1.934 Å) and 2 long (2.32 Å) Mn – O bonds, which converts to a regular environment, 6 Mn – O bonds of 1.901 Å, when Mn^{3+} is oxidized to Mn^{4+}. Upon further oxidation (CM2), the Mn environment distorts again forming 4 short (1.885 Å) and 2 long (2.38 Å) Mn – O bonds, while its oxidation state remains constant (4+) implying a non-passive role of the anionic network. During reduction, the Mn environment converts back to the pristine following nearly the same transformation while Mn continuously reduces from +4 to +3.

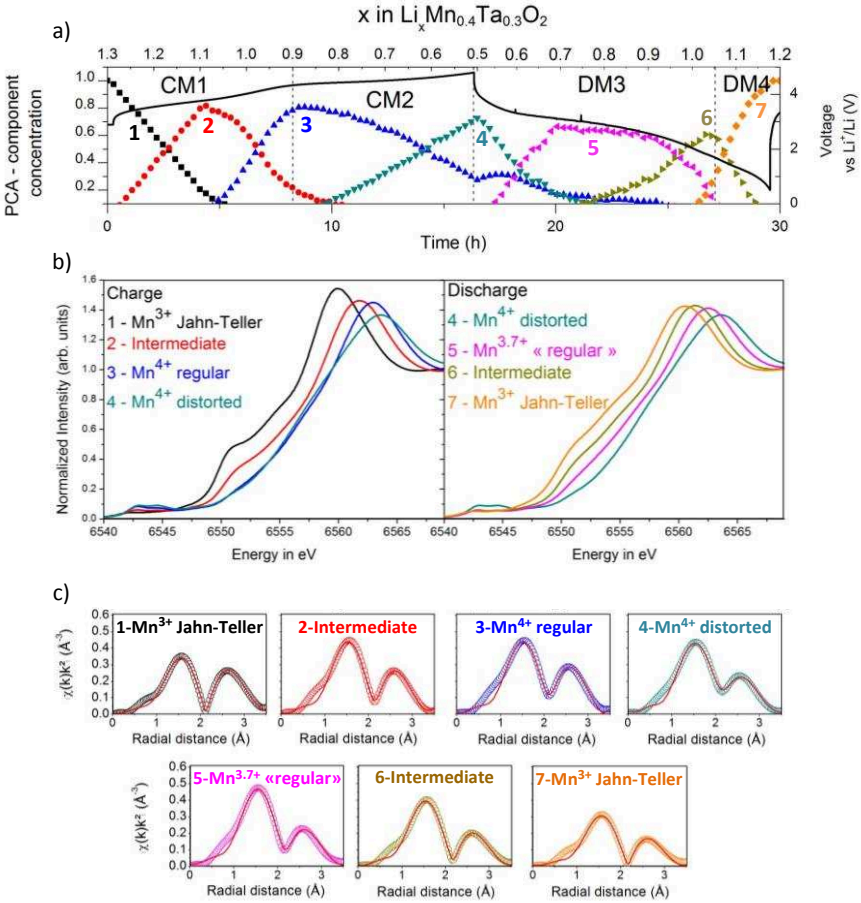

Figure III-16: a) Concentration evolution obtained by MCR-ALS during the operando measurement, dots, together with the galvanostatic cycling, C/20, in black. b) Mn K-edge XANES spectra of the reconstructed components. c) Fit of the magnitude of the Fourier transforms of the EXAFS oscillations performed on the reconstructed spectra of the components.

Reconstructed components	1st Mn – O shell					2nd Mn-Mn shell				2nd Mn – Ta shell			
	CN	dMn-O	CN	dMn-O	σ *10³	CN	dMn-Mn	CN	dMn-Mn	CN	dMn-Ta	σ *10³	R*10³
Mn^{3+} Jahn-Teller	4	1.934(8)	2	2.32(4)	6.3(6)	0.8	2.61(4)	1.6	3.01(2)	1.8	3	7.3(7)	1.8
Intermediate	5	1.91(2)	1	2.35(15)	5.7(7)	0.4	2.62(18)	2	2.976(14)	1.8	3	9.1(9)	6.2
Mn^{4+} regular	6	1.901(4)	-	-	7.0(5)	-	-	2.4	2.951(9)	1.8	3	9.8(9)	7.1
Mn^{4+} distorted	4	1.885(4)	2	2.394(14)	3.8(5)	-	-	2.4	2.954(14)	1.8	3	13.4(15)	7.2
$Mn^{3.7+}$ « regular »	2	1.811(15)	4	1.943(3)	2.1(12)	-	-	2.4	2.967(7)	1.8	3	11.1(7)	3.6
Intermediate	5	1.918(5)	1	2.32(5)	6.2(4)	0.4	2.64(6)	2	3.002(11)	1.8	3	11.5(12)	4.2
Mn^{3+} Jahn-Teller	4	1.928(5)	2	2.29(3)	7.4(6)	0.8	2.60(4)	1.6	3.021(12)	1.8	3	9.9(9)	6.7

Table III-4: Structural parameters obtained by fitting the Mn K-edge EXAFS oscillations of the reconstructed components during operando measurements for LMTO. CN, d, and σ stand for Coordination Number, distance in Å and the Debye-Waller factor in Å². The difference energy threshold, E0, and the amplitude reduction factor (S_0^2) are fixed during fit. S_0^2 was taken equal to 1 for all analysis.

Figure III-17 and Figure III-18 show ex situ Ta L_3-edge XAS measured after CM1, CM2, DM3 and DM4 to assess to participation of Ta in the redox mechanism. It can be seen that nearly no change could be observed in the XANES or EXAFS region proving Ta is inactive during the electrochemical cycle.

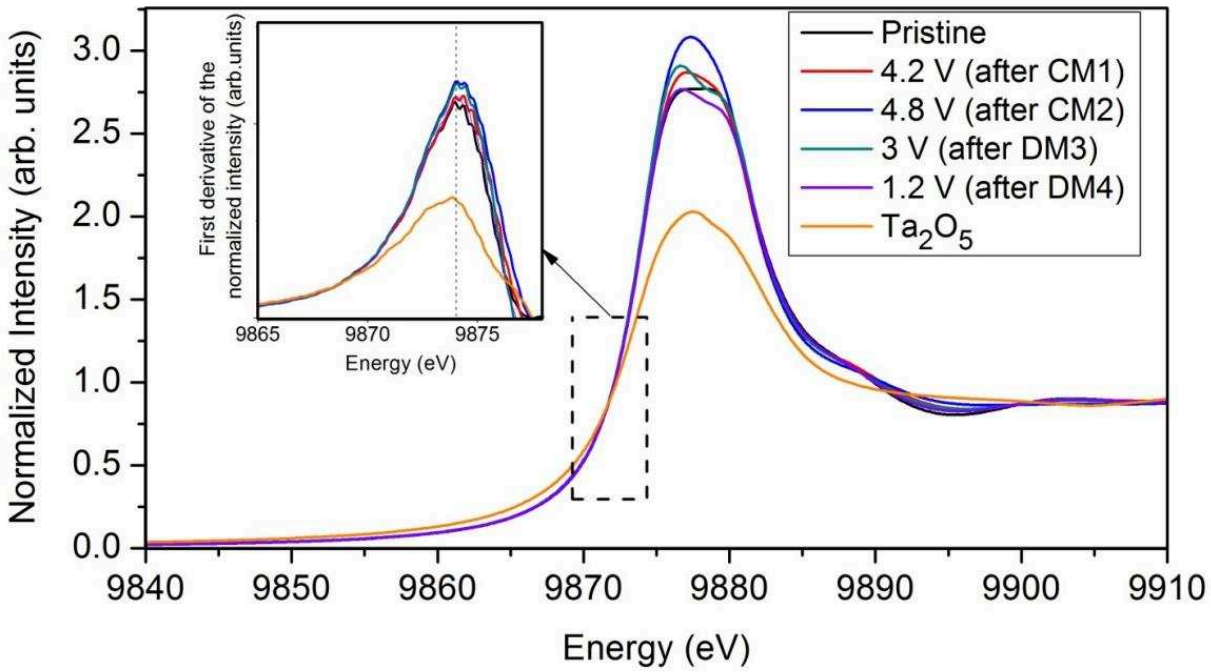

Figure III-17: Ex situ Ta L3-edge XANES spectra together with their first derivative curve for ex situ samples along the galvanostatic cycling of LMTO.

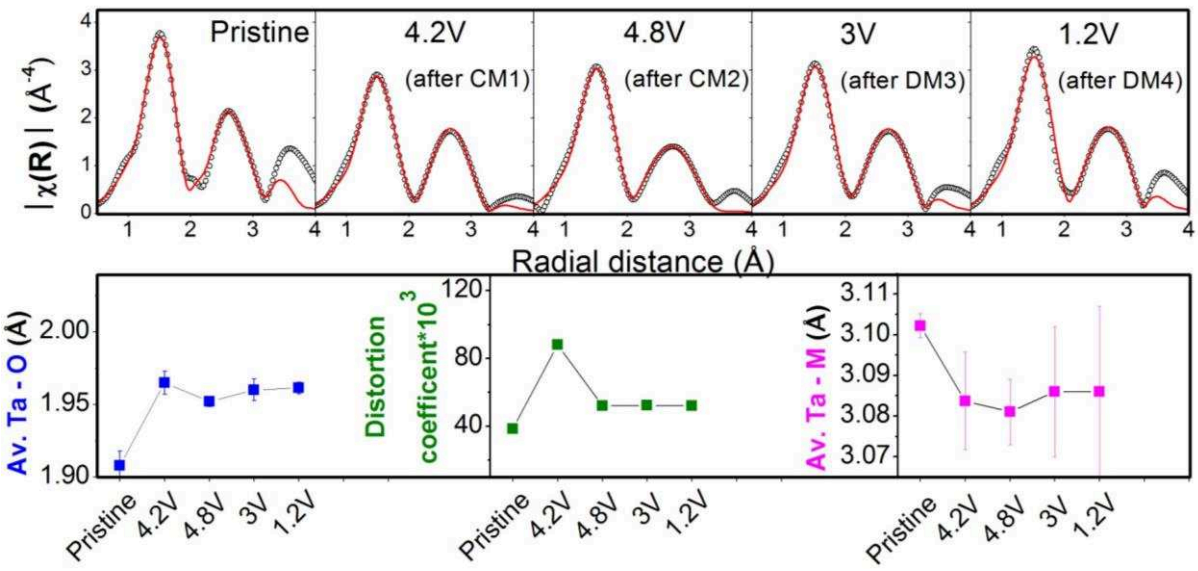

Figure III-18: On the top, magnitude of the Fourier transforms of the Ta L_3-edge EXAFS oscillations on ex situ LMTO with the solid representing the model fitting. On the bottom and from left to right, average Ta-O bond length, distortion coefficient of TaO_6 and average Ta – M bond length as extracted from the EXAFS fitting. Distortion coefficient is calculated according the formula: $\Delta^{M-O} = \frac{1}{6}\sum_{i=1}^{6}\left[\frac{d_i - <d>}{<d>}\right]$

At this stage, to interrogate the oxygen activity, ex situ O K-edge spectra were collected on samples recovered from $Li_{1.3}Mn_{0.4}Ta_{0.3}O_2$ /Li cells stopped at the end of CM1 (4.2 V and x = 0.4), CM2 (4.8 V and x = 0.9) and DM4 (1 V and x = 1.2). The results are shown in Figure III-19a together with the spectra differences, processed as before showing the main evolution is centered at 527 eV and 528.7 eV. From O pDOS calculated via DFT (Figure III-19b), we can attribute the 527 eV feature to Mn-O states which is consistent with the observed intensity increase during CM1 and its constancy through CM2. Similarly, the second peak at 528.7 eV which increases during CM2 is attributed to the anionic redox bearing in mind that Mn and Ta are inactive in this region. It is worth mentioning that in both LNTO and LMTO, the O K-edge feature associated to anionic redox appears at the same energy. This is consistent with the fact that anionic redox involves the oxidation of non-bonding levels which energy only depends on electrostatic interactions being of similar amplitude in LNTO and LMTO.

Overall, it results that LNTO and LMTO compounds show anionic redox activity associated to a voltage hysteresis, but it still remains to understand why the hysteresis is larger in LNTO compared to LMTO

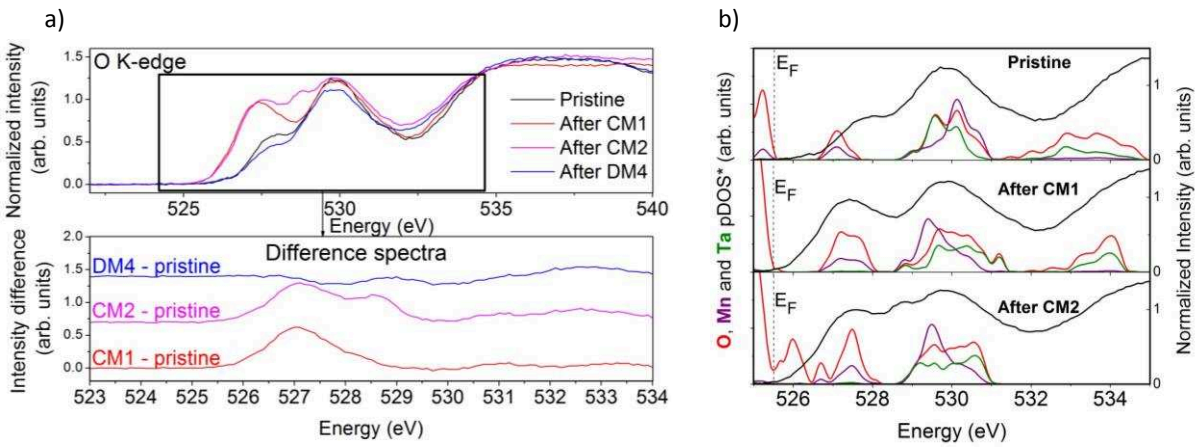

Figure III-19: a) O K-edge XAS, acquired in total fluorescence mode (TFY), spectra for ex situ samples of LMTO during the charge and discharge, together with the difference spectra between the pristine and the spectra of the ex situ samples in the bottom insert. b) Comparison of the TFY O K edge data (black) at various state-of-charge with the empty O, Mn and Ta pDOS in red, purple and green, respectively. Note that the intensity of the Mn and Ta pDOS has been modified for graphical purposes. Oxidized oxygen states could not appear at the correct energy on the pDOS due to the valence shift of the O1s states.

III.4.c Gas evolution

To check the outcome of the anionic redox species in LMTO, we performed OEMS. No gas evolution (Figure III-20) was detected through CM1 while a copious amount of CO_2 which is likely coming from electrolyte decomposition, is observed afterwards (CM2).[141] Minute traces of O_2 towards the extreme end of the charge are observed in contrast with the large O_2 release observed for the Ni-based compound.

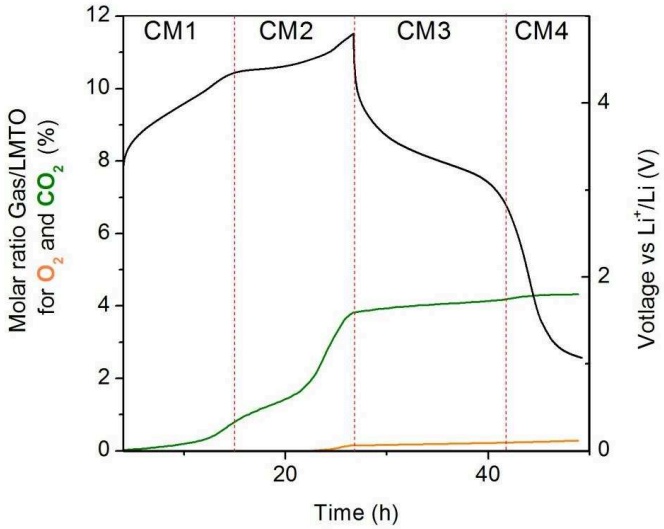

Figure III-20: OEMS results for LMTO, showing the evolution of the molar ratio between O2 and CO2 and the active material, in orange and green, together with the galvanostatic cycling data at C/30.

III.4.d Structural evolution

Further assessing the difference between LNTO and LMTO, operando XRD has been carried on. Figure III-21 presents the voltage-composition curve together with the XRD patterns and the a cell parameter obtained from Rietveld refinement of LMTO during cycling. Interestingly, a decreases from 4.1975(11) Å to 4.129(3) Å during Mn^{3+}/Mn^{4+} oxidation, in agreement with EXAFS data, and then remains constant while showing a peak broadening. A continuous decrease of a is observed on the subsequent discharge. We recall that under the same oxidation process for LNTO, we have note the appearance of an extra phase which is not observed here. One should notice that at the very end of discharge, there is the appearance of an asymmetric peak broadening. It is attributed to the formation of a shoulder peak that can be indexed with a 2nd phase having the same structure as the pristine with slightly larger cell parameters, 4.211(3) Å compared to 4.1975(11) Å for the pristine.

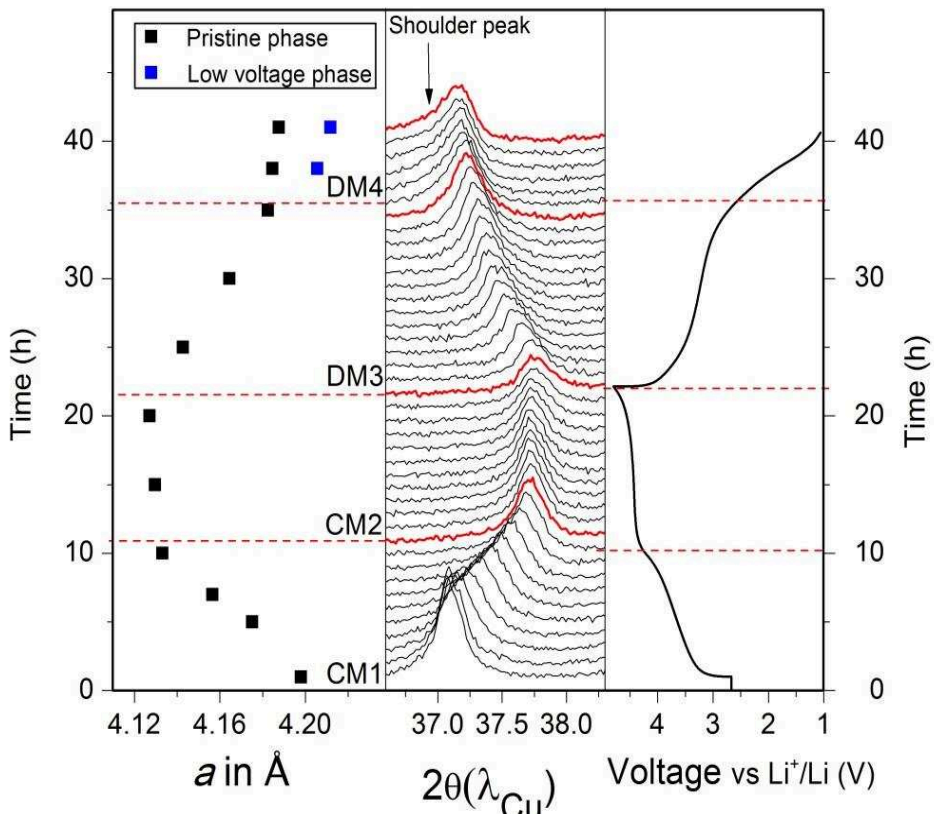

Figure III-21: Voltage-composition curve at C/20, patterns and cell parameters extracted from Rietveld refinement of the operando XRD measurement from right to left.

III.4.e Overall picture

Overall, we could unveil the redox mechanism of $Li_{1.3}Mn_{0.4}Ta_{0.3}O_2$, schematized Figure III-22, thanks to complementary operando techniques. During the first part of charge, manganese oxidizes from Mn^{3+} to Mn^{4+}, resulting in the shrinkage of the unit cell volume, and then, for the second part of charge, oxygen oxidizes at higher potential without any long range structural change or gas released from the structure but local distortion around the Mn atoms During lithium insertion, both oxygen and manganese reduce at the same time causing a slow expansion of the unit cell. This mechanism drastically differs from the one previously established for LNTO by the potential at which anionic reduction occurs; 3V for LMTO as opposed to 1.5V for LNTO. Additionally, a greater stability of LMTO over LNTO against O_2 release was observed. Next, we try to rationalize this finding by DFT calculations.

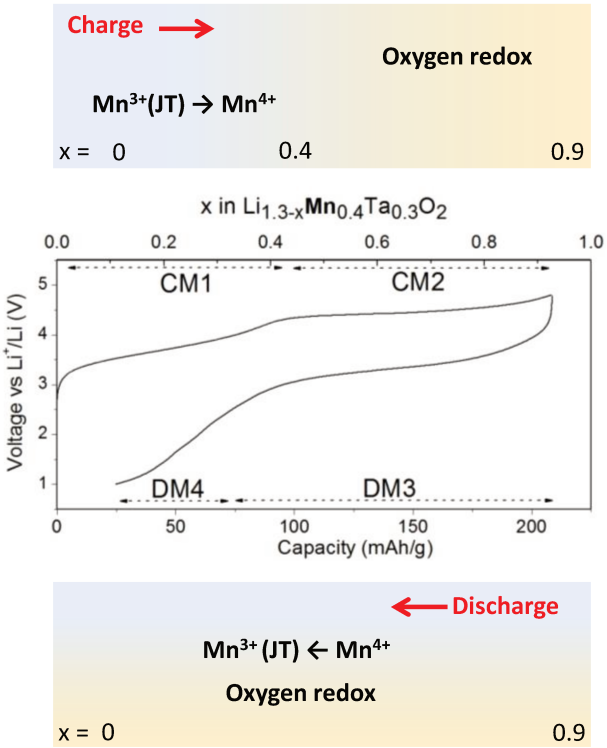

Figure III-22: Schematics representing the charge compensation mechanism for $Li_{1.3}Mn_{0.4}Ta_{0.3}O_2$

III.5 Understanding the different anionic redox mechanisms using DFT calculations

III.5.a Construction and validation of structural models

III.5.a.i Cluster expansion method

Bearing in mind DFT calculation cannot be performed on cation disordered configurations, ordered models need to be found for LNTO and LMTO. Along that line, a homemade cluster expansion code, described in the Annexe F.2, has been used to identify low energy cationic configurations in the pristine materials, $Li_{1.3}Ni_{0.27}Ta_{0.43}O_2$ and $Li_{1.3}Mn_{0.4}Ta_{0.3}O_2$. Note that, to avoid partial occupancy, the minimum unit cell for the $Li_{1.3}Ni_{0.27}Ta_{0.43}O_2$ composition would contain 200 cations and anions, which is too much for practical DFT calculations. Therefore, the chemical composition of the theoretical model was chosen to be $Li_{1.3}Ni_{0.3}Ta_{0.4}O_2$. The structural search was carried out in two steps. First, Ta networks minimizing the unfavorable Ta – Ta next-nearest neighbors (NNN) were chosen. Indeed, the energy of the structure is drastically influenced by the number of NNN Ta – Ta interactions as shown in Figure III-23a-b. Second, all the possible Li and Ni/Mn configurations were generated and the most stable structures were selected for further analysis. To assess the validity of our approach, we computed the DFT energy of the 50 lowest energy structures deduced from our cluster expansion calculations, and compare these energies to the DFT energy of random cation orderings, as shown in Figure III-23c-d. It can be seen that using our cluster expansion code, we could identify low energy cation ordering with negligible computational cost.

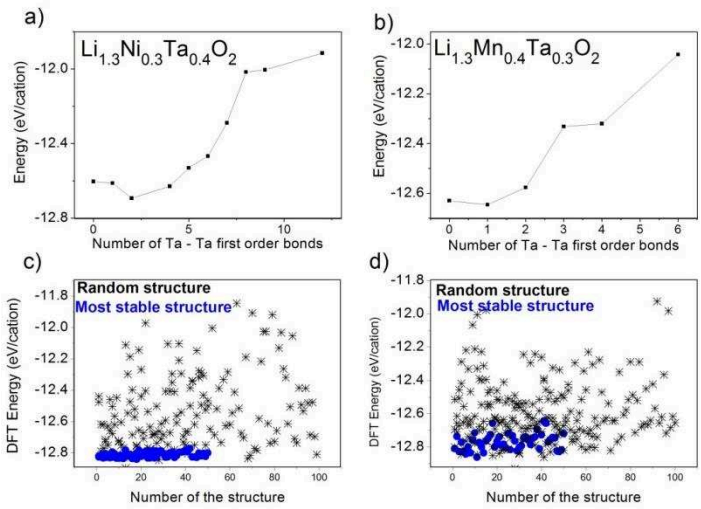

Figure III-23: a) and b) Variation of the average energy of the cation configuration, calculated by cluster expansion, with the number of first order Ta –Ta bonds for $Li_{1.3}Ni_{0.3}Ta_{0.4}O_2$ and $Li_{1.3}Mn_{0.4}Ta_{0.3}O_2$, respectively.

c) and d) DFT energy for random structures (black cross) and for the most stable structures (blue dots) found using the cluster expansion, for $Li_{1.3}Ni_{0.27}Ta_{0.43}O_2$ and $Li_{1.3}Mn_{0.4}Ta_{0.3}O_2$, respectively.

III.5.a.ii Validation of the structural models

Further assessing the goodness of our model structures, we compare the calculated electrochemical charge compensation mechanism with our experimental findings in Figure III-24. Convex Hull diagrams, produced from the delithiation of stable structural models, presented in Figure III-24a-b, show Li removal from LNTO and LMTO is done in two and five steps, respectively, with the calculated voltages in agreement with the GITT curves (Figure III-24c-d). Stability versus O release, assessed calculating the reaction enthalpy of $Li_xMO \rightarrow Li_xMO_{1-y} + y/2\ O_2$, shows LNTO should rapidly evolve O_2 upon charging while in the LMTO case, O_2 evolution should only be effective at the end of charge, in agreement with our OEMS data. Moreover, Ni and Mn Bader charges increase during the 1st part of charge and stay constant upon further charging (Figure III-24e-f), consistent with our XAS analysis. Concerning the O Bader charge, it increases at the beginning of charge due to the increase of the M-O covalency and upon further charging because of anionic redox (Figure III-24g-h). The activation of anionic redox can be seen (Figure III-25a-b) nicely by the presence of pure oxygen states at the fermi level for both compounds right after the cationic process, i.e. $Li_1Ni_{0.3}Ta_{0.4}O_2$ and $Li_{0.9}Mn_{0.4}Ta_{0.3}O_2$ compositions. Overall, the good agreement between theoretical and experimental findings suggests that our models are adequate.

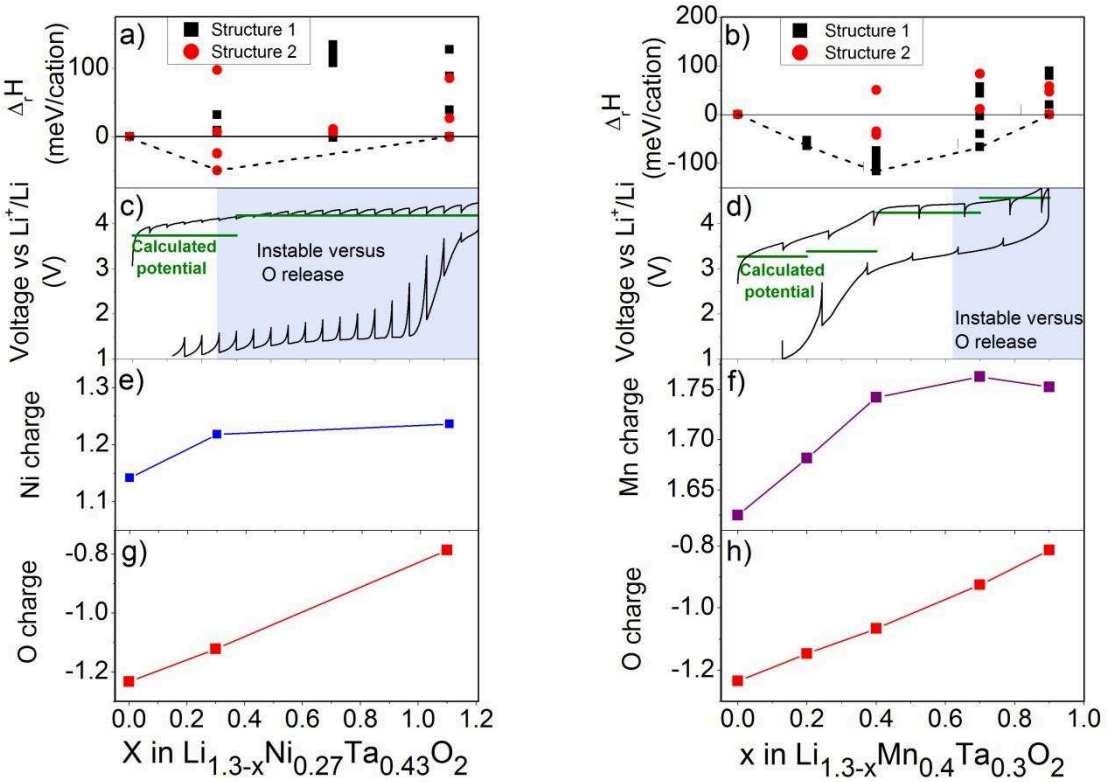

Figure III-24: a) and b) are Convex Hull diagrams, c) and d) are calculated voltage profiles superimposed on GITT data, in green and black, together with O release stability regions, e) and f) shows the variation of the Ni and Mn Bader charge, respectively, g) and h) the O bader charge, for LNTO and LMTO, respectively.

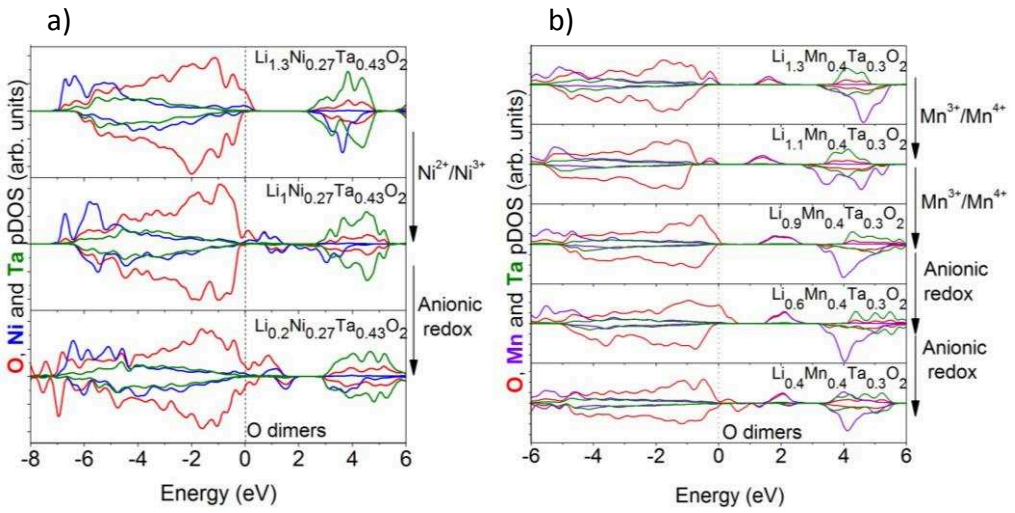

Figure III-25: a) and b) O, Ni, Mn and Ta pDOS in red, blue, purple and green, respectively for LNTO and LMTO at different state-of-charge.

III.5.b The band gap at the origin of the different anionic redox mechanism

Looking closely into the electronic band structure of $Li_{1.3}Ni_{0.3}Ta_{0.4}O_2$ (Figure III-26a), we found that while the pristine displays a large Mott-Hubbard band gap, consistent with the strong electronic stabilization expected for a half-filled system (Ni^{2+} $t_{2g}^6e_g^2$ electronic configuration),[142] $Li_{0.9}Ni_{0.3}Ta_{0.4}0_2$ displays a narrow charge transfer gap, denoted as Δ_{CT} in Figure III-26b, due to the Jahn-Teller distortion of Ni^{3+}. Amusingly, the partial delithiation of $Li_{1.3}Mn_{0.4}Ta_{0.3}O_2$ into $Li_{0.9}Mn_{0.4}Ta_{0.3}O_2$ leads to the reverse scenario. The narrow Jahn-Teller band gap (Mn^{3+}) for pristine LMTO becomes a wide charge transfer gap in the oxidized sample due to the large Mott splitting of the Mn^{4+} half-filled t_{2g}^3 states. This difference in charge transfer gaps prior the occurrence of the anionic activity is at the origin of the different anionic redox mechanism.

During anionic redox, for both compounds the top portion of the non-bonding oxygen band (magenta in Figure III-26b-c) is emptied.[79,78] Bearing in mind that we are dealing with disordered structure the oxygen non-bonding states are not equal with respect to their cationic environment, therefore the first oxidized oxygen atoms are those having the lowest cationic charge in their first coordination shells. Their oxidation leads to the formation of O – O dimers having σ, π, π* and σ* discrete bands, with the π* and σ* states being as high in energy as the O-O bond is short. When these antibonding states cross the first empty metallic band, electron transfer from the O to the metal is expected, leading to O_2 release together with the reduction of the transition metal (Figure III-26c). This situation is exemplified by the Ni-based material showing a small charge transfer band gap, significant O_2 release together with Ni reduction. In contrast, the Δ_{CT} in the Mn-based compound is large enough to stabilize the oxidized oxygen species preventing O_2 release. Turning to the discharge, as long as the σ* of the oxygen level remains lower than the first empty M band, no hysteresis is expected, and we will have the following redox process sequence cation → anion (charge) and anion → cation (discharge). In contrast, for the LNTO, in which the empty σ* is higher than empty M band, the sequence is inversed: cation→ anion and cation → anion for charge and discharge, respectively. Lastly, if the σ* and transition metal states are roughly at the same energy, cationic and anionic redox could proceed simultaneously in reduction, as found for LMTO. At this stage a remaining question regards the large difference in the anionic redox potential between LMTO (3 V) and LNTO (1.5V). A likely explanation is rooted in our previous

described inversion redox process for LNTO with the metallic reduction affecting the nature of the anionic species and hence their reduction potential.

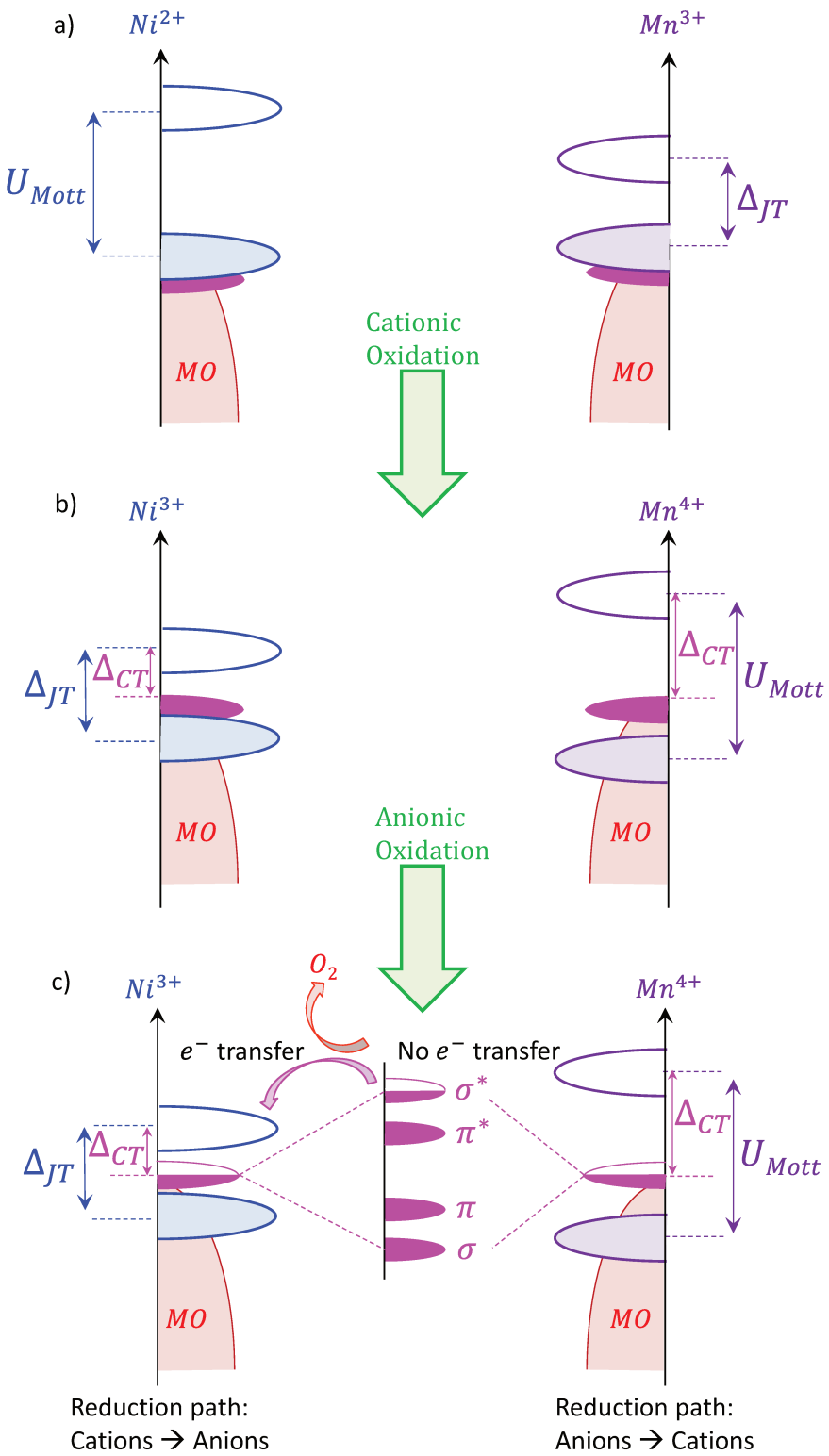

Figure III-26: a), b) and c) are schematics of the Density of State (DOS) for pristine LNTO and LMTO, after the cationic process and during the anionic process, respectively. Blue, purple, magenta and red states stand for Ni-O*, Mn-O*, O non-bonding and O(2p) states, respectively.

III.6 Conclusion of the chapter

We have provided a detailed description of the evolution of two new disordered rocksalt compounds during Li insertion/removal, namely $Li_{1.3}Ni_{0.27}Ta_{0.43}O_2$ and $Li_{1.3}Mn_{0.4}Ta_{0.3}O_2$. First, we found these materials to have similar characteristics than the Nb-based or Ti-based ones previously reported, suggesting that their redox mechanism is nearly transparent to the nature of d^0 transition metals provided they have similar ionic radii.[143] Second, we demonstrate that both compounds show anionic redox reactivity with a few differences, namely a higher hysteresis and instability against O_2 release in the Ni-based compound. We introduce the notion of charge transfer band gap to account for such a difference.

Turning to the origin of the voltage drop in the discharge curve, already observed in other disorder rocksalt phases ($Li_{1.2}Ni_{0.33}Ti_{0.33}Mo_{0.16}O_2$) showing anionic redox activity, it was proposed to be nested in kinetic limitations associated with diffusion/migration.[135] However, the constancy of the voltage hysteresis whatever the current rate applied, as experimentally determined, suggests that thermodynamics plays a key role as well. Besides, cationic migration in Li-rich layered oxides has also been proposed as source of the voltage hysteresis.[70] This claim is not inconsistent with our model, since cationic migration triggers new oxygen environment, depleted in charge, hence affecting the relative position of the oxygens states with respect to the band gap so that hysteresis can occur.

These findings open new perspectives to design Li-based disordered rocksalt compounds showing anionic redox with limited voltage hysteresis provide that we can tune the band gap. Several clues can be formulated. First, transition metals suffering electronic instabilities such as Fe^{4+} (d^4) and Ni^{3+} (d^7) should be banned, unless we could stabilize Fe^{5+} (d^3) which is quite unlikely without high chemical/physical pressure. Concerning Ni, destabilizing the Ni^{3+} to the expense of the Ni^{4+} by decreasing the framework covalency could be attractive. Along that line, Ceder et al. proposed the partial substitution of O by F to successfully increase Ni oxidation in $Li_{1.2}Ni_{0.33}Ti_{0.33}Mo_{0.16}O_2$, but with a limited effect on the hysteresis due the narrow substitution range.[144] An alternative strategy has been the use of other closed shells metals like d^{10} in $Li_{1.15}Ni_{0.52}Sb_{0.38}O_2$ or Li_4NiTeO_6 favoring the Ni^{2+}/Ni^{4+} redox couple but with the drawback of suppressing the anionic redox activity.[145,146] An attractive midway scenario could consist in mixing d^0 and d^{10} cations to have Ni^{4+} coexisting with anionic redox. At last, using the charge transfer band gap as an indicator, it appears that Mn is the best element for disordered rocksalt phases showing both anionic redox and low hysteresis.

Whether purely coincidentally or not the recently reported disordered rocksalt phases $Li_{1.2}Mn_{0.4}Ti_{0.4}O_2$ and $Li_4Mn_2O_5$ (RT) show hysteresis of 0.6 V (50°C) and 1.3 V (RT), respectively.[77,56]

Discussion and General Conclusion

Anionic redox is hot a topic because it allows to drastically increase the specific energy of Li-ion batteries thanks to the participation of the oxide anions in the redox reactions. However, it is the source of kinetic limitation and voltage hysteresis, hence the need to understand and master this intriguing phenomenon. Along that line, we designed models compounds to investigate two important characteristics of anionic redox, namely, i) its limit in terms of capacity and ii) its redox potential.

To push anionic redox to its limits, we focused on A_3MO_4 compounds (A and M being an alkali and a transition metal) having a high O/M ratio and consequently, an elevated number of oxygen lone pairs. First, we synthetized binary compounds $Li_3M_yM'_{1-y}O_4$ (M and M' being Ru, Ir, Nb, Sb and Ta) and unveiled a rich crystal chemistry, based on different cation orderings in a rocksalt lattice, caused by the competition between electrostatic and electronic effects (Second order Jahn-Teller). Turning to the redox mechanism, anionic redox in Li_3IrO_4 was shown to lead to massive O_2 release, due to the destabilization of the oxidized oxygen species, which is also observed in the $Li_3Ru_yIr_{1-y}O_4$ compounds for $y > 0$. Interestingly, no O_2 evolution is found during the oxidation of Li_3RuO_4 which could be explained by the presence of cationic redox, at the end of charge, limiting anionic redox. The relative cationic/anionic capacities can be tuned by the nature of the alkali ions as shown by the existence of Na_2RuO_4 (having Ru^{6+}) during Na removal from Na_3RuO_4. Finding the right balance between cationic and anionic redox could be beneficial for the battery performances; however, cationic redox leads to the dissolution of high oxidation state Ru species (RuO_4/RuO_4^-) causing irreversibility. Blocking the dissolution using a solid electrolyte, for instance, is an interesting perspective for Li_3RuO_4 and Na_3RuO_4 since it would allow the use of the full capacity of these materials, 430 and 360 mAh/g, respectively. As a perspective, also Ru dissolution plagues the materials electrochemical behavior as Li/Na cathode materials, the formation of RuO_4/RuO_4^- paves the way towards a rich Ru solution chemistry, especially in terms of synthesis pathways. Indeed a controlled reduction of these high oxidation state species in soft conditions could lead to the formation of metastable phase as suggested by the study of Hiley et al.[147]

In a second part, we studied the correlation between anionic redox and electrochemical potential in the framework of disordered rocksalt. Indeed, Ni-based disordered rocksalt oxides, having anionic redox activity, suffer from low energy efficiency due to the presence of a voltage drop during discharge, in contrast to the Mn-based ones. To elucidate the origin of this behavior, we reported the comparison between two new disordered rocksalt compounds showing anionic redox activity, $Li_{1.3}Ni_{0.27}Ta_{0.43}O_2$ and $Li_{1.3}Mn_{0.4}Ta_{0.3}O_2$. We found that the voltage drop is nested in the anionic redox mechanism, which is dependent on the nature of the transition metal through the charge transfer gap but not on the type of d^0 substituted element. Indeed, in the Ni-based compound, the presence of a Jahn-Teller Ni^{3+} during charge leads to the formation of a narrow charge transfer band gap triggering O_2 release and Ni reduction upon anionic oxidation. During the subsequent discharge, hysteresis and voltage drop are observed. In contrast, in the Mn-based compounds, due the presence of Mn^{4+} which shows half-filled t_{2g}^3, a large charge transfer band gap is found stabilizing oxidized oxygen species and therefore leading to weak O_2 release and moderate hysteresis. These results give evident guidelines to design cathode materials for Li-ion battery, i.e. opening the band gap to limit O_2 release. However, O_2 release is not always negative. Oxygen Evolution Reaction (OER), being the formation of O_2 from the oxidation of water, is an important reaction for energy conversion with the most active catalysts being oxides having a small charge transfer band gap.[148,149,150] For these materials, recent studies have shown that part of the O_2 formed actually comes from the material itself in agreement with our findings. Without surprise, we found a very high OER activity for LNTO as compared to LMTO showing the narrow connection between these two fields and the need to further assess the activity of Li/Na-ion battery cathode material as OER catalysis.[151]

As a conclusion, let's think about the next steps for anionic redox. Practically speaking, Li-rich NMC have been discovered more than 15 years ago[60] and, despite great research efforts, are still not ready for application mostly because of kinetic and voltage hysteresis issues limiting their power performances and energy efficiency.[75] In only 5 years, fundamental studies have being able to understand the origin of these drawbacks but practical ways to solve these issues still has to be found.[66,78] Therefore, the dream of anionic redox is slowly vanishing and the battery research is now moving towards Ni-rich NMC or oxyfluorides cathodes, mainly relying on cationic redox. Despite this disillusion, studying anionic has allowed the development of characterization techniques such as gas analysis[108], operando

EPR[72], or spectroscopic techniques enlisting XAS[152] or RIXS and the formulation of new solid state theoretical models[79]. All these tools will be very useful to study other redox mechanisms.

Moreover stepping away from battery, compounds showing anionic redox are also called, in the solid state physics community, negative charge transfer compounds.[87] They have interesting physical properties enlisting superconductivity,[153,154] oxygen 2p magnetism in d-free compounds [155,156] or exotic metal-insulator transition.[157,158,159] In our quest towards high capacity electrode materials, we have synthetized a myriad of negative charge transfer compounds whose electronic regime can be tuned by Li/Na insertion/extraction, representing, hopefully, a rich and still unexplored playground for solid state chemists and physicists.

Annexe

A Synthesis and sample preparation

A.1 Precursor grinding

The synthesis of the new compounds, having a high number of different elements in their chemical composition, has been possible thanks to careful grinding which permits an intimate mixing of the precursors before reaction. Planetary ball mill, Pulverizette 7, with zirconia jars of 45 mL, 12 zirconia balls of 10 mm diameter and 1 g of precursor mix has been used. Grinding time varied from 1 h to 13 h with a rotation speed of 600 rpm.

B Structural characterization

B.1 X-Ray Diffraction (XRD)

XRD patterns were collected with a BRUKER D8 Advance diffractometer with Cu Kα radiation ($\lambda_{K\alpha1}$=1.54056 Å, $\lambda_{K\alpha2}$=1.54439 Å) and a Lynxeye XE detector. Air sensitive samples are measured in a special air-tight sample holder. Operando X-ray powder diffraction (XRD) measurements were done using a home-made airtight electrochemical cell equipped with a Be window, reported by Leriche et al. [160]

B.2 Synchrotron X-Ray Diffraction (SXRD)

Synchrotron X-ray diffraction measurements (SXRD) were performed on the 11-BM beamline of the Advanced Photon Source (APS) at Argonne National Laboratory (ANL), with a wavelength ranging from 0.459259 Å to 0.414167 Å depending on the samples. The powder was mixed with an appropriate amount of amorphous silica to limit absorption, and placed in kapton capillary (Ø 0.7 mm). Ex situ samples that are air-sensitive, were sealed in a glass capillary (Ø 0.7 mm).

B.3 Neutron Powder Diffraction (NPD)

Neutron powder diffraction patterns were measured on the D1B powder diffractometer at ILL (Institut Laue-Langevin) with $\lambda \approx 1.29$ Å. Vanadium sample holders of 5 mm diameter were used. For air sensitive samples, the holders are sealed in an argon filled glovebox.

Absorption of the samples was calculated, from the NIST website, and taken into account in the analysis.

B.4 Rietveld refinements

XRD simulations, Rietveld refinements and bond valence sum calculations were performed using the Fullprof suite.[161]

C Electrochemical characterization

C.1 Electrode preparation

The positive electrode material was ground in SPEX-type ball mill for 20 min with 20% carbon SP, for A_3MO_4 compounds (M being Ru, Ir, Nb and A Li or Na) and 60 min with 20% carbon SP, for $Li_{1.3}Ni_{0.27}Ta_{0.43}O_2$ and $Li_{1.3}Mn_{0.4}Ta_{0.3}O_2$. The grinding conditions were: loading of 200 mg in a 15 mL stainless steel vial using 1 ball of 10 mm diameter. The formed active material/carbon composite was used as such for electrochemical testing or mixed with PTFE to form self-standing electrodes. For the electrode preparation, 10% in weight of PTFE is ground with the active material/carbon mix in a pestle and mortar until a paste is obtained. The paste is then rolled and folded many times using a volatile solvent (DMC) until a plastic film is formed. Once the film is formed, the solvent is dried under vacuum.

C.2 Electrochemical cells

All the electrochemical characterization was performed in Swagelok-type cells. Whatmann GF/D borosilicate glass fiber sheets were used as separators. The anode was a Li/Na metal foil. The electrolyte was LP100 – 1/1/3 EC/PC/DMC with 1M $LiPF_6$ for Li-ion batteries, unless something else is specified. For Na-ion batteries, 1M $NaPF_6$ in PC is used as the electrolyte. All cells were assembled in Ar-filled glovebox.

Operando XRD or XAS experiments are conducted in specific cells possessing 1 or 2 beryllium windows, respectively, described by Leriche et al.[160] Be is used because it is nearly transparent to X-rays (weak z). Note that over 3.5 V, vs Li^+/Li, Be suffers oxidation, therefore a very thin aluminum foil is placed between the Be window and the cathode material.

Operando UV-visible was performed in a homemade cell (UVC cell, SPHERE-ENERGY, France). I thank D. Alves Dalla Cortes for developing the cell.

Pressure measurements were performed in a homemade cell, which characteristics have been reported in by Lepoivre et al.[162] It is adapted from a Swagelock with the top part replaced by a pressure sensor having a volume of 9 cm^3. Pressure cells were assembled into an argon

filled glovebox and cycled at 25°C. The pressure variation can be converted into mol of gas evolution using the simple ideal gas law.

C.3 Electrochemical techniques

Galvanostatic cycling is the standard battery test. It consists into applying a constant current to the battery and measuring the potential variation between the two electrodes. Unless specified, all electrochemical measurements are performed in galvanostatic mode. C/n, specifies the current of the galvanostatic cycling, it corresponds to the removal of 1 $Li^+/1e^-$ in n hours. Galvanostatic Intermittant Titration Technique (GITT) is a technic alternating galvanostatic cycling with open circuit voltage (OCV) periods. It allows the determination of the equilibrium potentials, being the potential at the end of the relaxation.
All electrochemical characterizations were performed with a VMP3 potentiostat/galvanostat (Biologic, S.A.).

D X-ray Absorption Spectroscopy

D.1 Hard X-ray Absorption Spectroscopy (XAS)

D.1.a Measurements

Hard XAS measurements were performed in transmission mode at the ROCK[163] beamline of synchrotron SOLEIL (France). Si (111) or Si (220) channel-cut quick-XAS monochromators with an energy resolution of 0.8 eV at 8 keV and 2 eV at 22 keV, respectively, were used depending on the absorption edge energy. The intensity of the monochromatic X-ray beam was measured with three consecutive ionization detectors. The samples or the operando cells were placed between the first and the second ionization chambers. For each measurement, successive spectra were collected at a rate of 2 Hz and averaged out over periods of 5 minutes. The energy calibration was established with simultaneous absorption measurements on a standard placed between the second and the third ionization chambers. Chosen standards for each edge are shown Table A 1.

Edges	Energy	Reference	k range of the Fourier Transforms	k weighted	Fitting Range
Ru K-edge	22117 eV	RuO_2	4.2 to 14.9 $Å^{-1}$	k^2 or k^3	1-3.5 Å
Sb K-edge	30491 eV	Sb_2O_3	3.7 to 14.7 $Å^{-1}$	k^2	1-2 Å
Nb K-edge	18986 eV	Nb	3.5 to 13.3 $Å^{-1}$	k^2	1-2 Å
Ni K-edge	8333 eV	Ni	3.5 to 12 $Å^{-1}$	k^2	1-3.5 Å
Mn K-edge	6539 eV	Mn	5.1 to 11 $Å^{-1}$	k^2	1-3.5 Å
Ta L_3-edge	9881 eV	Zn	3.7 to 13.7 $Å^{-1}$	k^3	1-3.5 Å

Table A 1: Experimental data for the HXAS measurement and analysis

D.1.b Data treatment

The data was treated using the Demeter package for energy calibration and normalization and Extended X-ray Absorption Fine Structure (EXAFS) oscillations were fitted using the Artemis software.[164] Fourier transforms of EXAFS oscillations were carried out in different k-ranges (Table A 1). EXAFS amplitudes and phase-shifts were calculated by FEFF7 starting from the calculated lattice parameters of the structures determined by Rietveld refinement. Except the radial distance (R) and the Debye-Waller factor (σ^2), all other parameters were kept constant (CN_i the coordination number, E_0 the difference energy threshold and S_0^2 the amplitude reduction factor) in the conventional least squares modelling using the phase and amplitude factors calculated by FEFF7.

D.1.c PCA-MCRLS analysis

The normalized spectra of obtained during operando measurement were globally analyzed with Principal Component Analysis (PCA)[110] in order to individuate the orthogonal components able to describe the whole evolution during cycling. The number of principal components was then used as basis for Multivariate Curve Resolution-Alternating Least Squares (MCR-ALS)[111]

D.2 Soft X-ray Absorption Spectroscopy

O K-edge Soft XAS measurements were performed at the 4-ID-C beamline of the Advanced Photon Source, in Argonne National Lab. 400 l/mm grating was used providing the best flux

and resolution in the range of energy of interest (500 – 900 eV). Energy calibration is done measuring Sr_2RuO_4 as a reference. Total Fluorescence Yield (TFY) measurements were performed. It consists in collecting the photons emitted during the relaxation of the excited state created after the absorption of the X-ray beam. It interest of TFY is that it is relatively bulk sensitive (≈100nm), however, its signal suffers from self-absorption issues that modify the relative intensities of the signal. For the data treatment, the background removal and normalization were performed using Athena.

E Ultra Violet – Visible Absorption Spectroscopy (UV-visible)

Operando UV-visible spectroscopy was performed in air tight electrochemical cell (UVC cell, SPHERE-ENERGY, France). PTFE self-standing electrode of Li_3RuO_4 (72%wt), carbon SP (18%wt) and PTFE (10%wt) coated on stainless steel mesh are used as positive while the negative electrode is Li foil coated on another stainless steel mesh. 2mL of LP100 is used as electrolyte without any separator. UV-visible spectrometer is a Mettler Toledo UV5bio.

F Density Functional Theory (DFT) calculation

F.1 Parameters for the calculations

Spin-polarized density functional theory (DFT) calculations were performed using the plane-wave density functional theory VASP (Vienna ab initio simulation package) code [165,166] within the generalized gradient approximation of Perdew−Burke−Ernzerhof (PBE) to describe electron exchange and correlation.[167] The rotationally invariant Dudarev method (DFT + U)[168] was used to correct the self-interaction error of conventional DFT for correlated d-electrons. U values used for the calculations are shown Table A 2.

Element	Ru	Nb	Sb	Ni	Mn	Ta	Ir
U (eV)	3 - 0	0	0	6.4	5	0	0 - 2

Table A 2: U values used for the DFT+U calculations

For structural relaxation, the conjugate gradient method was used until the forces on atoms were below 0.005 eV/Å. Plane-wave cutoff of 600 eV was used for the atomic description.

Electrostatic energies and Madelung constants were calculated from formal and Bader charges using a homemade program.

F.2 Cluster expansion code

F.2.a General principle

Cluster expansion is a method used to estimate the energy of a configuration in a much faster way than from ab initio method. It is useful to describe configurational disorder in alloys or oxides.[169,170] Cluster expansion method relies on expressing the free energy, E, of a given structure by a simple sum of parameters: the effective cluster interactions, E_i, of the cluster, i, pondered by the number of such cluster, n_i, normalized by the number of atoms in the unit cell, N (17).

$$E = \frac{1}{N}\sum_i E_i * n_i \qquad (17)$$

Clusters are usually pairs, triangles …etc. with a specific chemical composition. For examples, in a binary system AB, clusters could be pair of next nearest neighbor (NNN) A-A or A-B, triangles of NNN A-A-A or A-B-B…etc. The effective cluster interactions (ECI) are obtained by fitting the free energies, obtained by ab initio method, of a series of ordered configurations.

F.2.b Aim

We used this cluster expansion method to screen the cation configuration space in the rocksalt anionic lattice in order to find low energy cationic configuration and take these configurations as structural model for further theoretical analysis.

F.2.c The code

A homemade cluster expansion code was been used for this work. In our case, we are interested into finding a stable cationic ordering between Li, Ni/Mn and Ta. Considering a unit cell of 20 cations (a ≈ 6 Å, b ≈ 6 Å, c ≈ 12 Å, α = 90°, β =90°, γ = 60°), we have more than 2.10^7 possible cationic configurations, hence motiving the split of the structural search in two steps. First, we will determine a Ta network, and, in a second step, with the Ta position being fix, we will determine the Li and Ni/Mn positions.

1) Determining the relative Ta positions.

1.a) 1000 rocksalt structures, having the composition $Li_{13}Ni_3Ta_4O_{20}$ and $Li_{13}Mn_4Ta_3O_{20}$, with different cationic configuration minimizing the electrostatic interactions are produced using a code based on Pymatgen library[171] and Enumlib code[172]. J. Vergnet is warmly acknowledged for providing the code.

1.b) For the 1000 structures, the cluster distribution is calculated by simply enumerating the different clusters present in the structures. Considered clusters are pairs, triangles and tetrahedral with all possible independent chemical compositions.

1.c) From these 1000 structures, a batch of 100 structures is chosen having the same statistical distribution of clusters than the 1000 structure batch. In other words, the 100 structure batch is representative of the larger one.

1.d) Single point DFT energies, E_{DFT}, are calculated for the 100 structures

1.e) The set of ECI for both compositions is obtained finding the Ei which minimizes the quantity A shown in equation (18).

$$A = \sum_{a\ structure\ of\ the\ 100\ batch} (E^{a}_{DFT} - \frac{1}{N}\sum_{i} E_i \ * n_i)^2 \qquad (18)$$

1.f) E is calculated for the 1000 structure. To estimate the goodness of the energy determination, the obtained energies, E, are compared to energies computed by DFT for random structure among the batch of 1000 structures. Doing so, we find the average error is of 50 and 135 meV/cations for the Mn and Ni-based compounds respectively. Looking into the energy variation depending on the number of nearest neighbors Ta-Ta bond, shown in Figure III-23a, we can clearly see that the low energy Ta network should minimize the number of NNN Ta-Ta. Therefore, we select among the most stable structures the one having the best Ta framework.

2) Li and Ni/Mn ordering.

2.a) We generate all the possible configurations of Li and Ni/Mn in the Ta framework. We have around 500 structures for each composition.

2.b) we repeat the steps 1.b) – 1.ef). With these batches of structures, the error between the energy computed by cluster expansion and the energy computed by DFT is of 20 meV/cations. This energy resolution is enough because due to the disordering of the cations, we are expecting to have the ground state represented by different ordered configurations having less than 20 meV/cations energy difference (thermal agitation energy). Figure III-23b shows the DFT energy for random structure and for the most stable structure found using the

cluster extension. It can be seen that the structures found via the cluster expansion method are among the most stable validating the goodness of the approach

G Electron count for the charge/discharge of Li_3RuO_4

<u>During charge:</u>

We have a total of 2.7 e^- per Ru.

Starting with the cationic redox: two contributions should be considered i) the dissolved species and ii) the bulk of the material. Concerning the dissolved species, we know that 35% of the active material dissolves into the electrolyte forming RuO_4^- and/or RuO_4 species having Ru in the 7+ and/or 8+ oxidation state, respectively. Supposing that we form RuO_4^-, the number of electrons per Ru needed to oxidize 35% of the Ru from 5+ to 7+ is: 0.35*2 = 0.7. Similarly, if we form RuO_4, 0.35*3 = 1.05 electrons are needed. Since we cannot differentiate these species, we'll assume an average number of electron: 0.875 e^-. Regarding the second contribution to the cationic redox, i.e. the bulk of the material, 65% of the Ru oxidizes from 5+ to 5.4+, which makes 0.4 * 0.65 = 0.26 e^-. Overall, 0.26 + 0.875 = 1.135 e^- can be attributed to cationic redox.

By difference, i.e. 2.7 – 1.135 = 1.565, we get the number of electrons associated to the anionic redox.

<u>During Discharge:</u>

We have a total of 4.2 e^- per Ru

The cationic redox reaction is $Ru^{5.4+} \rightarrow Ru^{2.8+}$ making a total of 2.6 e^-. Once again the anionic redox activity is assessed by simple difference, making 1.6 e^-.

H Other techniques

H.1 Transmission electron microscopy (TEM)

Samples for transmission electron microscopy were prepared by grinding materials in a mortar and dispersing the powder onto holey carbon TEM grids. High angle annular dark field scanning transmission electron microscopy (HAADF-STEM) images were acquired using a probe aberration corrected FEI Titan3 80-300 microscope operated at 300 kV. TEM

experiments on members of the $Li_3Ru_yNb_{1-y}O_4$ phase diagram has been carried out by D. Batuk and G. Van Tendeloo at EMAT (Antwerp, Belgium)

H.2 Scanning Electron Microscopy (SEM)

Powder samples were deposited on a conductive carbon tape. Scanning electron microscopy (SEM) and energy dispersive X-ray spectrometry (EDX) analysis were carried out by D. Alves Dalla Corte (Collège de France) using a SU-70, HITACHI.

H.3 Differential Electrochemical Mass Spectrometry (DEMS)

A detailed schematic of the OEMS setup is provided elsewhere.[173] Briefly, the OEMS operates with a quadrupole mass spectrometer (QMS 200, Pfeiffer, Germany) for partial pressure measurements and a pressure transducer (PAA-33X, Keller Druck AG, Switzerland) for total cell pressure recordings, temperature, and internal volume determination. Swagelok stainless steel gas pipes and fittings (3 mm compression tube fittings, Swagelok, OH, USA) are employed to connect a homemade OEMS cell, a set of solenoid valves (2-way magnetic valve, Series 99, silver-plated nickel seal, Parker, USA) and a scroll pump (nXDS15i, EDWARDS GmbH, UK) for efficient flushing. The valves are electronically controlled with a Solid State Relay Module (NI 9485 measurement System, National Instruments, TX, USA) connected to a computer with a LabView Software (NI Labview 2013, National Instruments, TX, USA). For partial pressure and gas evolution rate analysis 0.8 mL of gas are extracted from the headspace (~ 4 mL) of the cell and replaced by pure Ar (quality 5.0). Calibration gas bottles were utilized to relate the MS ion-current signals at m/z = 32 and 44 to known concentrations of O2 and CO2 (1000 ppm of O2 and CO2 in Ar, respectively), before and after the measurement. DEMS experiments were conducted by E.J. Berg at the Electrochemistry Laboratory (PSI, Villigen).

H.4 Inductively Coupled Plasma Atomic Emission Spectroscopy

ICP-AES in a ThermoFisher iCAP 6000 device analysis was performed on ion exchanged IE-Li_2RuO_4. Dissolution was performed in 1 M KOH solution with NaOCl as an oxidating agent. Due to the presence of Na in NaOCl, Na quantification has not been performed. The measurements were performed by D. Giaume at Chimie Paristech (Paris, France).

H.5 DSC

The thermal stability of the materials was investigated by DSC. ~10 mg of sample was used and heated under Air at 5°C/min. The measurements were performed by M. Courty at LRCS (Amiens, France).

H.6 XPS

XPS measurements were carried out at the O 1s peak with a Kratos Axis Ultra spectrometer. The XPS spectrometer was directly connected, through a transfer chamber, to an Ar dry box to avoid sample exposure to air. The binding energy scale was calibrated using the C 1s peak at 285.0 eV from the invariable contamination. XPS measurements and analysis were performed by D. Foix in IPREM (Pau, France).

List of Figures

Figure I-1: Schematic of a Li-ion battery 5
Figure I-2: Schematic of different intercalation systems.....9
Figure I-3: Evolution, over the years, of the specific energy of practical cathode materials ...12
Figure I-4: The chemical potential of a transition metal isolated in vaccum, in a ionic molecule, iono-covalent molecule and iono-covalent crystal.....15
Figure I-5: Effect of late transition metal or high oxidation state on the chemical potential ...17
Figure I-6: Schematic representation of the electronic structures for $LiMO_2$ (x = 0), Li_2MO_3 (x = 1/3) and Li_5MO_6 (x = 2/3) with the |O2s and |O2p lone-pair states being highlighted.....22
Figure I-7: Schematic presenting the different electronic regimes depending on U and Δ_{CT} values. 24
Figure I-8: Evolution of the electronic regime of the MS_2 compounds going from early to late transition metals. 25
Figure I-9: Dynamics of Li-removal in strongly covalent compounds 27
Figure I-10: Dynamics of the oxidation process in compounds being in the charge transfer regime. 29
Figure II-1: Schematic presenting the structure of some Li_3MO_4 compounds with M being Nb, Ru, Sb and Ta. All are rocksalt with different Li/M ordering. 36
Figure II-2: Rietveld refinements of the XRD pattern of compounds among the solid solution $Li_3Ru_yIr_{1-y}O_4$ for y = 1, 0.75, 0.5, 0.25 and 0 together with a view of the structures 39
Figure II-3: Rietveld refinements of $Li_3Ru_{0.5}Ir_{0.5}O_4$ using the structural model of Li_3IrO_4 described in R -3m (top) and the P 1 2/a 1 structural model of Li_3RuO_4 (bottom) 39
Figure II-4: SXRD patterns for the $Li_3Ru_ySb_{1-y}O_4$ samples with y = 1, 0.7, 0.5, 0.3, and 0 41
Figure II-5: SXRD patterns for the $Li_3Ru_yNb_{1-y}O_4$ and $Li_3Nb_ySb_{1-y}O_4$ samples with y = 1, 0.7, 0.5, 0.3, 0.1 and 0 42
Figure II-6: Schematic of the structures of the $Li_3Ru_yNb_{1-y}O_4$, $Li_3Ru_ySb_{1-y}O_4$, and $Li_3Sb_yNb_{1-y}O_4$ for y = 1, 0.7, 0.5, 0.3, and 0. 43
Figure II-7: Rietveld refinements of NPD patterns for $Li_3Ru_{0.7}Sb_{0.3}O_4$, $Li_3Ru_{0.5}Sb_{0.5}O_4$ and $Li_3Ru_{0.3}Sb_{0.7}O_4$, together with the obtained cell parameters.....44
Figure II-8: Rietveld refinements of NPD patterns for $Li_3Sb_{0.7}Nb_{0.3}O_4$, $Li_3Sb_{0.5}Nb_{0.5}O_4$ and $Li_3Sb_{0.3}Nb_{0.7}O_4$ and $Li_3Ru_{0.7}Nb_{0.3}O_4$, $Li_3Ru_{0.5}Nb_{0.5}O_4$ and $Li_3Ru_{0.3}Nb_{0.7}O_4$ 44

Figure II-9: Volume/Z, average M-O distance and MO_6 distortion obtained by diffraction in a-b-d) and average M-O distance and MO_6 distortion obtained by XAS in c-e) for $Li_3M_yM'_{1-y}O_4$ (M and M' being Ru, Sb and Nb).....49
Figure II-10: Magnitude of the Fourier transforms of the EXAFS oscillations extracted at the Sb K-edge, Ru K-edge, and Nb K-edge. 51
Figure II-11: Rietveld refinements of the SXRD pattern of $Li_3Ru_{0.5}Nb_{0.5}O_4$ without or with considering Li2 and Ru/Nb cationic mixing together with HAADF-STEM images showing the crystal contains numerous cooperative defects in the cation ordering pattern.....53
Figure II-12: Coupled SXRD and HADDF-STEM analysis of the antiphase boundaries in $Li_3Ru_{0.1}Nb_{0.9}O_4$ 55
Figure II-13: a) Phase stability for Li_3NbO_4, Li_3RuO_4 and Li_3SbO_4 computed with simple electrostatic considerations and DFT calculations. b) XRD patterns of Li_3RuO_4 synthetized at different temperatures and for different times 57
Figure II-14: Impact of the metal displacement in the MO_6 octahedra on the structural stability assessed by DFT calculations 59
Figure II-15: Electrochemical behavior of Li_3RuO_4, $Li_3Ru_{0.7}Nb_{0.3}O_4$, $Li_3Ru_{0.5}Nb_{0.5}O_4$ and $Li_3Ru_{0.3}Nb_{0.7}O_4$ starting on discharge.....63
Figure II-16: Operando XRD patterns collected during the reduction of Li_3RuO_4, with the corresponding galvanostatic curve. 65
Figure II-17: Operando XRD patterns collected during the reduction of $Li_3Ru_{0.5}Nb_{0.5}O_4$ with the corresponding galvanostatic curve. 67
Figure II-18: 1st, 2nd and 3rd galvanostatic cycles for Li_3RuO_4 at C/10 with 4.2 V – 1.5 V cutoff voltages.....68
Figure II-19: Operando XRD patterns collected during the oxidation of Li_3RuO_4. 69
Figure II-20: SEM image of the Li counter electrode after the 1st charge using Li_3RuO_4 as cathode material together with the EDX spectra highlighting the presence of Ru 69
Figure II-21: Operando UV-visible and mass loss during the charge of Li_3RuO_4 71
Figure II-22: Pictures of reaction vials showing the evolution with time of a $KRuO_4$ and LP100 mixture.....71
Figure II-23: OEMS measurements on Li_3RuO_4 during galvanostatic cycling. 72
Figure II-24: Operando Ru K-edge XANES spectra for Li_3RuO_4.....73
Figure II-25: Results of the PCA and MCR-ALS analysis on the operando XAS of Li_3RuO_4 together the edge position – oxidation state calibration 75

Figure II-26: a) Magnitude of the Fourier transforms of the EXAFS oscillations and b) XANES spectra of the MCR-ALS components.....76
Figure II-27: O1s XPS spectra performed on ex situ samples of Li_3RuO_4. 77
Figure II-28: Operando XRD patterns collected during the 1st cycle of $Li_3Ru_{0.5}Nb_{0.5}O_4$ starting on oxidation. 78
Figure II-29: a) First cycle upon oxidation of all the compounds among the $Li_3Ru_yNb_{1-y}O_4$ series. b) Cycling performances for $Li_3Ru_{0.5}Nb_{0.5}O_4$ 79
Figure II-30: Operando Ru K-edge XANES spectra for $Li_3Ru_{0.5}Nb_{0.5}O_4$ 80
Figure II-31: Operando UV-visible spectroscopy for $Li_3Ru_{0.5}Ir_{0.5}O_4$. 81
Figure II-32: a) 1st cycle of galvanostatic cycling and b) molar ratio of the gas/active material evolution inside the cell for $Li_3Ru_yIr_{1-y}O_4$ with y = 1, 0.75, 0.5, 0.25 and 0 82
Figure II-33: Operando XRD for $Li_3Ru_{0.5}Ir_{0.5}O_4$ during the 1st charge 83
Figure II-34: Convex Hull diagrams for Li_xRuO_4 and Li_xIrO_4 calculated from DFT+U.....85
Figure II-35: Scheme explaining the impact of the stability of the MO_4 end member with respect to the formation of intermediates, O_2 gas release and dissolution. 86
Figure II-36: Rietveld refinement of the SXRD patterns of Na_3RuO_4 and Na_2RuO_4 together with SEM images 89
Figure II-37: Electrochemical properties of Na_3RuO_4 towards Na extraction/insertion.....91
Figure II-38: Operando XRD patterns collected during the 1st cycle of Na_3RuO_4 together with Rietveld refinement of the SXRD patterns of EX-Na_2RuO_4 and EX-$NaRuO_4$. 93
Figure II-39: a) and b) Ru K-edge XANES spectra of Na_3RuO_4, Na_2RuO_4, EX-Na_2RuO_4, EX-$NaRuO_4$, "RuO_4" and discharged Na_3RuO_4. c) Ru-O and Ru-Ru distances and coordination numbers in Na_3RuO_4, Na_2RuO_4, EX-Na_2RuO_4 and EX-$NaRuO_4$ obtained fitting the EXAFS oscillations d-e-f-g) 97
Figure II-40: Operando UV-visible spectra of Na_3RuO_4 during oxidation.....98
Figure II-41: Gas pressure evolution in a cell using Na_3RuO_4 as cathode material.....99
Figure II-42: Schematics summarizing the investigated compounds and their synthesis. 100
Figure II-43: a) Rietveld refinement of the SXRD pattern with SEM image and structure of IE-Li_2RuO_4. b) ICP and EDX elemental analysis performed on IE-Li_2RuO_4. c) DSC of IE-Li_2RuO_4 under air. 101
Figure II-44: a) Ru K-edge XANES spectra of Na_3RuO_4, IE-Li_2RuO_4, Na_2RuO_4 and $Li_{0.3}RuO_4$. b) Magnitude of the Fourier transforms of the EXAFS oscillations with their fit for

IE-Li_2RuO_4. c) Ru-O and Ru-Ru distances and coordination numbers of Na_2RuO_4 and IE-Li_2RuO_4 obtained from EXAFS analysis. 103
Figure II-45: Charge-discharge curves of a) Na_2RuO_4 and b) EX-Na_2RuO_4. c) Operando XRD patterns of Na_2RuO_4 during the oxidation and reduction processes and d) Ex situ XRD pattern of Td-$NaRuO_4$. e) Structure of Td-$NaRuO_4$. 105
Figure II-46: Convex Hull for the Na_xRuO_4 system obtained by DFT calculations 108
Figure II-47: Energy above the convex hull of the most stable structure depending on the oxidation state for Li_xMnO_4, Na_xMnO_4 and K_xMnO_4 systems. 110
Figure III-1: Rietveld refinement of XRD and NPD patterns of $Li_{1.3}Ni_{0.27}Ta_{0.43}O_2$ and $Li_{1.3}Mn_{0.4}Ta_{0.3}O_2$ together with a representation of the structure 114
Figure III-2: 1st, 2nd and 10th galvanostatic cycles of $Li_{1.3}Ni_{0.27}Ta_{0.43}O_2$ and $Li_{1.3}Mn_{0.4}Ta_{0.3}O_2$. 115
Figure III-3: a) 1st galvanostatic cycle and dQ/dV profile for $Li_{1.3}Ni_{0.27}Ta_{0.43}O_2$. b) and c) voltage-composition curve of the 1st cycle with different state-of-charge at 25°C and 55°C. d) GITT measurement. 117
Figure III-4: Galvanostatic cycling of LNTO realized at different depths of discharge 117
Figure III-5: Variation of the Ni K-edge measured operando during the 1st charge and discharge of $Li_{1.3}Ni_{0.27}Ta_{0.43}O_2$ 118
Figure III-6: Evolution of the Ni K-edge energy position obtained from the operando measurement of LNTO. b) Component concentration evolution obtained by MCR-ALS analysis on the operando measurement. c) Fit of the magnitude of the Fourier transforms performed on the reconstructed spectra of the three components. 119
Figure III-7: a) Ni K-edge XANES spectra of the reconstructed components. b) ex situ Ni K-edge XANES spectra for LNTO 120
Figure III-8: a) Ex situ Ta L_3-edge XANES spectra. b) Magnitude of the Fourier transforms of the Ta L_3-edge EXAFS oscillations on ex situ LNTO. c) Average Ta-O bond lengths, distortion coefficients of TaO_6 and average Ta – M bond lengths as extracted from the EXAFS fitting 121
Figure III-9: a) O K-edge XAS spectra for ex situ samples for LNTO. b) Comparison of the TFY O K-edge data with the empty O, Ni and Ta pDOS computed via DFT calculations ... 122
Figure III-10: Molar ratio of O_2/LNTO and CO_2/LNTO measured via mass spectrometry during galvanostatic cycling 123

Figure III-11: Voltage-composition curve for LNTO with the charge and discharge performed in the same cell, in red, and charge and discharge performed in different fresh cell in black. 124
Figure III-12: a) Operando XRD patterns measured during the 1st cycle of LNTO, together with the cell parameter variation extracted using Rietveld refinement b-c-d).....125
Figure III-13: Schematics presenting the charge compensation mechanism in $Li_{1.3}Ni_{0.27}Ta_{0.43}O_2$. 126
Figure III-14: a) 1st galvanostatic cycle of LMTO together with its dQ/dV profile. b) 1st galvanostatic cycle at different SOC. c) GITT measurements 127
Figure III-15: a) Variation of the Mn K-edge measured operando during the 1st charge and discharge of $Li_{1.3}Mn_{0.4}Ta_{0.3}O_2$. b) Ex situ Mn K-edge XANES spectra. c) Evolution of the Mn K-edge energy position.....128
Figure III-16: a) Component concentration evolution obtained by MCR-ALS during the XAS operando measurement of LMTO. b) Mn K-edge XANES spectra and the fit of the magnitude of the Fourier transforms of the EXAFS oscillations of the reconstructed components.....129
Figure III-17: Ex situ Ta L_3-edge XANES spectra of LMTO.....130
Figure III-18: Magnitude of the Fourier transforms of the Ta L_3-edge EXAFS oscillations on ex situ LMTO with the average Ta-O bond length, distortion coefficient of TaO_6 and average Ta – M bond length as extracted from the EXAFS fitting 131
Figure III-19: a) O K-edge XAS spectra for ex situ samples of LMTO. b) Comparison of the O K-edge data with the empty O, Mn and Ta pDOS calculated from DFT 132
Figure III-20: OEMS results for LMTO.....132
Figure III-21: Voltage-composition curve, XRD patterns and cell parameters extracted from Rietveld refinement of the operando XRD measurement 133
Figure III-22: Schematics representing the charge compensation mechanism for $Li_{1.3}Mn_{0.4}Ta_{0.3}O_2$ 134
Figure III-23: a) and b) Variation of the average energy of the cation configuration with the number of first order Ta –Ta bonds for $Li_{1.3}Ni_{0.3}Ta_{0.4}O_2$ and $Li_{1.3}Mn_{0.4}Ta_{0.3}O_2$. c) and d) DFT energy for random structures (black cross) and for the most stable structures (blue dots) found using the cluster expansion, for $Li_{1.3}Ni_{0.27}Ta_{0.43}O_2$ and $Li_{1.3}Mn_{0.4}Ta_{0.3}O_2$, respectively.....135
Figure III-24: a) and b) are Convex Hull diagrams, c) and d) are calculated voltage profiles superimposed on GITT data, in green and black, together with O release stability regions, e)

and f) shows the variation of the Ni and Mn Bader charge, respectively, g) and h) the O bader charge, for LNTO and LMTO, respectively. 137
Figure III-25: a) and b) O, Ni, Mn and Ta pDOS in red, blue, purple and green, respectively for LNTO and LMTO at different state-of-charge. 137
Figure III-26: a), b) and c) are schematics of the Density of State (DOS) for pristine LNTO and LMTO, after the cationic process and during the anionic process, respectively. 139

List of Tables

Table II-1: Synthesis conditions for $Li_3M_yM'_{1-y}O_4$ (M and M' being Ru, Sb, Nb and Ir) 37
Table II-2: Crystallographic data for $Li_3Ru_{0.75}Ir_{0.25}O_4$, $Li_3Ru_{0.5}Ir_{0.5}O_4$, and $Li_3Ru_{0.25}Ir_{0.75}O_4$ ..40
Table II-3: Crystallographic table for $Li_3Ru_{0.7}Sb_{0.3}O_4$, $Li_3Ru_{0.5}Sb_{0.5}O_4$ and $Li_3Ru_{0.3}Sb_{0.7}O_4$ ..45
Table II-4: Crystallographic data for $Li_3Sb_{0.7}Nb_{0.3}O_4$ 46
Table II-5: Crystallographic data for $Li_3Sb_{0.5}Nb_{0.5}O_4$ 46
Table II-6: Crystallographic data for $Li_3Sb_{0.3}Nb_{0.7}O_4$ 47
Table II-7: Crystallographic data for $Li_3Ru_{0.3}Nb_{0.7}O_4$.....47
Table II-8: Crystallographic data for $Li_3Ru_{0.7}Nb_{0.3}O_4$ and $Li_3Ru_{0.5}Nb_{0.5}O_4$ 48
Table II-9: Structural parameters obtained by fitting the EXAFS oscillations for $Li_3M_yM'_{1-y}O_4$ (M and M' being Ru, Sb, Nb) compositions. 52
Table II-10: Summary of the systems which electrochemical properties will be studied 62
Table II-11: Crystallographic data for $Li_{4.6}RuO_4$. 64
Table II-12: Proposed structural model for $Li_4Ru_{0.5}Nb_{0.5}O_4$ 66
Table II-13: Local structure obtained by fitting the EXAFS oscillations for the PCA components obtained for the operando measurements of Li_3RuO_4 76
Table II-14: Crystallographic data for Na_3RuO_4. 90
Table II-15: Crystallographic data for Na_2RuO_4 (prepared by solid state method), EX-Na_2RuO_4 and EX-$NaRuO_4$. 95
Table II-16: Structural parameters obtained by fitting the Fourier transforms of the EXAFS oscillations of Na_3RuO_4, Na_2RuO_4, EX-Na_2RuO_4 and EX-$NaRuO_4$ 97
Table II-17: Crystallographic data for IE-Li_2RuO_4. 102
Table II-18: Structural parameters obtained by fitting the Fourier transforms of the EXAFS oscillations of IE-Li_2RuO_4 103
Table II-19: Crystallographic data for Td-$NaRuO_4$. 106
Table III-1: Composition, observed potential drop during discharge and the origin of such feature for reported Ni-based compounds. 112
Table III-2: Crystallographic data for $Li_{1.3}Ni_{0.27}Ta_{0.43}O_2$ and $Li_{1.3}Mn_{0.4}Ta_{0.3}O_2$.....114
Table III-3: Structural parameters obtained by fitting the Ni K-edge EXAFS oscillations of the reconstructed components from the operando measurements on LNTO.. 120

Table III-4: Structural parameters obtained by fitting the Mn K-edge EXAFS oscillations of the reconstructed components during operando measurements for LMTO. 130

References

(1) Jacobson, A. J.; Nazar, L. F. **Intercalation Chemistry**. In Encyclopedia of Inorganic and Bioinorganic Chemistry; American Cancer Society, 2011.

(2) Grand View Research. **Global Zeolite Market Size & Analysis**. Industry Report, 2012-2022. 2018.

(3) Bish, D. L. **Rietveld Refinement of the Kaolinite Structure at 1.5 K**. Clays Clay Miner. **1993**, 41, 738–744.

(4) Miyata, S. **Syntheses of Hydrotalcite-like Compounds and Their Structures and Physicochemical Properties .1. Systems Mg^{2+}-Al^{3+}-NO^{3-},Mg^{2+}-Al^{3+}-Cl^{-},Mg^{2+}-Al^{3+}-ClO^{-4},Ni^{2+}-Al^{3+}-Cl^{-} and Zn^{2+}-Al^{3+}-Cl^{-}**. Clays Clay Miner. **1975**, 23, 369.

(5) Boehm, H.-P.; Steinle, J.; Vieweger, C. **$[Zn_2Cr(OH)_6]_X \cdot 2H_2O$, New Layer Compounds Capable of Anion Exchange and Intracrystalline Swelling**. Angew. Chem. Int. Ed. Engl. **1977**, 16, 265–266.

(6) Dresselhaus, M. S.; Dresselhaus, G. **Intercalation Compounds of Graphite**. Adv. Phys. **1981**, 30, 139–326.

(7) Hannay, N. B.; Geballe, T. H.; Matthias, B. T.; Andres, K.; Schmidt, P.; MacNair, D. **Superconductivity in Graphitic Compounds**. Phys. Rev. Lett. **1965**, 14, 225–226.

(8) Rüdorff, W. Chimia **1965**, 489.

(9) Rüdorff, W.; Sick, H. H. **Einlagerungsverbindungen von Alkali- Und Erdalkalimetallen in Molybdän- Und Wolframdisulfid**. Angew. Chem. **1959**, 71, 127–127.

(10) Gamble, F. R.; Osiecki, J. H.; Cais, M.; Pisharody, R.; DiSalvo, F. J.; Geballe, T. H. **Intercalation Complexes of Lewis Bases and Layered Sulfides: A Large Class of New Superconductors**. Science **1971**, 174, 493–497.

(11) Morosan, E.; Zandbergen, H. W.; Dennis, B. S.; Bos, J. W. G.; Onose, Y.; Klimczuk, T.; Ramirez, A. P.; Ong, N. P.; Cava, R. J. **Superconductivity in Cu_xTiSe_2**. Nat. Phys. **2006**, 2, 544–550.

(12) Whittingham, M. S. **Electrical Energy Storage and Intercalation Chemistry**. Science **1976**, 192, 1126–1127.

(13) Haering, R. R.; Stiles, J. A. R.; Brandt, K. **Lithium Molybdenum Disulphide Battery Cathode**. US patent 4224390, 1980.

(14) Armand, M. **The History of Polymer Electrolytes**. Solid State Ion. **1994**, 69, 309–319.

(15) Murphy, D. W.; Di Salvo, F. J.; Carides, J. N.; Waszczak, J. V. **Topochemical Reactions of Rutile Related Structures with Lithium**. Mater. Res. Bull. **1978**, 13, 1395–1402.

(16) Lazzari, M. A Cyclable **Lithium Organic Electrolyte Cell Based on Two Intercalation Electrodes**. J. Electrochem. Soc. **1980**, 127, 773.

(17) Fong, R. Q **Studies of Lithium Intercalation into Carbons Using Nonaqueous Electrochemical Cells**. J Electrochem Soc **1990**, 137, 5.

(18) Delmas, C.; Fouassier, C.; Hagenmuller, P. **Structural Classification and Properties of the Layered Oxides**. Phys. BC **1980**, 99, 81–85.

(19) Delmas, C.; Braconnier, J.-J.; Fouassier, C.; Hagenmuller, P. **Electrochemical Intercalation of Sodium in Na_xCoO_2 Bronzes**. Solid State Ion. **1981**, 3, 165–169.

(20) Pauling, L. **The Nature of the Chemical Bond. IV. The Energy of Single Bonds and the Relative Electronegativity of Atoms**. J. Am. Chem. Soc. **1932**, 54, 3570–3582.

(21) Mizushima, K.; Jones, P. C.; Wiseman, P. J.; Goodenough, J. B. **Li_xCoO_2 (0 < X < -1): A New Cathode Material for Batteries of High Energy Density**. Mater. Res. Bull. **1980**, 15, 783–789.
(22) Koetschau, I.; Richard, M. N.; Dahn, J. R.; Soupart, J. B.; Rousche, J. C. **Orthorhombic $LiMnO_2$ as a High Capacity Cathode for Li-Ion Cells**. J. Electrochem. Soc. **1995**, 142, 2906-2910.
(23) Armstrong, A. R.; Bruce, P. G. **Synthesis of Layered $LiMnO_2$ as an Electrode for Rechargeable Lithium Batteries**. Nature **1996**, 381, 499–500.
(24) Capitaine, F. **A New Variety of $LiMnO_2$ with a Layered Structure**. Solid State Ion. **1996**, 89, 197–202.
(25) Dahn, J. R. **Rechargeable $LiNiO_2$/Carbon Cells**. J. Electrochem. Soc. **1991**, 138, 5.
(26) Dahn, J. R.; Von Sacken, U.; Michal, C. A. **Structure and Electrochemistry of $Li_{1+y}NiO_2$ and a New Li_2NiO_2 Phase with the $Ni(OH)_2$ Structure**. Solid State Ion. **1990**, 44, 87–97.
(27) Yabuuchi, N.; Ohzuku, T. **Novel Lithium Insertion Material of $LiCo_{1/3}Ni_{1/3}Mn_{1/3}O_2$ for Advanced Lithium-Ion Batteries**. J. Power Sources **2003**, 119–121, 171–174.
(28) Ohzuku, T.; Ueda, A.; Kouguchi, M. **Synthesis and Characterization of $LiAl_{1/4}Ni_{3/4}O_2$ (R -3 m) for Lithium-Ion (Shuttlecock) Batteries**. J. Electrochem. Soc. **1995**, 142, 4033–4039.
(29) Thackeray, M. M.; David, W. I. F.; Bruce, P. G.; Goodenough, J. B. **Lithium Insertion into Manganese Spinels**. Mater. Res. Bull. **1983**, 18, 461–472.
(30) Amatucci, G. G.; Pereira, N.; Zheng, T.; Tarascon, J.-M. **Failure Mechanism and Improvement of the Elevated Temperature Cycling of $LiMn_2O_4$ Compounds Through the Use of the $LiAl_xMn_{2-x}O_4$-zF_z Solid Solution**. J. Electrochem. Soc. **2001**, 148, A171.
(31) Masquelier, C.; Croguennec, L. **Polyanionic (Phosphates, Silicates, Sulfates) Frameworks as Electrode Materials for Rechargeable Li (or Na) Batteries**. Chem. Rev. **2013**, 113, 6552–6591.
(32) Rousse, G.; Tarascon, J. M. **Sulfate-Based Polyanionic Compounds for Li-Ion Batteries: Synthesis, Crystal Chemistry, and Electrochemistry Aspects**. Chem. Mater. **2014**, 26, 394–406.
(33) Padhi, A. K.; Nanjundaswamy, K. S.; Goodenough, J. B. **Phospho-olivines as Positive-Electrode Materials for Rechargeable Lithium Batteries**. J. Electrochem. Soc. **1997**, 144, 1188–1194.
(34) Andre, D.; Kim, S.-J.; Lamp, P.; Lux, S. F.; Maglia, F.; Paschos, O.; Stiaszny, B. **Future Generations of Cathode Materials: An Automotive Industry Perspective.** J Mater Chem A **2015**, 3, 6709–6732.
(35) Ceder, G.; Chiang, Y.-M.; Sadoway, D. R.; Aydinol, M. K.; Jang, Y.-I.; Huang, B. **Identification of Cathode Materials for Lithium Batteries Guided by First-Principles Calculations**. Nature **1998**, 392, 694–696.
(36) Aydinol, M. K.; Kohan, A. F.; Ceder, G.; Cho, K.; Joannopoulos, J. **Ab Initio Study of Lithium Intercalation in Metal Oxides and Metal Dichalcogenides**. Phys. Rev. B **1997**, 56, 1354–1365.
(37) Saubanère, M.; Yahia, M. B.; Lebègue, S.; Doublet, M.-L. **An Intuitive and Efficient Method for Cell Voltage Prediction of Lithium and Sodium-Ion Batteries**. Nat. Commun. **2014**, 5, 5559.
(38) Pearson, R. G. **Chemical Hardness and Density Functional Theory**. J. Chem. Sci. **2005**, 117, 369–377.
(39) Madelung, E. Phys. Z **1918**, 19, 524.

(40) Li, G.; Azuma, H.; Tohda, M. **$LiMnPO_4$ as the Cathode for Lithium Batteries**. Electrochem. Solid-State Lett. **2002**, 5, A135.
(41) Okada, S.; Sawa, S.; Egashira, M.; Yamaki, J.; Tabuchi, M.; Kageyama, H.; Konishi, T.; Yoshino, A. **Cathode Properties of Phospho-Olivine $LiMPO_4$ for Lithium Secondary Batteries**. J. Power Sources **2001**, 97–98, 430–432.
(42) Wolfenstine, J.; Allen, J. **Ni^{3+}/Ni^{2+} Redox Potential in $LiNiPO_4$**. J. Power Sources **2005**, 142, 389–390.
(43) Arroyo-de Dompablo, M. E.; Armand, M.; Tarascon, J. M.; Amador, U. **On-Demand Design of Polyoxianionic Cathode Materials Based on Electronegativity Correlations: An Exploration of the Li_2MSiO_4 System (M=Fe, Mn, Co, Ni)**. Electrochem. Commun. **2006**, 8, 1292–1298.
(44) Ohzuku, T.; Takeda, S.; Iwanaga, M. **Solid-State Redox Potentials for $Li[Me_{1/2}Mn_{3/2}]O_4$ (Me: 3d-Transition Metal) having Spinel-Framework Structures: A Series of 5 Volt Materials for Advanced Lithium-Ion Batteries**. J. Power Sources. **1999**, 5, 90-94.
(45) Padhi, A. K. **Mapping of Transition Metal Redox Energies in Phosphates with NASICON Structure by Lithium Intercalation**. J. Electrochem. Soc. **1997**, 144, 2581.
(46) Sun, M.; Rousse, G.; Abakumov, A. M.; Saubanère, M.; Doublet, M.-L.; Rodríguez-Carvajal, J.; Van Tendeloo, G.; Tarascon, J.-M. **$Li_2Cu_2O(SO_4)_2$: A Possible Electrode for Sustainable Li-Based Batteries Showing a 4.7 V Redox Activity vs Li^+/Li**. Chem. Mater. **2015**, 27, 3077–3087.
(47) Mercier, M.; Bauer, P. **Magnetoelectric Effects in $LiNiPO_4$**. C R Math Acad Sci Paris **1968**, 267, 465.
(48) Kornev, I.; Bichurin, M.; Rivera, J.-P.; Gentil, S.; Schmid, H.; Jansen, A. G. M.; Wyder, P. **Magnetoelectric Properties of $LiCoPO_4$ and $LiNiPO_4$**. Phys. Rev. B **2000**, 62, 12247–12253.
(49) Liang, G.; Park, K.; Li, J.; Benson, R. E.; Vaknin, D.; Markert, J. T.; Croft, M. C. **Anisotropy in Magnetic Properties and Electronic Structure of Single-Crystal $LiFePO_4$**. Phys. Rev. B. **2008**, 77, 064414.
(50) Cava, R. J. **Lithium Insertion in Wadsley-Roth Phases Based on Niobium Oxide**. J. Electrochem. Soc. **1983**, 130, 2345.
(51) James, A. C. W. P.; Goodenough, J. B. **Structure and Bonding in Li_2MoO_3 and $Li_{2-x}MoO_3$ ($0 \leq x \leq 1.7$)**. J. Solid State Chem. **1988**, 76, 87–96.
(52) Ma, J.; Zhou, Y.-N.; Gao, Y.; Yu, X.; Kong, Q.; Gu, L.; Wang, Z.; Yang, X.-Q.; Chen, L. **Feasibility of Using Li_2MoO_3 in Constructing Li-Rich High Energy Density Cathode Materials**. Chem. Mater. **2014**, 26, 3256–3262.
(53) Hoshino, S.; Glushenkov, A. M.; Ichikawa, S.; Ozaki, T.; Inamasu, T.; Yabuuchi, N. **Reversible Three-Electron Redox Reaction of Mo^{3+}/Mo^{6+} for Rechargeable Lithium Batteries**. ACS Energy Lett. **2017**, 2, 733–738.
(54) Baddour, R.; Pereira-Ramos, J. P.; Messina, R.; Perichon, J. A **Thermodynamic, Structural and Kinetic Study of the Electrochemical Lithium Intercalation into the Xerogel $V_2O_5 \cdot 1.6\ H_2O$ in a Propylene**. J. Electroanal. Chem. Interfacial Electrochem. **1991**, 314, 81–101.
(55) Delmas, C.; Cognac-Auradou, H.; Cocciantelli, J. M.; Ménétrier, M.; Doumerc, J. P. **The $Li_xV_2O_5$ System: An Overview of the Structure Modifications Induced by the Lithium Intercalation**. Solid State Ion. **1994**, 69, 257–264.
(56) Freire, M.; Kosova, N. V.; Jordy, C.; Chateigner, D.; Lebedev, O. I.; Maignan, A.; Pralong, V. **A New Active Li–Mn–O Compound for High Energy Density Li-Ion Batteries**. Nat. Mater. **2016**, 15, 173-177.

(57) Diaz-Lopez, M.; Freire, M.; Joly, Y.; Colin, C. V.; Fischer, H. E.; Blanc, N.; Boudet, N.; Pralong, V.; Bordet, P. **Local Structure and Lithium Diffusion Pathways in $Li_4Mn_2O_5$ High Capacity Cathode Probed by Total Scattering and XANES**. Chem. Mater. **2018**, 30, 3060–3070.

(58) A. Kitchaev, D.; Lun, Z.; D. Richards, W.; Ji, H.; J. Clément, R.; Balasubramanian, M.; Kwon, D.-H.; Dai, K.; K. Papp, J.; Lei, T.; et al. **Design Principles for High Transition Metal Capacity in Disordered Rocksalt Li-Ion Cathodes**. Energy Environ. Sci. **2018**, 11, 2159-2171.

(59) Lee, J.; Kitchaev, D. A.; Kwon, D.-H.; Lee, C.-W.; Papp, J. K.; Liu, Y.-S.; Lun, Z.; Clément, R. J.; Shi, T.; McCloskey, B. D.; et al. **Reversible Mn^{2+}/Mn^{4+} Double Redox in Lithium-Excess Cathode Materials**. Nature **2018**, 556, 185–190.

(60) Lu, Z.; Dahn, J. R. **Understanding the Anomalous Capacity of $Li/Li[Ni_xLi_{1/3-2x/3}Mn_{2/3-x/3}]O_2$ Cells Using In Situ X-Ray Diffraction and Electrochemical Studies**. J. Electrochem. Soc. **2002**, 149, A815.

(61) Johnson, C. S.; Li, N.; Vaughey, J. T.; Hackney, S. A.; Thackeray, M. M. **Lithium–Manganese Oxide Electrodes with Layered–Spinel Composite Structures $xLi_2MnO_3\cdot(1-x)Li_{1+y}Mn_{2-y}O_4$ ($0 < x < 1$, $0 \leqslant y \leqslant 0.33$) for Lithium Batteries**. Electrochem. Commun. **2005**, 7, 528–536.

(62) Kalyani, P.; Chitra, S.; Mohan, T.; Gopukumar, S. **Lithium Metal Rechargeable Cells Using Li_2MnO_3 as the Positive Electrode**. J. Power Sources **1999**, 80, 103–106.

(63) Tarascon, J. M.; Vaughan, G.; Chabre, Y.; Seguin, L.; Anne, M.; Strobel, P.; Amatucci, G. **In Situ Structural and Electrochemical Study of $Ni_{1-x}Co_xO_2$ Metastable Oxides Prepared by Soft Chemistry**. J. Solid State Chem. **1999**, 147, 410–420.

(64) Armstrong, A. R.; Holzapfel, M.; Nova, P.; Kang, S.-H.; Thackeray, M. M.; Bruce, P. G. **Demonstrating Oxygen Loss and Associated Structural Reorganization in the Lithium Battery Cathode $Li[Ni_{0.2}Li_{0.2}Mn_{0.6}]O_2$.** J. Am. Chem. Soc. 2006, 128, 8694-8698.

(65) Koga, H.; Croguennec, L.; Ménétrier, M.; Douhil, K.; Belin, S.; Bourgeois, L.; Suard, E.; Weill, F.; Delmas, C. **Reversible Oxygen Participation to the Redox Processes Revealed for $Li_{1.20}Mn_{0.54}Co_{0.13}Ni_{0.13}O_2$**. J. Electrochem. Soc. **2013**, 160, A786–A792.

(66) Sathiya, M.; Rousse, G.; Ramesha, K.; Laisa, C. P.; Vezin, H.; Sougrati, M. T.; Doublet, M.-L.; Foix, D.; Gonbeau, D.; Walker, W.; et al. **Reversible Anionic Redox Chemistry in High-Capacity Layered-Oxide Electrodes**. Nat. Mater. **2013**, 12, 827–835.

(67) Qiu, B.; Zhang, M.; Wu, L.; Wang, J.; Xia, Y.; Qian, D.; Liu, H.; Hy, S.; Chen, Y.; An, K.; et al. **Gas–Solid Interfacial Modification of Oxygen Activity in Layered Oxide Cathodes for Lithium-Ion Batteries**. Nat. Commun. **2016**, 7, 12108.

(68) Boulineau, A.; Simonin, L.; Colin, J.-F.; Bourbon, C.; Patoux, S. **First Evidence of Manganese–Nickel Segregation and Densification upon Cycling in Li-Rich Layered Oxides for Lithium Batteries**. Nano Lett. **2013**, 13, 3857–3863.

(69) Assat, G.; Foix, D.; Delacourt, C.; Iadecola, A.; Dedryvère, R.; Tarascon, J.-M. **Fundamental Interplay between Anionic/Cationic Redox Governing the Kinetics and Thermodynamics of Lithium-Rich Cathodes**. Nat. Commun. **2017**, 8, 2219.

(70) Gent, W. E.; Lim, K.; Liang, Y.; Li, Q.; Barnes, T.; Ahn, S.-J.; Stone, K. H.; McIntire, M.; Hong, J.; Song, J. H.; et al. **Coupling between Oxygen Redox and Cation Migration Explains Unusual Electrochemistry in Lithium-Rich Layered Oxides**. Nat. Commun. **2017**, 8, 2091.

(71) Foix, D.; Sathiya, M.; McCalla, E.; Tarascon, J.-M.; Gonbeau, D. **X-Ray Photoemission Spectroscopy Study of Cationic and Anionic Redox Processes in High-Capacity Li-Ion Battery Layered-Oxide Electrodes**. J. Phys. Chem. C. **2016**, 120, 862–874.

(72) Sathiya, M.; Leriche, J.-B.; Salager, E.; Gourier, D.; Tarascon, J.-M.; Vezin, H. Electron **Paramagnetic Resonance Imaging for Real-Time Monitoring of Li-Ion Batteries**. Nat. Commun. **2015**, 6, 6276.
(73) McCalla, E.; Abakumov, A. M.; Saubanère, M.; Foix, D.; Berg, E. J.; Rousse, G.; Doublet, M.-L.; Gonbeau, D.; Novák, P.; Van Tendeloo, G.; et al. **Visualization of O-O Peroxo-like Dimers in High-Capacity Layered Oxides for Li-Ion Batteries**. Science. **2015**, 350, 1516.
(74) Assat, G.; Delacourt, C.; Dalla Corte, D. A.; Tarascon, J.-M. **Editors' Choice—Practical Assessment of Anionic Redox in Li-Rich Layered Oxide Cathodes: A Mixed Blessing for High Energy Li-Ion Batteries**. J. Electrochem. Soc. **2016**, 163, A2965–A2976.
(75) Assat, G.; Tarascon, J.-M. **Fundamental Understanding and Practical Challenges of Anionic Redox Activity in Li-Ion Batteries**. Nat. Energy **2018**, 3, 373–386.
(76) Luo, K.; Roberts, M. R.; Hao, R.; Guerrini, N.; Pickup, D. M.; Liu, Y.-S.; Edström, K.; Guo, J.; Chadwick, A. V.; Duda, L. C.; et al. **Charge-Compensation in 3d-Transition-Metal-Oxide Intercalation Cathodes through the Generation of Localized Electron Holes on Oxygen**. Nat. Chem. **2016**, 8, 684–691.
(77) Yabuuchi, N.; Nakayama, M.; Takeuchi, M.; Komaba, S.; Hashimoto, Y.; Mukai, T.; Shiiba, H.; Sato, K.; Kobayashi, Y.; Nakao, A.; et al. **Origin of Stabilization and Destabilization in Solid-State Redox Reaction of Oxide Ions for Lithium-Ion Batteries**. Nat. Commun. **2016**, 7, 13814.
(78) Seo, D.-H.; Lee, J.; Urban, A.; Malik, R.; Kang, S.; Ceder, G. **The Structural and Chemical Origin of the Oxygen Redox Activity in Layered and Cation-Disordered Li-Excess Cathode Materials**. Nat. Chem. **2016**, 8, 692-697.
(79) Xie, Y.; Saubanère, M.; Doublet, M.-L. **Requirements for Reversible Extra-Capacity in Li-Rich Layered Oxides for Li-Ion Batteries**. Energy Env. Sci **2017**, 10, 266–274.
(80) Becke, A. D.; Edgecombe, K. E. **A Simple Measure of Electron Localization in Atomic and Molecular Systems**. J. Chem. Phys. **1990**, 92, 5397–5403.
(81) Savin, A.; Jepsen, O.; Flad, J.; Andersen, O. K.; Preuss, H.; von Schnering, H. G. **Electron Localization in Solid-State Structures of the Elements: The Diamond Structure**. Angew. Chem. Int. Ed. Engl. **1992**, 31, 187–188.
(82) Ben Yahia, M.; Vergnet, J.; Saubanère, M.; Doublet, M.-L. **Unified Picture of Anionic Redox in Li/Na-Ion Batteries**. Submitted **2018**.
(83) Zaanen, J.; Sawatzky, G. A.; Allen, J. W. **Band Gaps and Electronic Structure of Transition-Metal Compounds**. Phys. Rev. Lett. **1985**, 55, 418–421.
(84) Hubbard, J. **Electron Correlations in Narrow Energy Bands**. Proc R Soc Lond A **1963**, 276, 238–257.
(85) Rouxel, J. **The Importance of Anions in Redox-Type Chimie Douce**. Mol. Cryst. Liq. Cryst. **1998**, 310, 1–4.
(86) Rouxel, J. **Anion–Cation Redox Competition and the Formation of New Compounds in Highly Covalent Systems**. Chem. – Eur. J. **1996**, 2, 1053–1059.
(87) Mizokawa, T.; Namatame, H.; Fujimori, A.; Akeyama, K.; Kondoh, H.; Kuroda, H.; Kosugi, N. **Origin of the Band Gap in the Negative Charge-Transfer-Energy Compound $NaCuO_2$**. Phys. Rev. Lett. **1991**, 67, 1638–1641.
(88) Saubanère, M.; McCalla, E.; Tarascon, J.-M.; Doublet, M.-L. **The Intriguing Question of Anionic Redox in High-Energy Density Cathodes for Li-Ion Batteries**. Energy Env. Sci **2016**, 9, 984–991.
(89) Zhan, C.; Yao, Z.; Lu, J.; Ma, L.; Maroni, V. A.; Li, L.; Lee, E.; Alp, E. E.; Wu, T.; Wen, J.; et al. **Enabling the High Capacity of Lithium-Rich Anti-Fluorite Lithium**

Iron Oxide by Simultaneous Anionic and Cationic Redox. Nat. Energy **2017**, 2, 963–971.

(90) Perez, A. J.; Jacquet, Q.; Batuk, D.; Iadecola, A.; Saubanère, M.; Rousse, G.; Larcher, D.; Vezin, H.; Doublet, M.-L.; Tarascon, J.-M. **Approaching the Limits of Cationic and Anionic Electrochemical Activity with the Li-Rich Layered Rocksalt Li_3IrO_4**. Nat. Energy **2017**, 2, 954.

(91) Jacquet, Q.; Perez, A.; Batuk, D.; Van Tendeloo, G.; Rousse, G.; Tarascon, J.-M. **The $Li_3Ru_yNb_{1-y}O_4$ ($0 \leq y \leq 1$) System: Structural Diversity and Li Insertion and Extraction Capabilities**. Chem. Mater. **2017**, 29, 5331–5343.

(92) Jacquet, Q.; Rousse, G.; Iadecola, A.; Saubanère, M.; Doublet, M.-L.; Tarascon, J.-M. **Electrostatic Interactions versus Second Order Jahn–Teller Distortion as the Source of Structural Diversity in Li_3MO_4 Compounds (M = Ru, Nb, Sb and Ta)**. Chem. Mater. **2017**, 30, 392–402.

(93) Jacquet, Q.; Iadecola, A.; Saubanère, M.; Lemarquis, L.; Berg, E. J.; Alves Dalla Corte, D.; Rousse, G.; Doublet, M.-L.; Tarascon, J.-M. **Competition between Metal Dissolution and Gas Release in Li-Rich $Li_3Ru_yIr_{1-y}O_4$ Model Compounds Showing Anionic Redox**. Chem. Mater. **2018**, just accepted.

(94) Ukei, K.; Suzuki, H.; Shishido, T.; Fukuda, T. **Li_3NbO_4**. Acta Crystallogr. C **1994**, 50, 655–656.

(95) Alexander, A.; Battle, P. D.; Burley, J. C.; Gallon, D. J.; Grey, C. P.; Kim, S. H. **Structural and Magnetic Properties of Li_3RuO_4**. J. Mater. Chem. **2003**, 13, 2612.

(96) Skakle, J. M.; Castellanos, M. A., Tovar, S. T.; Fray, S. M.; West, A. R. **The Crystal Structure of Li_3SbO_4**. J. Mater. Chem. **1996**, 6, 1939–1942.

(97) Du Boulay, D.; Sakaguchi, A.; Suda, K.; Ishizawa, N. **Reinvestigation of β-Li_3TaO_4**. Acta Crystallogr. Sect. E **2003**, 59, i80–i82.

(98) Zocchi, M.; Gatti, M.; Santoro, A.; Roth, R. S. **Neutron and X-Ray Diffraction Study on Polymorphism in Lithium Orthotantalate, Li_3TaO_4**. J. Solid State Chem. **1983**, 48, 420–430.

(99) Mather, G. C.; Dussarrat, C.; Etourneau, J.; West, A. R. **A Review of Cation-Ordered Rock Salt Superstructure Oxides**. J. Mater. Chem. **2000**, 10, 2219–2230.

(100) Shannon, R. D. **Revised Effective Ionic Radii and Systematic Studies of Interatomic Distances in Halides and Chalcogenides**. Acta Crystallogr. Sect. A **1976**, 32, 751–767.

(101) Klein, W.; Jansen, M. **Trisilver Oxoruthenate(V), Ag_3RuO_4**. Acta Crystallogr. Sect. C **2005**, 61, i1–i2.

(102) Kunz, M.; David Brown, I. **Out-of-Center Distortions around Octahedrally Coordinated D0 Transition Metals**. Journal of Solid State Chemistry. 1995, 115, pp 395–406.

(103) Ok, K. M.; Halasyamani, P. S.; Casanova, D.; Llunell, M.; Alemany, P.; Alvarez, S. **Distortions in Octahedrally Coordinated d^0 Transition Metal Oxides: A Continuous Symmetry Measures Approach**. Chem. Mater. **2006**, 18, 3176–3183.

(104) Casas-Cabanas, M.; Kim, C.; Rodríguez-Carvajal, J.; Cabana, J. **Atomic Defects during Ordering Transitions in $LiNi_{0.5}Mn_{1.5}O_4$ and Their Relationship with Electrochemical Properties**. J Mater Chem A **2016**, 4, 8255–8262.

(105) Bader, R. F. W.; Nguyen-Dang, T. T. **Quantum Theory of Atoms in Molecules–Dalton Revisited**. In Advances in Quantum Chemistry; Löwdin, P.-O., Ed.; Academic Press, 1981; Vol. 14, pp 63–124.

(106) Connick, R. E.; Hurley, C. R. **Chemistry of Ru (VI),-(VII) and-(VIII). Reactions, Oxidation Potentials and Spectra**. J. Am. Chem. Soc. **1952**, 74, 5012–5015.

(107) Plietker, B. **Selectivity versus Reactivity - Recent Advances in RuO4 - Catalysed Oxidations**. Synthesis. 2005, 15, 2453-2472.

(108) Castel, E.; Berg, E. J.; El Kazzi, M.; Novák, P.; Villevieille, C. **Differential Electrochemical Mass Spectrometry Study of the Interface of $xLi_2MnO_3 \cdot (1-x)LiMO_2$ (M = Ni, Co, and Mn) Material as a Positive Electrode in Li-Ion Batteries**. Chem. Mater. **2014**, 26, 5051–5057.

(109) Renfrew, S. E.; McCloskey, B. D. **Residual Lithium Carbonate Predominantly Accounts for First Cycle CO_2 and CO Outgassing of Li-Stoichiometric and Li-Rich Layered Transition-Metal Oxides**. J. Am. Chem. Soc. **2017**, 139, 17853–17860.

(110) Massart, D. L., Desiré L.; 1941-. Handbook of Chemometrics and Qualimetrics; Elsevier, 1997.

(111) Juan, A. de; Jaumot, J.; Tauler, R. **Multivariate Curve Resolution (MCR). Solving the Mixture Analysis Problem**. Anal. Methods **2014**, 6, 4964–4976.

(112) Kimber, S. A. J.; Mazin, I. I.; Shen, J.; Jeschke, H. O.; Streltsov, S. V.; Argyriou, D. N.; Valentí, R.; Khomskii, D. I. **Valence Bond Liquid Phase in the Honeycomb Lattice Material Li_2RuO_3**. Phys. Rev. B **2014**, 89, 081408.

(113) Mogare, K. M.; Friese, K.; Klein, W.; Jansen, M. **Syntheses and Crystal Structures of Two Sodium Ruthenates: Na_2RuO_4 and Na_2RuO_3**. Z. Für Anorg. Allg. Chem. **2004**, 630, 547–552.

(114) Rozier, P.; Sathiya, M.; Paulraj, A.-R.; Foix, D.; Desaunay, T.; Taberna, P.-L.; Simon, P.; Tarascon, J.-M. **Anionic Redox Chemistry in Na-Rich $Na_2Ru_{1-y}Sn_yO_3$ Positive Electrode Material for Na-Ion Batteries**. Electrochem. Commun. **2015**, 53, 29–32.

(115) Mortemard de Boisse, B.; Liu, G.; Ma, J.; Nishimura, S.; Chung, S.-C.; Kiuchi, H.; Harada, Y.; Kikkawa, J.; Kobayashi, Y.; Okubo, M.; et al. **Intermediate Honeycomb Ordering to Trigger Oxygen Redox Chemistry in Layered Battery Electrode**. Nat. Commun. **2016**, 7, 11397.

(116) Perez, A. J.; Batuk, D.; Saubanère, M.; Rousse, G.; Foix, D.; McCalla, E.; Berg, E. J.; Dugas, R.; H. W. van den Bos, K.; Doublet, M.-L.; et al. **Strong Oxygen Participation in the Redox Governing the Structural and Electrochemical Properties of Na-Rich Layered Oxide Na_2IrO_3**. Chem. Mater. **2016**, 28, 8278–8288.

(117) Maitra, U.; House, R. A.; Somerville, J. W.; Tapia-Ruiz, N.; Lozano, J. G.; Guerrini, N.; Hao, R.; Luo, K.; Jin, L.; Pérez-Osorio, M. A.; et al. **Oxygen Redox Chemistry without Excess Alkali-Metal Ions in $Na_{2/3}[Mg_{0.28}Mn_{0.72}]O_2$**. Nat. Chem. **2018**, 10, 288–295.

(118) Bai, X.; Sathiya, M.; Mendoza-Sánchez, B.; Iadecola, A.; Vergnet, J.; Dedryvère, R.; Saubanère, M.; Abakumov, A. M.; Rozier, P.; Tarascon, J.-M. **Anionic Redox Activity in a Newly Zn-Doped Sodium Layered Oxide P2-$Na_{2/3}Mn_{1-y}Zn_yO_2$ ($0 < y < 0.23$)**. Adv. Energy Mater. **2018**, just accepted.

(119) Regan, K. A.; Huang, Q.; Cava, R. J. I**solated Spin 3/2 Plaquettes in Na3RuO4**. J. Solid State Chem. **2005**, 178, 2104–2108.

(120) Mogare, K. M.; Sheptyakov, D. V.; Bircher, R.; Güdel, H.-U.; Jansen, M. **Neutron Diffraction Study of the Magnetic Structure of Na_2RuO_4**. Eur. Phys. J. B **2006**, 52, 371–376.

(121) Darriet, J. **Sur Les Composés Na_3TO_4 (T = Nb, Ta et Ru). Structure Cristalline de Na_3NbO_4**. Bull. Société Fr. Minéralogie Cristallogr. **1974**, 97, 3–5.

(122) Fischer, D.; Hoppe, R.; Mogare, K. M.; Jansen, M. Syntheses, **Crystal Structures and Magnetic Properties of Rb_2RuO_4 and K_2RuO_4**. Z. Für Naturforschung B **2014**, 60, 1113–1117.

(123) Stephen, H.; Stephen, T. **Solubilities of Inorganic and Organic Compounds**; Oxford: Pergamon Press; 1963.
(124) Marjerrison, C. A.; Mauws, C.; Sharma, A. Z.; Wiebe, C. R.; Derakhshan, S.; Boyer, C.; Gaulin, B. D.; Greedan, J. E. **Structure and Magnetic Properties of $KRuO_4$**. Inorg. Chem. **2016**, 55, 12897–12903.
(125) Rard, J. **Chemistry and Thermodynamics of Ruthenium and Some of Its Organic Compounds and Aqueous Species**. Chem Rev **1985**, 85, 1–39.
(126) Tolbert, S. H.; Alivisatos, A. P. **Size Dependence of a First Order Solid-Solid Phase Transition: The Wurtzite to Rock Salt Transformation in CdSe Nanocrystals**. Science **1994**, 265, 373–376.
(127) Edwards, A. L.; Drickamer, H. G. **Effect of Pressure on the Absorption Edges of Some III-V, II-VI, and I-VII Compounds**. Phys. Rev. **1961**, 122, 1149–1157.
(128) Bassett, W. A.; Takahashi, T.; Mao, H.; Weaver, J. S. **Pressure-Induced Phase Transformation in NaCl**. J. Appl. Phys. **1968**, 39, 319–325.
(129) Stishov, S. M.; Popova, S. V. **New Dense Polymorphic Modification of Silica**. Geokhimiya **1961**, 10, 837–839.
(130) Jain, A.; Hautier, G.; Ong, S. P.; Moore, C. J.; Fischer, C. C.; Persson, K. A.; Ceder, G. **Formation Enthalpies by Mixing GGA and GGA + U Calculations**. Phys. Rev. B **2011**, 84, 045115.
(131) Adamczyk, E.; Pralong, V. $Na_2Mn_3O_7$: **A Suitable Electrode Material for Na-Ion Batteries?** Chem. Mater. **2017**, 29, 4645–4648.
(132) Mortemard de Boisse, B.; Nishimura, S.; Watanabe, E.; Lander, L.; Tsuchimoto, A.; Kikkawa, J.; Kobayashi, E.; Asakura, D.; Okubo, M.; Yamada, **A. Highly Reversible Oxygen-Redox Chemistry at 4.1 V in $Na_{4/7-x}[\square_{1/7}Mn_{6/7}]O_2$ (□: Mn Vacancy)**. Adv. Energy Mater. **2018**, 8, 1800409.
(133) Yabuuchi, N.; Takeuchi, M.; Nakayama, M.; Shiiba, H.; Ogawa, M.; Nakayama, K.; Ohta, T.; Endo, D.; Ozaki, T.; Inamasu, T.; et al. **High-Capacity Electrode Materials for Rechargeable Lithium Batteries: Li_3NbO_4-Based System with Cation-Disordered Rocksalt Structure**. Proc. Natl. Acad. Sci. **2015**, 112, 7650–7655.
(134) Lee, J.; Urban, A.; Li, X.; Su, D.; Hautier, G.; Ceder, G. **Unlocking the Potential of Cation-Disordered Oxides for Rechargeable Lithium Batteries**. Science **2014**, 343, 519–522.
(135) Lee, J.; Seo, D.-H.; Balasubramanian, M.; Twu, N.; Li, X.; Ceder, G. **A New Class of High Capacity Cation-Disordered Oxides for Rechargeable Lithium Batteries: Li–Ni–Ti–Mo Oxides**. Energy Env. Sci **2015**, 8, 3255–3265.
(136) Zhao, W.; Yamaguchi, K.; Sato, T.; Yabuuchi, N. **$Li_{4/3}Ni_{1/3}Mo_{1/3}O_2$– $LiNi_{1/2}Mn_{1/2}O_2$ Binary System as High Capacity Positive Electrode Materials for Rechargeable Lithium Batteries**. J. Electrochem. Soc. **2018**, 165, A1357–A1362.
(137) Kumakura, S.; Komaba, S.; Kubota, K. **Li_4MeWO_6 (Me=Ni, Mn, Co) As Positive Electrode Materials for Li-Ion Batteries.** Meet. Abstr. **2015**, MA2015-02, 481–481.
(138) Yabuuchi, N.; Tahara, Y.; Komaba, S.; Kitada, S.; Kajiya, Y. **Synthesis and Electrochemical Properties of Li_4MoO_5-NiO Binary System as Positive Electrode Materials for Rechargeable Lithium Batteries**. Chem. Mater. **2015**, 28, 416–419.
(139) COLIN, J.-F.; Bourbon, C.; JACQUET, Q. **Cathode Material for Li-Ion Batteries**. WO2017098113A1, June 15, 2017.
(140) Urban, A.; Abdellahi, A.; Dacek, S.; Artrith, N.; Ceder, G. **Electronic-Structure Origin of Cation Disorder in Transition-Metal Oxides**. Phys. Rev. Lett. **2017**, 119, 176402.

(141) Yang, L.; Ravdel, B.; Lucht, B. L. **Electrolyte Reactions with the Surface of High Voltage $LiNi_{0.5}Mn_{1.5}O_4$ Cathodes for Lithium-Ion Batteries**. Electrochem. Solid-State Lett. **2010**, 13, A95–A97.

(142) de' Medici, L. **Hund's Coupling and Its Key Role in Tuning Multiorbital Correlations**. Phys. Rev. B **2011**, 83, 205112.

(143) Ji, H.; Urban, A.; Kitchaev, D. A.; Kwon, D.-H.; Artrith, N.; Ophus, C.; Huang, W.; Cai, Z.; Shi, T.; Kim, J. C.; et al. **Hidden Structural Order Controls Li-Ion Transport in Cation-Disordered Oxides for Rechargeable Lithium Batteries**. ArXiv180606096 Cond-Mat **2018**.

(144) Lee, J.; Papp, J. K.; Clément, R. J.; Sallis, S.; Kwon, D.-H.; Shi, T.; Yang, W.; McCloskey, B. D.; Ceder, G. **Mitigating Oxygen Loss to Improve the Cycling Performance of High Capacity Cation-Disordered Cathode Materials**. Nat. Commun. **2017**, 8, 981.

(145) Sathiya, M.; Ramesha, K.; Rousse, G.; Foix, D.; Gonbeau, D.; Guruprakash, K.; Prakash, A. S.; Doublet, M. L.; Tarascon, J.-M. **Li_4NiTeO_6 as a Positive Electrode for Li-Ion Batteries**. Chem. Commun. **2013**, 49, 11376.

(146) Twu, N.; Li, X.; Urban, A.; Balasubramanian, M.; Lee, J.; Liu, L.; Ceder, G. **Designing New Lithium-Excess Cathode Materials from Percolation Theory: Nanohighways in $Li_xNi_{2-4x/3}Sb_{x/3}O_2$**. Nano Lett. **2015**, 15, 596–602.

(147) Hiley, C. I.; Lees, M. R.; Fisher, J. M.; Thompsett, D.; Agrestini, S.; Smith, R. I.; Walton, R. I. **Ruthenium(V) Oxides from Low-Temperature Hydrothermal Synthesis**. Angew. Chem. Int. Ed. **2014**, 53, 4423–4427.

(148) Grimaud, A.; Diaz-Morales, O.; Han, B.; Hong, W. T.; Lee, Y.-L.; Giordano, L.; Stoerzinger, K. A.; Koper, M. T. M.; Shao-Horn, Y. **Activating Lattice Oxygen Redox Reactions in Metal Oxides to Catalyse Oxygen Evolution**. Nat. Chem. **2017**, 9, 457–465.

(149) Grimaud, A.; May, K. J.; Carlton, C. E.; Lee, Y.-L.; Risch, M.; Hong, W. T.; Zhou, J.; Shao-Horn, Y. **Double Perovskites as a Family of Highly Active Catalysts for Oxygen Evolution in Alkaline Solution**. Nat. Commun. **2013**, 4, 2439.

(150) Hong, W. T.; Stoerzinger, K. A.; Lee, Y.-L.; Giordano, L.; Grimaud, A.; Johnson, A. M.; Hwang, J.; Crumlin, E. J.; Yang, W.; Shao-Horn, Y. **Charge-Transfer-Energy-Dependent Oxygen Evolution Reaction Mechanisms for Perovskite Oxides**. Energy Environ. Sci. **2017**, 10, 2190–2200.

(151) Grimaud, A.; Hong, W. T.; Shao-Horn, Y.; Tarascon, J.-M. **Anionic Redox Processes for Electrochemical Devices**. Nat. Mater. **2016**, 15, 121–126.

(152) Yang, W.; Devereaux, T. P. **Anionic and Cationic Redox and Interfaces in Batteries: Advances from Soft X-Ray Absorption Spectroscopy to Resonant Inelastic Scattering**. J. Power Sources **2018**, 389, 188–197.

(153) Cava, R. J.; Hewat, A. W.; Hewat, E. A.; Batlogg, B.; Marezio, M.; Rabe, K. M.; Krajewski, J. J.; Peck, W. F.; Rupp, L. W. **Structural Anomalies, Oxygen Ordering and Superconductivity in Oxygen Deficient $Ba_2YCu_3O_x$**. Phys. C Supercond. **1990**, 165, 419–433.

(154) Guo, Y.; Langlois, J.-M.; Goddard, W. A. **Electronic Structure and Valence-Bond Band Structure of Cuprate Superconducting Materials**. Science **1988**, 239, 896–899.

(155) Arčon, D.; Anderle, K.; Klanjšek, M.; Sans, A.; Mühle, C.; Adler, P.; Schnelle, W.; Jansen, M.; Felser, C. **Influence of O_2 Molecular Orientation on p-Orbital Ordering and Exchange Pathways in Cs_4O_6**. Phys. Rev. B **2013**, 88, 224409.

(156) Knaflič, T.; Klanjšek, M.; Sans, A.; Adler, P.; Jansen, M.; Felser, C.; Arčon, D. **One-Dimensional Quantum Antiferromagnetism in the p-Orbital CsO_2 Compound Revealed by Electron Paramagnetic Resonance**. Phys. Rev. B **2015**, 91, 174419.
(157) Khomskii, D. **Unusual Valence, Negative Charge-Transfer Gaps and Self-Doping in Transition-Metal Compounds**. ArXivcond-Mat0101164 **2001**.
(158) Torrance, J. B.; Lacorre, P.; Nazzal, A. I.; Ansaldo, E. J.; Niedermayer, C. **Systematic Study of Insulator-Metal Transitions in Perovskites $RNiO_3$ (R=Pr,Nd,Sm,Eu) Due to Closing of Charge-Transfer Gap**. Phys. Rev. B **1992**, 45, 8209–8212.
(159) Subedi, A.; Peil, O. E.; Georges, A. **Low-Energy Description of the Metal-Insulator Transition in the Rare-Earth Nickelates**. Phys. Rev. B **2015**, 91, 075128.
(160) Morcrette, M.; Chabre, Y.; Vaughan, G.; Amatucci, G.; Leriche, J.-B.; Patoux, S.; Masquelier, C.; Tarascon, J.-M. **In Situ X-Ray Diffraction Techniques as a Powerful Tool to Study Battery Electrode Materials**. Electrochimica Acta **2002**, 47, 3137–3149.
(161) Rodríguez-Carvajal, J. **Recent Advances in Magnetic Structure Determination by Neutron Powder Diffraction**. Phys. B Condens. Matter **1993**, 192, 55–69.
(162) Lepoivre, F.; Grimaud, A.; Larcher, D.; Tarascon, J.-M. **Long-Time and Reliable Gas Monitoring in Li-O2 Batteries via a Swagelok Derived Electrochemical Cell**. J. Electrochem. Soc. **2016**, 163, A923–A929.
(163) Briois, V.; La Fontaine, C.; Belin, S.; Barthe, L.; Moreno, T.; Pinty, V.; Carcy, A.; Girardot, R.; Fonda, E. **ROCK: The New Quick-EXAFS Beamline at SOLEIL**. J. Phys. Conf. Ser. **2016**, 712, 012149.
(164) Ravel, B.; Newville, **M. ATHENA, ARTEMIS, HEPHAESTUS: Data Analysis for X-Ray Absorption Spectroscopy Using IFEFFIT**. J. Synchrotron Radiat. **2005**, 12, 537–541.
(165) Kresse, G.; Furthmüller, J. **Efficiency of Ab-Initio Total Energy Calculations for Metals and Semiconductors Using a Plane-Wave Basis Set** - ScienceDirect. Computational Materials Science. 6th ed. 1996, pp 15–50.
(166) Kresse, G.; Hafner, J. **Ab Initio Molecular Dynamics for Liquid Metals**. Physical Review B. **1993**, 48, 558.
(167) Perdew, J. P.; Burke, K.; Ernzerhof, M. **Generalized Gradient Approximation Made Simple**. Phys. Rev. Lett. **1996**, 77, 3865–3868.
(168) Dudarev, S. L.; Botton, G. A.; Savrasov, S. Y.; Humphreys, C. J.; Sutton, A. P. **Electron-Energy-Loss Spectra and the Structural Stability of Nickel Oxide: An LSDA+ U Study**. Phys. Rev. B **1998**, 57, 1505.
(169) Fontaine, D. D. **Cluster Approach to Order-Disorder Transformations in Alloys**. In Solid State Physics; Elsevier, 1994; Vol. 47, pp 33–176.
(170) Ceder, G.; Ven, A. V. der; Marianetti, C.; Morgan, D. **First-Principles Alloy Theory in Oxides**. Model. Simul. Mater. Sci. Eng. **2000**, 8, 311–321.
(171) Ong, S. P.; Richards, W. D.; Jain, A.; Hautier, G.; Kocher, M.; Cholia, S.; Gunter, D.; Chevrier, V. L.; Persson, K. A.; Ceder, G. **Python Materials Genomics (Pymatgen): A Robust, Open-Source Python Library for Materials Analysis**. Comput. Mater. Sci. **2013**, 68, 314–319.
(172) Hart, G. L. W.; Nelson, L. J.; Forcade, R. W. **Generating Derivative Structures at a Fixed Concentration**. Comput. Mater. Sci. **2012**, 59, 101–107.
(173) He, M. **Elucidating Interface Reactions in Li-Ion Batteries and Supercapacitors by in Situ Gas Analysis. Doctoral Thesis**, ETH Zurich, 2016.

Li-rich Li_3MO_4 model compounds for deciphering capacity and voltage aspects in anionic redox electrodes for Li-ion Batteries

Abstract

Global warming, due to the increasing CO_2 concentration in the atmosphere, is a major issue of the 21th century. Fossil fuel based energy production and transportation represent 60% of the overall CO_2 emissions, hence the need to move towards the use of renewable energies for which electrical storage devices are mandatory. Among the existing technologies, Li-ion batteries show the best performances which still needs to be improved to ensure the market penetration of electric vehicle and widespread the use of solar farms. Along that line, a new electrode material called Li-rich NMCs have been developed, having higher capacity, 290 mAh/g, than commercial materials, like $LiCoO_2$ (150 mAh/g), thanks to participation of oxygen anions into the redox reaction. This process, called anionic redox, unfortunately comes with voltage hysteresis preventing the commercialization of Li-rich NMC. To alleviate this issue while increasing the capacity, fundamental understanding on anionic redox is needed, specifically concerning two points: is anionic redox limited in terms of capacity? And what is the origin of the voltage hysteresis? In a first part, with the aim to assess the limit of anionic redox capacity, we designed new compounds, having enhanced oxygen oxidation behavior, belonging to the A_3MO_4 family (A being Li or Na and with M a mix of Ru, Ir, Nb, Sb or Ta). We performed their synthesis, deeply characterized their structure, and, by studying their charge compensation mechanism, we showed that anionic redox is always limited by either O_2 release or metal dissolution. In a second part, we designed two new materials, $Li_{1.3}Ni_{0.27}Ta_{0.43}O_2$ and $Li_{1.3}Mn_{0.4}Ta_{0.3}O_2$, having different voltage hysteresis, in order to identify the origin of this phenomenon. Coupling spectroscopic techniques with theoretical calculations, we suggest that the electronic structure, namely the size of the charge transfer band gap, plays a decisive role in voltage hysteresis.

Keywords: Li-ion, Na-ion, cathode materials, transition metal oxides

Composés modèles Li_3MO_4 pour comprendre l'impact du réseau anionique sur la capacité et le potentiel des électrodes de batteries Li-ion

Résumé:

Le réchauffement climatique, provoqué par l'augmentation de la concentration de CO_2 dans l'atmosphère, est un problème majeur du 21ème siècle. Sachant que 60% de la production de CO_2 provient de la combustion de matériaux fossiles dans les secteurs de la production d'énergie et du transport, il est d'une importance capitale de valoriser l'utilisation des énergies renouvelables. A cause de la nature intermittente des énergies renouvelables, les technologies de conversion d'énergie doivent nécessairement s'accompagner de dispositif de stockage. Parmi les dispositifs existants, les batteries Li-ion possèdent la plus grande densité d'énergie, ce qui explique leur incroyable développement durant ces vingt dernières années. Néanmoins, leurs performances doivent encore être améliorées pour permettre, par exemple, une plus grande pénétration du marché de la voiture électrique ou le développement à grande échelle des fermes solaires. Suivant ce but, les chercheurs ont mis au point un nouveau matériau d'électrode, le Li-rich NMC, permettant d'atteindre une capacité de 290 mAh/g, deux fois plus élevée que celle des matériaux commerciaux tels que le $LiCoO_2$ (150 mAh/g). Cette augmentation de capacité est due à la participation des oxygènes du réseau dans la réaction électrochimique, appelée la redox anionique. Malheureusement, le Li-rich NMC souffre d'une hystérésis de potentiel qui empêche sa commercialisation. Afin de proposer une solution à l'hystérésis de potentiel tout en continuant à augmenter la capacité des matériaux de cathode, des études fondamentales sont nécessaires. En particulier, les points suivants sont étudiés : la redox anionique a-t-elle une limite de capacité ? et, quelle est l'origine de l'hystérésis ? Pour répondre à la première question, nous avons conçu des matériaux ayant une redox anionique exacerbée, de composition chimique A_3MO_4 (A étant du Li ou Na, et M un mix de Ru, Sb, Nb, Ta ou Ir). Après avoir caractérisé la structure de ces nouveaux matériaux, nous avons étudié leur mécanisme électrochimique et montré que la redox anionique est limitée par la décomposition du matériaux via formation de O_2 ou dissolution. Dans un second temps, par l'étude de deux nouveaux matériaux, $Li_{1.3}Ni_{0.27}Ta_{0.43}O_2$ et $Li_{1.3}Mn_{0.4}Ta_{0.3}O_2$ ayant des hystérésis de potentiel très différentes, nous avons montré le lien entre la redox anionique, les propriétés électroniques du matériaux, notamment la taille de la bande interdite définie par le transfert de charge, et l'hystérésis de potentiel.

Mots-clefs: Li-ion, Na-ion, cathode, oxide de métaux de transition